Investigating the vestibular and optokinetic systems: insights from neural recording, behavior, and modeling

Mohammad Mohammadi

Department of Biomedical Engineering

McGill University

Montreal, Quebec, Canada

August 15, 2023

A thesis submitted to McGill University in partial fulfillment of the requirements of the degree of Doctorate in Philosophy

Table of Contents

ABSTRACT

By detecting head motion in space, the vestibular system generates reflexes required for stabilizing gaze and posture and mediates our subjective sense of self-motion and orientation. Previous studies have characterized the neural response and substrates underlying the vestibular functions and their environmental adaptations. Yet, how such neural populations integrate information to generate reflexes and perception remains elusive primarily due to two reasons: firstly, the previous studies have mainly used single-unit recordings, which ignore the impact of correlated variability in the population coding; secondly, these studies have predominantly used artificial stimuli which are not suited for the study of the possible adaptation of the vestibular system to natural self-motion stimuli. Additionally, the study of simpler animal models such as larval zebrafish is insightful in the systematic understanding of principles of the behavior and linking the function of neural substrates to the activity of neural populations. Such studies substantially benefit from the control system models that have long been used to investigate the vestibular and optokinetic system reflexes across species. Thus, in this thesis, I studied population coding of self-motion perception in monkeys during naturalistic and artificial self-motion. Furthermore, I investigated optokinetic reflex and its adaption in larval zebrafish using control system models.

First, by recording simultaneously from multiple neurons in vestibular nuclei (VN), we demonstrated that trial-to-trial variability is remarkably correlated during naturalistic stimuli contrary to that during artificial stimuli. Moreover, I show that VN neurons display substantial heterogeneity in their response. Using a physiological model incorporating the known properties of vestibular neurons in VN, including the correlation structure and heterogeneity, we demonstrated that noise correlations benefit information transmission when neural populations are heterogeneous. As such, self-motion information was transmitted more efficiently during naturalistic stimulation. Furthermore, we recorded from vestibular neurons in the parietoinsular vestibular cortex (PIVC), revealing that neural variability is decorrelated regardless of the stimuli used. Our model illustrated that decorrelation benefited population coding by reducing redundancies, and thus, population coding of self-motion is efficient in PIVC.

Finally, I propose a control system model that explains the optokinetic response observed in larval zebrafish. The model successfully explains the gradual reduction in the slow phase velocity of optokinetic response during unidirectional and bidirectional optokinetic stimulation as well as the reversal in the eye movement after the stimulus is removed. The model also predicts the lack of adaptation during symmetric stimulations. When used to simulate the observed data from individual fish, the model predicts that an innate bias in the neural substrate of the optokinetic system accounts for an asymmetric response during symmetric stimulation.

Taken together, the results from my thesis provide evidence for efficient population coding in the early vestibular pathway. It also signifies the importance of variability and heterogeneity in the neural coding of natural self-motion. My modeling study in larval zebrafish predicts a leaky neural integrator could account for observed adaptation displayed by larval zebrafish during prolonged unilateral and asymmetric bilateral optokinetic stimulation. Notably, the modeling study suggests adaptation has functional relevance to the adjustment of innate disequilibrium in the optokinetic system.

RÉSUMÉ

En détectant les mouvements de la tête dans l'espace, le système vestibulaire génère des réflexes nécessaires pour stabiliser le regard et la posture, et médie notre sensation de deplacement et d'orientation. La réponse neuronale et les substrats sous-jacents des fonctions vestibulaires et de leurs adaptations environnementales ont été characterisé. Cependant, la manière dont les populations neuronales intègrent l'information pour générer des réflexes et des perceptions reste énigmatique principalement pour deux raisons: premièrement, les études antérieures ont principalement utilisé des enregistrements de neurones individuels, ignorant l'impact des corrélations dans le codage de la population; deuxièmement, ces études ont principalement utilisé des stimuli artificiels qui ne conviennent pas à l'étude de l'adaptation du système vestibulaire aux stimuli naturels. De plus, l'étude de modèles animaux plus simples tels que les poissons-zèbres larvaires est éclairante pour la compréhension des principes du comportement et pour relier la fonction à l'activité des populations neuronales. De telles études bénéficient grandement des modèles de systèmes de contrôle qui ont longtemps été utilisés pour étudier les réflexes du système vestibulaire et optokinétique chez différentes espèces. Ainsi, dans cette thèse, j'ai étudié le codage de la perception de deplacement chez les singes lors de deplacement naturels et artificiels. De plus, j'ai étudié le réflexe optokinétique et son adaptation chez les poissons-zèbres larvaires en utilisant des modèles de systèmes de contrôle.

Tout d'abord, en enregistrant simultanément de multiples neurones dans les noyaux vestibulaires (VN), nous avons démontré que la variabilité d'essai en essai est corrélée pendant les stimuli naturels contrairement à celle pendant les stimuli artificiels. De plus, je montre que les neurones VN affichent une hétérogénéité de leur réponse. En utilisant un modèle physiologique incorporant les propriétés des neurones VN, y compris la structure de corrélation et l'hétérogénéité, nous démontrons que les corrélations du bruit bénéficient à la transmission de l'information lorsque les populations sont hétérogènes. En tant que tel, l'information sur le déplacement était transmise plus efficacement pendant la stimulation naturelle. De plus, nous avons enregistré les neurones vestibulaires dans le cortex vestibulaire pariéto-insulaire (PIVC), révélant que la variabilité est décorrélée quel que soit le stimulus utilisé. Notre modèle a illustré que la décorrélation bénéficiait au codage de la

population en réduisant les redondances, et ainsi, le codage de la population du déplacemente est efficace dans le PIVC.

Enfin, je propose un modèle de système de contrôle qui explique la réponse optokinétique observée chez les poissons-zèbres larvaires. Le modèle explique avec succès la réduction graduelle de la vitesse de la phase lente de la réponse optokinétique lors d'une stimulation optokinétique unidirectionnelle et bidirectionnelle. Le modèle prédit également l'absence d'adaptation lors de stimulations symétriques. Lorsqu'il est utilisé pour simuler les données observées, le modèle prédit qu'un biais inné dans le substrat neuronal du système optokinétique explique une réponse asymétrique lors d'une stimulation symétrique.

Dans l'ensemble, les résultats de ma thèse apportent les preuves d'un codage efficace de la population dans la voie vestibulaire précoce. Cela souligne également l'importance de la variabilité et de l'hétérogénéité dans le codage neuronal du mouvement propre naturel. Mon étude de modélisation chez les poissons-zèbres larvaires prédit qu'un intégrateur neuronal fuyant pourrait expliquer l'adaptation lors d'une stimulation optokinétique unilatérale prolongée et d'une stimulation bilatérale asymétrique. Notamment, la modélisation suggère que l'adaptation a une pertinence fonctionnelle pour l'ajustement du déséquilibre inné dans le système optokinétique.

ACKNOWLEDGMENT

I am incredibly fortunate to have had the privilege to collaborate with exceptional individuals throughout my Ph.D. journey. First and foremost, I extend my sincere gratitude to my supervisor, Dr. Maurice J. Chacron. His unwavering dedication, innovative problem-solving approach, and critical thinking, as well as his guidance, patience, and continuous support, have been instrumental in my development as a researcher. Additionally, I wish to express my sincere thanks to my co-supervisor, Dr. Kathleen E. Cullen, for her support and invaluable feedback and discussions and for allowing me to benefit from her mentorship.

I wish to express my thanks to my committee members, Drs. Christopher Pack, Curtis Baker, and Henrieta Galiana for their valuable guidance and support. Their meticulous feedback has proven incredibly beneficial. I've been privileged to collaborate with esteemed colleagues Drs. Melody Huang and Ting-Feng Lin. I am grateful for their assistance with data collection and experiments on larval zebrafish projects.

I would like to say a sincere “thank you” to Dr. Jerome Carriot and Dr. Isabelle Mackrous, two distinguished scientists, for their warm welcome to the lab and their continuous support, encouragement, and mentorship. I will never forget my long discussions with Jerome, who is also the nicest scientist I have ever met, and Isabelle’s warmth and encouragement through research and the challenging times of the Covid era. I would like to extend thanks to Dr. Jessica Brooks for dedicating substantial time during experiments—her remarkable ability to solve problems and provide intuitive insights has been inspiring for me. I would also like to thank Steve Nuara who was always there to care for the animals even when he was on vacation.

I am grateful to have worked with talented lab mates throughout my Ph.D. journey. Graham McAllister with exceptional dedication and integrity, Tabitha Jimenez and Mitchell Prostebby, with encouragement, positivity, and support, and Elisha Krauss with innovative perspectives have been valuable aspects of my experience. I would like to also thank members of the fish lab, Drs. Michael Metzen, Volker Hofmann, Mariana Marquez, as well as Myriah Haggard and Amin Akhshi for their support and constructive feedback on the manuscripts.

Lastly, I reserve a special place of honor in my heart for my parents, Aliakbar Mohammadi and Mahlegha Nasiri, and I am grateful for their incredible support, love, and their many sacrifices. Sarah, you have always stood by me no matter which direction I ventured into, always lending your hand to make my dreams come true. Your love and unwavering support hold a significance that words cannot fully convey. I am grateful to all the support I received from my siblings and friends. I dedicate this thesis to the memory of my father who supported me relentlessly.

-Mohammad

CONTRIBUTION TO ORIGINAL KNOWLEDGE

In this thesis, we first investigated the population coding of natural self-motion in the vestibular system of rhesus macaque monkeys. We found that in the early vestibular pathway, neurons involved in population coding of self-motion demonstrate remarkably correlated variability in neural activity during naturalistic self-motion, contrary to that during artificial self-motion. Additionally, our findings revealed that the neural activity of these neurons is highly heterogeneous. By incorporating the structure of correlation and the heterogeneity found in our study in a neural population model, we demonstrated that the observed correlation benefit information transmission during naturalistic self-motion. Together, our findings revealed population coding of natural self-motion in the early central pathway is efficient. Furthermore, we investigated population coding of naturalistic self-motion in the cortex. Our findings revealed no correlated variability in the response of these neurons despite a high degree of heterogeneity in neural response. Our modeling study revealed that decorrelation is beneficial to information transmission in the cortex indicative of efficient population coding.

Next, we investigated the optokinetic response of larval zebrafish and proposed a set-point adaptation mechanism that underlies the behavior of animals during the stimulation. First, we used prolonged unidirectional stimulation which robustly elicited an optokinetic response adaptation and negative optokinetic afternystagmus. We incorporated the set-point adaptation into a mathematical model and showed, together with habituation mechanism, set-point adaption indeed explained our experimental findings. In addition to unidirectional stimuli, we exposed the animals to bidirectional stimuli that resembled natural stimuli. Our findings showed that bidirectional stimuli that were sufficiently asymmetric robustly elicited optokinetic response adaptation and negative afternystagmus. As such, we showed that response adaptation and ensuing aftereffects arise in natural settings and are relevant to the animals' physiology. Additionally, we observed some individual larvae may exhibit response adaptation and ensuing aftereffects even during symmetric stimulation. Our model predicted such behavior arises from innate bias in the animals' oculomotor system. As such, our experimental data and model demonstrated that set-point adaptation plays a key role in mitigating such inherent bias and asymmetry in the oculomotor system.

CONTRIBUTION OF AUTHORS

This thesis is the outcome of in-depth discussions with my advisors, Drs. Maurice J. Chacron and Kathleen E. Cullen. Additionally, it involved collaborative efforts with Dr. Ting Feng Lin and Dr. Melody Huang, our partners, in investigating the optokinetic response of larval zebrafish.

As of drafting this thesis, the results in chapters 3 and 4 are submitted for peer review. Mohammadi M, Carriot J, Mackrous I, Cullen KE, Chacron MJ. Population coding in early vestibular pathways is adapted to the statistics of natural self-motion stimuli. For this study, I collected and analyzed the behavioral and multiunit recording data, prepared the figures, and contributed to the preparation of the first draft of the manuscript. Dr. Carriot and Dr. Mackrous assisted with the collection of data. My thesis advisors provided guidance and instructions in all the steps of the study, from experiments to analysis and interpretation of the data and during the drafting of the manuscript.

Chapter 5 contains a published manuscript: Lin TF, Mohammadi M, Fathalla AM, Pul D, Luthi D, Romano F, Straumann D, Cullen KE, Chacron MJ, Huang MYY. Negative optokinetic afternystagmus in larval zebrafish demonstrates set-point adaptation. Scientific Reports 9 (1), 19039, 2019. I analyzed the data, proposed, and constructed the model, prepared the figures, and contributed to the preparation of the manuscript. Dr. Lin designed the research, collected and analyzed the data, prepared the figures, and wrote the manuscript. Ahmed Fathalla, Duygu Pul, and Dennis Luthi contributed to data collection. Fuatso Romano and Dominik Straumann contributed to data analysis, and Dr. Cullen and Dr. Chacron contributed to model design, analysis, and drafting and review of the manuscript. Dr. Huang designed the research, performed analysis, and wrote the manuscript.

Chapter 6 contains a published manuscript: Lin TF, Mohammadi M, Cullen KE, Chacron MJ, Huang MYY. Optokinetic set-point adaptation functions as an internal dynamic calibration mechanism for oculomotor disequilibrium. iScience 25 (11), 2022. I analyzed the data, proposed, and constructed the model, prepared the figures, and contributed to the preparation of the manuscript. Dr. Lin designed the research, collected and analyzed the data, prepared the figures, and wrote the manuscript. Dr. Cullen and Dr. Chacron contributed to the model design, analysis, drafting, and review of the manuscript. Dr. Huang designed the research, performed analysis, and wrote the manuscript.

LIST OF FIGURES

Chapter 1

Chapter 2

Chapter 3

Chapter 4

Chapter 5

Chapter 6

LIST OF TABLES

Chapter 5

Chapter 6

LIST OF ABBREVIATIONS

AA: Asymmetric alternating

ADN: Anterodorsal thalamus

AOS: Accessory optic system

aVOR: Angular vestibulo-ocular reflex

BUH: Body-under-head

CV: Coefficient of variation

DLPN: Dorsolateral pontine nucleus

Dpf: Days post-fertilization

DTN: Dorsal terminal nucleus (OKN pathway)

DTN: Dorsal tegmental nucleus (in anterior pathway)

DVN: Descending vestibular nuclei

EH: Eye-head

ELL: Electrosensory lateral line

EOD: Electric organ discharge

FTN: Floccular target neurons

INS: Infantile nystagmus syndrome

LIF: Leaky integrate-and-fire

LVN: Lateral vestibular nuclei

MIP: Medial intraparietal area

MLN: Manifest latent nystagmus

MSE: Mean squared error

MST: Medial superior temporal

MT: Medial temporal

MVN: Medial vestibular nuclei

NOT: Nucleus of optic tract

NPH: Nucleus propositus hypoglossi

NRTP: Nucleus reticularis tegmenti pontis

OKAN: Optokinetic afternystagmus

OKN: Optokinetic nystagmus

PIVC: Parietoinsular vestibular reflex

pWBR: Passive whole-body rotation

PVP: position-vestibular-pause

QPF: Quick-phase Frequency

SA: Symmetric alternating

SNR: Signal-to-noise ratio

SPV: Slow-phase velocity

SVN: Superior vestibular nuclei

TVOR: Translational vestibulo-ocular reflex

VCR: Vestibulo-colic reflex

VIP: Ventral intraparietal area

VN: vestibular nuclei

VO: Vestibular-only

VOR: Vestibulo-ocular reflex

VORc: Vestibulo-ocular reflex cancelation

VPL: Ventral posterior lateral nucleus

VPS: Visual posterior sylvian

VSR: Vestibulo-spinal reflex

1. GENERAL INTRODUCTION AND LITERATURE REVIEW

1.1 General overview

This thesis investigates how neural responses to sensory stimuli give rise to perception and behavior through data analysis and computational modeling. The main focus is on understanding how vestibular information is encoded and processed in neural populations, particularly in the central vestibular pathway. The vestibular system plays a vital role in stabilizing gaze, maintaining balance, and providing spatial orientation. Unlike other primary senses, such as seeing and hearing, the vestibular sense often goes unnoticed as its sensory apparatus constantly receives stimulus signals (e.g., gravity). However, individuals with impaired vestibular systems can experience issues with balance and vision, impacting their daily activities.

Natural and artificial stimuli present fundamental differences in intensity, spatiotemporal characteristics, and statistical features. Sensory systems have presumably adapted to process natural stimuli more efficiently as they contain inherent redundancies and correlations. Recently, natural vestibular stimuli have been characterized. These stimuli contain a wide range of frequencies and amplitudes and, as such, differ from the sinusoidal head motion stimuli that have been typically used to characterize vestibular processing. While recent studies have demonstrated that some vestibular neurons efficiently encode natural stimuli through temporal whitening, such studies have considered efficient coding at the single-neuron level. As behavior in general results from the activity of neural populations, it remains unknown whether population coding is efficient in the vestibular pathway. As such, in the first part of the thesis, we address the neural computations and principles involved in processing natural stimuli. Using simultaneous recordings from multiple neurons in the central vestibular pathway and a physiological computational model, we investigate whether, and if so, how populations of neurons efficiently encode naturalistic self-motion stimuli and how these population codes contribute to vestibular perception.

In the next step, we go beyond neural ensembles by considering the neural substrate underlying behavior. Specifically, we study how optokinetic response in larval zebrafish during prolonged optokinetic stimulation undergoes adaptation, and a secondary behavior emerges after the stimulus is removed. We propose a mathematical model and a mechanism that explains the observed behavioral data. Such models have been essential in understanding neural circuits involved in eye movements and reflexes.

In the following, I provide a comprehensive review of the relevant literature. Firstly, I review natural stimuli and efficient coding hypotheses across sensory systems. Next, I introduce adaptation as well as the peripheral and central vestibular systems. Following this, I review signal processing in the vestibular system. Following this section, I provide and overview of correlations and their importance in the study of efficient population coding. Finally, I determine the scope of the research and declare my contribution to the manuscript published or submitted to peer-reviewed journals.

1.2 Efficient coding

Through natural selection, organisms have developed biological capacities that are suited to match the characteristics of their environment. Likewise, it is hypothesized that sensory systems have adapted to effectively respond to stimuli naturally occurring in the environment, commonly referred to as natural stimuli. Natural stimuli display correlations in their attributes and are thus redundant. Given constraints on sensory processing (e.g., metabolic costs), it is crucial for neurons and sensory systems, in general, to efficiently and parsimoniously use computational resources during the transmission, processing, and storage of information. As such, it has been hypothesized that through evolution, sensory systems have become adept in processing natural stimuli by removing redundancies in the stimuli and thereby maximising information transmission, commonly referred to as the *efficient coding hypothesis* (Attneave, 1954; Barlow, 1961). Therefore, it is important to study the statistics of natural stimuli and characterize how it shapes neural coding.

1.2.1. Natural visual stimuli and efficient coding

The statistics of natural stimuli have been characterized across sensory modalities. For example, Laughlin demonstrated that the intensity of visual stimuli seen by flies follows a bell curve and that the response of the first-order neurons in the fly's compound eye matches the cumulative integration of this distribution as predicted by optimal coding theory (Laughlin, 1981). Natural images are not random; they demonstrate correlations rendering them redundant (reviewed in (Ruderman, 1994; Simoncelli and Olshausen, 2001)). Indeed, many studies have shown that the spectral power density of the natural images diminish by a power law, $1/f^p$ and the autocorrelation function of intensity decreases with the relative distance of the objects (e.g. pixels) in the scene (Ruderman and Bialek, 1994; Simoncelli and Olshausen, 2001). It should be noted that the studies above do not consider the temporal dynamics of the stimulus as the retinal image of the environment is not static; Instead, due to movements of the animal or the objects in the scene, the local and global features of the images changes through time. Although dynamic natural scene (also referred to as natural movies in the literature) have been studied extensively for computer vision and artificial intelligence applications, its implications in sensory systems have been investigated to lesser extent (Cadieu and Olshausen, 2012; Desbordes et al., 2008; Roberts et al., 2022; Vig et al., 2014; Xia et al., 2021; Zheng et al., 2021).

Efficient coding by the visual system has been observed ubiquitously across brain areas and species (reviewed in (Tesileanu et al., 2022)). As mentioned above, Laughlin was among the first to explore the efficient coding in the visual system using electrophysiological recordings (Laughlin, 1981). By recording from first order interneurons from fly's compound eye, he showed the contrast-response distribution of the neurons was matched to the statistics of the natural scenes. Following upon the same notion, many other studies found signatures of efficient coding of natural visual stimuli at single neurons as well as population level (see for example (Franke et al., 2016; Gupta et al., 2023; Pitkow and Meister, 2012; Simmons et al., 2013); see also (Clifford et al., 2007; Tesileanu et al., 2022) for review).

1.2.2. Natural auditory stimuli and efficient coding

Similarly, auditory stimuli in natural soundscapes are complex compared to pure tones used in earlier studies of the auditory system. Natural sounds are often a blend of sounds from different auditory sources that vary in distance and orientation with respect to the receiver and may contain broad or narrow spectral components (Johannesma and Aertsen, 1982; Nelken et al., 1999). Natural sounds are diverse, yet, the analysis of statistical regularities has shown that most natural sounds exhibit power spectra similar to 1/f (Voss and Clarke, 1975). Similarly, Attias and Schreiner showed that the power spectra of the amplitude of natural sound ensembles decay with frequency and exhibit a power law relation (Attias and Schreiner, 1997). Furthermore, sound ensembles displayed remarkable self-similarity and invariance in the amplitude of the sound differential resolution ranges. As such, natural sound stimuli exhibit correlation across frequencies and are redundant (reviewed in (Gervain and Geffen, 2019)).

There is strong evidence that single neurons and neural populations are tuned to natural sounds so that their response is optimal (Escabí et al., 2003; Garcia-Lazaro et al., 2006; Lewicki, 2002; Machens et al., 2005; Rieke et al., 1995; Woolley et al., 2005). It has been shown that models developed to predict neural responses using pure tones cannot reliably predict the response to more complex natural auditory stimuli ((Carruthers et al., 2013; Laudanski et al., 2012); see also (Mizrahi et al., 2014)). An intriguing finding was observed in a study on zebra finches where their exposure to artificial auditory stimuli after birth resulted in atypical vocalization patterns (Amin et al., 2013). Electrophysiological recordings from these animals demonstrated dramatically increased redundancy in population coding and reduced sensitivity to natural sound features.

1.2.3. Natural somatosensory stimuli and efficient coding

Natural stimuli have widely been used in the study of somatosensory systems. The characterization of vibrations and frictional forces when subjects slide their fingertips over smooth and flat surfaces, have shown that the background noise on vibration signal follows a 1/f trend, signifying the presence of power law in tactile stimuli (Klöcker et al., 2013; Wiertlewski et al., 2011). It is important to note that the tactile signal depends on multiple factors, such as surface texture, scanning speed, and active or passive motion. For example, Manfredi et al. showed that the biomechanics of the fingertip can filter the tactile stimulus and generate vibration stimuli that do not necessarily follow the power law (Manfredi et al., 2014). In their study, they used different fabrics with differential levels of regularities with surface profiles that followed the power law function. The vibrations generated by sliding the fingertip of the surface did not translate on a one-to-one basis; Instead, a pick appeared over the background power spectra at a frequency that increased with the scanning speed. This study, however, was consistent with the study of Wiertlewski et al. (2011), as the background noise resembled that of a power law.

The efficient coding has been studied in rat and mice barrel somatosensory cortex (Adibi et al., 2013; Lee et al., 2020; Panzeri et al., 2001; Petersen et al., 2001). For example, Adibi et al. quantified the effects of adaptation in population coding of whisker vibrations in the whisker-barrel system and found that despite an increase in noise correlation, the adaptation increases information in the population (Adibi et al., 2013). In another study, the same authors showed that noise correlations in rat barrel cortex are detrimental to information. However, a linear optimal decoder that considers noise correlations performed best even when the effect of noise correlations was removed and regardless of the adaptation state of the population. This study signifies that whether the information available to the downstream neurons decreases or increases not only depends on the noise correlations and correlation structure (the relationship between noise and signal correlations; see 1.7) but also on how this information is integrated and decoded in the downstream neurons (Adibi et al., 2014). Panzeri et al. recorded the activity of pairs of neurons from rat barrel cortex and showed that individual spike times accounted for 85% of whisker stimulus location (Panzeri et al., 2001; Petersen et al., 2001). They reported that pairs in the same column demonstrated redundant population coding, whereas pairs in adjacent columns exhibited decorrelated activity.

1.2.4. Natural olfactory stimuli and efficient coding

Studies exploring natural odor scenes are very few, mainly due to the complex nature of the odorants and the diffusion process. Odors are spatially and temporally a function of the turbulence in the air and can be emitted passively and actively by animated and inanimate odor sources. Natural olfactory stimuli are a combination of diverse chemical structures with concentration profiles varying in order of magnitude in a given odorant (Knudsen et al., 1993). The spatiotemporal characteristic of odor plumes, temporal fluctuation and diffusion in the medium, the intensity of the odor, the correlation between odorant concentrations, and the ratio of the natural odorants have been studied extensively (see (Wright and Thomson, 2005) for a comprehensive review).

Recent studies have addressed the efficient coding hypothesis in the olfactory system. Zwicker et al. used a simple model of olfactory receptors to study how the receptor activity encodes the composition of natural odorants and the concentration of the constituents (Zwicker et al., 2016). Based on the data from fly and human olfactory receptors (for which the sensitivity of the receptors is lognormally distributed), they concluded the olfactory system efficiently encodes natural odor stimuli. In another study, Tiberiu et al. leveraged the heterogeneity in receptor types and their lognormal distribution to show that receptor distribution is tuned to the statistics of natural odor stimuli (Teşileanu et al., 2019). Interestingly, their model predicts the change in the distribution of receptors due to exposure to various odorants in mice. Together, these studies and others suggest that the distribution of receptors is matched to the statistics of the natural odor stimuli and changes as the composition of odor stimuli is varied to adapt to the altered stimulus profile.

1.2.5. Natural electrosensory stimuli and efficient coding

Natural electrosensory stimuli are characterized by sinusoidal variations in the amplitude of the fish's electric organ discharge (EOD). Such modulations of the amplitude are referred to as the envelope signal and convey information about the distance and relative orientation when fishes move in close proximity to each other. Metzen and Chacron studied the statistics of natural electrosensory envelopes and demonstrated that over a wide behaviorally relevant range, the statistics of the envelope signal follow a power law relations (Metzen and Chacron, 2014). Interestingly, they reported that the animals altered their EOD to match that of the envelope stimulus. In another study, Fotowat et al. studied the amplitude modulation (first-order statistics) as well as envelope (second-order statistics) of the EOD of freely swimming fish while freely exploring the environment or interacting with conspecifics.

They showed that AM modulation and envelope signals displayed power law statistics indicating spectral invariance (Fotowat et al., 2013).

Recent studies have demonstrated evidence of efficient coding in electrosensory systems. Huang et al. studied the response of pyramidal neurons in the electrosensory lateral line lobe and showed that these neurons response to natural stimuli efficiently through temporal whitening (Huang et al., 2016). Particularly, they showed SK channels enable the neurons to display high-pass tuning properties, which compensates for the power decrease in the frequency domain, thereby whitening the neural response. In another study, Huang et al. investigated the effect of feedback pathways in efficient coding (Huang et al., 2018). They demonstrated that electrosensory lateral line (ELL) pyramidal cells receive feedback input through an indirect pathway that attenuates the response to low-frequency stimuli, thereby resulting in the high-pass tuning property and, subsequently, efficient coding via temporal whitening. Marquez and Chacron studied the effect of serotonin modulation on neural response and found that the application of serotonin increased neural sensitivity due to burst firing (Marquez and Chacron, 2020). As such, neural and behavioral responses to second-order stimuli were optimized. Another study from the same group used multi-unit recording and characterized the correlations in the ELL of electric fish. They found that the correlated variability decreases the transmitted information; however, its spatial dependence mitigates this deleterious effect (Haggard and Chacron, 2023).

1.2.6. Natural vestibular stimuli and efficient coding

The studies of the vestibular system have mainly used artificial stimuli when characterizing the response of the cell to head or eye motion. These stimuli consisted of sinusoidal rotations or translations with magnitudes much lower than that of the animal experiences (Cullen, 2012). Some studies used filtered white noise with a power spectrum resembling that of natural stimuli (Sadeghi et al., 2007a). The latter stimuli resembled natural stimuli in the frequency domain; however, whether the distribution of the amplitude of stimulus was similar to that of natural stimuli remained to be elucidated. Carriot et al. recorded the head movement of human, rhesus macaque monkeys, as well as mice to characterize the statistics of the natural self-motion in these species (Carriot et al., 2014, 2017a; Carriot et al., 2017b). Unlike natural stimuli in other sensory modalities, the natural self-motion stimuli did not exhibit scale invariance characterized by $1/f^a$ power law relation. Instead, the power spectra during translation and rotation decrease faster with higher frequencies. As an exception, the natural translation stimuli for mice displayed the aforementioned scale invariance property. Furthermore, the studies demonstrated that natural stimuli experienced by macaques and humans are similar, whereas they are qualitatively different than that of mice.

Recent studies in the vestibular system using single-unit recordings have provided evidence of efficient coding in early vestibular pathways. In particular, Mitchell et al. recorded from vestibular-only (VO) neurons in vestibular nuclei (VN) of rhesus macaque and reported that these neurons displayed temporally whitened responses when naturalistic head rotation stimuli were used (Mitchell et al., 2018). The demonstrated that variability, together with the high-pass tuning property of the cells, compensated for the decrease in the power of the stimulus to provide a whitened representation of naturalistic self-motion in VN. In a follow-up study, Mackrous et al. recorded the activity of vestibular neurons in VN that mediate vestibulo-ocular reflex (VOR) and its adaptation (Mackrous et al., 2020). They investigated the relation between the variability of neural response and efficient coding and showed that neurons with high variability efficiently encode naturalistic stimuli, whereas neurons with lower variability faithfully encode the stimuli. Efficient coding in the vestibular system at the population level is understood to a lesser extent. While multiunit recordings have reported negligible correlated variability in the early vestibular pathway (Liu et al., 2013; Yu et al., 2014), it is important to note that such studies used artificial stimuli (sinusoidal stimuli) and therefore are not suited for the study of efficient coding of natural self-motion in the vestibular system.

1.3 Adaptation

As stimulus probability distribution varies over time, the neural response properties (e.g., tuning functions) may change in order to allocate limited computation resources to the current local distribution of the stimulus (Stanley, 2008; Wark et al., 2007; Weber and Fairhall, 2019). Such changes in coding strategies are termed adaptation. Adaptation can also refer to a gradual reduction in neural responses following the onset of a stimulus (Wark et al., 2007; Weber and Fairhall, 2019). Furthermore, adaptation can modify both temporal and input-output characteristics of the neurons and is a signature of efficient coding in the brain (Sharpee et al., 2014; Wark et al., 2007; Weber and Fairhall, 2019).

Adaptation can be viewed as changes in the function of the neurons that occurs in different timescales(Whitmire and Stanley, 2016). Gain adaptation, which is the change in the input-output characteristic of the neuron to match neurons output to statistics of the input, also occurs at different timescales (Wark et al., 2007; Weber and Fairhall, 2019; Whitmire and Stanley, 2016). At least in the early visual and auditory system, experiments have shown that two mechanisms underlie adaptive gain rescaling: a fast component that rescales the gain of the neuron in response to rapid changes in variance or contrast of the stimulus (Fairhall et al., 2001; Wark et al., 2009; Weber and Fairhall, 2019) and slower component that changes the mean firing rate of the neurons (Wark et al., 2007; Weber and Fairhall, 2019).

1.4 The sensory endorgans and afferents in the vestibular periphery

The vestibular periphery consists of vestibular endoragns that sense the head motion as well as the afferents that innervate the sensory apparatus and transmits head motion information to the central pathway (Goldberg et al., 2012a, c).

1.4.1 The vestibular sensory organs

The head motion stimuli are sensed through sensory organs that reside in the membranous labyrinth located in the temporal bone near the cochlea (see (Goldberg et al., 2012c) for a comprehensive description). There are two sets of sensory organs in each of the ears: the semicircular canals consisting of anterior, posterior, and horizontal which are arranged nearly orthogonally and detect angular head motion in different planes; and the otolith organs comprising the utricle and saccule, which sense linear translation of the head motion and the changes in the orientation of our head with respect to gravity (Rabbitt, 1999). Within each of these sensory organs lie hair cell structures that move during head motion and are the primary receptors in the vestibular system.

1.4.1.1 Semicircular canals

The semicircular canals are curved structures, each making about two-thirds of a circle, which are located within each inner ear and detect head rotation (Lindeman, 1969). There are three semicircular canals that lie within three approximately perpendicular planes. Each of the semicircular canals detects angular head motion around a specific axis. The horizontal (or lateral) semicircular canal lies in a plane that make an approximately 30-degree angle with the transverse plane and primarily detects yaw rotations (rotation around the vertical axis). The anterior (or superior) semicircular canal makes a roughly 45-degree angle with the sagittal plane and mainly detects the rotations in the sagittal plane (around the horizontal axis). The posterior semicircular canal is oriented on the frontal plane and mainly detects rotation in that plane (i.e., roll). When the head rotates in another plane, all of the canals differentially are activated with the ones whose plane is closer to the rotation plane being most activated (Lindeman, 1969).

The semicircular canals are filled with endolymph, a viscous fluid that has a high concentration of K^+ ions and a low concentration of Na^+ and Ca^{2+} ions (Ghanem et al., 2008; Smith et al., 1954). Each of the canals has a dilated segment known as the ampulla, which contains *crista ampullaris* and *cupula*. Cupula is a gelatinous structure within which lie hair cell bundles, each consisting of 20-100 stereocilia associated with a kinocilium. These hair bundles are arranged in a staircase pattern and are oriented in a specific direction inside the gelatinous membrane. During a head rotation, due to inertia, the endolymph initially lags behind and pushes against the cupula. The generated force displaces the cupula and bends the hair bundles, thereby opening or closing the mechano-transducer channels carrying a transducer current. If the cupula pushes the stereocilia towards the kinocilium, K^+ and Ca^{2+} channels open and depolarizes the cell, leading to the release of glutamate in the synaptic cleft where a postsynaptic afferent terminal is present. A sustained glutamate release depolarizes the afferent terminal and generates a spike which is then transmitted to the central vestibular areas. On the other hand, if the cupula pushes the stereocilia towards the short end, this hyperpolarizes the cell and leads to a reduction in glutamate release and, consecutively, afferent firing rate. Although the inertia from the rotation or the angular acceleration is responsible for the deflection of the hair bundles, the mechanics of the cupula and viscosity of the endolymph act as an integrator, thereby making semicircular canals responses in phase with angular velocity rather than acceleration at low frequencies.

1.4.1.2 Otolith organs

The otolith organs are responsible for the sensation of linear translation of the head as well as its relative change with respect to gravity. There are two otolith organs: the utricle, which senses the acceleration along the transverse plane, and the saccule, which senses the acceleration along the vertical axis (Fernandez et al., 1972; Goldberg et al., 2012a, c; Lindeman, 1969). The otolith organs are tiled with hair cells whose stereocilia are embedded inside an otolithic membrane, a gelatin membrane covered by calcium carbonate crystals known as otoconia. During a linear movement, the otoconia, which is denser than the otolithic membrane, lags behind due to the inertia and bends the stereocilia of the hairs cell. Similar to the cupula in semicircular canals, depending on the orientation of the deflection of the stereocilia of the hair cells, the cell could increase or decrease the activity of the innervating afferent neurons. Unlike semicircular canals in which the orientation of the stereocilia is similar, in utricle and saccule, the stereocilia are oriented towards an imaginary line passing through the otolith organ. Therefore, during the movement of the head, some hair cells become depolarized while others become hyperpolarized.

1.4.1.3 Hair cells

Hair cells are the primary receptors in the vestibular pathway, which convert mechanical force due to movement into electrical signals, thereby performing mechano-electrical transduction. When the cell is depolarized or hyperpolarized, the amount of glutamate released rises above or dips below the baseline level, leading to an increase or decrease of membrane potential in the postsynaptic terminal. There are two types of hair cells in the vestibular system: flask-shaped type 1 hair cells and cylindrical type 2 hair cells. Type 1 hair cells are innervated by cup-shaped afferent endings (calyx), while type 2 hair cells receive inputs through bouton endings (Eatock and Songer, 2011). Type 1 hair cells have input conductance due to large K^+ conductance and exhibit fast voltage responses. Additionally, type 1 hair cells have more stereocilia than their type 2 counterparts, causing differences in the bundle mechanics and peak mechanoelectrical transduction currents (Contini et al., 2012). Accumulating evidence shows that type 1 hairs cells are more adept in detecting acceleration in high-frequency movements compared to their type 2 counterparts owing to their physiological and morphological differences (Curthoys et al., 2021).

1.4.2 The vestibular afferents

The other main component of the vestibular periphery is the afferent neurons innervating the hair cells in sensory endorgans (Goldberg et al., 2012c; Sadeghi and Cullen, 2015). Vestibular afferents transmit self-motion information via spiking activity to vestibular nuclei in the brainstem. There are two types of afferents in terms of their resting discharge variability characterized by the coefficient of variation (CV) of their interspike intervals, the ratio of the standard deviation of the interval and mean of the intervals: the regular afferents which have low variability in their interspike intervals and the irregular afferents which exhibit high variability in their interspike intervals (Goldberg, 2000). The variability is associated with the morphological and physiological differences between the two types of afferents. The regular afferents have axons with smaller diameters and bouton terminals preferentially innervating type 2 hair cells. The irregular afferents, on the other hand, have axons with large diameters and calyceal endings preferentially innervating type 1 hair cells. Such differences have implications for differential information transmission, which will be discussed later in section 1.6.1.

1.5 The central vestibular pathway

In the previous section, we focused on the peripheral vestibular pathway, including the sensory endorgans and vestibular afferents. In this section, we focus on the central vestibular pathway, which is involved in postural and gaze stabilization, self-motion estimation, and spatial orientation (see (Cullen, 2016) for a comprehensive review). Vestibular afferents project to the vestibular nuclear complex in the brainstem, which consists of four main nuclei (Brodal, 1984): medial, lateral, superior, and descending vestibular nuclei. The medial vestibular nucleus (MVN) is the largest subdivision within the vestibular nuclei. The rostral segment of the MVN is mostly associated with vestibulo-ocular neurons, whereas the caudal MVN is primarily linked to vestibulo-spinal and autonomic functions. The neurons in the lateral vestibular nuclei (LVN) contribute to the lateral vestibulospinal tract and mediate vestibulo-spinal reflex (VSR)(Hernandez and J, 2023; Kheradmand and Zee, 2012). While a subset of neurons (magnocellular neurons) in the superior vestibular nucleus (SVN) mainly mediate vestibulo-ocular functions as well as the conscious perception of gravity, others (parvocellular neurons) mainly contribute to commissural pathways. The neurons in the descending vestibular nuclei (DVN) receive information about head tilt and gravity and mediate autonomic functions (see also (Goldberg et al., 2012b)).

There is a topographical division between the five vestibular otolith organs and semicircular canals (Beitz and Anderson, 1999; Imagawa et al., 1998; Imagawa et al., 1995). The vestibular nerve consists of superior and inferior divisions. While the superior division carries fibers innervating horizontal and anterior semicircular canals as well as the utricular macula and anterior parts of the saccular macula, the inferior division mainly carries fibers from the saccular macula and posterior semicircular canal. Furthermore, the SVN receives inputs from all three semicircular canals, while MVN and LVN receive inputs from all five sensory endorgans. Additionally, canal inputs are more abundant in the rostral parts of the MVN and DVN. Both MVN and DVN receive otolith inputs; the saccular projections are dense in DVN, whereas the utricular projections are heavier on the rostral segments. Unlike auditory and visual systems, the vestibular nuclei do not have well-defined topographic representations of peripheral organs; instead, they have considerable overlap in their projections, allowing for multi-organ convergence onto individual neurons. In the next sections, I will overview the reflexes that the vestibular system is involved in and their corresponding pathways.

1.5.1 The VOR pathway

The VOR is a crucial mechanism that enables coordinated eye movements to stabilize the image on the retina for clear vision during motion (Cullen et al., 2009; Sadeghi and Cullen, 2015). The eye movement is equal to that of head motion in magnitude and in the opposite direction, thereby effectively canceling the effects of head motion to maintain gaze. Angular head motions are canceled by the angular VOR (AVOR), whereas the gaze position during head translation is instead canceled by the translational VOR (TVOR) (see also (Goldberg et al., 2012d)).

AVOR is elicited by angular head motions that have negligible translation components. The latency of the eye movement relative to the head movement is remarkably short (approximately 5 to 7 ms; (Huterer and Cullen, 2002)) owing to a relatively simple three-neuron arc and fast muscle contractions. During the reflex, mainly the semicircular canals are stimulated. This information is transmitted to ipsilateral VN, and from there, to the contralateral abducens nucleus. Premotor neurons in the abducens nucleus project to the lateral rectus muscles of the eye on the contralateral side, whereas the internuclear neurons in the abducens nucleus project to medial rectus premotor neurons on the ipsilateral side. Therefore, head rotation leads to the contraction of the medial rectus muscle on the ipsilateral side and the lateral rectus muscle on the contralateral side. At the same time, the medial rectus muscles on the contralateral side and the lateral rectus muscles on the ipsilateral side become relaxed due to increased activity in the afferents of the contralateral canals.

The signal generated by semicircular canals is proportional to the angular head velocity, yet, compensatory eye movements are proportional to head position. During horizontal head rotations, this computation is done in nucleus propositus hypoglossi by integrating the eye velocity signals in the vestibular nucleus (VN) as well as burst neurons and generating a sustained position signal (Cannon and Robinson, 1987; Cheron et al., 1986).

For vertical and torsional head rotations, the integration is done in the interstitial nucleus of Cajal (Crawford et al., 1991; Glasauer, 2001). Additionally, the head motion signal generated by semicircular canals decay in 3 to 5 seconds, whereas corresponding output signals neurons in VN decay with a larger time constant of order 12-20 seconds (Raphan et al., 1979). This difference is attributed to the velocity storage integrator represented by distributed networks in VN in the brainstem as well as nodulus and uvula in the cerebellum which integrates vestibular signals helping to prolong and maintain a stable perception of self-motion (Cohen et al., 1981; Reisine and Raphan, 1992).

The AVOR has been characterized by linear control systems features, gain, and phase, as it displays linear behavior (Raphan et al., 1979; Robinson, 1981). In monkeys, the AVOR gain is close to 1, and the phase is small over a wide range of frequencies, whereas for humans, the AVOR gain hovers around 0.5-0.8. Interestingly, despite the fact that the 5 ms lag translates into 45 deg of phase shift during a 25 Hz AVOR, the behavior's phase remains close to zero. It is hypothesized that the neural signals in VN possess significant phase lead which would compensate for the phase lag expected from the delayed response.

The VOR is also activated during head orientation relative to the gravity or head translation evoking otolith-ocular reflexes. Tilt VOR is evoked when the head is tilted and functions to stabilize the gaze in space by vertical and torsional eye movements (Angelaki, 1998; Paige and Seidman, 1999). The translational VOR (TVOR) functions to stabilize gaze during head translation and, unlike AVOR, involves a combination of eye movements (i.e., activation of multiple eye muscles in synergy) (Paige and Tomko, 1991). TVOR is functionally important, primarily in near-target viewing during high-frequency translations (Busettini et al., 1991; Paige and Tomko, 1991; Schwarz et al., 1989).

The signal processing of VOR in VN and the response dynamics of the associated neurons are discussed in detail in 1.6. Briefly, there are two types of neurons in VN that mediate VOR (see (Cullen, 2012) for review). The primary driver neurons in VOR are the position-vestibular-pause (PVP) neurons which respond to head velocity in one direction and the eye position in the opposite direction. These neurons project to abducens motoneurons which drive the eye muscles. In addition, there are eye-head neurons (EH) that respond to head velocity and eye velocity in the same direction and contribute to calibration and adaptation in the VOR pathway. In situations where the head movements displace the direction of the head significantly, the VOR is not enough to stabilize the image on the retina, and a compensatory reflex mediated by the optokinetic system comes to play, which is discussed in further detail below.

1.5.2 The OKN pathway

The optokinetic reflex (OKN) is an involuntary response that is elicited in response to the motion of large visual fields (Cohen et al., 1977). It complements the VOR system by matching the velocity of the eye to the visual surround. In laboratory settings, the OKN is elicited by rotating a stripped drum while the subject is looking. When the drum begins to rotate, the motion of the image on the retina induces an error signal, manifested as the retinal slip, causing the eye of the subject to track the movement of the drum. As the rotation of the drum continues, the eyes reset their position by quickly moving in the direction opposite the rotation of the drum. The phase during which the eyes are following the stimulus is called the “slow phase,” and the phase at which the eyes reset their position is called the “quick phase.” This behavior is also known as optokinetic nystagmus. If the light is extinguished during OKN, the eye movements during the slow phase decrease and gradually decay to zero. The latter component is known as optokinetic afternystagmus (OKAN) (Cohen et al., 1977; Ter Braak, 1936).

OKN is most effective when the visual surround is moving at velocities below 60 deg/s with a gain close to unity (Mustari and Ono, 2009). However, the gain decreases significantly for higher velocity optokinetic stimuli. The neural substrate involved in OKN is well understood (Kato et al., 1986; Mustari et al., 1994; Precht and Strata, 1980; Schiff et al., 1990; Waespe et al., 1983). In mammals, horizontal OKN involves the pretectum nucleus of the optic tract (NOT) and dorsal terminal nucleus (DTN) of the accessory optic system (AOS). For vertical OKN, the lateral and medial terminal nuclei (LTN and MTN) of AOS are involved. These nuclei comprise neurons that are sensitive to the retinal slip in specific directions. For example, neurons in NOT and DTN selectively respond to ipsiversive retinal slip, whereas the neurons in LTN and MTN respond to vertical retinal slip. DTN and NOT receive signals directly from retinal ganglion cells through retinofugal projections and indirectly through cortical and subcortical areas such as lateral geniculate nuclei and primary visual cortex. The retinal slip signals are then projected to various subcortical areas such as dorsolateral pontine nucleus (DLPN), nucleus propositus hypoglossi (NPH), inferior olive, nucleus reticularis tegmenti pontis (NRTP), which then find their way to vestibular, floccular, and abducens nuclei, from which tracking and resetting eye movement commands are executed.

1.5.3 The VCR pathway

When the head moves in space, the vestibulocollic reflex (VCR) is evoked to stabilize the head in space. This reflex is essential for maintaining balance and stabilizing our gaze to allow us to achieve optimal motor action as well as accurate perception of visual stimuli by dampening unattenuated head motions. Similar to VOR, VCR is mediated by a three-neuron arc: the vestibular afferents, the vestibular interneuron, commonly referred to as the vestibulocollic neuron, and the neck motoneuron (Wilson et al., 1995a). The main pathways of VCR are lateral and medial vestibulospinal tracts which provide direct connections to neck motoneurons as well as indirect connections via spinal interneurons.

While the nature of the vestibulocollic neurons in VN that mediate VCR remains unclear, there is evidence suggesting that VO neurons can fulfill this role (reviewed in (Cullen, 2016; Goldberg and Cullen, 2011)). Firstly, VO neurons project to the spinal cord, and their responses are significantly attenuated during active motion, consistent with the notion that VCR is suppressed during voluntary movements (Peterson and Boyle, 2004; Wilson et al., 1995b). Furthermore, the cancelation signal during active motion arises from the comparison between active movement and the neck afferent signal, which further supports this suggestion (Roy and Cullen, 2004).

1.5.4 The VSR pathway

The vestibulospinal reflex (VSR) plays a crucial role in controlling posture. During head motion, the vestibular information is used to act on the limb muscles to stabilize the position of the trunk and posture (reviewed in (Cullen, 2016)). There are two types of reflexes that act on limb muscles: tonic and phasic reflexes (Manzoni, 2009). The former maintain their response to changes in the head position and are originated from stimulation of otolith organs. The latter originate from semicircular canals and are essential for high-frequency reflexes (Angelaki and Dickman, 2000). A roll tilt would lead to the extension of the ipsilateral and the flexion of the contralateral limbs. Similar to the VCR, the VSR pathway is mediated via lateral and medial vestibulospinal tracts. As in VCR, VO neurons in VN also project to cervical and lumbar levels of the spinal cord and likely contribute to VSR.

1.5.5 The ascending vestibular pathways

Some of the vestibular neurons in VN further project to thalamus, and from there to the cortex. These vestibulo-thalomo-cortical projections mediate our subjective sense of self-motion and orientation in space. Mainly, there are two ascending pathways from VN to cortex: the anterior pathway, which consists of projections from NPH to the head direction cell network and contributes to the brain's representation of the spatial orientation(Cullen and Taube, 2017); and the posterior thalamic pathway including projections from VO neurons to ventral posterolateral thalamus which in turn project to multiple cortical areas and underlies our subjective perception of self-motion(Cullen, 2016).

1.5.5.1 The anterior thalamic pathway and head direction cell network

NPH receives vestibular signals from VOR neurons to generate a sustained firing rate proportional to the position of the eye in orbit by integrating the eye and head velocity signals from VN. Additionally, neurons in NPH also project to dorsal tegmental nuclei (DTN), and from there to the anterodorsal thalamus (ADN). DTN is considered the input gate of the head direction cell network. Head direction cells are sensitive to specific angular positions of the head and are found in DTN, ADN, and lateral mammillary nuclei (reviewed in (Cullen and Taube, 2017)). ADN and lateral mammillary nucleus, in turn, project to the entorhinal cortex and other areas in the limbic system where the head direction signals are modulated by visual landmarks as well as vestibular information. The vestibular input to the head direction network is critical as studies have shown that the abolition of such inputs alters the head direction cells' selectivity and sensitivity to the position (Stackman and Taube, 1997).

1.5.5.2 The posterior thalamic pathway and self-motion perception

In the posterior thalamic pathway, VO neurons in VN project to the ventral posterior lateral nucleus (VPL) thalamus, relaying vestibular sensory information between the vestibular nuclei and cortical processing areas (Marlinski and McCrea, 2008a, b; Meng and Angelaki, 2010; Meng et al., 2007). Interestingly, unlike most other sensory modalities, thalamus lacks nuclei exclusively dedicated to vestibular processing. Instead, vestibular sensitive neurons are distributed throughout the posterior lateral thalamic nuclei with a notable presence in the ventral posterolateral and ventral posterior nuclei. These areas primarily are somatosensory areas but also include neurons that respond to oculomotor, visual, and proprioceptive signals (Meng et al., 2007). In addition to these areas, sparse vestibular responses have been found in pulvinar.

Furthermore, studies have found that vestibular neurons responding to head rotation, translation, tilt, or a combination of these stimuli are distributed without any discernable topographical organization or preference for specific types of movements(Marlinski and McCrea, 2008a; Meng and Angelaki, 2010). While there is a coarse organization to the structure of VN in terms of projection association with vestibular endorgans and their functional differences (i.e., MVN, SVN, DVN, and LVN), vestibular target neurons in VPL are functionally intermixed and lack any functional differentiation. Anatomical studies have suggested that vestibular target neurons in VPL receive bilateral projections from both ipsilateral and contralateral vestibular nuclei(Lopez and Blanke, 2011). The response of VPL neurons has been characterized in detail and will be covered in 1.6.1.

Most vestibular thalamus neurons are multimodal. Indeed, not only do they receive convergent vestibular input from multiple vestibular endorgans, but they also receive input from other sensory modalities. Specifically, about 50% of vestibular thalamus neurons receive proprioceptive inputs from the limb and neck (Deecke et al., 1977). Moreover, many vestibular neurons in the vestibular thalamus neurons exhibit eye movement sensitivity in the opposite direction to the vestibular sensitivity (Lopez and Blanke, 2011). In Addition, few vestibular neurons in thalamus receive whole-field optic flow signals (Lopez and Blanke, 2011). It should be noted that during passive motion, neurons that are sensitive to vestibular and proprioceptive stimuli but not to oculomotor or visual stimuli resemble that of VO in VN. These neurons are believed to contribute to self-motion perception via their projections to cortical areas (Wijesinghe et al., 2015).

The vestibular neurons in thalamus project to multiple cortical areas (reviewed in (Lopez and Blanke, 2011)). Although the projection patterns are slightly different across different monkey species, the thalamus sends projections to somatosensory areas 2V and 3aV, as well as the parietoinsular vestibular cortex (PIVC). PIVC is considered to be the primary vestibular center in the cortex, as this area primarily receives input from the VPL thalamus. Other areas—such as area 3a—instead primarily receive vestibular inputs from ventral posteromedial and ventral intermediate nuclei of thalamus (reviewed in (Hitier et al., 2014)). A study in humans using diffusion tensor imaging has shown that there are five projection pathways from VN to PIVC, four of which pass through the thalamus (Kirsch et al., 2016). Two of these pathways ascend ipsilaterally and do not cross the midline. One of these pathways passes through the VPL thalamus, whereas the other pathway includes the paramedian thalamus. The two remaining pathways cross the midline at the pons and midbrain and pass through the contralateral VPL. Because of the technique used, each of the mentioned pathways could originate from the cortex or thalamus and can be involved in the corticothalamic loop.

1.5.6 Vestibular cortex

Unlike other sensory modalities, the “vestibular cortex” is not well defined in the sense that, unlike other modalities (e.g., vision, audition, somatosensory), there is no “primary vestibular cortex.” This is because vestibular representation in the brain is not only highly distributed but also, as mentioned above, multisensory. Multiple areas in the cortex have been shown to respond to vestibular stimulation (reviewed in (Cullen, 2016; Lopez and Blanke, 2011)). Consistent with anatomical studies showing that PIVC and areas 2V and 3a receive projections from the vestibular thalamus, cells with vestibular sensitivity have been identified in these areas. For example, in area 3aNv –which is referred to as the neck-vestibular region of 3a—about 30-50% of neurons respond to vestibular stimuli. More than 50% of neurons in PIVC are driven by vestibular stimuli, more than any other area in which neurons with vestibular sensitivity have been found (Guldin and Grüsser, 1998). This, together with the findings that PIVC receives direct input from the vestibular thalamus and convergent inputs from other vestibular areas in the brain, has led to the notion that PIVC is the core area in vestibular signal processing. PIVC has been shown to be critical for the subjective perception of self-motion. Posterior to PIVC, 30% of the neurons in visual posterior sylvian (VPS) area neurons also respond to vestibular stimuli (Guldin and Grüsser, 1998). In the posterior parietal cortex of the monkey, it has been shown that some neurons in area 7, the ventral intraparietal area (VIP), and the medial intraparietal area (MIP) are driven by vestibular stimulation. Furthermore, the cingulate cortex is connected to PIVC, VPS, and area 3a, where neurons with vestibular sensitivity have been found. Additionally, frontal and supplementary eye field areas have been shown to demonstrate vestibular sensitivity when the vestibular nerve was stimulated electrically (reviewed in (Lopez and Blanke, 2011)). Vestibular sensitivity has also been identified in the area of MST, which is involved in visual perception as well as self-motion perception based on optic flow signals (DeAngelis and Angelaki, 2012).

1.5.7 Corticofugal projections to brainstem and thalamus

Anatomical studies such as those that have used retrograde tracer injections have demonstrated that VN receives corticofugal feedback projections from multiple areas in the cortex in monkeys, including PIVC, VPS, 2v, 3aV, 6, and anterior cingulate cortex (Akbarian et al., 1994; Akbarian et al., 1993). Interestingly, anatomical feedback projections are found to be associated with the functional relevance of the structure in VN. Specifically, areas in VN that are mostly associated with VOR (i.e., SVN and MVN) predominantly received feedback projections from PIVC, whereas areas involved in VSR and VCR (i.e., LVN and MVN) received feedback projections from somatosensory and motor areas 3a and 6 (Akbarian et al., 1994). Although generally, the cortical feedback projections are bilateral, projections from PIVC dominated ipsilaterally, whereas the somatosensory and motor areas (2v, 3aV, 6) preferentially project to contralateral VN. Corticothalamic feedback projections to the thalamus are less known as anatomical studies demonstrating such projections are lacking. However, recently, several imaging studies have provided strong evidence that the ventroposterior thalamus, and especially VPL, receive ipsilateral cortical feedback projections from PIVC (Conrad et al., 2023; Kirsch et al., 2016; Wirth and et al., 2018).

1.5.8 Multisensory integration in the central vestibular pathway

The self-motion information available for the brain is not solely provided by the vestibular input. In fact, in natural settings, visual, somatosensory, and proprioceptive information provides significant information about self-motion. This is reflected in the response of the neurons in the vestibular pathway by many neurons that respond to other sensory modalities or multiple vestibular sensory organs (reviewed in (Cullen, 2012)). One of the unique features of the vestibular systems is that multimodal sensory convergence appears as early as in the secondary vestibular neurons. As mentioned earlier (see 1.5.2), large-field motion produces an optic flow signal that evokes OKN, which complements VOR by stabilizing the gaze in space. The optic flow signal is ultimately delivered to abducens nuclei via PVP and EH neurons, which are the secondary vestibular neurons that integrate the vestibular and visual information. Note that VO neurons are not involved in vestibular-visual signal integration, although they contribute to OKN by mediating the velocity storage mechanism (Raphan et al., 1979; Yakushin et al., 2017).

As VN receives projections from cortical areas sensitive to somatosensory and proprioceptive signals, it is not surprising that at least some neurons in VN respond to such stimuli. For example, VO neurons respond to proprioceptive stimulation in monkeys, with the exception of rhesus monkeys (Gdowski and McCrea, 2000; Sadeghi et al., 2009). However, even in rhesus monkeys, neck proprioception sensitivity was observed after unilateral labyrinthectomy, demonstrating the vestibular-proprioceptive integration in VO neurons in VN (Sadeghi et al., 2011). Furthermore, in addition to multimodal sensory integration in VN, some neurons in VN respond to convergent inputs from multiple vestibular sensory endorgans. For example, canal-canal convergence, when a neuron responds to stimulation of two of the semicircular canals (e.g., rotation around two different axes), or otolith-canal convergence, where the neuron is sensitive to both head rotation and translation, are important in computing translation and resolving tilt-translation ambiguity. Finally, the vestibular sensitive neurons in thalamus and cortex are highly multisensory as many vestibular neurons also respond to visual, somatosensory, and proprioceptive neurons. As self-motion perception involves the integration of information from all sensory modalities, it is believed that such multimodal neuronal sensitivity underlies the integration of information about self-motion to give rise to our subjective sense of self-motion and orientation.

1.6 Vestibular signal processing

The characterization of vestibular cells and their signal processing traditionally have been done using low-amplitude sinusoidal stimuli and linear control systems analysis. Under these conditions, the response of the cell is linear and can be characterized and predicted by neural response gain (the ratio of the response modulation to the stimulus modulation) and phase (the delay between the stimulus and response) (Robinson, 1968, 1981). Additionally, the variability of the neural response plays a key role in information processing done by afferents and central vestibular neurons. In the following sections, I will review the characteristics of vestibular neurons and information processing in peripheral and central pathways.

1.6.1 Vestibular signal processing in vestibular afferents

The baseline firing rate of the canal afferents is 50-100 spikes/s in monkeys (Goldberg, 2000). Furthermore, afferents with CV<0.15 are usually considered regular afferents and are considered irregular otherwise (Sadeghi et al., 2007b). Both regular and irregular canal vestibular afferents demonstrate high-pass tuning properties over the relevant frequency range (0-20 Hz) in response to sinusoidal stimuli as their gain increases with the frequency of the stimulus (Sadeghi et al., 2007a). Furthermore, the response leads the stimulus, and the phase lead increases with the stimulus frequency (Hullar et al., 2005; Sadeghi et al., 2007b; Schneider et al., 2015).

Regular and irregular afferents have been shown to differentially encode vestibular stimuli. Sadeghi et al. (Sadeghi et al., 2007a) used information theoretic measures and demonstrated that regular afferents, on average, transmitted two times more information than their irregular counterparts during sinusoidal and random stimuli. Additionally, the detection threshold calculated from regular afferents was 50% less than that calculated from irregular afferents. However, spike jitter analysis which displaced the spikes randomly showed a substantial decrease in the information carried by regular afferents but insignificant changes in the information encoded by irregular afferents. Similar results were obtained when naturalistic stimuli were used in another study (Jamali et al., 2016).

Interestingly, studying otolith afferents revealed qualitatively different results. In contrast to canal afferents, irregular otolith afferents conveyed significantly more information compared to their regular counterparts (Jamali et al., 2019). Interestingly, however, the detection threshold of both irregular and regular otolith afferents was similar to each other across frequencies (Jamali et al., 2013). The latter resulted from higher variability for irregular afferents matching higher gains when comparing the detection threshold of regular and irregular afferents.

When canal and otolith afferents were tested for precise spike-timing coding, different results were obtained. Irregular canal afferents performed better than regular canal afferents through precise spike timing in discriminating the naturalistic stimuli despite carrying less information about the stimulus through firing rate (Jamali et al., 2016). However, irregular otolith afferents performed better in discriminating naturalistic stimuli through precise spike timing and carried more information through firing rate compared to their regular counterparts owing to the nonlinearities and phase-locking displayed by the former (Jamali et al., 2019; Schneider et al., 2015).

1.6.2 Vestibular signal processing in vestibular nuclei

The response of VO, PVP, and EH neurons in VN has been characterized by a multitude of studies (Cullen, 2011, 2012). Here, I focus on the information processing in the first stage of the central vestibular system and describe the response of the neurons and the role of variability in the neural coding of vestibular stimuli.

1.6.2.1 VO neurons optimally encode natural self-motion stimuli in the temporal domain

Similar to afferents, VO neurons display high-pass tuning properties with phase leads during both sinusoidal and naturalistic stimulation (Massot et al., 2011; Mitchell et al., 2018). The baseline firing rate and CV vary from 20-80 spikes/s and 0.1-0.6, respectively (Mackrous et al., 2020). Recently, Mitchell et al. studied the neural coding of naturalistic self-motion stimuli in VO neurons and demonstrated that the response of VO neurons is adapted to the statistics of the natural self-motion stimuli (Mitchell et al., 2018). In particular, they showed that the power of the VO neural responses remains relatively constant over the relevant stimulus frequency range, whereas the response of the afferents does not. Therefore, whitening is not inherited from the afferents and appears in VN. Notably, the high-pass tuning property of VO neurons did not account for the whitened response alone. Importantly, VOs displayed high levels of variability and heterogeneity in their resting discharge, which, together with the high-pass tuning of the VO neurons, matched the power of the stimulus and thereby whitened the response.

The response of VO neurons to low-amplitude sinusoidal stimuli can be effectively modeled by linear systems analysis techniques (Sadeghi et al., 2007a). However, when more complex stimuli consisting of low- and high-frequency component is presented, the VOs display a nonlinear response by attenuating the response to a low-frequency stimulus when presented with a high-frequency stimulus (Massot et al., 2012). Notably, afferents' response to a combination of low and high-frequency stimuli is linear and matches that of when each stimulus is presented individually, and therefore, the observed nonlinearity cannot be attributed to the afferents. Massot et al., using a linear-nonlinear cascade model, demonstrated that such nonlinearities can be accounted for with a static nonlinear relationship between their output firing rate and input afferent response.

Most of the studies of vestibular systems have been done by stimulating vestibular organs in a single dimension (e.g., yaw rotation); however, natural stimuli stimulate canals and otolith organs simultaneously (Carriot et al., 2013a; Carriot et al., 2014, 2017a). Many VO neurons in VN receive convergent input from multiple canals and/or otolith organs, raising the question of whether VO neurons integrate information from multiple vestibular organs linearly. Previous studies have addressed this question by recording the response of VO neurons during active/passive rotation, translation, and combined rotation and translation (Carriot et al., 2013a; Carriot et al., 2015; Musallam and Tomlinson, 2001). Response of the VO neurons that responded to both rotation and translation were well explained by linear models when each stimulus (translation or rotation) was applied in isolation. However, when the stimuli were applied simultaneously, the model overestimated the response of the VO neuron. Similarly, the response of the VO neurons to combined passive/active rotation and translation stimuli is sub-additive and violates the principle of superposition (Carriot et al., 2013a).

1.6.2.2 PVP neurons faithfully encode VOR during natural head motion

Similar to VO neurons and afferents, PVP neurons display high-pass tuning properties with phase leads during both sinusoidal and naturalistic stimulation (see (Cullen, 2012) for review). The baseline firing rate is higher than that of VOs and comparable to the afferents' baseline firing rate, ranging from 25-100 spikes/s. Compared to VO and EH neurons, the response of PVP neurons is more regular, with CV ranging from 0.1-0.45. Mackrous et al. investigated the neural coding of VN neurons during naturalistic self-motion (Mackrous et al., 2020). They showed that optimal coding (e.g., via whitening) and faithful coding (e.g., via transmitting information with higher rates) of the stimulus during slow phases happened on a spectrum even for a given subclass of neurons in VN, and that depended on the neural variability the neuron exhibited. For PVP, VO, and EH neurons, those displaying high resting discharge variability and CV, on average, exhibited optimal coding via whitening, whereas those displaying lower resting discharge variability and CV demonstrated faithful encoding. However, on average, PVP neurons displayed lower resting discharge variability and more faithful encoding, which had implications for VOR and detailed compensatory eye movements to stabilize gaze during natural self-motion.

1.6.2.3 EH neurons optimally encode head motion information

Unlike afferents, VOs, and PVPs, EH neurons do not exhibit high-pass tuning (see (Cullen, 2012) for review). Instead, EH neural gain stayed relatively constant across the relevant frequency range, whereas the phase lead decreased with frequency. EH neurons are relatively irregular in their resting discharge patterns, with CV values ranging from 0.2-0.8, and their baseline firing rate is relatively lower, ranging from 20-70 spike/s (Mackrous et al., 2020). Similar to PVP and VO neurons, the coding strategy of EH neurons depends on the variability displayed by the neuron; EH neurons with high resting discharge variabilities optimally encode vestibular information, whereas those with low resting discharge variability faithfully encode vestibular signals. As EH neurons display more variability and heterogeneity in their response, they preferentially encode vestibular information optimally rather than faithfully.

1.6.3 VPL neurons optimally encode naturalistic self-motion stimuli

Vestibular processing in VPL had long been assumed to be linear over the physiological ranges; however, recent studies have shown otherwise. In a study on squirrel monkeys, Marlinski and McCrea used 1Hz sinusoidal rotation and translation stimuli with amplitudes of 4 to 100 deg/s and demonstrated that the response of the VPL neurons is, in fact, sub-homogeneous and nonlinear (Marlinski and McCrea, 2008a). Specifically, the average gain of the VPL neurons to sinusoidal rotation is near 1 (spk/s)/(deg/s) when the head velocity magnitude is 4 deg/s, whereas the sensitivity of the VPL neurons decreases to about 0.1 (spk/s)/(deg/s) when the head velocity is 100 deg/s Later, Dale and Cullen (Dale and Cullen, 2019) showed that consistent with the study of Marlinski and McCrea in squirrel monkeys, the sensitivity of the VO neurons in thalamus VPL of rhesus monkeys decreases with the amplitude. These studies indicated that the gain of VPL neurons responding to sinusoidal and active/passive stimuli decreased. However, whether such nonlinearities are inherited from VO neurons in VN, or their observation is due to nonlinearities of thalamus neurons in VPL was not clarified.

Accordingly, Carriot et al. recorded from VPL and VO neurons during naturalistic stimulation (Carriot et al., 2022). In response to sinusoidal stimuli, VPL neurons displayed high-pass tuning with phase lead increasing with the stimulus frequency, similar to VO neurons in VN. In this condition, both VO and VPL neurons displayed ambiguity in the coding of artificial self-motion stimuli. However, unlike VO neurons, VPL neurons exhibited strikingly different tuning properties during naturalistic stimulation: the gain of VPL neurons stays relatively constant across the relevant frequency range. The phase lead disappeared, and the response of the VPL neurons was in-phase with the stimulus, thereby eliminating the ambiguity in coding. Further analysis revealed that the gain and phase of VPL neurons decreased with the stimulus amplitude due to contrast gain control adaptation which accounted for the differences between the response of VPL neurons to artificial and naturalistic stimuli. Additionally, VPL neurons consistently demonstrated more optimal coding during naturalistic stimulation when compared to VO neurons.

1.6.4 Cortical vestibular processing

Cortical processing of vestibular information is highly distributed (see 1.5.6). As mentioned above, amongst the cortical areas containing neurons that respond to vestibular stimuli, PIVC is presumed to be the primary vestibular cortical processing area (Guldin and Grüsser, 1998; Lopez and Blanke, 2011). Previous studies have characterized the response of vestibular neurons in PIVC (Akbarian et al., 1988; Grusser et al., 1990; Guldin and Grüsser, 1998; Shinder and Newlands, 2014). Akbarian et al. characterized the response of vestibular neurons in PIVC of Java and squirrel monkeys (Akbarian et al., 1988). They found that these neurons responded to stimulation of horizontal and vertical semicircular canals but not to tilt, suggesting that these neurons received primarily input from semicircular canals. Many vestibular neurons in their study also responded to optokinetic stimulation, proprioception stimuli (head-on-body stimuli), and somatosensory and visual stimuli. In a follow-up study, Grusser et al. characterized the response of the vestibular neurons by obtaining response gain and phase of PIVC neurons (Grusser et al., 1990). PIVC neurons displayed a relatively low baseline firing rate (10-20 spk/s). These neurons exhibited high-pass tuning properties with gain values ranging from 0.05-0.6 (spk/s)/(deg/s) over 0.2-1 Hz sinusoidal stimulation with a maximum head velocity of 30 deg/s. The phase values stayed relatively the same over the frequency range but varied substantially across the population averaging approximately ~30 deg. Moreover, Shinder and Newlands investigated the convergence of proprioception, vestibular, and visual in PIVC using an extensive battery of stimuli (Shinder and Newlands, 2014). They demonstrated that most PIVC neurons received convergent input from the head, neck, and/or target motion. Additionally, they characterized the response gain and phase during vestibular stimulation. Their findings were consistend with that of Grusser et al. The average gain at 0.2 Hz was approximately 0.25 (spk/s)/(deg/s) whereas the phase values were distributed from -180 to 180 deg. Interestingly, they calculated the gain using sinusoidal stimuli with the same frequency (0.2 Hz), but half the maximum amplitude (15 deg/s vs. 30 deg/s) and showed the gain value increased approximately twice which suggest an adaptation mechanism is involved.

1.7 Population coding

In a seminal paper, Zohary et al. (Zohary et al., 1994) showed that neural activities in neural populations can be correlated. Although weak, these correlations can potentially have significant and, in some cases, dramatic effects on the coding efficiency of neural large populations (Moreno-Bote et al., 2014; Zohary et al., 1994). The following theoretical and experimental work illustrated that the study of population coding is incomplete without considering correlations and therefore, correlations should be investigated in population codes (reviewed in (Averbeck and Lee, 2006); See also (Abbott and Dayan, 1999; Kohn et al., 2016)).

Correlations can be decomposed into two types: *signal correlations* which are correlations between the mean neural responses to different stimuli and quantify the degree to which neurons have similar tuning and functional properties; and 2- *noise correlations*, which are correlations between the trial-to-trial variabilities of neural responses to repeated presentations of identical stimuli and quantify the extent to which response variability is shared between neurons (Cohen and Kohn, 2011; Schneidman et al., 2006). Importantly, noise correlations can be affected by various factors, such as stimulus statistics (Chacron and Bastian, 2008; de la Rocha et al., 2007; Franke et al., 2016; Haggard and Chacron, 2023; Josić et al., 2009; Kohn and Smith, 2005; Lyamzin et al., 2015; Pola et al., 2003), attention (Cohen and Maunsell, 2009; Cohen and Newsome, 2008; Srinath et al., 2021), and learning (Gutnisky and Dragoi, 2008; Komiyama et al., 2010), and therefore are plastic (i.e., can change with the factors). Theoretical and experimental studies have shown that these effects can be either detrimental (Cohen and Maunsell, 2009; Moreno-Bote et al., 2014; Pitkow and Meister, 2012; Zohary et al., 1994) or beneficial (Chelaru and Dragoi, 2016; Downer et al., 2015; Franke et al., 2016) to the coding of the stimulus, and this depends on the structure of the correlation (i.e. the relationship between noise and signal correlations) in the population response as well as the decoder (Averbeck et al., 2006; Kohn et al., 2016; Moreno-Bote et al., 2014). This

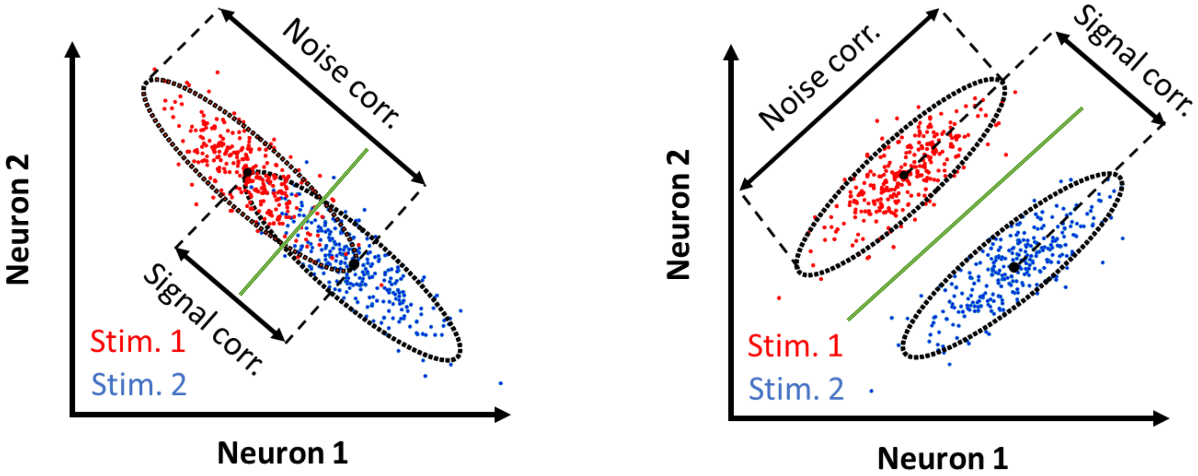

Figure 1.1. Correlation structure affects information in the population. The joint activity of a pair of neurons is illustrated when signal and noise correlations have similar signs (left) and when they have opposite signs (right). Each colored dot represents the joint response of the pair to repeated presentation of one of the stimulus conditions (stimulus 1 in red and stimulus 2 in blue). Filled block circles demonstrate the mean response of the neurons to the stimuli and the ellipses denote a 95 % interval of the response distribution. The green lines denote the optimal decoder.

is illustrated in Figure 1.1: in this example, if the signal and noise correlations are of the same sign, or in general, the correlation eigenvectors are parallel, the response distributions overlap, and the optimal linear decoder fails to discriminate stimuli without error (left panel); However, if the correlation structure of the pair response is such that noise and signal correlations have opposing signs, or in general, the correlation eigenvectors are orthogonal, a linear decoder can distinguish the two stimuli reliably (right panel). Therefore, it is of paramount importance to take the correlation structure into account in the study of population coding and revisit previous findings based on independent neural response assumption.

1.7.1 Implications of stimulus-dependent correlation plasticity in population coding

If the correlation structure is a critical factor in determining information that can be encoded (decoded) in (from) the neural population, what is (are) its implication(s) in population coding? Previous studies have shown that correlation structures depend on stimulus features. For instance, Frankie et al. recorded from a population of direction-selective retinal ganglion cells of rabbits and showed that correlations depend on the direction of the stimulus (Franke et al., 2016). Importantly, they demonstrated that the stimulus-dependency of the correlation structure is the key: when the correlation structure is stimulus-independent (i.e., static), the coding improvement is minimal compared to that of independent neural responses. In contrast, and of particular importance and relevance to my research, when the correlation structure was stimulus-dependent, they found considerable coding improvement (in some experiments, as much as a two-fold increase in coding improvement) compared to that of independent neural responses. Using a phenomenological model, they demonstrate that the beneficial effect of stimulus-dependent correlations arises when variations of response are perpendicular to the informative curve defined mean response of the ensemble of neurons to the stimulus (Figure 1.1).

Correlation plasticity has been characterized in other brain areas and systems. For example, Pola et al. provide an information-theoretic approach to distinguish the contribution of the static and stimulus-dependent noise correlations (Pola et al., 2003). The authors apply the method to two datasets obtained from rat barrel cortex and macaque area MT. They demonstrated that stimulus-dependent noise correlations in the rat barrel cortex were synergistic, i.e., they increased overall information, whereas reduced noise correlations in both the rat barrel cortex and macaque MT area decreased information via redundancy. Kohn and Smith investigated the effect of stimulus orientation and contrast in the primary visual cortex (Kohn and Smith, 2005). Indeed, they observed that correlation structure depended on stimulus features, and these features differentially modulated the correlation structure. By varying the orientation of the stimulus, they observed that noise correlation was highest between the neurons that demonstrated similar tuning to the stimulus. This is consistent with the redundant correlation structures in which noise and signal correlations have similar signs. Additionally, the dependence of the correlation on stimulus orientation was specific to low timescales (1-100 ms): the correlation did not depend on the stimulus orientation for large timescales (>100 ms). Moreover, by changing the stimulus contrast, they demonstrated that noise correlations increase for low timescales with stimulus contrast. Interestingly, by decreasing the stimulus contrast, the noise correlation increased on longer timescales. This study provided evidence that correlation plasticity was further mosulated across timescales.

Chacron and Bastian investigated the population coding in electrosensory systems of weakly electric fish during naturalistic behavior: prey-like and conspecific-like stimuli (Chacron and Bastian, 2008). They showed that while prey-like stimuli increase noise correlations, conspecific-like stimuli decrease the noise correlations. By investigating the neural firing patterns of the neurons, they demonstrated that the differential effect of the stimuli on correlations was primarily due to changes in the bursting activity of the neurons. In a recent study, Haggard and Chacron explored population coding of stimuli in different spatial locations (Haggard and Chacron, 2023). They showed that noise correlations depended on stimulus location and were plastic. Additionally, they compared the information derived from the population with plastic correlations to that where the correlations were independent of the stimulus location. They found that stimulus-dependence of the correlation mitigates the deleterious effect of the noise correlations.

De la Rocha et al. used a slightly different approach to study stimulus dependence of correlation structure and identify the underlying intrinsic mechanism (de la Rocha et al., 2007). They recorded in vitro from unconnected pairs of neurons in slices from auditory and somatosensory neurons in mice. They found that noise correlations were always less than input correlations but increased with the firing rate of the neurons. Using a threshold-linear model, they illustrated that intrinsic and threshold nonlinearities shaped the correlation-rate relationship and underlie the decreased output correlations. In another study, Lyamzin et al. adopted a similar approach to study how transformations in correlations are shaped by intrinsic mechanisms (Lyamzin et al., 2015). They used in vitro and in vivo recordings to investigate whether the correlation structure is affected by the intensity of the stimulus. Specifically, they injected current into the pyramidal cells in mice V1 slices in vitro and demonstrated that noise correlation increases with signal correlation; however, noise correlations decrease with the intensity of the signal (i.e., input signal variance). Moreover, they recorded the response of pairs of neurons in gerbil A1 to FM inputs. Their findings in vivo agree with that of the in vitro experiment: noise correlations are stimulus-dependent (positive correlation) and decrease with signal intensity. Additionally, using a model, they showed that the transformation of signal and noise correlations in cortical sensory processing arose mainly due to threshold nonlinearities involved in spike generation, as observed previously (de la Rocha et al., 2007). Additionally, the observed effects were affected by cortical states: under anesthesia, when the cortical activity was synchronized, noise correlations, as well as their relation with signal correlations and stimulus intensity, were stronger. However, during desynchronized stater, the noise correlations were smaller, and the effect of signal correlations and input intensity on noise correlations was diminished.

Altogether, these studies indicate that variation in the stimuli (Franke et al., 2016; Haggard and Chacron, 2023) could change the correlation structure. Additionally, different features of the stimulus (Kohn and Smith, 2005) or different behaviors of the animal (Chacron and Bastian, 2008) differentially modulate correlations in the population. These transformations are not only a representation of network states (Doiron et al., 2016) but also due to the inherent mechanism that shapes them.

1.7.2. Population coding in the vestibular system

Population coding in the vestibular system is not well understood, as mainly single-unit recordings have been used to date. However, with the advent of neural probes that can record the activity of multiple neurons in deep brain structures, we begin to understand how neural populations encode self-motion information in the vestibular system. Yu et al. recorded from afferents to study the detection threshold before and after unilateral vestibular lesion (Yu et al., 2014). Although they did not focus on simultaneous recording from multiple neurons, they were able to identify pairs of neurons across their dataset. They reported that noise correlations were negligible and close to zero before the lesion (n=5); however, after the lesion, the noise correlations became significantly positive (n=9). Note that the number of pairs in this study is limited, and the results may not be conclusive. Similarly, Dale et al. reported insignificant noise correlations between irregular afferents (Dale et al., 2013).

To the best of our knowledge, two published studies have performed multiunit recordings from vestibular-only (VO) neurons in the central vestibular pathway and have characterized the correlation structure in VN. Dale et al. reported negligible noise correlations between neural responses in VN during spontaneous activity. However, the amount of noise correlation was slightly higher during sinusoidal rotation. Additionally, they reported that noise correlations during active and passive stimulation —which resembled naturalistic self-motion— were not significant. Similarly, Liu et al. recorded pairs of VO neurons in VN during sinusoidal rotation (Liu et al., 2013). The study revealed that noise correlations in VN were small but significant during sinusoidal stimulation. The average noise correlation was positive, indicative of redundant population coding of natural self-motion in VN during sinusoidal stimulation.

We note that in the studies above, the stimulus profile was either artificial (i.e., sinusoidal) or was not representative of natural stimuli observed during typical everyday behavior (Carriot et al., 2017a; Carriot et al., 2017b; Carriot et al., 2013b). As such, how natural self-motion information is encoded in the vestibular pathway remains elusive to this date. In my thesis, I investigated population coding of natural self-motion information in VN by characterizing correlations structure between VO pairs. Specifically, I recorded VO pairs during artificial as well as naturalistic stimulation and used biologically plausible models to explain how natural self-motion information is encoded in the vestibular pathway. Additionally, the neural coding in PIVC remains elusive as all previous studies have used single-unit recordings during low-frequency artificial stimulation. In this thesis, I perform multiunit recordings in PIVC during sinusoidal rotations over a wide range of frequencies (0.5-17 Hz) and naturalistic stimulation to provide insight into population coding in PIVC and whether natural self-motion perception is efficiently encoded in PIVC neural populations.

1.8 Scope and organization of the thesis

The general theme of this thesis is to shed light on how behavior emerges in response to sensory stimuli using a combination of data analysis and computational modeling. We investigate how vestibular information is encoded and transmitted in neural populations by focusing on neural population activities. We use a physiological computational model that captures intricate details of neural activities to address how natural self-motion stimuli are processed in the central vestibular pathway. In addition to this cellular-level study, we further look at the optokinetic system —which shares neural substrates with the vestibular system— at the circuit level and use a functional computational model to explain the behaviors that emerge during optokinetic stimulation.

In the study of population coding of natural self-motion, we hypothesize that population coding of self-motion is adapted to the statistics of the natural self-motion stimuli; That is to say, we believe similar to other sensory systems, population coding of vestibular stimuli (and here, natural self-motion) is efficient. To test our hypothesis, we address the following questions:

- Are neural activities, particularly the variability in the population, correlated? If so, what is the structure of correlation?

- Does correlation structure depend on whether the head motion stimuli are relevant (i.e., whether they are natural)? Do artificial and natural stimuli give rise to different correlation structures?

- What is the significance of the correlation structure and heterogeneity during naturalistic self-motion?

In Chapter 2, I provide a summary of general methods used throughout the thesis. Next, in Chapter 3, I present our data gathered in the central vestibular pathway of rhesus macaques and report our analysis results. Chapter 4 introduces our computational model used in the study of population coding of natural self-motion. By varying key elements in the model, the correlation structure, and heterogeneity, we investigate the efficiency of population coding in the central vestibular pathway in encoding natural and artificial self-motion stimuli.

Next, we studied the optokinetic response in larval zebrafish. We hypothesized whether a set-point adaptation mechanism could explain the OKN response and the emergence of the following negative OKAN. To test this hypothesis, we addressed the following questions:

- Does a model incorporating the set-point adaptation mechanism explain the observed negative OKAN during prolonged unidirectional stimulation?

And if so,

- Does the model generalize to observed behavior during bidirectional stimulation?

- Is the model able to explain variations in the response of individual larvae to the stimuli?

- What is the functional relevance of set-point adaptation?

To address these questions, we propose a mathematical model in Chapter 5 and present the behavioral data gathered during prolonged unidirectional stimulation for comparison.

In Chapter 6, we adapt the model to study the behavior of the animals during symmetric and asymmetric bidirectional stimulation. We used the model to explain OKN adaptation and negative OKAN during bidirectional stimuli. Additionally, the model is used to explain the variation in individual larvae's response. Based on our model, we provide some answers regarding the functional significance of set-point adaptation. Finally, in Chapter 7, I present a summary of findings from our study and provide a general discussion of our results and possible directions for future research.

2. GENERAL METHODS

This chapter introduces the methods for gathering the electrophysiology and behavior data used in this thesis. Furthermore, I review the methods used to analyze the data. The electrophysiology data was collected in Dr. Chacron's lab at McGill University by myself and with the assistance of Dr. Jerome Carriot and Dr. Isabelle Mackrous. The behavioral data from larval zebrafish was gathered by Dr. Ting Feng Lin in Dr. Melody Huang's lab at the University of Zurich.

2.1. Multiunit extracellular recording from behaving rhesus macaque monkeys

2.1.1. Ethics statement

All procedures, including surgeries, experiments, and housing of the animals, were approved by the McGill University Animal Care Committee (protocol #4096) and in accordance with the guidelines of the Canadian Council on Animal Care. The animals were housed in 10 m^2 enclosures and were paired with animals of the opposite sex when possible. Animals followed a Teklad diet (2-4% of body weight) and had access to toys as a part of their enrichment plan. During the testing days, the animals were moved to play cages which consisted of two to four connected 1 m^2 cages. The dividers between the cages allowed to place the animal in one of the cages before placing them in the chair.

Experiments were conducted on two male (Monkey D, aged 8 years, 7.1 kg; Monkey O, aged 6, years, 6.3 Kg) and one female (Monkey B, aged 10, 11.3 kg) rhesus macaques (Macaca Mulatta). The animals were transferred to laboratories where extracellular recordings were conducted in a two-hour session for the experiments. After the experiment, the animals were returned to their housing units.

The animals were constantly observed for any changes in physiological or psychological state, such as changes in diet, level of aggression, response to people, social interaction, and behavioral abnormalities indicative of distress. No such changes were observed for the animals in our experiments. When the animals were required to be euthanized, the recommendations of the International Council of Laboratory Animal Science (ICLAS). Animals were deeply anesthetized by administering 35mg/kg of pentobarbital, were euthanized by intravenous injection of ketamine hydrochloride (15mg/kg), and then were perfused.

2.1.2 Surgical Procedure

In preparation for recording the animals' head motion and eye movement during natural self-motion, two male and one female rhesus macaque monkeys underwent MRI-guided aseptic surgeries (Carriot et al., 2022). Animals were pre-anesthetized using ketamine hydrochloride (12-15mg/kg, IM). Additionally, atropine sulfate (0.04 mg/kg, IM) and valium (1mg/kg, IM) were administered to decrease salivation. The animals were put under anesthesia using 2-3% isoflurane gas and were maintained using surgical levels of isoflurane (0.8-1.5%). During the surgery, a custom-made medical-grade titanium head post was secured to the animals' skull using titanium screws. The head post allows immobilization of the head of the animal by attaching it to the primate which is mounted on the movement platform.

Additionally, a frontal search coil was sutured to animals' sclera to allow online measurement of the animals' eye movement (Fuchs and Robinson, 1966). The eye coil comprised five turns of coated stainless-steel wire with a diameter of 16-18 mm, depending on the size of the animal's eye. Furthermore, we implanted recording chambers on the animals' skulls to access the VN, thalamus, and PIVC. The head post and the recording chamber were secured on the skull by dental acrylic and were positioned based on the co-registration of MRI, CT scan, and rhesus brain atlas in Brainsight (Brainsight 2 Vet, Rouge Research, Montreal, Canada). After the surgery, the animals were provided with post-operative analgesics (buprenorphine, 0.01 mg/kg, IM) and antibiotics (Cephazoline, 25mg/kg, IM for five days). The target locations were confirmed post-surgically by co-registering of a second CT scan and the recording electrode placed at the center of the recording grid on the recording chamber. The animals recovered for at least two weeks before any experimental procedures.

2.1.3. Data acquisition

During the experiment, animals were head-fixed and seated comfortably on a primate chair mounted on a motion platform that delivered head motion stimuli during passive whole-body rotation (pWBR). We recorded simultaneously from multiple VO neurons in VN and and vestibular neurons in PIVC using neural probes (NeuroNexus vector array, Ann Arbor, MI). The probe was inserted in a guide tube and directed toward the VN or PIVC. The angular velocity and gaze position signals were measured using a gyroscope and a magnetic search coil, respectively, and the signals were sampled at 1000 Hz and low pass filtered at 125 Hz. Extracellular recording data were sampled at 30 kHz, band-pass filtered at 300 – 3000 Hz, and collected via Cerebus Neural Signal Processor (Blackrock Systems).

2.1.4. Experimental paradigm

In addition to co-registration of CT scan and MRI of the animals, we confirmed the location of the VN relative to the abducens nucleus based on the characteristic discharge of the abducens neurons —the "singing beehive" sound— during spontaneous eye movements. PIVC was localized using co-registration of MRI scans, CT scans, stereotaxic coordinates, as well as post-operative CT scans. Furthermore, during recordings, we used white/grey matter transitions and non-vestibular physiological properties such as sensitivity to visual stimuli, somatosensory, and auditory stimuli (Grusser et al., 1990; Lopez and Blanke, 2011). To identify vestibular-only (VO) neurons within the VN, isolated cells were tested for vestibular sensitivity and lack of eye movement sensitivity. The animals were trained to perform smooth pursuit, saccades, and VOR cancellation (VORc), and we recorded the activity of the neurons during the behaviors. Specifically, a fixed target was displayed at the center of a screen in front of the animal. After the fixation period, saccadic eye movements were elicited via the presentation of a target at positions ±10°, ±20°, and ±30°. Smooth pursuit movements were elicited by moving a target sinusoidally on the screen with a span of ±30°. The monkeys performed VOR by fixating on a fixed target at the center of the screen during 0.5 Hz sinusoidal pWBR. Moreover, the animals performed VORc during 0.5 Hz pWBR while fixating on a target on the screen, which moved synchronously with the primate chair and animal. VO neurons were modulated during VORc but not during smooth pursuit. Furthermore, the resting activity of the VO neurons did not depend on the eye's position during fixation. Furthermore, the sensitivity of the neurons was similar during VOR and VORc. To determine the sensitivity of vestibular neurons in PIVC, we also performed body-under-head (BUH) rotation by rotating the body of the animal while its head was fixed. Vestibular neurons in PIVC responded robustly during pWBR. Some of the vestibular neurons also displayed neck proprioceptive sensitivity by responding during BUH rotations. Multiunit recordings were initiated after isolating at least two VO neurons in VN or two vestibular neurons in PIVC based on lack of sensitivity to eye movements.

2.1.5 Stimulus protocol

Following the characterization of the neurons, an interval of 20 seconds was used to record the resting discharge activity of the neurons. Next, sinusoidal stimuli with maximum angular velocities of 15 deg/s and frequencies of 0.5, 1, 2, 3, 4, 5, 8, and 17 Hz were delivered to the animal. Each stimulus was presented at least for a minimum of 10 cycles. Neural responses to sinusoidal stimuli were used for the characterization of VO neurons as well as the study of population coding during artificial self-motion. Furthermore, at least four trials of naturalistic stimuli with a maximum head velocity of 200 deg/s in each direction were delivered. Naturalistic stimuli used here are a 60s snippet of a recording of horizontal angular velocity from naturally behaving rhesus macaques (Carriot et al., 2014, 2017). We note that the maximum amplitude of the naturalistic stimulus was higher than that of the artificial sinusoidal stimuli, irrespective of frequency. However, the actual amplitude of each frequency component of the naturalistic self-motion stimulus was lower than that of the artificial sinusoids (i.e., 15 deg/s). As such, the effective signal-to-noise ratio for each frequency is then expected to be lower during naturalistic as compared to artificial self-motion stimulation, which would then give rise to lower coherence values overall.

2.1.6. Data analysis

Data was imported into MATLAB (MathWorks, Natick, MA) programming environment for analysis. The extracellular recording data was appropriately visualized to match the recording sites on the probe. This allowed us to estimate the distance between the neurons as well as the drift of the neurons across the channels should that occur. Visual inspection and preliminary analysis determined isolated neurons for further analysis. The isolated units were then saved and imported to MATLAB coding environment for replaying neuronal recordings and sorting action potentials using custom-written scripts. Binary sequences of unit activities were then generated by setting the sequences at a given time to 1 if a spike happened at that time and to 0 otherwise and were resampled at 1000 Hz. The head position signal was calculated by integrating the head velocity signal. The eye position signal was computed as the difference between gaze and head position signals. The firing rate of the neurons was estimated by applying an optimal lowpass Kaiser filter to unit activities (Cherif et al., 2008). A neuron in VN was categorized as a VO neuron if its response to pWBR stimulus did not depend on the eye movement (saccade as well as smooth pursuit) and if the response to VOR and VORc were identical. Each VO neuron in VN was also characterized as either type 1 or type 2 if it displayed increased activity in response to head movements towards the ipsilateral or contralateral sides, respectively (Massot et al., 2011). A neuron in PIVC was characterized as a vestibular neuron if it responded during pWBR but not during smooth pursuit (Shinder and Newlands, 2014). Note that some vestibular neurons in PIVC responded to neck proprioception during BUH rotation and were included in our dataset.

2.1.7 Linear systems analysis

Neural response gain and phase values were computed for VO neurons in response to sinusoidal stimuli using traditional system identification techniques. VO neurons respond to a sinusoidal stimulus, s(t), as

$$\mathrm{fr}(t) = g.\, s(t - t_d) \ + \ b \tag{2.1}$$

where fr(t) is the estimated firing rate of the neuron; g is the neural gain; t_d is latency, the time by which the response of the neurons is leading the stimulus; and b is the bias. fr(t) was estimated by lowpass filtering the unit activities with a cutoff frequency that exceeded the frequency of the stimulus by 0.1 Hz (Cherif et al., 2008). The response of the neuron across at least 10 trials was used to estimate b, t_d, and g. t_d was estimated as the time at which the cross-correlation of s(t) and fr(t) had maximum absolute value; Next, g and b were obtained by performing a linear regression between fr(t) and s(t-td). The response phase lead, p, was obtained as

$$p = 360^\circ\, t_d f \tag{2.2}$$

where f is the frequency of the stimulus. To calculate the gain and phase during naturalistic stimulation, I computed the frequency response of the neuron, G(f), as

$$G(f) = \frac{P_{sr}(f)}{P_{ss}(f)} \tag{2.3}$$

where $P_{sr}(f)$ is the cross power spectral density between stimulus and firing rate, and $P_{ss}(f)$ is the power spectral density of the stimulus. The gain and phase of the neuron in response to naturalistic stimulus were characterized as

$$g(f) = \sqrt{\mathrm{Re}\big(G(f)\big)^2 + \mathrm{Im}\big(G(f)\big)^2} \tag{2.4}$$

$$p(f) = \arctan\left(\frac{\mathrm{Im}\big(G(f)\big)}{\mathrm{Re}\big(G(f)\big)}\right) \tag{2.5}$$

where Re(·) and Im(·) denote real and imaginary parts of the complex number.

2.1.8 Quantification of heterogeneity

I quantified the heterogeneity of the response of neurons across trials and across populations by calculating the response-response coherence of the neurons (Jamali et al., 2016). I computed the response-response coherence for a given neuron across trials as

$$C_{RR}(f) = \frac{\left| < P_{R_iR_j}(f) >_{i \neq j} \right|^2}{\left(< P_{R_iR_i}(f) >_i \right)^2} \tag{2.6}$$

where $P_{R_iR_j}(f)$ is the power spectrum between binary sequences R_i and R_j obtained from the response of the neuron in trials i and j, and <.> denotes the average across all possible combinations. The response-response coherence of two neurons was calculated as

$$C_{RR}(f) = \frac{\left| < P_{R_iR_j}(f) > \right|^2}{\left(< P_{R_iR_i}(f) >_i < P_{R_jR_j}(f) >_j \right)} \tag{2.7}$$

where here, R_i is the response of the first neuron in trial i, and R_j is the response of the second neuron in trial j. Heterogeneity, H(f), was quantified as

$$\mathrm{H(f)} = 1 - \mathrm{C_{RR}(f)}. \tag{2.7}$$

When computing the heterogeneity during naturalistic stimulation, I averaged the heterogeneity values over 0-5 Hz since the stimulus power primarily dominated in this frequency range. For artificial stimuli, I adopted the heterogeneity value at the stimulus frequency (i.e., averaged the heterogeneity over a 1 Hz window centered at the stimulus frequency).

2.1.9. Correlation analysis

The correlation between the activities of a pair of neurons was quantified by computing spike count correlations (Cohen and Kohn, 2011). To compute spike-count correlations, I first generated the corresponding spike-count sequences. A spike-count sequence is a sequence of numbers, each of which denotes the number of spiking activities of the neurons during a given temporal window or timescale (Figure 2.1). The temporal window could be overlapping or non-overlapping. In our simulations, the temporal windows overlapped by

50% to generate smoother graphs. The sequences of spike counts were generated for each neuron by counting the spikes within the temporal window. This procedure produced a pair of spike-count sequences for a given pair of neurons (Figure 2.1). To study the effect of correlations on population coding, I decomposed the correlations to signal and noise correlations, as in below.

2.1.9.1 characterization of signal correlations

Signal correlation refers to the correlation observed between the mean activity of the neurons in response to a given stimulus. The computation of signal correlations between the response of a pair of neurons has been mainly done using two methods: the first method entails averaging the spike counts over trials assuming the variability of the neurons is uncorrelated; The second method involves shuffling the response of the second neuron so that no response of the second neurons in a trial would match with the response of the first neurons in the same trial (Perkel et al., 1967). Therefore, if the variability in the response of the neurons is correlated, the shuffling would eliminate such effects when computing signal correlations. In this thesis, I computed the signal correlations using the latter methods. However, using the former method did not change the result qualitatively. Figure 2.2 is an illustration of how signal correlations are computed. The top panel shows four repetitions of a one-second segment selected from the naturalistic stimulus for illustration purposes. The middle panel displays the spiking activity of a specific pair of neurons, along with the *raw* spike-count sequence. The raw spike-count sequence refers to the computation of the spike counts for each neuron individually without any mathematical manipulation applied. Note that the temporal window (timescale) of the correlation is T = 250 ms and the windows are non-overlapping. In the bottom panel, the unit activity and the spike-count sequence for the second neuron are shuffled across trials. Note the change in the color coding of the response of the neurons across trials. Finally, the Pearson's correlation coefficient is calculated between the first neuron's spike-count sequence and the second neuron's shuffled spike-count sequence. In my simulations, the shuffling procedure was done at least 20 times. Furthermore, I used temporal windows overlapping 50% of the adjacent windows to obtain smoother correlation-timescale curves.

Figure 2.1. Schematic of generating spike-count sequence. For a given temporal window of length T which may or may not overlap with the adjacent windows, the number of spikes within are counted, generating a sequence of non-negative integer numbers referred to as the spike-count sequence.

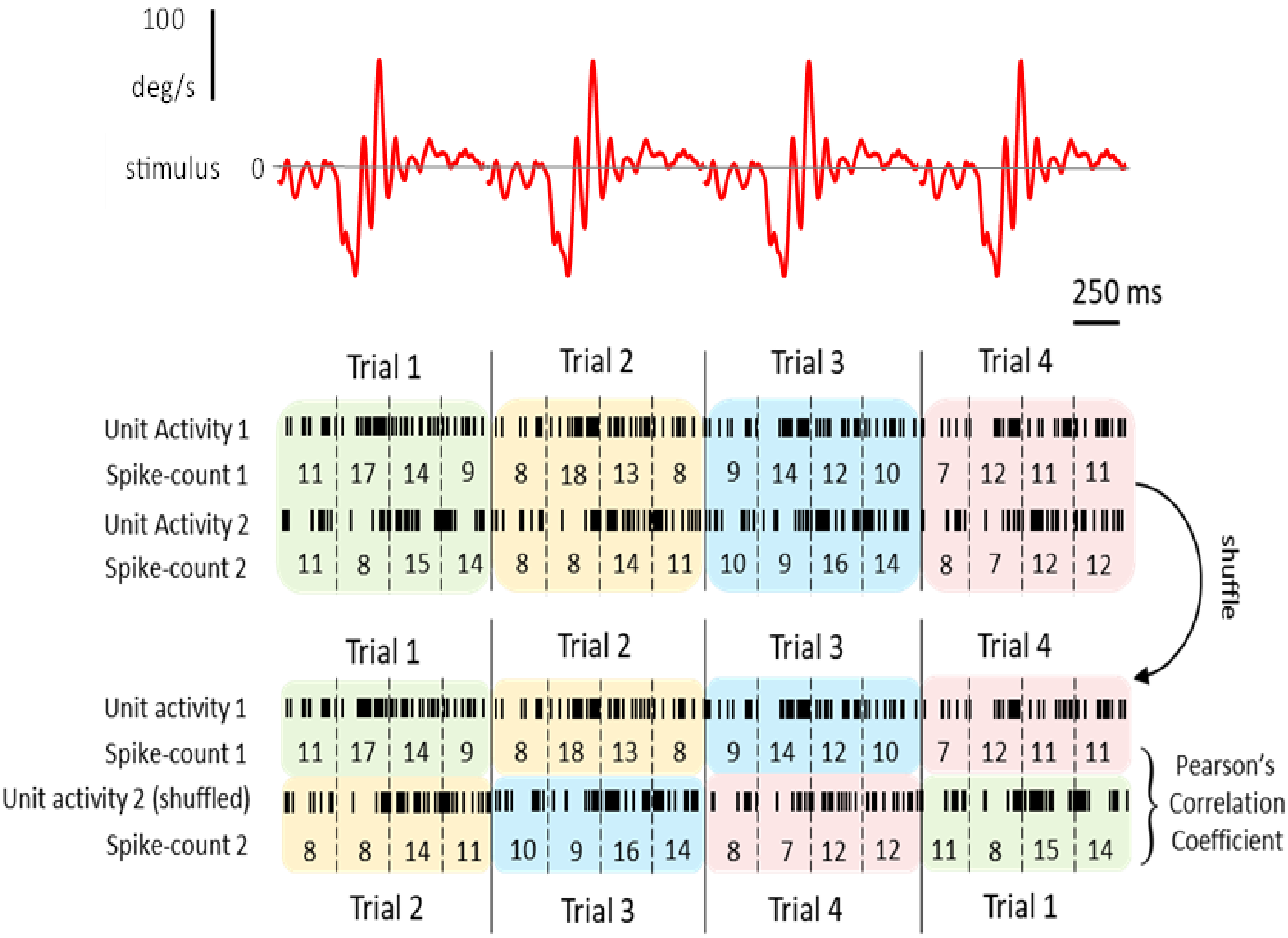

Figure 2.2. Methodology used to calculate signal correlation between the response of pair of VO neurons. The unit activity of cell 1 and cell 2 shown. Top: Four repetitions of a one-second snippet from the naturalistic stimulus is shown. Middle: for each cell, the number of spikes is counted for a given timescale (e.g., 250 ms) and raw spike-count sequences are generated. Bottom: the spike-count sequence for the second neuron is shuffled to exclude the effect noise correlations due to simultaneous common input. The signal correlation for the timescale is calculated by computing the latter spike-count sequences.

2.1.9.2 characterization of noise correlations

Noise correlation characterizes the similarity between the response variability of the neurons around the mean response. Thus, to calculate noise correlation, I obtained the variability of the neural response around the mean response by computing the residual spike-count sequence. Initially, the mean spike-count sequence (Figure 2.3; middle row in top and bottom panels) of the neurons is calculated by averaging the raw spike-count sequence (Figure 2.3; top row in top and bottom panels) across trials. By subtracting the mean spike-count sequence from the raw spike-count sequence, I obtained the residual spike-count sequence (Figure 2.3; bottom row in top and bottom panels). Finally, I computed the Pearson's correlation coefficient between the residual spike counts to obtain noise correlation values. Additionally, I used temporal windows with 50% overlap to obtain smoother correlation-timescale curves.

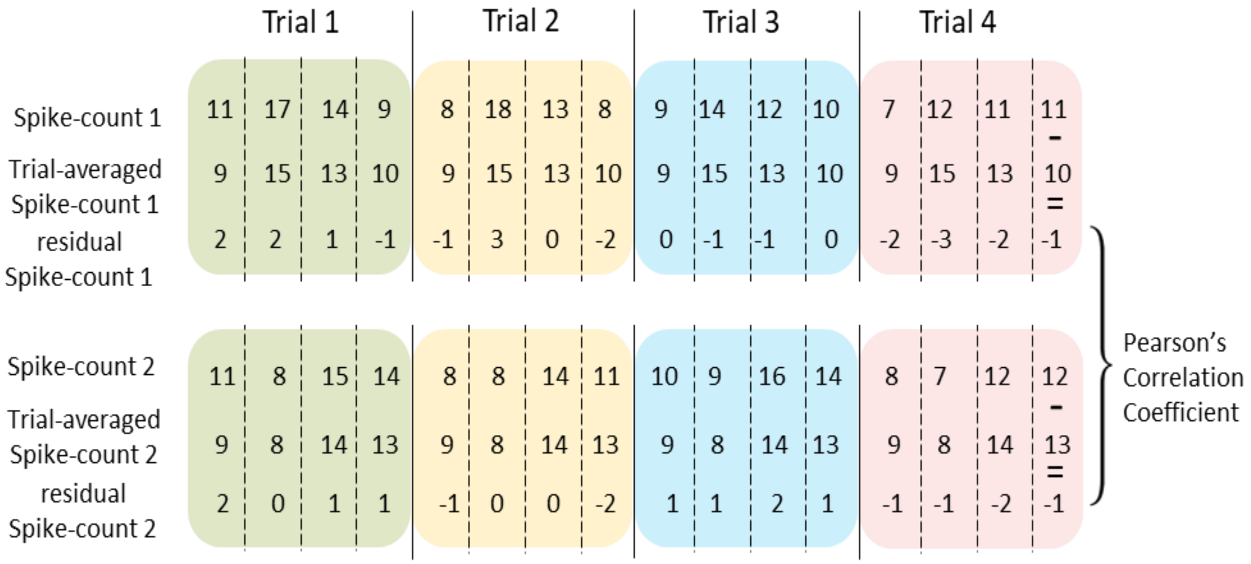

	Trial 1				Trial 2				Trial 3				Trial 4			
Spike-count 1	11	17	14	9	8	18	13	8	9	14	12	10	7	12	11	11
Trial-averaged Spike-count 1	9	15	13	10	9	15	13	10	9	15	13	10	9	15	13	10
residual Spike-count 1	2	2	1	-1	-1	3	0	-2	0	-1	-1	0	-2	-3	-2	-1
Spike-count 2	11	8	15	14	8	8	14	11	10	9	16	14	8	7	12	12
Trial-averaged Spike-count 2	9	8	14	13	9	8	14	13	9	8	14	13	9	8	14	13
residual Spike-count 2	2	0	1	1	-1	0	0	-2	1	1	2	1	-1	-1	-2	-1

Figure 2.3. Methodology used to calculate noise correlation between the response of pair of VO neurons. The spike-count sequences for the same cells (cell 1 and cell 2 in figure 2.2) as well as trial averaged spike counts using the same temporal window (timescale) is shown. For each cell, the residual spike-count is calculated by subtracting the trial-averaged spike counts from raw spike counts. The noise correlation coefficient is calculated by computing the Pearson's correlation coefficient of the residual spike count sequences.

2.2. Eye movement measurement of larval zebrafish

As mentioned earlier, the data collection for the study of the larval zebrafish eye movement during and after the prolonged optokinetic stimulus was gathered by Dr. Ting Feng Lin in Dr. Melody Huang's lab at the University of Zurich. The methods are briefly mentioned here to clarify how the data is collected for the study.

2.2.1 Materials and method

The study adhered to the ethical guidelines set by the Federal Veterinary Office of Switzerland (FVO) for animal welfare. Additionally, all experiments were conducted in accordance with the Association for Research in Vision and Ophthalmology (ARVO) Statement for the Testing of Animals in Ophthalmic and Vision Research, ensuring the well-being of the animals and upholding ethical standards throughout the research.

2.2.2 Fish breeding and upkeep

Zebrafish embryos from the TU and AB wild-type lines were bred and maintained in a 28°C E3 solution (consisting of 5 mM NaCl, 0.17 mM KCl, 0.33 mM CaCl2, and 0.33 mM MgSO4) under a light-dark cycle of 14 hours and 10 hours, respectively. The experiments were conducted using 5-day-old post-fertilization (dpf) larvae from both zebrafish lines. The breeding and maintenance protocols followed previously established methods (Haffter et al., 1996; Mullins et al., 1994) to ensure consistency and compliance with ethical guidelines for animal welfare in ophthalmic and vision research.

2.2.3 Experimental overview

The zebrafish larvae were positioned at the center of an optokinetic cylinder, surrounded by either moving or stationary visual stimuli (Figure 2.4). The experiments consisted of three phases: a baseline period where spontaneous eye movements were recorded in darkness or in the presence of illuminated stationary gratings, followed by an

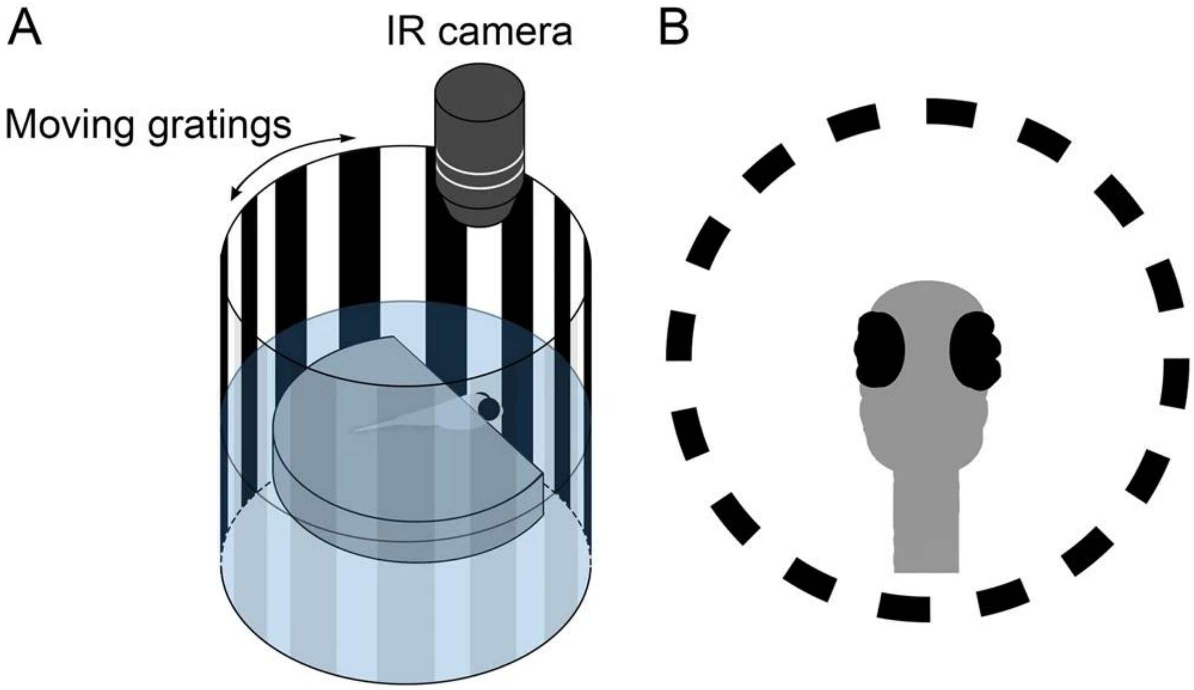

Figure 2.4. Experimental setup to elicit optokinetic nystagmus in larval zebrafish. (A) zebrafish larvae were fixed in agarose submerged in a water tank surrounded by a cylinder with verstical gratings. A infrared camera captured the eye movement of the animal. (B) The schematic of pictures captured by the infrared camera. To elicit optokinetic nystagmus (OKN), the cylinder was rotated with a given velocity while the eye movement was recorded. Adapted from (Lin et al., 2019).

optokinetic stimulatory phase, and finally, a post-optokinetic stimulatory phase either in darkness or surrounded by illuminated stationary gratings.

2.2.4. stimulation of optokinetic nystagmus

Experiments were conducted between 8:00 AM to 7:00 PM. Zebrafish larvae were immobilized with low-melting agarose and positioned at the center of an optokinetic drum, with their eyes left free to move (Arrenberg, 2016). Optokinetic nystagmus (OKN) was induced using four digital light projectors (Samsung SP-H03 Pico Projector). The optokinetic stimulus consisted of a moving black and white vertical sinusoidal grating pattern with 100% contrast, projected onto a transparent screen at a given angular velocity depending on the experiment.

In all experiments, the spatial frequency of the grating was 0.053 cycles per degree, and the maximum illumination reached 1524 lux. For unidirectional optokinetic stimulation, the fish were exposed to 10 degrees per second of stimulation for 3, 4, 5, 6, 7, 10, 20, 30, or 40 minutes, followed by a maximum of 20 minutes of poststimulatory darkness (Figure 2.5A). In the case of the alternating stimulation paradigm, the experiment consisted of two sessions of stimulatory phases, interspersed with pre-, inter-, and post-stimulatory phases. Each

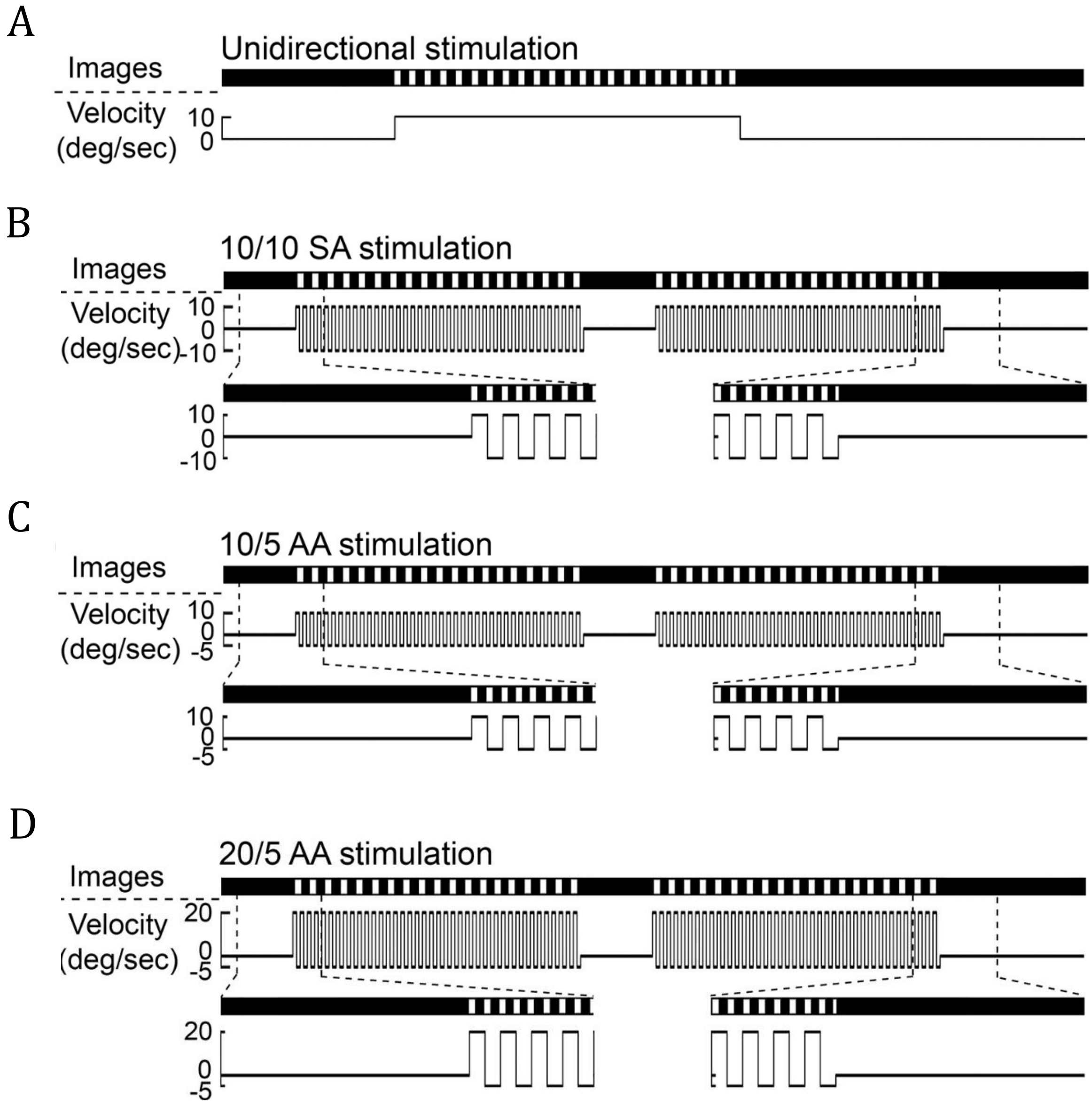

Figure 2.5. Schematic illustrations depict various optokinetic stimulations. (A) Unidirectional +10 deg/sec stimulation. (B) Symmetric alternating stimulation at +/−10 deg/sec (10/10 SA). (C) Asymmetric alternating stimulation at +10/−5 deg/sec (10/5 AA). (D) Asymmetric alternating stimulation at +20/−5 deg/sec (20/5 AA). For all these stimulus conditions, a 5-minute dark period before the stimulation and a 10-minute dark period after the stimulation were included. The duration of the stimulus was 10 minutes for case (i) and twice 20 minutes for cases (ii)-(iv), with a 5-minute dark period between each stimulus. Adapted from (Lin et al., 2022).

experiment began with 5 minutes of pre-stimulatory eye movement recording in darkness, followed by 20 minutes of direction-alternating moving grating (the first stimulatory phase). Then, a 5-minute inter-stimulatory phase was introduced, testing the aftereffect in the dark. Subsequently, another 20-minute session of alternating stimulation was given (the second stimulatory phase), followed by 10 minutes of poststimulatory darkness (Figure 2.5B-D). Both symmetric and asymmetric alternating optokinetic stimulations were used. In symmetric stimulation (10/10 SA stimulation; Figure 2.5B), the fish experienced 10 degrees per second of stimulation in both directions. In asymmetric stimulation (20/5 and 10/5 AA stimulations; Figures 2.5C,D), the fish were exposed to 20 degrees or 10 degrees per second in one direction and 5 degrees per second in the other direction. Throughout the 20-minute stimulatory phases, a cycle of a 15-second stimulus in one direction was followed by a 15-second stimulus in the other direction, with the starting direction of the stimulus randomized. To control all aspects of the experiment, including frame processing, data recording, visual stimulus properties, and lighting, a custom-made program written in LabVIEW (National Instruments, Austin, Texas, USA) was utilized (Chen et al., 2014b).

2.2.5 Eye movement recording and analysis

The movements of both eyes were recorded at a sampling rate of 40 frames per second by an IR-sensitive charge-coupled device (CCD) camera. The area around the eyes was manually selected as the region of interest. Throughout the thesis, both the horizontal eye rotation and the rotating optokinetic stimulus in the counterclockwise direction are marked as positive. After the stimulus ended, either the light was turned off, or the gratings were turned to stationary, and the recording of the OKAN eye movement continued until the larva regained its spontaneous eye movements. Data were analyzed using custom-developed software written in MATLAB (MathWorks, Natick, MA, USA).

Eye-position traces were smoothened by applying a Gaussian filter with a cutoff frequency of 5.5 Hz. This filtering process aimed to improve the signal-to-noise ratio. To determine eye movement velocity, we calculated the derivative of the eye-position traces. However, to avoid any distortion of saccades in the data during the smoothing procedure, we implemented a three-step de-saccading process. This process allowed us to identify quick and slow phases accurately. During the de-saccading procedure, quick phases and/or saccade eye movements were identified based on a velocity threshold of 20 deg/sec. This threshold was applied to median velocities within each 0.5-second time window. Additionally, an eye dislocation threshold of 1 degree was used in conjunction with manual adjustments to ensure precise identification of quick and slow phases.

Following de-saccading, the slow-phase velocity (SPV) was estimated as the median velocity in the first second of each slow phase. Similarly, we also computed the median eye position and used both data to draw the V-P (SPV versus Position) plot. The linear regression of velocity on the position was estimated with ordinary least squares by applying the *fitlm* function in MATLAB. We categorized the quick phases according to the velocity sign into positive and negative groups, followed by computing the quick-phase frequency (QPF) by counting the number of quick-phase eye movements in a time window of every 10 sec. To estimate the kinetics of the OKN adaptation, we fitted both the SPV and the change in quick-phase frequency (ΔQPF), which was obtained by subtracting the positive QPF from the negative QPF with a second-order exponential decay function:

After removing the saccade, we proceeded with the estimation of slow-phase velocity (SPV) by calculating the median velocity during the initial second of each slow phase. The median eye position was obtained using the same smoothening process and was used to create the V-P (SPV versus Position) plot. Furthermore, we used ordinary least squares using the MATLAB *fitlm* function to determine the linear regression of velocity on position. For categorizing quick phases, we separated them into positive and negative groups based on the velocity sign. Subsequently, we determined the quick-phase frequency (QPF) by counting the number of quick-phase eye movements in successive 10-second time windows. To assess the kinetics of the OKN (optokinetic nystagmus) adaptation, we fitted both the SPV and the change in quick-phase frequency (ΔQPF) — which was obtained by subtracting the positive QPF from the negative QPF— with a second-order exponential decay function:

$$f(t) = g_1 \cdot e^{-\frac{t-t0}{\tau_1}} + g_2 \cdot e^{-\frac{t-t0}{\tau_2}} + b \tag{2.8}$$

where f(t) represents SPV or ΔQPF function of time (t), g_1 is the gain of the first decay phase, t_0 is the onset of optokinetic simulation, τ_1 is the time constant of the first decay phase, g_2 is the gain of the second decay phase, and τ_2 is the time constant of the second decay phase. To estimate the decay kinetics of negative OKAN, we fitted both the SPV and ΔQPF with a first-order exponential decay function:

$$f(t) = g \cdot e^{-\frac{t-t_c}{\tau}} \tag{2.9}$$

where f(t) represents the SPV or ΔQPF function of time (t), g is the gain, t_c is the cessation of optokinetic simulation, τ is the time constant of decay, and "offset" is not considered because SPV and ΔQPF are assumed to return to 0 gradually after the stimulation.

3. POPULATION CODING OF NATURAL SELF-MOTION STIMULI IN SUBCORTICAL AND CORTICAL AREAS

In this chapter, we investigate the population coding of natural self-motion in subcortical and cortical areas. Despite a myriad of studies, how information is represented in neural ensembles and, in general, population coding, is not well understood. Notably, individual neurons within a population exhibit difference in their spiking activities in response to a given stimulus, which is known as response heterogeneity (Bannister and Larkman, 1995a, b; Gjorgjieva et al., 2016). Theoretical studies have demonstrated that such heterogeneity can be beneficial for information transmission under certain conditions, as it increases the coding range (Berry Ii et al., 2019; Ecker et al., 2011; Hunsberger et al., 2014; Marsat and Maler, 2010; Mejias and Longtin, 2012; Montijn et al., 2015; Osborne et al., 2008; Perez-Nieves et al., 2021b; Shamir and Sompolinsky, 2006; Tripathy et al., 2013; Zeldenrust et al., 2021). Additionally, correlations between neural activities can either enhance or reduce information transmission depending on their specific structure (Kohn et al., 2016; Panzeri et al., 2022; Wilke and Eurich, 2002). The influence of correlations on information transmission becomes more complex due to their high plasticity. Various factors, such as attention (Cohen and Kohn, 2011; Cohen and Maunsell, 2009), single neuron firing properties such as firing rate and response nonlinearities (de la Rocha et al., 2007; Hong et al., 2012; Lyamzin et al., 2015) and stimulus attributes such as spatial extent, frequency content, and intensity (Chacron and Bastian, 2008; deCharms and Merzenich, 1996; Lyamzin et al., 2015; Usrey and Reid, 1999) can regulate correlations (see (Doiron et al., 2016) for review).

Herein, I present here the results we obtained from multiunit recordings performed in vestibular nuclei (VN) and parieto-insular vestibular cortex (PIVC) during naturalistic and artificial self-motion stimulation. The chapter is organized as follows. First, I present the data obtained from multiunit recordings from vestibular-only (VO) neurons in VN. I go over the characteristics of the individual neurons (neural gain, phase, and heterogeneity) as well as their ensemble features (i.e., correlation structure). Next, I present the results obtained from vestibular neurons in PIVC. Similarly, I characterize the response of neurons and correlation structure for the vestibular neurons in PIVC.

3.1. Multiunit recordings in vestibular nucleus

The goal of this study was to investigate how neural populations within the vestibular nuclei encode naturalistic self-motion stimuli. To address this question, we delivered self-motion stimuli to head-fixed Macaca mulatta that were comfortably seated on a turntable while recording multiunit activity from vestibular-only neurons within the vestibular nuclei (Figure 3.1). Our dataset comprised of neurons recorded from three awake behaving animals for which we were able to maintain isolation from multiple neurons during the highly dynamic self-motion stimuli described below (49 neurons in total: 11 from monkey D; 34 neurons from monkey B; 4 neurons from monkey O; see section 2.1). Neurons were classified as either type 1 or 2 (33 type 1 and 16 type 2 neurons) depending on whether they responded with excitation to rotations towards the ipsilateral or contralateral sides, respectively. We note that these correspond to ON and OFF-type cells in other systems.

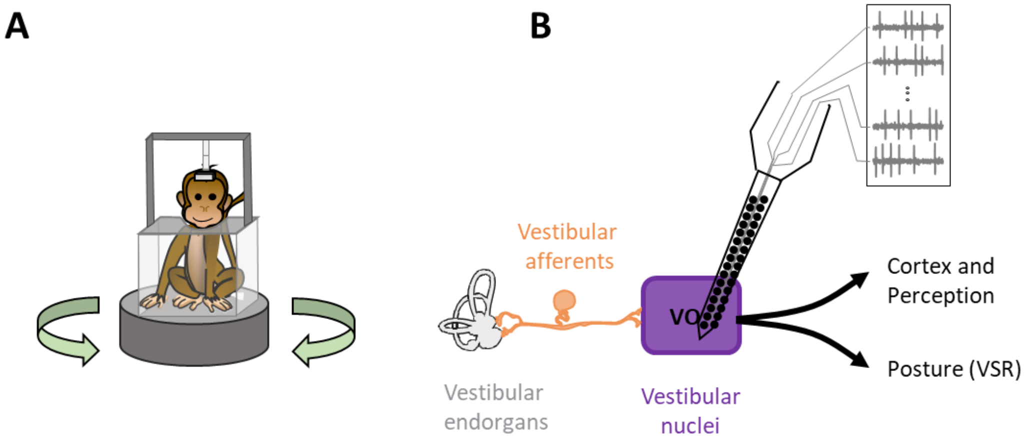

Figure 3.1. Schematic of recording setup and experiment. (A) A schematic of the animals positioned on a motion platform. During the experiments, the animal is head-fixed and seated comfortably on a turntable. (B) A schematic of early stages of the neural circuits involved in self-motion perception. Vestibular afferents transmit head motion information to VO neurons in vestibular nuclei which in turn project to spinal cord as well as thalamus and cortical areas and mediate postural reflexes and self-motion perception, respectively. A vector array probe was used to record neural activity of multiple VOs simultaneously in vestibular nuclei.

Self-motion stimuli consisted of rotations whose timecourse closely mimicked that recorded while the animal performed natural behaviors such as walking and jumping (Figure 3.2) (Carriot et al., 2017a). These stimuli are henceforth referred to as naturalistic. For comparison, artificial self-motion stimuli consisting of sinusoids with an amplitude of 15 deg/s at frequencies 0.5, 1, 2, 3, 4, 5, 8, and 17 Hz were also used (Figure 3.3). While naturalistic self-motion stimuli contain a spectrum of frequencies and can reach large amplitudes (200 deg/s) and, as such, strongly differ from sinusoids in that each sinusoidal stimulus contains only one frequency and reaches lower amplitudes (compare panels A and B in Figure 3.3).

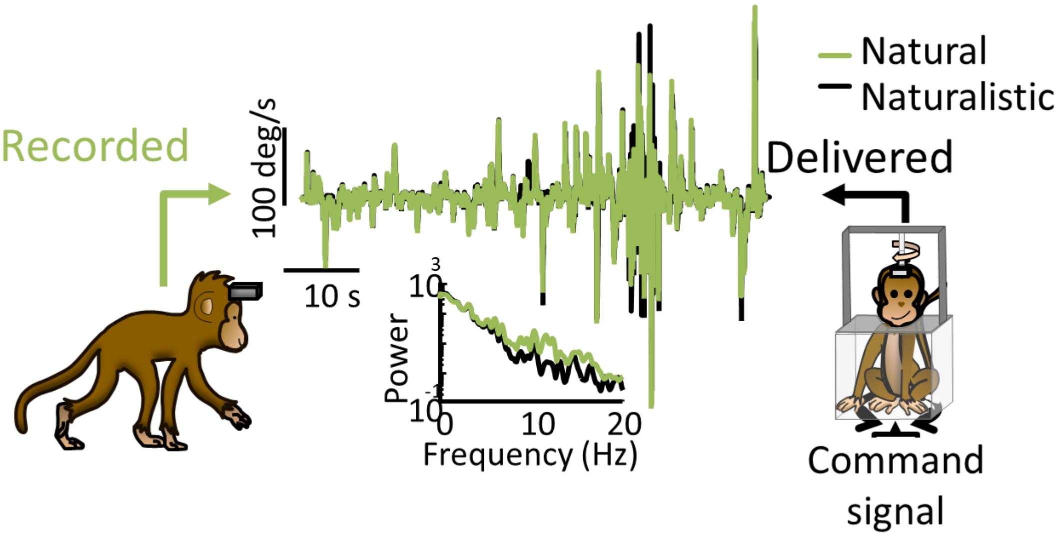

Figure 3.2. Schematic of stimulus delivery in our experiments. The head motion of the animal was recorded while freely moving in a natural environment using accelerometer and gyroscope sensor across three axes of rotation and three axes of translation (shown in green). The yaw rotation component of this signal then was replayed to animal using rotation platform (shown in black). The middle panels compare the original yaw head rotation and the head rotation recorded during naturalistic stimulation. As seen above, the semicircular canals are being stimulated with the same statistics as in during natural self-motion.

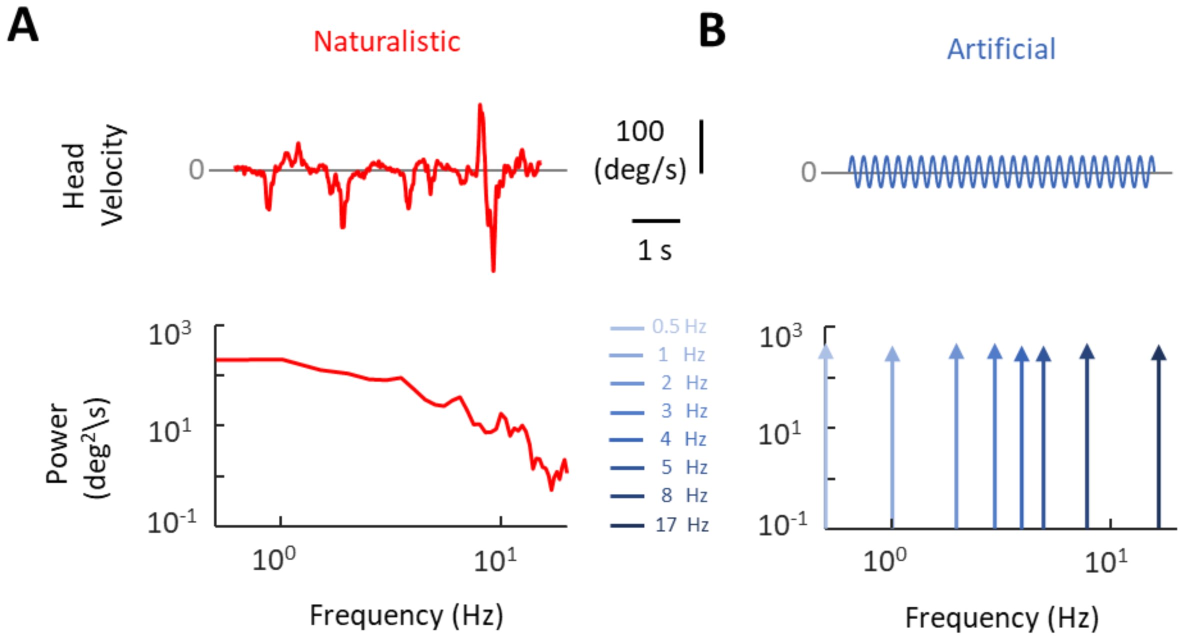

Figure 3.3. Comparing the stimuli used in the study. (A) Top: A 6-second segment of the naturalistic stimulus; Bottom: the power spectra of the naturalistic stimulus. (B) Top: A 6-second segment of the artificial (i.e., sinusoidal) stimulus, f = 4Hz; Bottom: the power spectra of the artificial stimuli used in the studies. The stimuli are color coded from light to dark blue for f=0.5, 1, 2, 3, 4, 5, 8, and 17 Hz stimuli.

3.2. Characterization of VO neural response to artificial and naturalistic stimuli in VN

First, we investigated the response of individual VO neurons in VN and characterized their response by calculating their response gain and phase (see section 2.1.7 for more details). The response profiles of VO neurons in VN in our dataset to sinusoidal were similar to those previously reported during both artificial and naturalistic stimulation as quantified by neural gain and phase (Carriot et al., 2022; Mackrous et al., 2020; Massot et al., 2011; Mitchell et al., 2018). Figure 3.4 demonstrates the population-averaged gain and phase lead of the VO neurons in response to naturalistic stimulus (depicted in solid red lines) and artificial stimuli (shown with filled circles and color-coded for different stimuli, similar to Figure 3.3B, bottom panel). The response dynamics of the neurons to artificial as well as naturalistic stimuli are similar. The response gain of the neurons increases from 0.5 to 2.5 (spk/s)/(deg/s) with frequency in the frequency range of 0-20Hz, rendering these neurons a high-pass neural filter. VO neurons in VN demonstrate phase lead in response to both artificial and naturalistic stimuli, which, similar to the gain, increases with frequency. For low

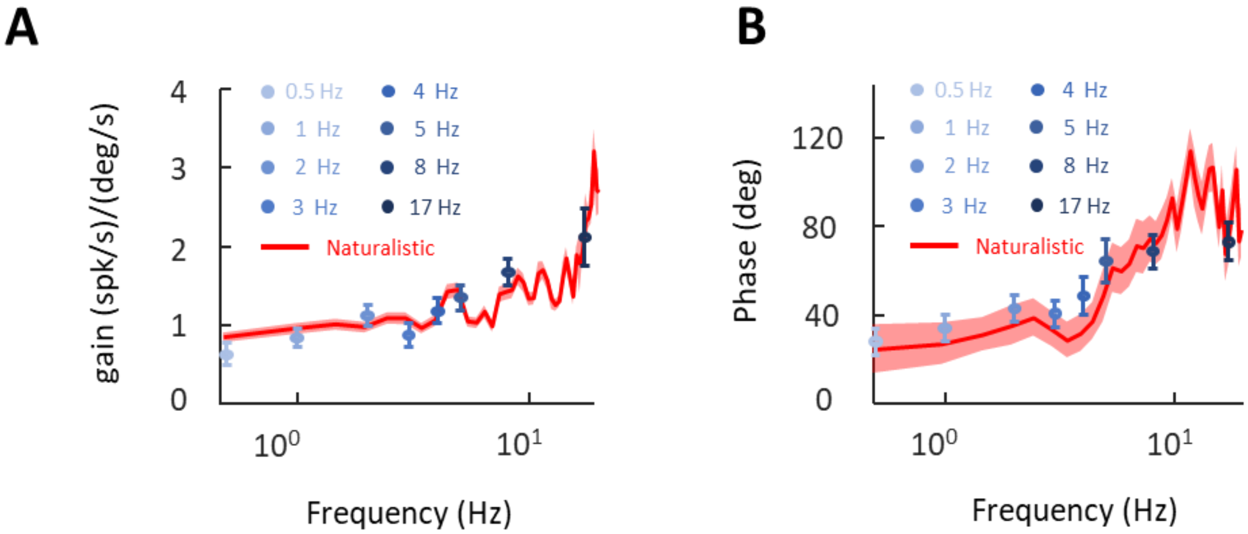

Figure 3.4. The response dynamic of VO neurons in VN during artificial and naturalistic stimuli. (A) Population-averaged gain for VO neurons during artificial stimuli (shown in shades of blue, similar to bottom panel in Figure 3.3B; N=42, f=0.5 HZ; N=42, f=1 HZ; N=40, f=2 HZ; N=41, f=3 HZ; N=40, f=4 HZ; N=41, f=5 HZ; N=39, f=8 HZ; N=37, f=17 HZ) and naturalistic stimulus (Shown in red; N=41). Error bars and the error band show 1 SEM for artificial and naturalistic stimuli, respectively. (B) Population-averaged phase for VO neurons during artificial (shown in shades of blue, similar to bottom panel in Figure 3.3B; N=42, f=0.5 HZ; N=42, f=1 HZ; N=40, f=2 HZ; N=41, f=3 HZ; N=40, f=4 HZ; N=41, f=5 HZ; N=39, f=8 HZ; N=37, f=17 HZ) and naturalistic stimulation (Shown in red; N=41). Error bars and the error band each show 1 SEM.

frequencies, the phase lead is approximately 25 degrees, whereas, for high frequencies (e.g., 20Hz), the phase lead increases to 80 degrees. In our dataset, VO neurons were not modulated with neck proprioceptive input, consistent with previous studies in rhesus macaque monkeys.

3.3. VO neural response heterogeneity in VN

We then investigated how neural populations within the vestibular nuclei responded to naturalistic vs. artificial stimulation. Our results demonstrated that the neural activity of VO neural populations is highly heterogenous, as discussed below.

3.3.1 Heterogeneity during naturalistic stimulus arises across neural variability.

We characterized the variability and heterogeneity during naturalistic and artificial stimuli. Specifically, during naturalistic stimulation (Figure 3.5A), we found that spiking

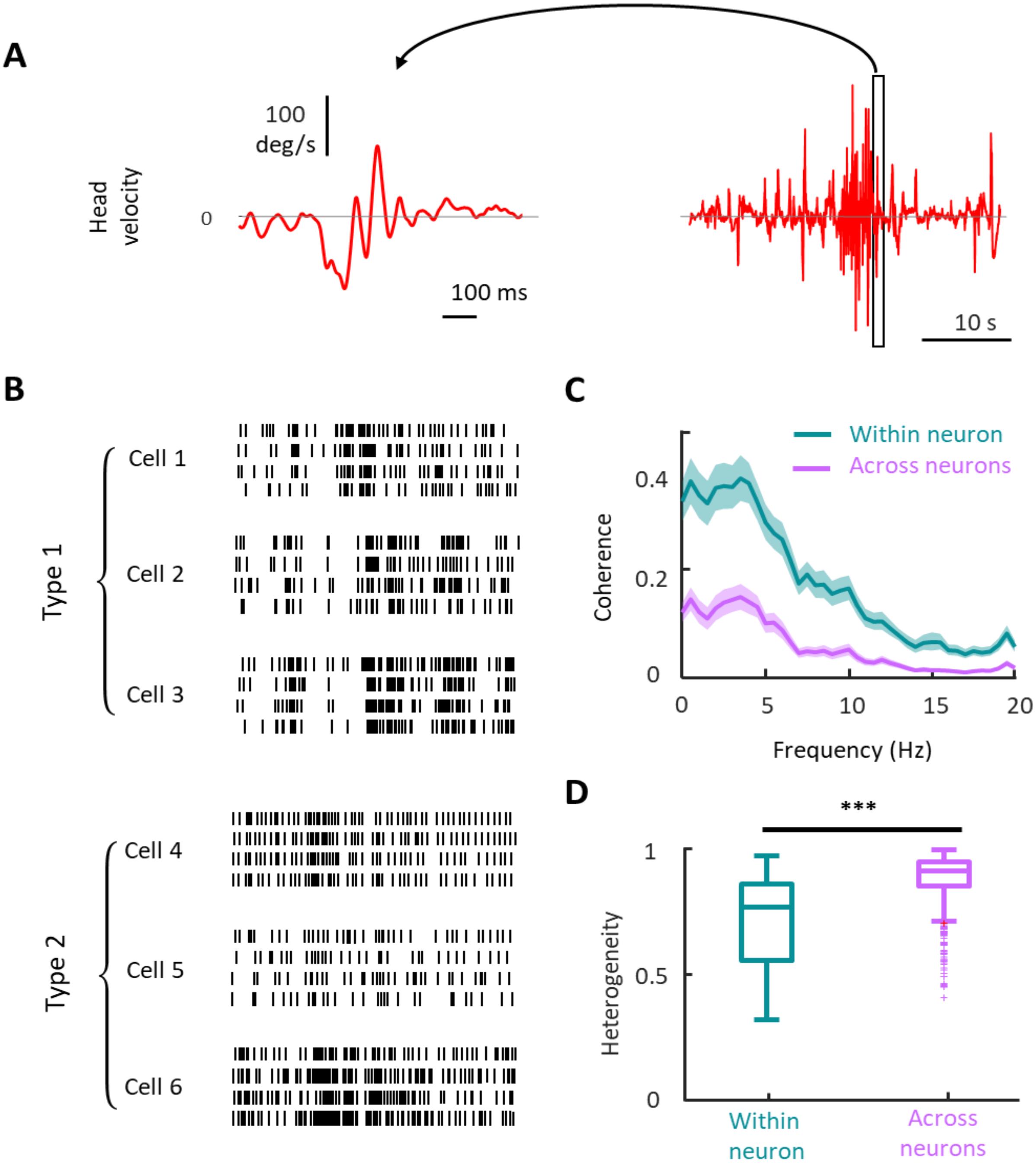

Figure 3.5. VO neural response in VN is highly heterogeneous across neurons in the population during naturalistic stimulus. (A) Right: the entire waveform of naturalistic head velocity stimulus used in the study; Left: a 1 second snippet of the stimulus magnified to demonstrate the detailed temporal dynamics of the stimulus. **(B)** Raster plots for 3 exemplar type 1 and 3 exemplar type 2 VO neurons during the same stimulus snippet in panel A. The temporal scale bar is shared between panels A and B. **(C)** The population-averaged response-response coherence across neurons (magenta) and trials (turquoise) (N=41). The error band show 1 SEM. **(D)** The population-averaged heterogeneity in VOs is significantly higher across neurons than across trials (Wilcoxon rank sum test, N=41, $p=5.6\times10^{-12}$).

responses were heterogeneous. This response heterogeneity resulted not only from different neurons displaying different spiking patterns (i.e., across neuron variability) but also from a given neuron displaying different spiking patterns to repeated stimulus presentations (i.e., trial-to-trial or within neuron variability; Figure 3.5B). To quantify the degree of heterogeneity, we computed the response-response coherence in two cases (Roddey et al., 2000): response coherence across the VO population or across-neurons coherence; And the coherence within the neural response of given neurons across trials or within-neuron coherence (see section 2.1.8 for more details). We note that the coherence is insensitive to phase differences between spike trains. Overall, we found higher response-response coherence values when considering spiking responses from a given neuron to repeated stimulus presentations (i.e., within-neuron coherence; Figure 3.5C, turquoise) than when considering spiking responses from different neurons (i.e., across-neurons coherence; Figure 3.5C, magenta). We next quantified the contributions of across- and within-neuron variability to response heterogeneity. We defined heterogeneity as the complement of the coherence values to one (see section 2.1.8, Eq. 2.7). Overall, we found significantly higher values across neurons Wilcoxon rank sum test, N=41 neurons, $p=5.6\times10^{-12}$; Figure 3.5D), indicating that heterogeneity primarily results from across-neuron variability.

3.3.2 Heterogeneity during artificial stimulation in VO neural population primarily arises from across neural variability

We next investigated heterogeneity under artificial stimulation (Figure 3.6A) and obtained markedly different results. Specifically, neural spiking activities were heterogeneous but to a lesser extent than what was observed under naturalistic stimulation (compare Figures 3.5B and 3.6B). Quantification of across- and within-neuron variability revealed higher values than during naturalistic stimulation (compare Figures 3.5B and 3.6B, 3.7). Interestingly, both within and across neuron variability made contributions to heterogeneity that were not significantly different from one another (Wilcoxon rank sum test, N=40 neurons, p=0.099; Figure 3.6C). Qualitatively similar results were observed for all frequencies (Figure 3.7) and when all frequencies were considered together (Wilcoxon rank

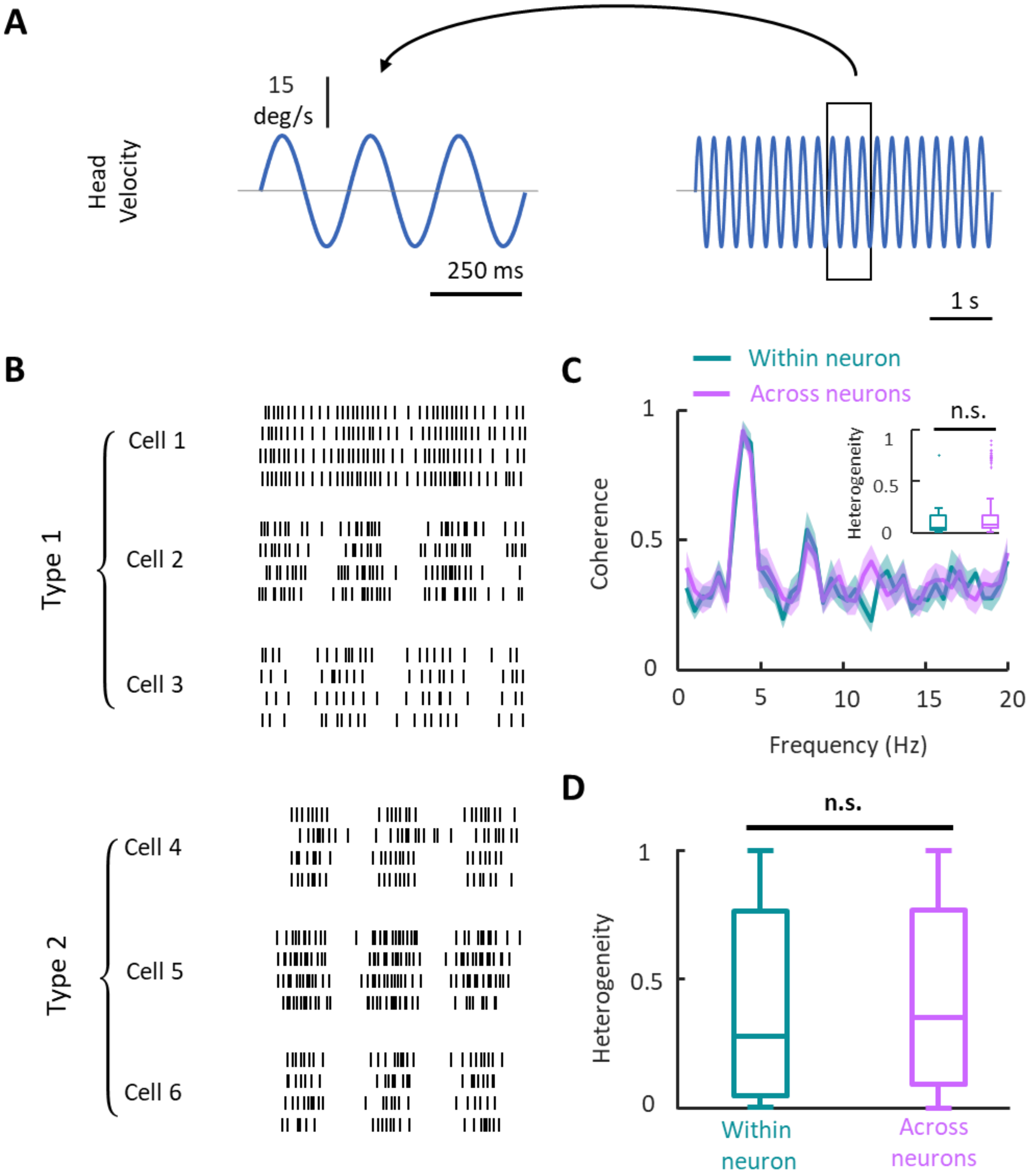

Figure 3.6. VO neural response in VN is heterogenous during artificial stimulation. (A) Right: Example artificial sinusoidal ¬¬head velocity stimulus (f=4 Hz) used in the study; Left: a 3-cycle snippet of the stimulus. **(B)** Raster plot of 3 exemplar type 1 and 3 exemplar type 2 VO neurons during the same stimulus snippet in panel A. The temporal scale bar is shared between panels A and B. **(C)** The population-averaged response-response coherence across neurons (magenta) and trials (turquoise) during 4 Hz artificial stimulation. Inset: Boxplots showing within and across neuron variability during 4 Hz artificial stimulation (Wilcoxon rank sum test, N=40, p=0.099). The error band indicates 1 SEM. The error band show 1 SEM. **(D)** The population-averaged heterogeneity in VOs is not significantly different across neurons and across trials (Wilcoxon rank sum test, N=322, p=0.26).

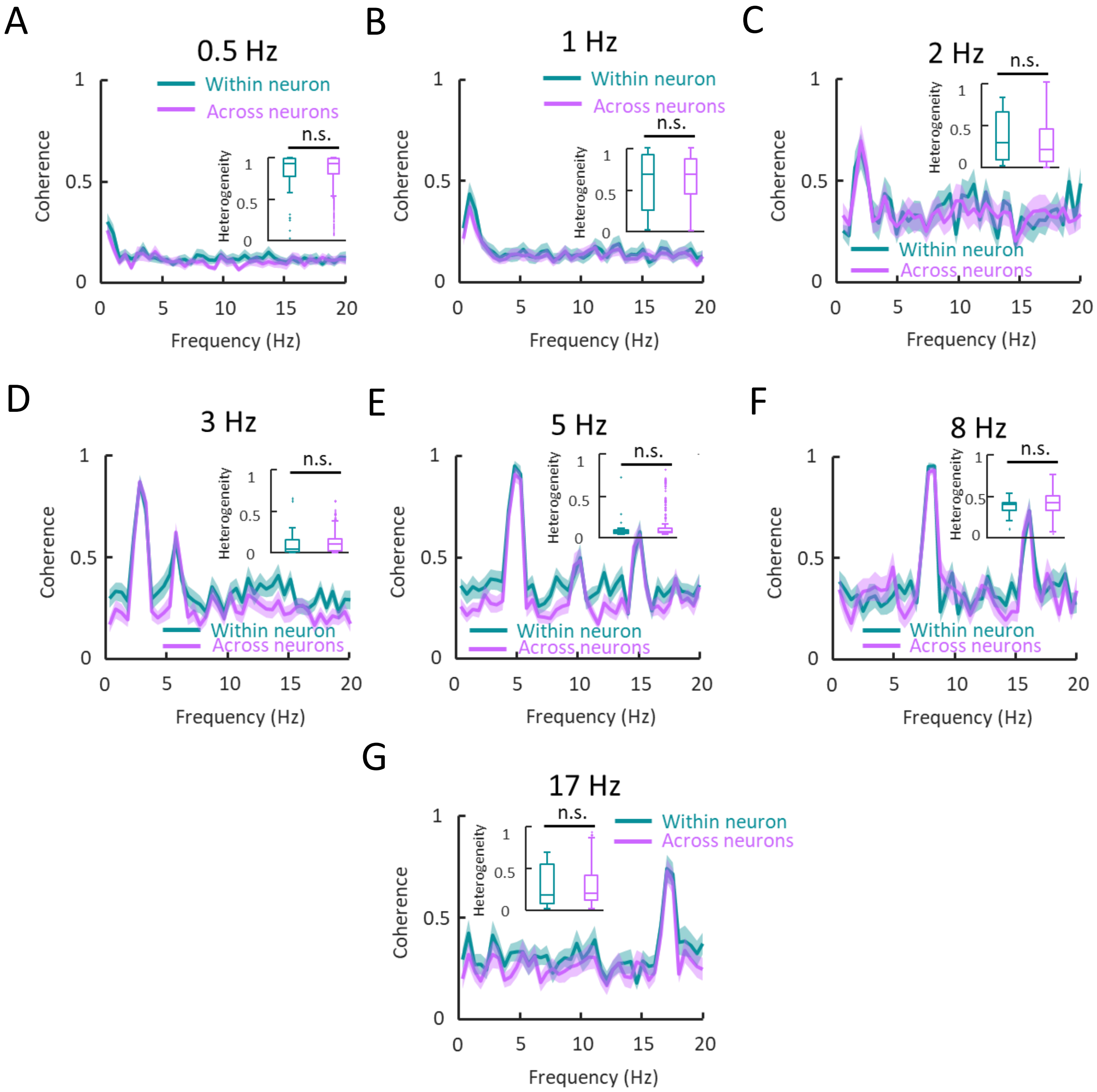

Figure 3.7. VO neural activity in VN is heterogenous in response to sinusoidal stimulation with differential frequency. The population-averaged response-response coherence, as well as the corresponding heterogeneity (inset), is shown across trials (turquoise) and neurons (magenta) for stimulation sinusoidal stimuli with the frequency of (A) 0.5 Hz (N=42 neurons), (B) 1 Hz (N=42 neurons), (C) 2 Hz (N=40 neurons), (D) 3 Hz (N=41 neurons), (E) 5 Hz (N=41 neurons), (F) 8 Hz (N=39 neurons), and (G) 17 Hz (N=37 neurons). Across all frequencies, the contribution of trial-to-trail variability and the variability across neurons to heterogeneity was not significantly different from each other (Wilcoxon rank sum test, insets: (A): p=0.86, N=42; (B): p=0.59, N=42; (C): p=0.62, N=40; (D): p=0.23, N=41; (E): p=0.25, N=41; (F): p=0.39, N=39; (G): p=0.49, N=37).

sum test, N=322, p=0.26, Figure 3.6D), showing that differences in the source of heterogeneity observed during naturalistic and artificial self-motion were robust.

3.4. Correlation structure of VO neural populations in VN is plastic.

We next investigated correlations between vestibular nuclei neural activities. As mentioned above, correlations can be separated between those that are due to the common stimulus (i.e., signal correlations) and correlations between the trial-to-trial variabilities of neural responses to repeated stimulus presentations (i.e., noise correlations). It is important to consider both signal and noise correlations since the relationship between these two measures (i.e., the correlation structure) is important for determining the effects of correlations on information transmission (Kohn et al., 2016; Panzeri et al., 2022).

3.4.1 Quantification of signal correlations in VO populations in VN

To quantify signal correlations in VN, we computed spike count sequences of pairs of VO neurons in VN over trials, shuffled the response across trials, and calculated Pearson's correlation coefficients (see section 2.1.9.1 and Figure 2.2 for more details) (Perkel et al., 1967), while systematically varying the timescale (1-1000 ms). Figures 3.8.A and 3.8.B show signal correlations obtained during naturalistic and 4 Hz artificial stimulation, respectively. In both cases, signal correlations tended to be positive for the same type (i.e., type 1-type 1 and type 2-type 2) pairs and negative for opposite (i.e., type 1-type 2) pairs. This is expected since type 1 and type 2 VO neurons in VN respond with excitation to rotations towards the ipsilateral and contralateral sides, respectively. In the case of naturalistic stimulation, the signal correlation magnitude was maximal for a timescale of 100 ms, which corresponds to the correlation time of the stimulus (Mitchell et al., 2018). In the case of 4 Hz artificial stimulation, signal correlation magnitude was maximal for a timescale of 125 ms, which corresponds to the stimulus half-period. These results were expected as signal correlation magnitude will be maximal on timescales for which the stimulus varies the most. Qualitatively similar results were obtained for other frequencies (Figure 3.9). The magnitude of signal correlations in either group (same-type and opposite-type pairs) increased with

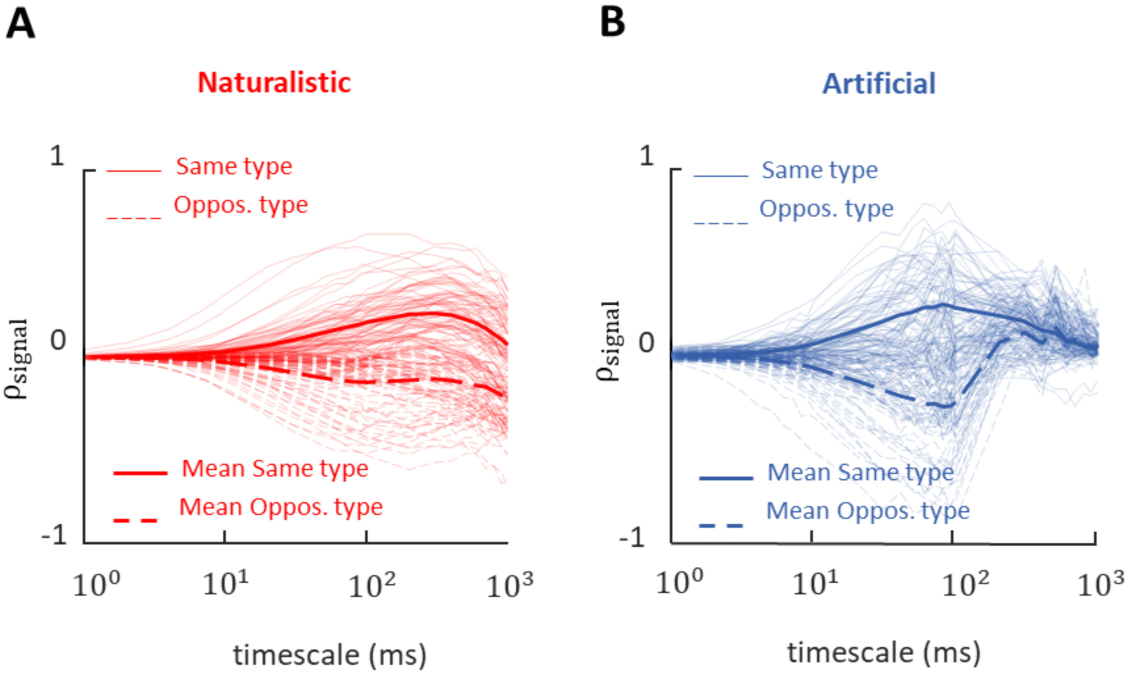

Figure 3.8. VO neurons in VN demonstrate wide range of signal correlations in VN. (A) Signal correlations as a function of timescale during naturalistic stimulus (N= 820 pairs). The solid and dashed lines represent the correlations for the same-type and opposite-type pairs, respectively. The thick solid and dashed lines are the average values of the correlations for the same-type and opposite-type pairs, respectively. **(B)** Same as in A except it was calculated for an artificial stimulus (f=4 Hz; N=780 pairs). For better visualization, we randomly selected 75 same-type and 75 opposite-type pairs. The mean traces are computed over all same-type and opposite-type pairs.

frequency while the mean value across groups remained close to zero. This is expected as the neural gain response increases with stimulus frequency (Figure 3.4A). Since average signal correlations were close to zero across all conditions, we pooled the signal correlation value on stimulus timescales across all frequencies and compared the mean correlation coefficient to that of naturalistic stimulus. Overall, signal correlations were similar during both naturalistic and artificial stimulation (Figure 3.10; Two-sample t-test, N=861 pairs, p=0.83). Additionally, we systematically varied the naturalistic stimulus magnitude below which the signal correlation was calculated. Signal correlations in all cases were qualitatively similar and no significant difference was found when compared to correlations calculated from the whole stimulus.

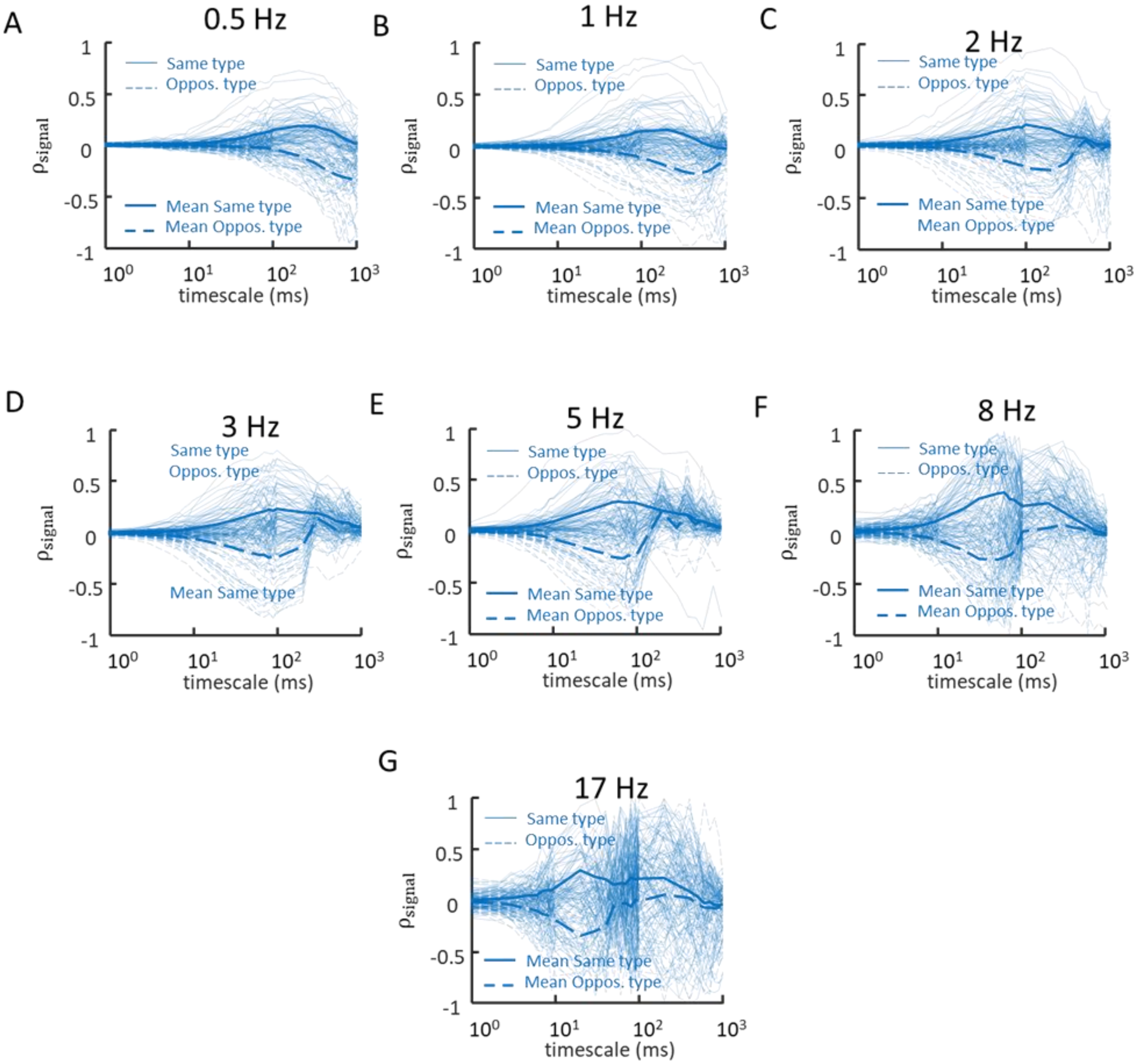

Figure 3.9. Signal correlation as a function of timescale during sinusoidal stimuli with different frequencies. **(A)**: 0.5 Hz, N=861 pairs; **(B)**: 1 Hz, N=861 pairs; **(C)**: 2 Hz, N=780 pairs; **(D)**: 3 Hz, N=820 pairs; **(E)**: 5 Hz, N=820 pairs; **(F)**: 8 Hz, N=741 pairs; and **(G)**: 17 Hz, N=666 pairs. The solid and dashed lines in each panel represent the correlations for the same-type and opposite-type pairs, respectively. The thick solid and dashed lines are the average values of the correlations for the same-type and opposite-type pairs, respectively. While the average values were calculated using all the pairs, only 75 traces of same and opposite-type pairs were shown for visualization purposes.

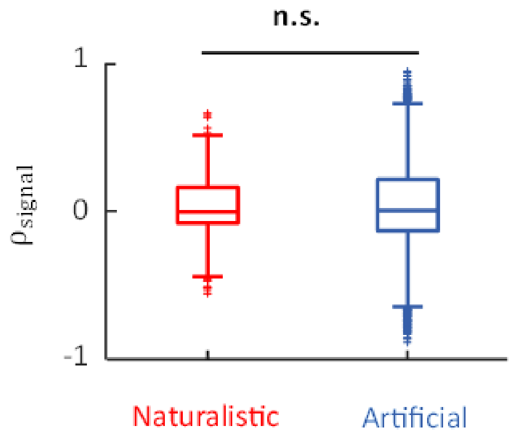

Figure 3.10. Signal correlations are similar during artificial and naturalistic stimulation in VN. Boxplots showing the signal correlation values during artificial (all frequencies) and naturalistic stimuli. Signal correlations during artificial and naturalistic stimuli are not significantly different (Two-sample t-test, N=861 pairs, p=0.83). For artificial stimuli, the timescale was chosen to be a quarter to a half-period of the sinewave period, where the signal correlations were maximum in magnitude on average. For naturalistic stimulus, the signal correlations were calculated for a 100 ms timescale that was consistent with the time scale of the stimulus and where signal correlations were highest in magnitude.).

3.4.2 Quantification of noise correlations in VO populations in VN

In the next step, we quantified noise correlations by computing the Pearson's correlation coefficient between the residual spike counts (i.e., the sequences obtained by subtracting the mean spike count across stimulus trials (see section 2.1.9.2 and Figure 2.3 for more details). Figures 3.11A and 3.11B demonstrate noise correlations obtained during naturalistic and 4 Hz artificial stimulation, respectively. We did not find a significant difference between the noise correlations obtained from same- or opposite-type pairs. Furthermore, qualitatively different results were obtained: while noise correlations tended to be positive during naturalistic stimulation and were thus on average positive (Figure 3.11A), they instead tended to be both positive and negative during 4 Hz artificial stimulation, such that their average was zero (Figure 3.11B). Additionally, we computed the noise correlation for the remaining artificial stimuli with differential frequencies and found that noise correlations were close to zero during artificial stimuli across all frequencies. To

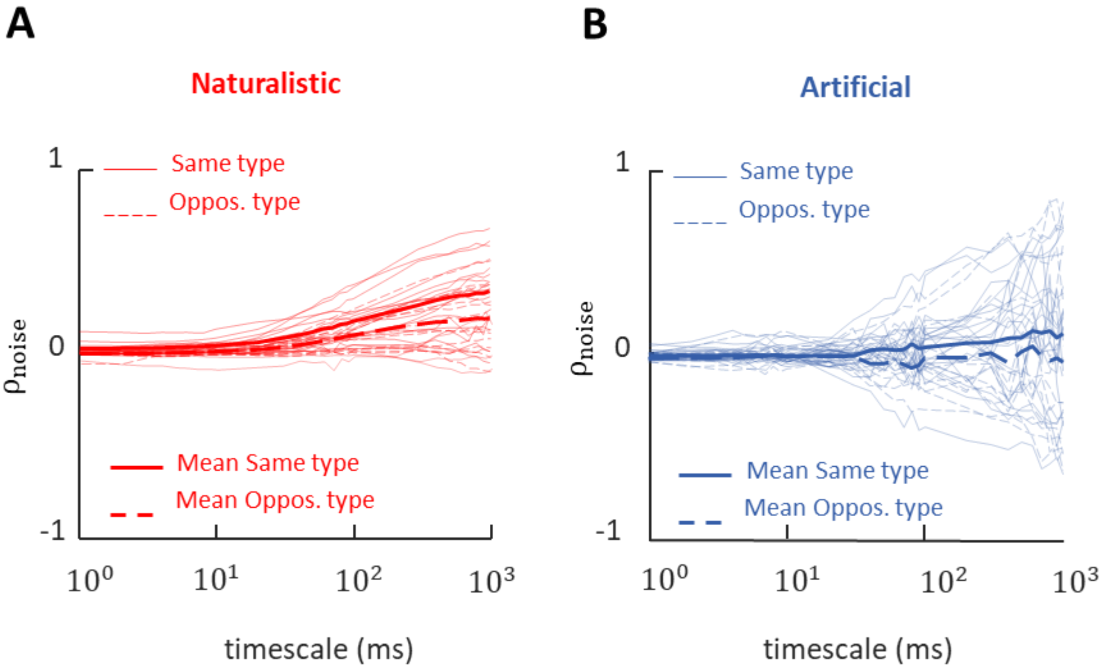

Figure 3.11. VO neurons in VN demonstrate wide range of noise correlations in VN. (A) Noise correlations as a function of timescale during naturalistic stimulus (N=35 pairs). The solid and dashed lines represent the correlations for the same-type and opposite-type pairs, respectively. The thick solid and dashed lines are the average values of the correlations for the same-type and opposite-type pairs, respectively. **(B)** Same as in A except during 4 Hz artificial stimulation (N=35 pairs).

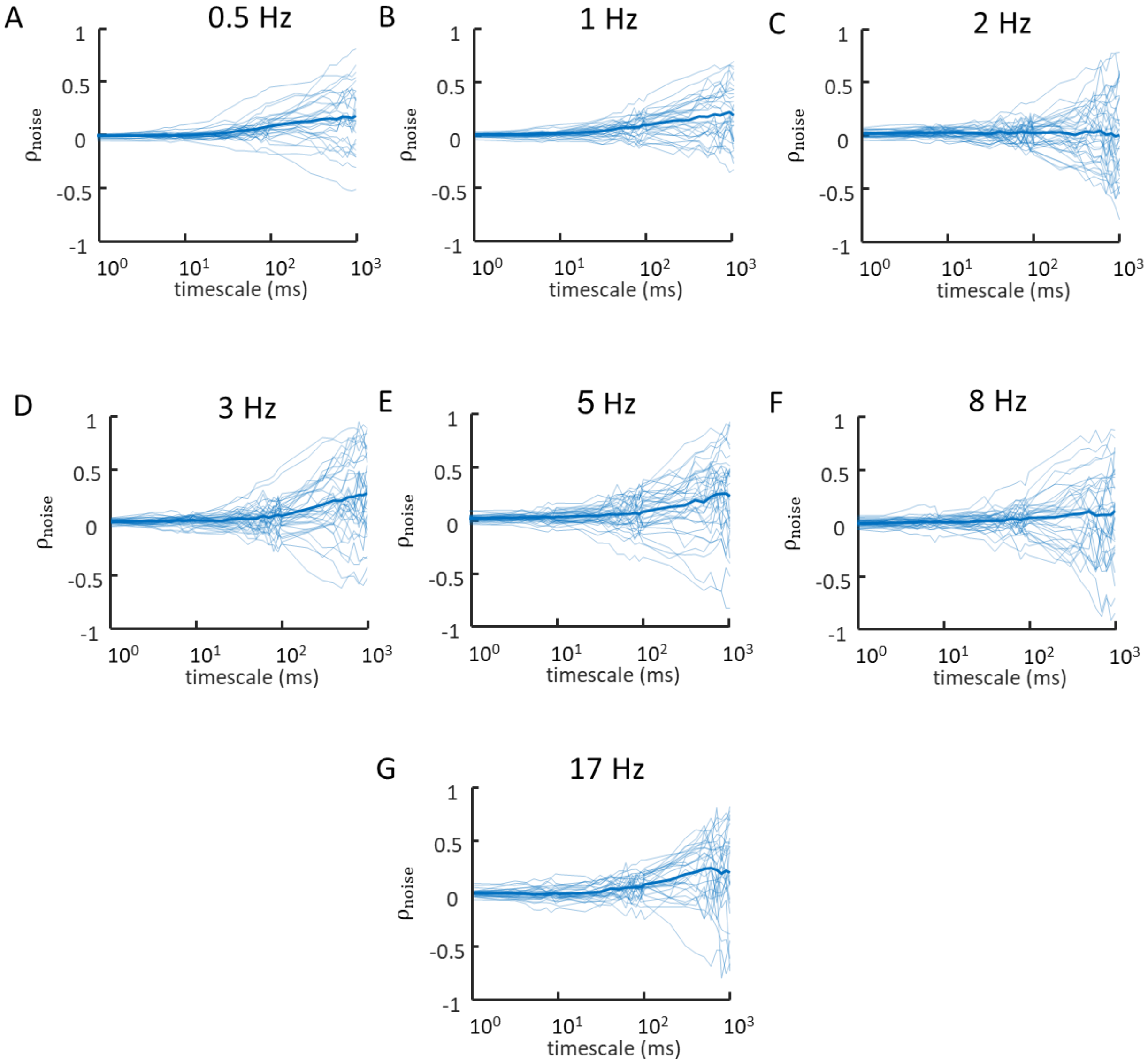

Figure 3.12. Noise correlation as a function of timescale during sinusoidal stimuli with different frequencies. (A): N=28 pairs, 0.5 Hz; **(B)**: 1 Hz, N=29 pairs; **(C)**: 2 Hz, N=35 pairs; **(D)**: 3 Hz, N=35 pairs; **(E)**: 5 Hz, N=34 pairs; **(F)**: 8 Hz, N=33 pairs; and **(G)**: 17 Hz, N=33 pairs. The thick solid lines are the average values of the correlations for all pairs.

compare the noise correlations between artificial and naturalist ic stimuli, we pooled noise correlation values computed at half of the stimulus period for all frequencies —as they were not significantly different than zero— and compared them to that of during naturalistic stimulus (Figure 3.13). Thus, overall noise correlations were significantly more positive during naturalistic than during artificial stimulation (Two-sample t-test, N=35, $p=3.2\times10^{-5}$;

Figure 3.13). Similar to signal correlations, we systematically varied the naturalistic stimulus magnitude below which the noise correlation was calculated. Noise correlations in all cases were qualitatively similar and no significant difference was found when compared to correlations calculated from the whole stimulus.

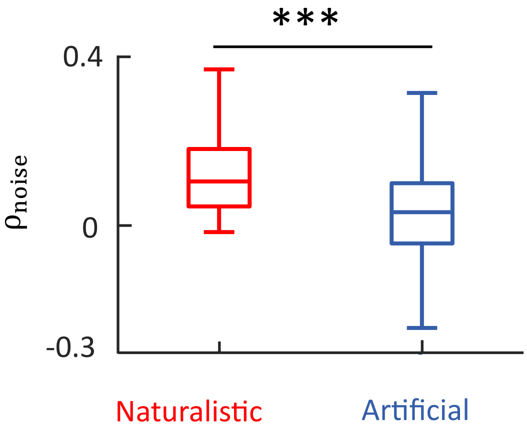

Figure 3.13. Noise correlations are significantly higher during naturalistic stimulus than during artificial stimulation. Boxplots showing noise correlation values during artificial (all frequencies) and naturalistic stimuli. Noise correlations during naturalistic stimuli are significantly higher than that of during artificial stimuli (Two-sample t-test, N=35 pairs, $p=3.2\times10^{-5}$). The timescales at which the noise correlations were computed were the same as those used above for signal correlations.

3.5. Characterization of vestibular neural response to artificial and naturalistic stimuli in PIVC

As mentioned in Chapter 1, the PIVC is the primary cortical area involved in the processing of natural self-motion information (see sections 1.5.6 and 1.6.1). Next, we studied how self-motion information during natural and artificial self-motion are encoded in PIVC vestibular populations. Accordingly, we recorded from PIVC during the same naturalistic and artificial stimuli used in our study of population coding in VN. Our dataset comprises 13-14 vestibular cells obtained from one animal (monkey O; see section 2.1 for more details).

First, we characterized the response of the vestibular neurons in PIVC. Consistent with previous literature, we found neurons in PIVC responded to head motion during pWBR, head-on-body rotation (proprioceptive stimuli), and visual stimuli (Akbarian et al., 1988; Chen et al., 2010, 2011; Chen et al., 2016; Chen et al., 2013b; Shinder and Newlands, 2014). Our stimulation protocol consisted of pWBR stimuli, and therefore, vestibular neurons with neck proprioceptive sensitivity only responded to vestibular stimuli. It is noteworthy to mention that we compared the gain and phase response of the vestibular neurons that only responded to vestibular stimuli with those that also had neck proprioceptive sensitivity and found no significant difference during pWBR. As such, we included vestibular neurons with proprioceptive sensitivity in our dataset. Furthermore, vestibular neurons with visual sensitivity (characterized by their response to pWBR and smooth pursuit) were excluded from our analysis. Hereafter, by vestibular neurons, we refer only to those neurons with proprioceptive sensitivity or lacking response to any other sensory modalities but vestibular stimuli.

We calculated the response gain and phase of the vestibular neurons in PIVC. Our results are consistent with previous reports of gain and phase values for vestibular neurons in PIVC during low-frequency sinusoidal stimulation (Shinder and Newlands, 2014). Specifically, Shinder and Newlands reported the gain and phase of vestibular neurons in PIVC to horizontal sinusoidal head rotation with a frequency of 0.2 Hz and maximum head velocity of 15 or 30 deg/s. The response gain of the vestibular neurons in their study was 0.44±0.10 and 0.25±0.04 (spk/s)/(deg/s) in response to later stimuli, respectively. The phase values ranged from -180 to 180 deg with no pattern, suggesting an average phase value near zero. In our study, we used sinusoidal stimulation with a maximum head velocity of 15 deg/s and the lowest stimulation frequency of 0.5 Hz. The values of gain and phase we obtained were 0.60±0.10 (spk/s)/(deg/s) and 32±13 (deg), which is consistent with values obtained by Shinder and Newlands. To the best of our knowledge, we are the first to characterize the response of vestibular neurons in PIVC during higher-frequency artificial stimuli as well as naturalistic stimuli. Overall, during both artificial and naturalistic stimuli, the vestibular neurons demonstrate high pass tuning to the stimulus. During sinusoidal stimuli, the gain varies between 0.6-3.4 (spk/s)/(deg/s). Interestingly, during naturalistic stimulation, the gain decreases markedly to 0.08-1.06 (spk/s)/(deg/s). Such decrease in gain during naturalistic stimulation may be due to, but not limited to, the adaptation of the neural response to the stimulus amplitude (as reported in (Shinder and Newlands, 2014)) as the envelope of the naturalistic stimuli are much larger than that of the artificial stimuli. The response phase demonstrated large variability during both artificial and naturalistic stimulation (Figure 3.14B). Specifically, during low-frequency artificial stimulation (f≤3Hz),

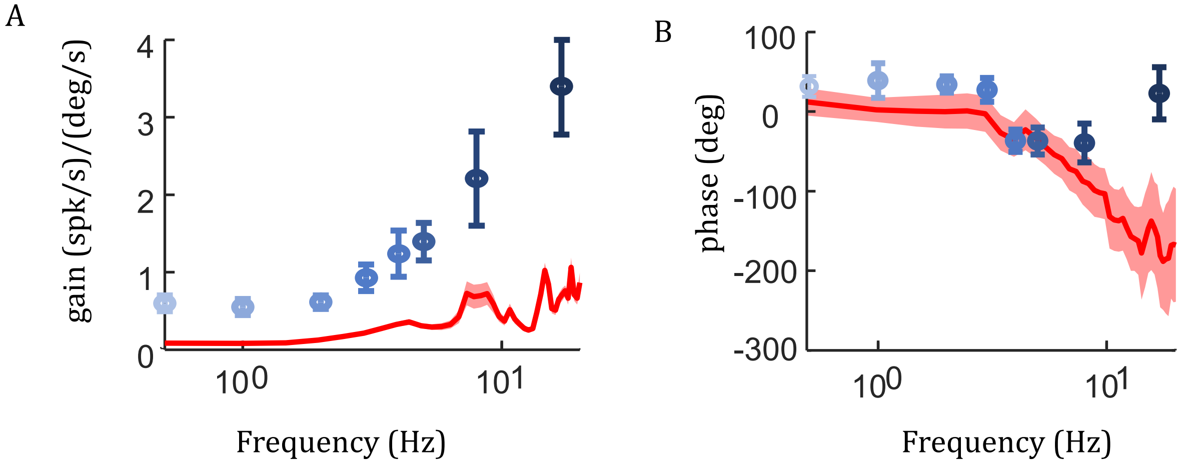

Figure 3.14. The response dynamic of vestibular neurons in PIVC during artificial and naturalistic stimuli. (**A**) Population-averaged gain for vestibular neurons during artificial stimuli (shown in shades of blue, similar to bottom panel in Figure 3.3B; N=5, f=0.5 HZ; N=7, f=1 HZ; N=13, f=2 HZ; N=13, f=3 HZ; N=13, f=4 HZ; N=13, f=5 HZ; N=13, f=8 HZ; N=12, f=17 HZ) and naturalistic stimulus (Shown in red; N=14). Error bars and the error band show 1 SEM for artificial and naturalistic stimuli, respectively. **(B)** Population-averaged phase for VO neurons during artificial (shown in shades of blue, similar to bottom panel in Figure 3.3B; =5, f=0.5 HZ; N=7, f=1 HZ; N=13, f=2 HZ; N=13, f=3 HZ; N=13, f=4 HZ; N=13, f=5 HZ; N=13, f=8 HZ; N=12, f=17 HZ) and naturalistic stimulation (Shown in red; N=14). Error bars and the error band each show 1 SEM.

the response of the neurons, on average, slightly leads the stimulus, whereas for middle frequencies (4Hz≤f≤8Hz), the response slightly lags the stimulus, and finally, for high-frequency stimulation (f=17Hz) the response is in phase with the stimulus. During naturalistic stimulation, the response of the neuron was in phase during low frequencies (f≤3Hz); however, it lagged for higher frequencies. Notably, the variability in phase values was markedly larger than during artificial stimuli. Additionally, the response during high frequencies becomes antiphase, a dramatic contrast to that of low-frequency components of the stimulus.

We attempted to classify the vestibular neurons as type 1 and type 2. Our results demonstrated a wide range of variability in the phase of the neural response across frequencies, as mentioned above (Figure 3.15B). Traditionally, the vestibular neurons in the peripheral or early central vestibular pathway are classified into type 1 or type 2 neurons based on the increased response to ipsilateral and contralateral stimulation at low-frequency stimulation, such as sinusoidal stimulation at 1 Hz. The phase lead in such neurons is positive and increases with frequency, and thereby, the response of such neurons consistently leads

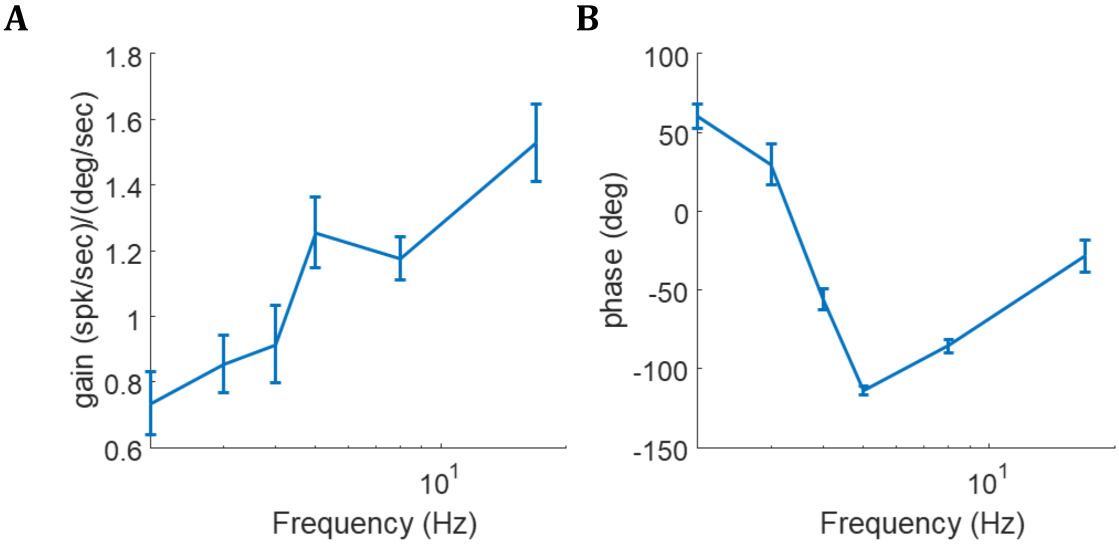

Figure 3.15. The vestibular neurons in PIVC exhibit high degrees of variability in their neural gain and phase. Characterization of an exemplar neuron to sinusoidal stimuli with frequencies of 1, 2, 3, 4, 5, 8, and 17 Hz. (A) Gain as a function of frequency. (B) Phase as a function of frequency. The vertical lines denote 1 SEM.

the stimulus. However, in general, the phase in PIVC neurons does not consistently lead or lag across the relevant frequency range (i.e., 0-20 Hz) due to high variability in the response. Figures 3.15A and 3.15B demonstrate the variability in the gain and phase of the neuron's response, respectively. As illustrated in Figure 3.15B, the response leads stimulus at low frequencies, thereby making them type 1 according to the traditional way of classifying neuronal types. However, the response of the same neurons lags the stimulus in higher frequencies which is not consistent with a type 1 response. All neurons in our dataset (N=14) exhibited both response lead and lag across frequencies. For this reason, we did not classify neurons in PIVC as type 1 or type 2 neurons. Furthermore, these neurons cannot be classified as type 3 neurons—in which the neurons respond to stimulation in both directions—as in stimulation with a given frequency, the peak response consistently appeared in one phase of the cycle and was not biphasic.

3.6. Neural response heterogeneity of vestibular neurons in PIVC

Given the high degree of variability in the response phase during both artificial and naturalistic stimulation, we hypothesized that the neural response in PIVC is highly heterogeneous. To test this hypothesis, we characterized the response heterogeneity in vestibular populations in PIVC during both artificial and naturalistic stimulation.

3.6.1 Heterogeneity in vestibular neural population in PIVC arises from within and across neural variability during naturalistic stimulus

We characterized the variability and heterogeneity during naturalistic stimuli (Figure 3.16A) and found that spiking responses were highly heterogeneous (Figure 3.16B). This response heterogeneity resulted from both across-neuron as well as trial-to-trial or within-neuron variability (Figure 3.16B). To quantify the degree of heterogeneity, we computed the response-response coherence across the response of the neurons in the population as well as the between the trial-to-trial responses. Overall, we found that response-response coherence was low in both cases. Additionally, the within-neuron coherence (Figure 3.16C, turquoise) was consistently higher than that of across-neuron coherence (Figure 3.16C,

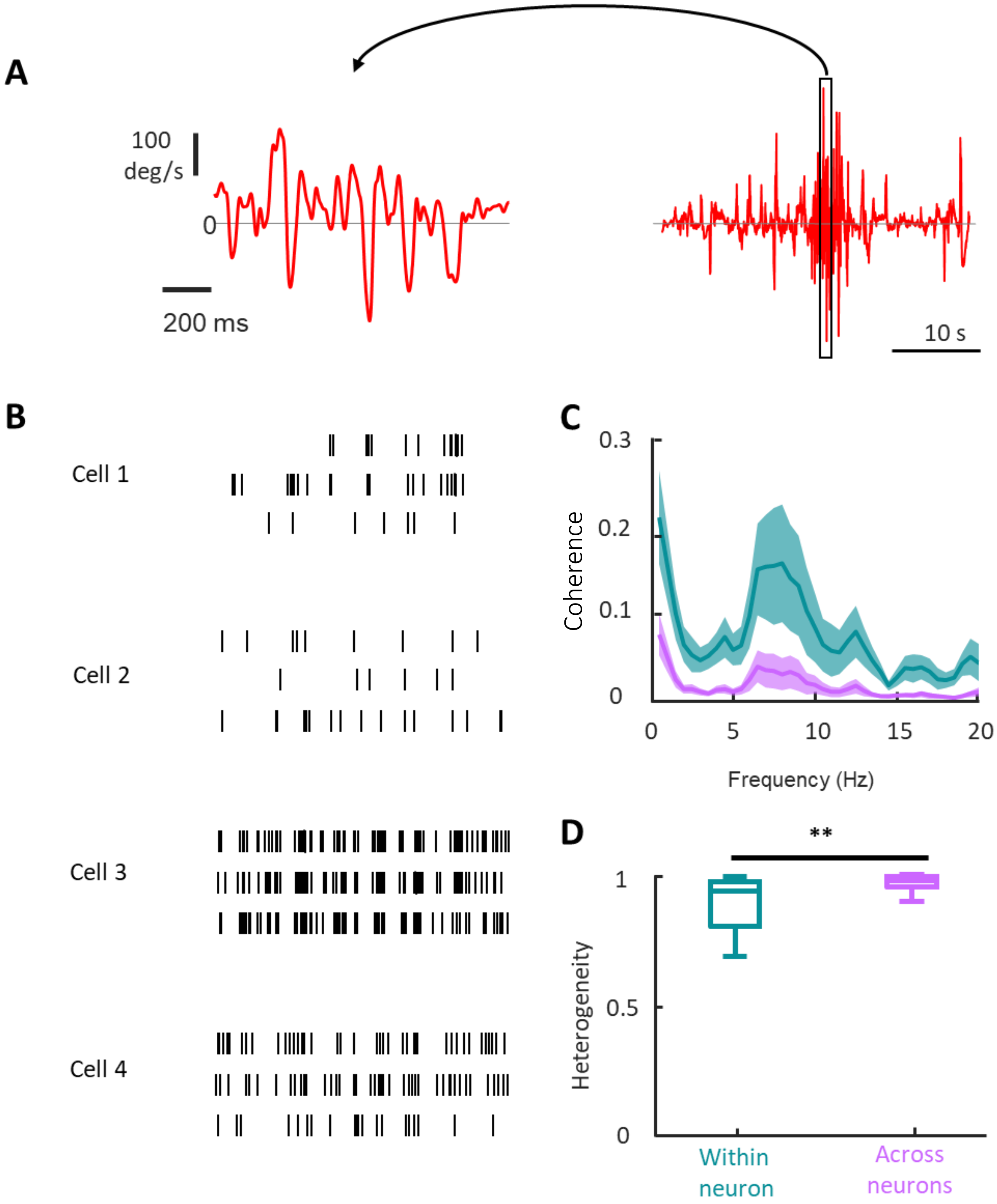

Figure 3.16. Vestibular neural response in PIVC is highly heterogeneous across neurons in the population during naturalistic stimulus. (A) Right: the entire waveform of naturalistic head velocity stimulus used in the study; Left: a one-second snippet of the stimulus magnified to demonstrate the detailed temporal dynamics of the stimulus. **(B)** Raster plots for 4 vestibular neurons during the same stimulus snippet in panel A. The temporal scale bar is shared between panels A and B. **(C)** The population-averaged response-response coherence across neurons (magenta) and trials (turquoise) (N=14). The error band show 1 SEM. **(D)** The population-averaged heterogeneity in vestibular neurons in PIVC is higher across neurons than across trials (Wilcoxon rank sum test, N=14, p=0.0012).

magenta) over the entire relevant frequency range (0-20 Hz). Interestingly, both within-neuron and across-neuron coherence initially decreased with frequency (i.e., between 0-3 Hz; Figure 3.16C) but started increasing with frequency and exhibited a peak in the 5-10 Hz frequency range. Next, we quantified the heterogeneity using the method used previously. The neural response exhibited high within-neuron and across-neuron heterogeneity with median values close to one (Figure 3.16D). However, the neural response demonstrated slightly higher, but significant, across-neuron heterogeneity than within-neuron heterogeneity (Wilcoxon rank sum test, N=14 neurons, p=0.0012). Overall, our results indicate that the neural response of vestibular neural populations in PIVC is highly heterogeneous during naturalistic stimuli resulting from both within-neuron and across-neuron variability, with the latter contributing more to the heterogeneity.

3.6.2 The heterogeneity in vestibular neural population in PIVC primarily arises from across neural variability during artificial stimulation

We next quantified the heterogeneity during artificial stimulation (Figure 3.17A). Overall, neural spiking activities were heterogeneous during artificial stimuli (Figure 3.17B). We computed the within-neuron and across-neuron coherence for artificial stimuli across frequencies. Both within-neuron and across-neuron coherence values were close to zero during low-frequency artificial stimulation (i.e., 0.5 Hz and 1 Hz; Figure 3.18A and 3.18B) and were comparable to that during naturalistic stimulation. For higher-frequency artificial stimulation, the values of coherence were significantly higher than zero and peaked at the stimulus frequency and its harmonics (Figure 3.17C and Figure 3.18C-F). To quantify the response heterogeneity, we computed the within-neuron and across-neuron heterogeneity during artificial stimulation and found significant heterogeneity in both within- and across-neural response. Additionally, we found that except for sinusoidal stimulation at 4, 5, and 8 Hz, within-neuron and across-neuron heterogeneity values were not significantly different from each other at stimulus frequency (0.5 Hz: p=0.43, N=12; 1 Hz: p=0.48, N=13; 2 Hz: p=1, N=13; 3 Hz: p=0.27, N=11; 4 Hz, p=0.033, N=13; 5 Hz: p=0.044, N=13; 8 Hz: p=0.018, N=13; 17 Hz: p=0.22, N=12; insets in Figure 3.17C and Figure 3.18A-F). However, when heterogeneity across all frequencies was pooled, across-neuron variability contributed

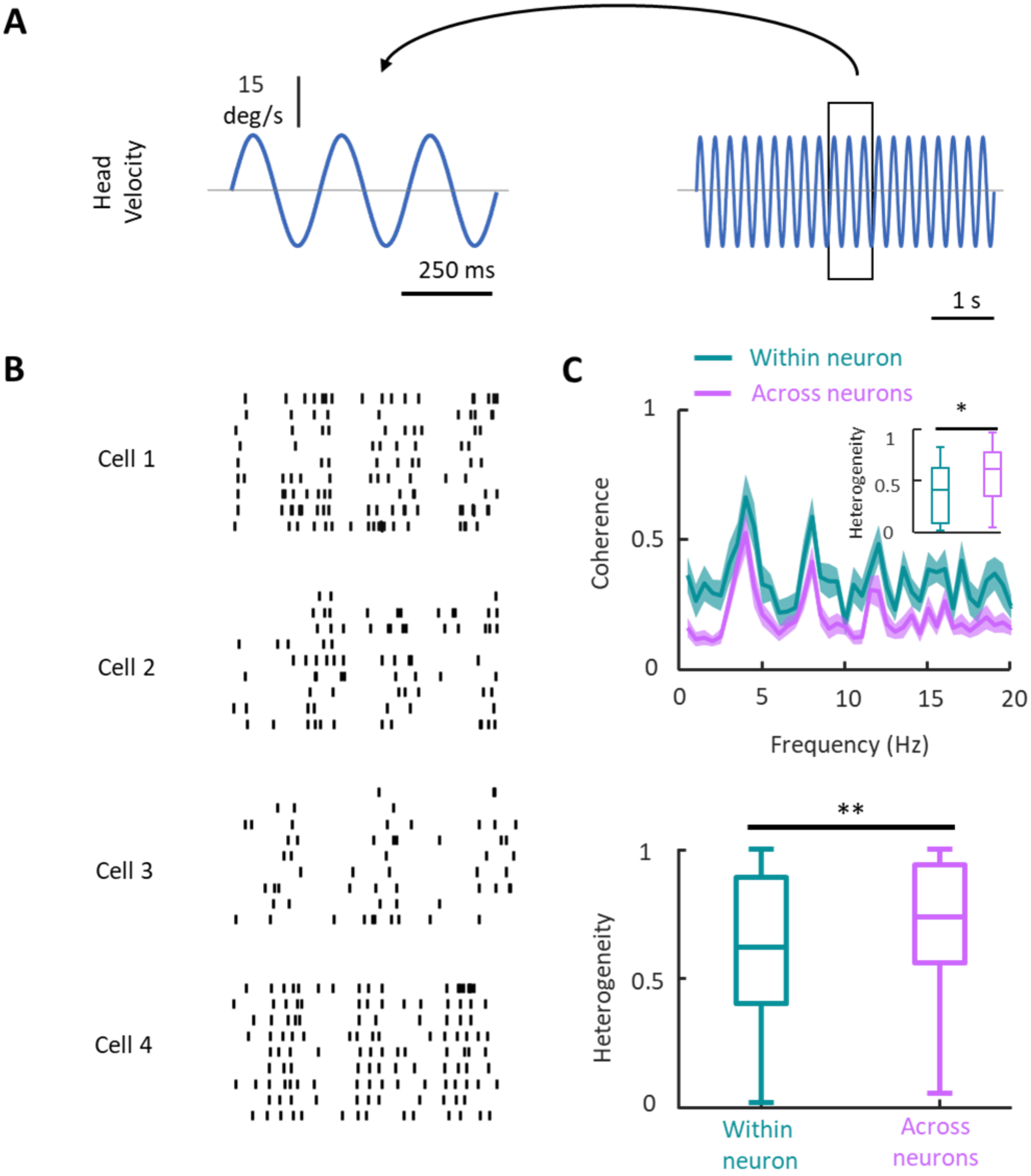

Figure 3.17. Vestibular neural response in PIVC is heterogenous during artificial stimulation. (A) Right: Example artificial sinusoidal head velocity stimulus (f=4 Hz) used in the study; Left: a 3-cycle snippet of the stimulus. **(B)** Raster plot of 4 exemplar vestibular neurons during the same stimulus snippet in panel A. The temporal scale bar is shared between panels A and B. **(C)** The population-averaged response-response coherence across neurons (magenta) and trials (turquoise) during 4 Hz artificial stimulation. Inset: Boxplots showing within and across neuron variability during 4 Hz artificial stimulation (Wilcoxon rank sum test, N=13, p=0.033). The error band indicates 1 SEM. The error band show 1 SEM. **(D)** The population-averaged heterogeneity in vestibular is significantly higher across neurons than across trials (Wilcoxon rank sum test, N=113, p=0.0076).

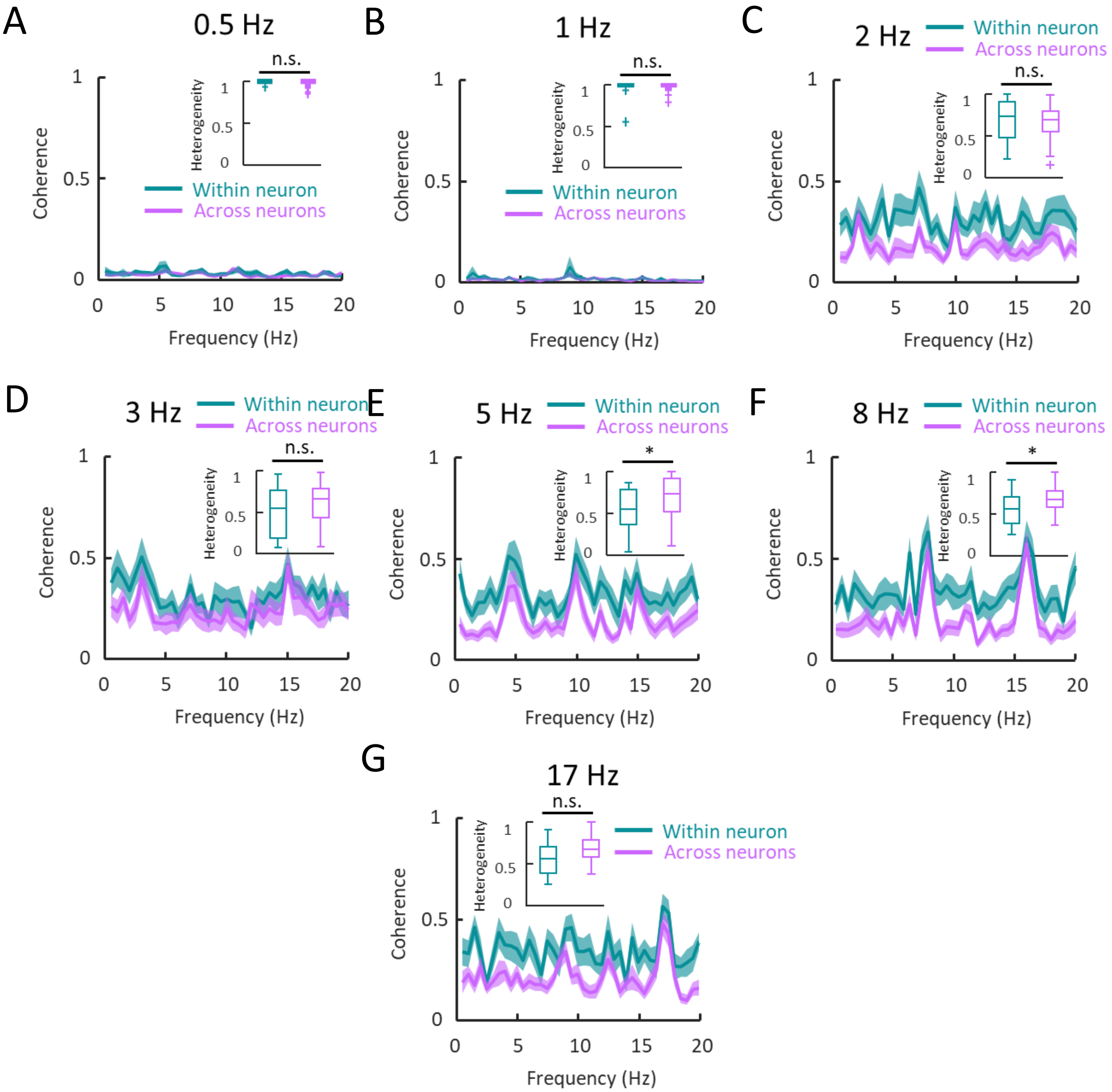

Figure 3.18. Vestibular neural activity in PIVC is heterogenous in response to sinusoidal stimulation with differential frequency. The population-averaged response-response coherence, as well as the corresponding heterogeneity (inset), is shown across trials (turquoise) and neurons (magenta) for stimulation sinusoidal stimuli with the frequency of (A) 0.5 Hz (N=14 neurons), (B) 1 Hz (N=13 neurons), (C) 2 Hz (N=13 neurons), (D) 3 Hz (N=11 neurons), (E) 5 Hz (N=13 neurons), (F) 8 Hz (N=13 neurons), and (G) 17 Hz (N=12 neurons). Across all frequencies, the contribution of trial-to-trail variability and the variability across neurons to heterogeneity was not significantly different from each other (Wilcoxon rank sum test, insets: (A): p=0.43, N=12; (B): p=0.48, N=13; (C): p=1.00, N=13; (D): p=0.27, N=11; (E): p=0.044, N=13; (F): p=0.018, N=13; (G): p=0.22, N=12).

significantly more to the response heterogeneity than within-neuron variability (Wilcoxon rank sum test, N=113, p=0.0076, Figure 3.18D). Overall, our results showed that neural responses during artificial stimuli are heterogeneous, albeit to a lesser degree than that during naturalistic stimulation.

3.7. Correlation structure of vestibular neural populations in PIVC in plastic.

To characterize the correlation structure in vestibular neural populations in PIVC, we computed signal and noise correlations as mentioned above (Kohn et al., 2016; Panzeri et al., 2022). We note that since we refrained from classifying vestibular neurons in PIVC into type 1 and type 2 neurons, we did not label correlation curves as a function of timescale to opposite- or same-type pairs.

3.7.1 Quantification of signal correlations in vestibular neural populations in PIVC

To quantify signal correlations in PIVC, we computed spike count sequences of pairs of vestibular neurons in PIVC over trials, shuffled the response across trials, and calculated Pearson's correlation coefficients (Perkel et al., 1967), while systematically varying the timescale (1-1000 ms). Figures 3.19A and 3.19B show signal correlations obtained during naturalistic and 4 Hz artificial stimulation, respectively. Signal correlation magnitude is expected to be maximal on timescales for which the stimulus varies the most. Interestingly, however, signal correlations peaked at timescales much larger than the stimulus timescale (i.e., ~600 ms compared to 100 ms; (Mitchell et al., 2018)). On the other hand, during 4 Hz artificial stimulation, signal correlation magnitude was maximal for a timescale of 125 ms, which corresponds to the stimulus half-period. As expected, similar results were obtained across artificial stimulation with differential frequencies (Figure 3.20 panels A-G). The magnitude of signal correlations increased with frequency, while the average value across the population remained close to zero. This is expected as the PIVC neural gain response, on

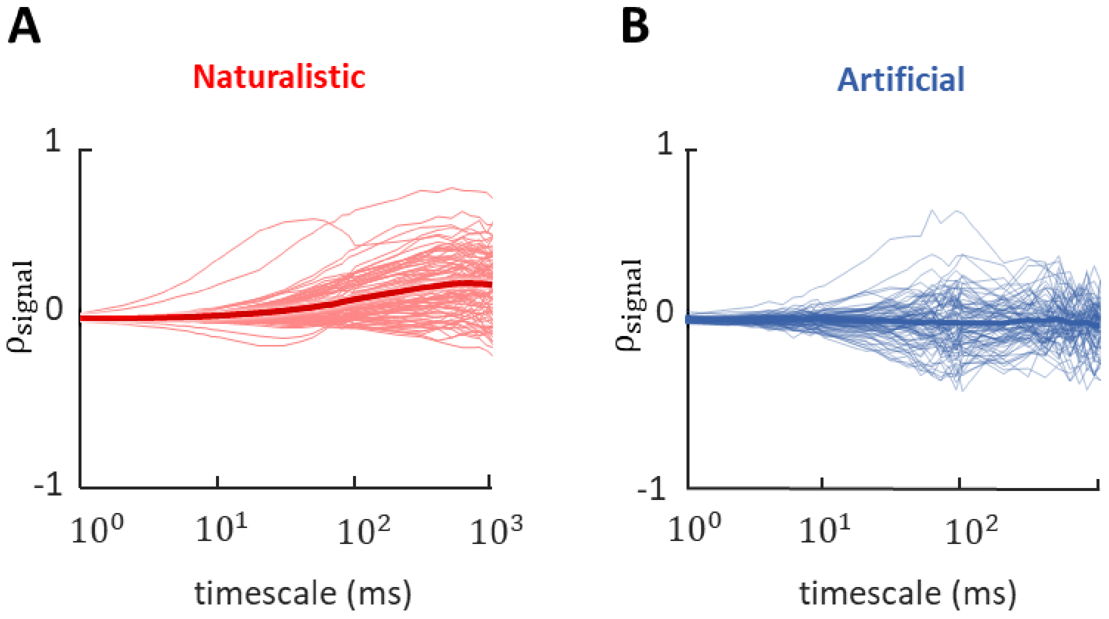

Figure 3.19. Vestibular PIVC neurons demonstrate wide range of signal correlations and are plastic. (A) Signal correlations as a function of timescale during naturalistic stimulus (N= 91 pairs). The thick solid lines are the average values of the correlations as a function of timescale. **(B)** Same as in panel A except it was calculated for an artificial stimulus (f=4 Hz; N=78 pairs). Note that the pairwise correlations in the case of signal correlations do not require simultaneous recordings and we calculated the correlation values over all possible pairs of neurons in our dataset.

average, increases with stimulus frequency (Figure 3.14A). Considering that the average signal correlations were nearly zero across all artificial stimulation conditions, we combined the signal correlation values for stimulus timescales across all frequencies and compared the mean correlation coefficient to that observed during the naturalistic stimulus and compared to that during naturalistic stimulation. We found that signal correlations were significantly higher during naturalistic stimulation when compared to artificial stimulation (Figure 3.21; Wilcoxon rank sum test, N=624 pairs, $p=4.5\times10^{-17}$) and, thus, were plastic.

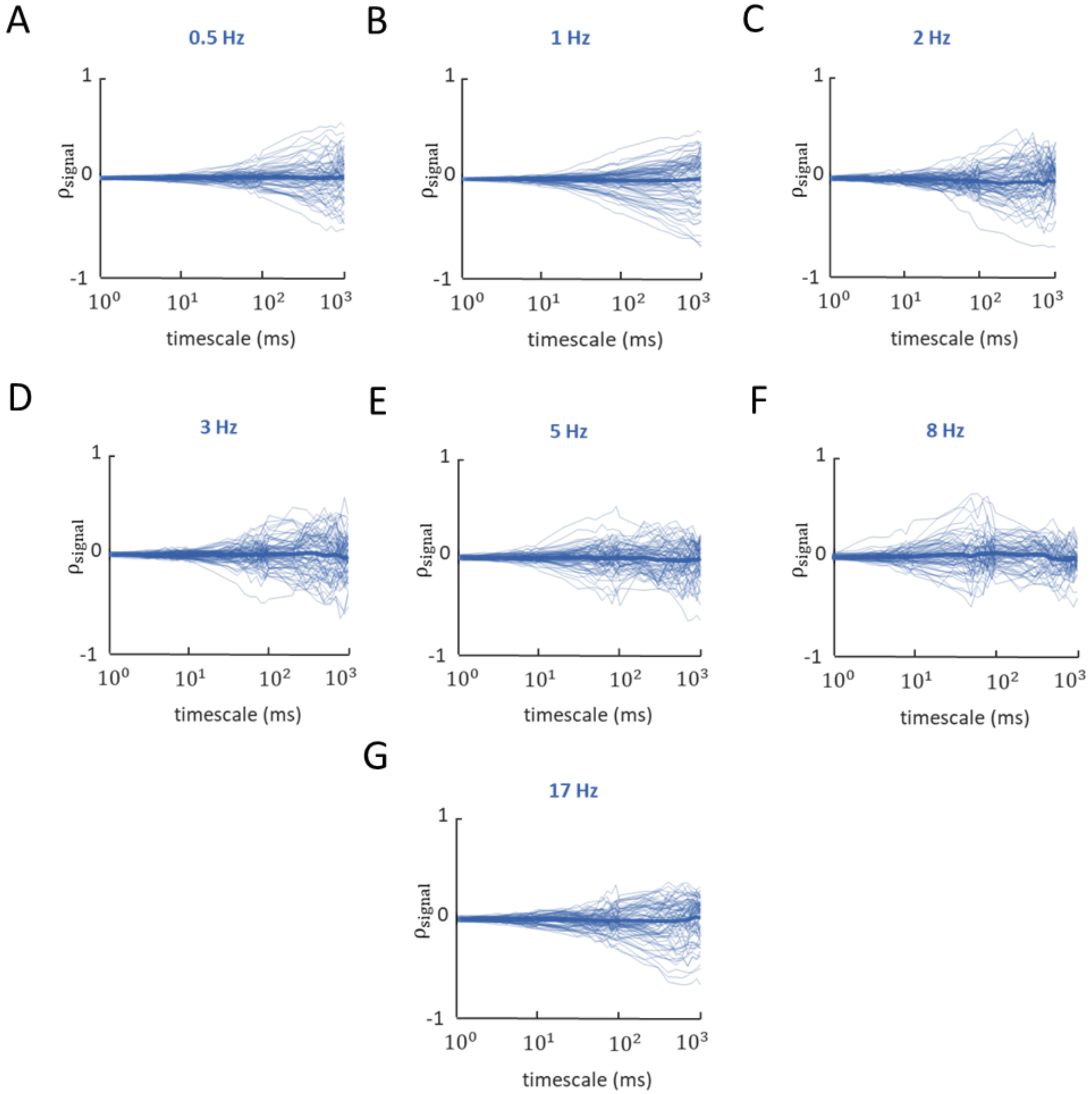

Figure 3.20. Signal correlation in PIVC as a function of timescale during sinusoidal stimuli with different frequencies. (A): 0.5 Hz, N=78 pairs; **(B)**: 1 Hz, N=78 pairs; **(C)**: 2 Hz, N=78 pairs; **(D)**: 3 Hz, N=78 pairs; **(E)**: 5 Hz, N=78 pairs; **(F)**: 8 Hz, N=78 pairs; and **(G)**: 17 Hz, N=78 pairs. The thick lines are the average values of the correlations as the function of timescale. As is the case with Figure 3.19, we calculated the correlation values over all possible pairs of neurons in our dataset.

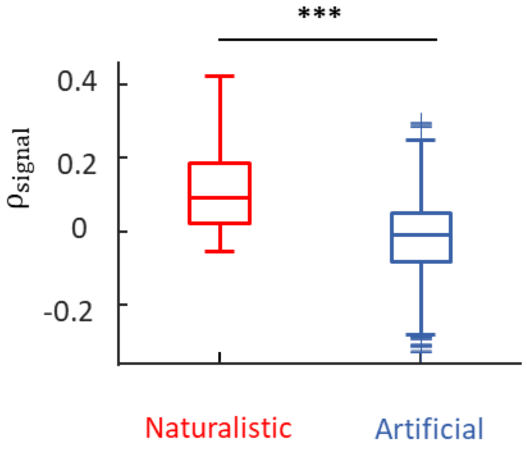

Figure 3.21. Signal correlations are similar during artificial and naturalistic stimulation in PIVC. Boxplots showing the signal correlation values during artificial (all frequencies) and naturalistic stimuli. Signal correlations during naturalistic stimulation is significantly higher than during artificial stimulation (Wilcoxon rank sum test, N=624 pairs, $p=4.5\times10^{-17}$). For artificial stimuli, the timescale was chosen to be a quarter to a half-period of the sinewave period, where the signal correlations were maximum in magnitude on average. For naturalistic stimulus, the signal correlations were calculated for a 100 ms timescale that was consistent with the time scale of the stimulus and where signal correlations were highest in magnitude.).

3.7.2 Quantification of noise correlations in vestibular neural populations in PIVC.

In the next step, we quantified noise correlations in vestibular neural populations in PIVC. Figures 3.22A and 3.22B demonstrate noise correlations obtained during naturalistic and 4 Hz artificial stimulation, respectively. Similar to the characterization of signal correlation, we did not attempt to classify noise correlations into groups of same- and opposite-type pairs due to a lack of clear definition of response type 1n PIVC. For both conditions, noise correlation magnitude increased with timescale, but was close to zero on average (Figure 3.22). Additionally, we computed the noise correlation for the remaining artificial stimuli with differential frequencies and found that noise correlations were close to zero during artificial stimuli across all frequencies (Figure 3.23). To compare the noise correlations between artificial and naturalistic stimuli, we pooled noise correlation values

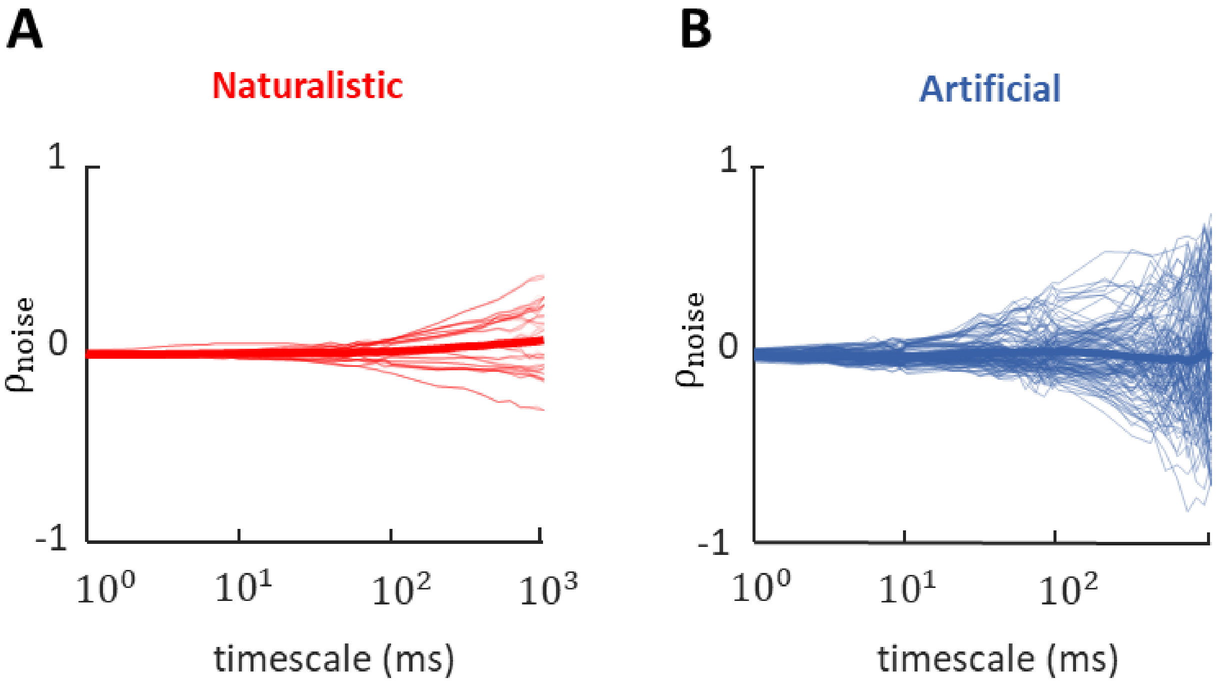

Figure 3.22. Vestibular neuronal activity in PIVC demonstrate wide range of noise correlation coefficient (A) Noise correlations as a function of timescale during naturalistic stimulus (N=16 pairs). The thick lines represent the mean correlations curve as the function of timescale **(B)** Same as in A except during 4 Hz artificial stimulation (N=12 pairs). Note that each curve denotes noise correlations calculated from a 1 second segment of simultaneous pairwise recording and therefore, for each pair, there are 10 curves plotted on the panels above.

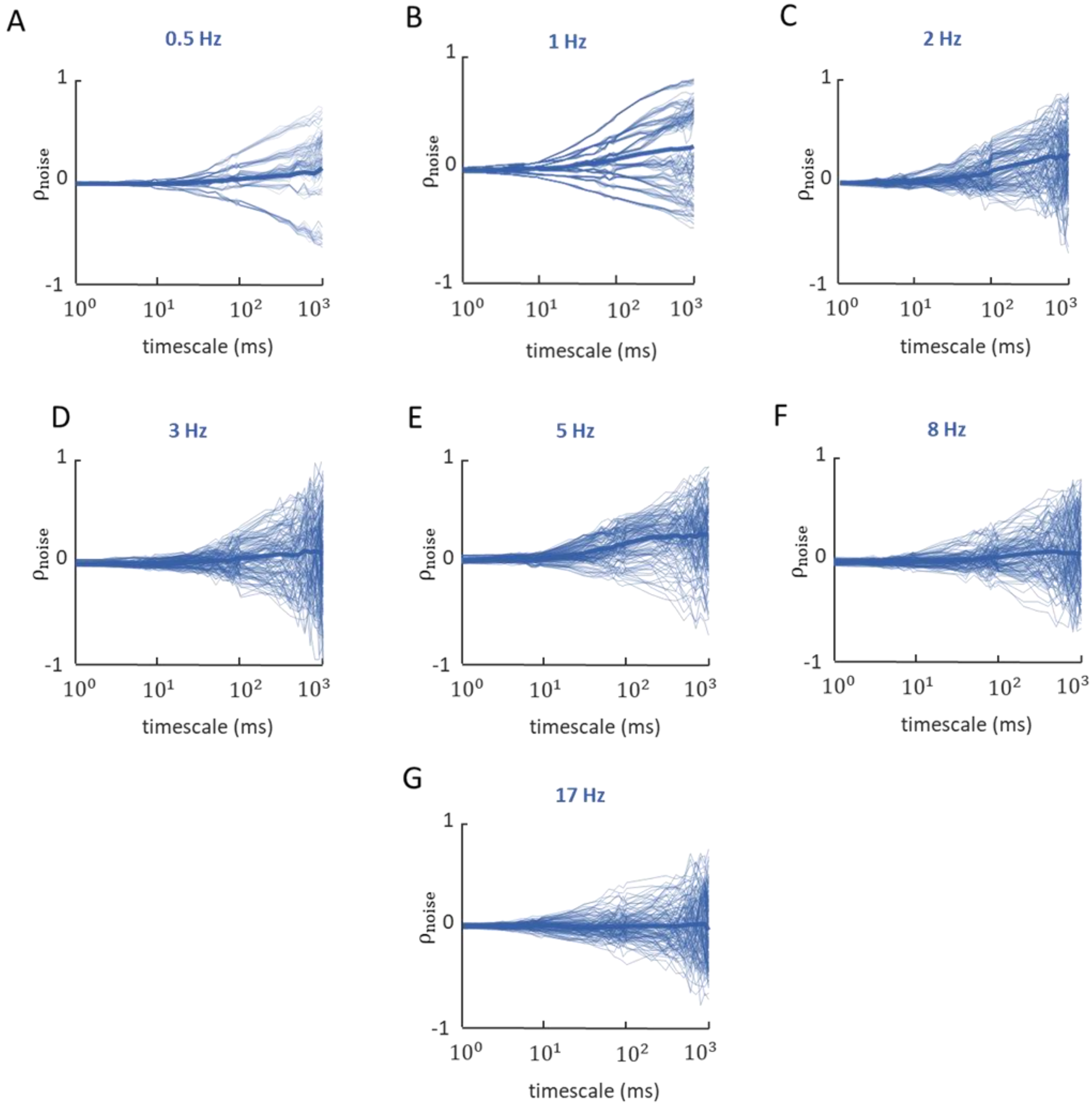

Figure 3.23. Noise correlation as a function of timescale during sinusoidal stimuli with different frequencies. (A): N=11 pairs, 0.5 Hz; **(B)**: 1 Hz, N=12 pairs; **(C)**: 2 Hz, N=12 pairs; **(D)**: 3 Hz, N=12 pairs; **(E)**: 5 Hz, N=12 pairs; **(F)**: 8 Hz, N=12 pairs; and **(G)**: 17 Hz, N=12 pairs. The thick solid lines are the average values of the correlations for all pairs. Note that each curve denotes noise correlations calculated from a 1 second segment of simultaneous pairwise recording and therefore, for each pair, there are 10 curves plotted on the panels above.

computed at half of the stimulus period for all frequencies —as they were not significantly different than zero— and compared them to that of during naturalistic stimulus (Figure 3.24). Thus, overall noise correlations were slightly higher during artificial stimuli

(ρ_{art}=0.040, ρ_{nat}=0.028; Wilcoxon rank sum test, p=0.0044; Figure 3.24) but were close to zero, suggesting that neural activities in PIVC become decorrelated.

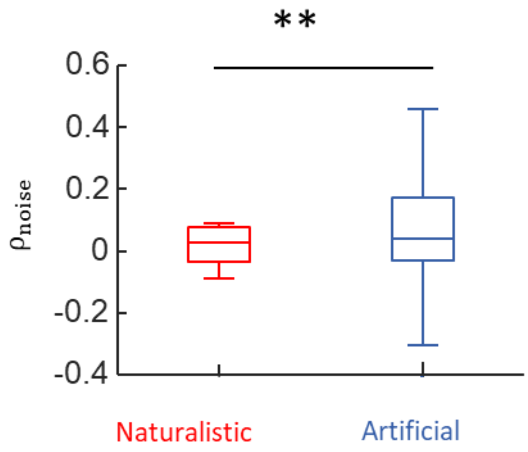

Figure 3.24. Noise correlations are close to zero during artificial and naturalistic stimulation. Boxplots showing noise correlation values during artificial (all frequencies) and naturalistic stimuli. Noise correlations during naturalistic and artificial stimuli are close to zero. Noise correlation values are slightly higher during artificial stimuli (i.e., ρ_{art}=0.040) compared to that of naturalistic stimulus i.e., ρ_{art}=0.028; Wilcoxon rank sum test, N=16 pairs, p=0.0044). The timescales at which the noise correlations were computed were the same as those used above for signal correlations.

3.8 Summary of results

In this chapter, we recorded vestibular neural populations in VN and PIVC that mediate self-motion perception and characterized single-unit and population characteristics of the neural activity, including correlation structure and heterogeneity. We found the neural activities were highly heterogenous in both VN and PIVC regardless of the stimuli condition used. Additionally, we showed while signal correlations in VN, on average, are close to zero across the neural population during artificial and naturalistic stimulation, noise correlations are significantly positive during naturalistic stimulation but not during artificial stimulation. Additionally, we found that noise correlation in PIVC was negligible regardless of the stimuli used. However, signal correlations were significantly positive during naturalistic stimuli but not during artificial stimulation. As such, our results indicate that correlation structures in VN and PIVC are plastic and have implications for efficient coding neural populations therein which will be investigated and discussed in the following chapter.

4. POPULATION CODING OF SELF-MOTION PERCEPTION: INSIGHTS FROM COMPUTATIONAL MODELING

In the previous chapter, we explored the response of the vestibular neurons in the central vestibular pathway and characterized their response to naturalistic and artificial self-motion stimuli. Our results so far show that the spiking activities of vestibular nuclei neurons are more heterogeneous during naturalistic than during artificial stimulation. Such changes were accompanied by changes in noise correlations, which were more positive during naturalistic stimulation. Such a change in noise correlations might seem surprising at first glance, as previous studies have shown that this can increase redundancy and thus impair information transmission (Zohary et al., 1994). It should be, however, noted that these assumed a homogeneous population, whereas our results show that this is not the case for vestibular nuclei neurons.

Understanding the implications of the observed heterogeneity and plastic correlation structure requires data from a large number of simultaneously recorded neurons (Kohn et al., 2016; Urai et al., 2022; Zohary et al., 1994). As in our dataset, the number of simultaneously recorded neurons did not exceed five neurons, we used biologically plausible computational models to build larger neural populations and study the effect of correlation structure and heterogeneity on self-motion information. In this chapter, first, I introduce the model, and then, I present the simulation results and its implication on self-motion information processing.

4.1. Model introduction

Our model consists of three main components: firstly, the stimulus is modulated via linear systems properties associated with the early vestibular pathway, including the linear dynamics of afferents and VO neurons in VN (Figure 4.1). Secondly, the generated signal is used to produce a set of signals that are correlated with a given magnitude and heterogeneity (i.e., the mean and standard deviation of the correlation coefficients; see below).

Additionally, a set of correlated Gaussian noise signals with a given magnitude and heterogeneity are generated. Together, the correlated signal and noise are used in a leaky-integrate-and-fire (LIF) model to generate a neural population with correlated spiking activity. So far, the head velocity stimulus is encoded in the population activity. Next, we use a stimulus reconstruction unit, which effectively is a set of optimal kernel functions, to decode the stimulus from spiking neural activity. In the following sections, I introduce the

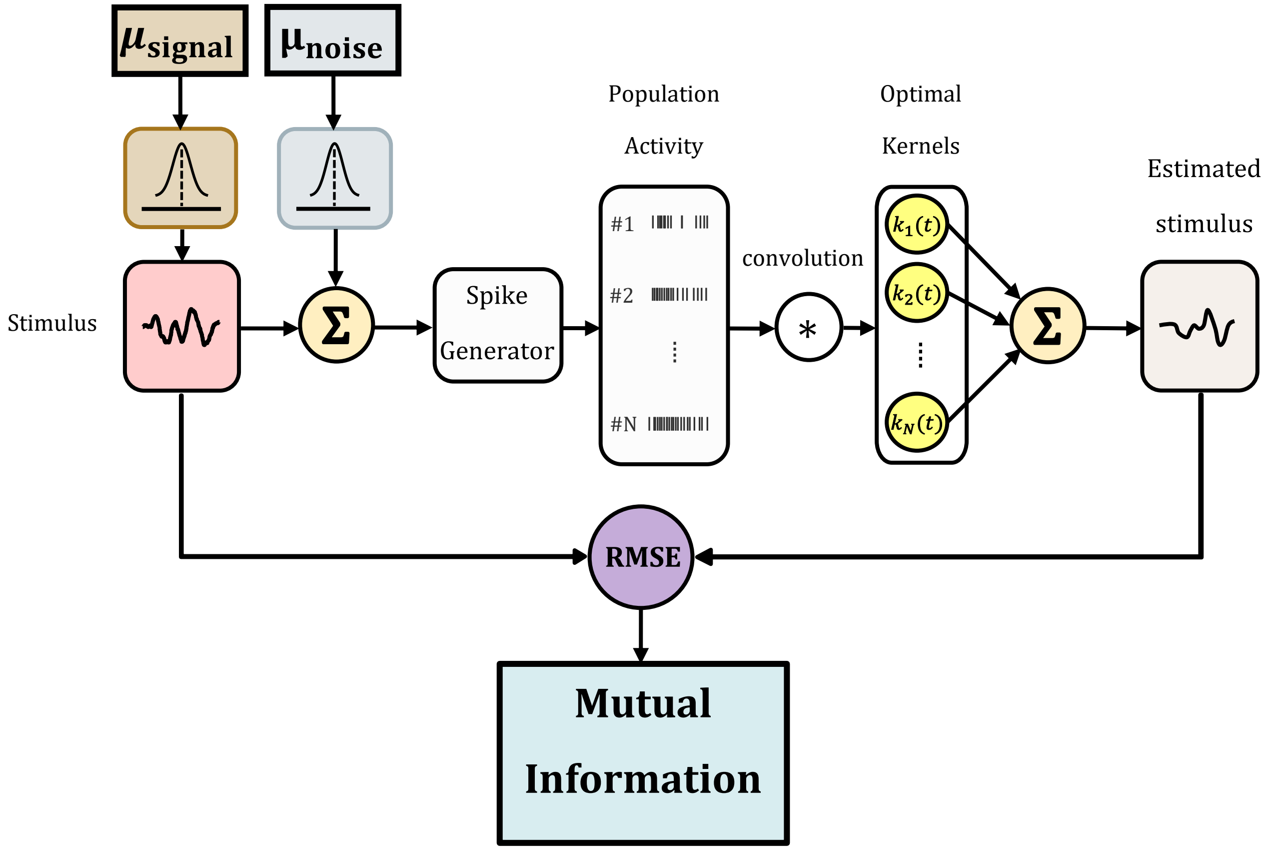

Figure 4.1. Schematic of the computational model. The model encodes the head velocity stimulus, generates correlated spiking neural activity, and decodes the stimulus velocity from the spiking activity. A set of stimuli is generated with power spectra similar to that of the naturalistic stimulus used in the study (light red box). Additionally, appropriate input signal (light brown box) and noise correlation (light blue box) matrices are generated so that the distribution of the resulting output correlation matrices satisfy input mean and variance requirements of the correlation coefficient distributions. The resulting correlated signal and noise vectors are used in a *Spike Generator* module to produce correlated spiking activity with the desired correlation structure and heterogeneity. This module is comprised of a transfer function, addressing the linear dynamics of the early vestibular pathway, and an LIF model to generate spiking activity of N neurons (light grey box; the encoded signal). The population activity is then convolved with a set of optimal kernels (yellow circles) to generate an estimation of the stimulus (grey box; the decoded signal). The error from the estimation is used to calculate the mutual information in the population. μ_{signal} and μ_{noise} denote mean input signal and noise correlations; RMSE: root mean squared error.

components of the model and provide the mathematical descriptions and/or computational implementations.

4.1.1. Head velocity stimuli

The stimulus used in the modeling study was a set of stimuli with power spectra resembling that of the naturalistic stimulus used in the experiments. This was to ensure the linear dynamics of neural substrates were not affected by the otherwise artificial temporal profile of the stimuli. Note that the stimulus used in the experiment is not sufficient for our modeling study for two reasons: first, it is unlikely that VO neurons receive the same synaptic currents across the populations; Secondly, a single stimulus vector would technically not be suitable as any correlation matrix multiplication would result in a set of identical set of stimulus vectors. To generate a set of stimuli displaying a power spectrum similar to that of the naturalistic stimulus, we calculated the Fourier transform of the signal. We calculated the magnitude and the phase of the signal in the frequency domain. To generate a new signal with the desired characteristic, we generated a new frequency domain signal with the same magnitude as in the original signal but with random values for the phase. The time domain signal was then obtained by taking the inverse Fourier transform and keeping the real part of the resulting signal.

4.1.2. The linear-nonlinear model

Understanding the implications of correlations and heterogeneity observed in our dataset required further investigation using computational modeling. Specifically, I simulated a population of VO neurons using linear-nonlinear cascade models (Chichilnisky, 2001; Schneider et al., 2015). In this model, the firing rate response of the neuron is given by:

$$r(t) = T(r_{lin}(t)) \tag{4.1}$$

in which $r_{lin}(t)$ is the linear estimation of the neural response, and $T(\cdot)$ is the nonlinear relation that relates $r_{lin}(t)$ to the actual firing rate calculated from data. Note that I did not estimate the nonlinear function explicitly, as the nonlinearity was accounted for by a leaky integrate-and-fire (LIF) model in the following module of the cascade model, and its effect is reflected in the parameters of LIF model. Additionally, the nonlineairy included the rectification and saturation of response for both afferents and VO neurons. To obtain the linear estimation of the neural response, $r_{lin}(t)$, I used the following estimation:

$$r_{lin}(t) = h(t) * s(t) + r_0. \tag{4.2}$$

r_0 is the baseline firing rate, which was calculated during baseline activity for each neuron, and $s(t)$ denotes the stimulus. Here, $h(\cdot)$ is the linear kernel of the model and the impulse response of the transfer function, $H_{VO}(f)$ as

$$H_{VO}(f) = \frac{P_{sr}(f)}{P_{ss}(f)} \tag{4.3}$$

where $P_{ss}(f)$ is the power spectrum of the stimulus, and $P_{sr}(f)$ is the cross-spectrum between the stimulus and binary sequence obtained from the neural response. $H_{VO}(f)$ was approximated with a transfer function similar to that of canal afferents with two poles and two zeros for each neuron as

$$H_{VO,est}(s) = \frac{ks\left(s + {}^{1}\!/_{T_1}\right)}{\left(s + {}^{1}\!/_{T_c}\right)\left(s + {}^{1}\!/_{T_2}\right)} \tag{4.4}$$

where $s=2\pi if$ and k, T_c, T_1, and T_2 are parameters of the model (Schneider et al., 2015). Power spectra and cross-spectrum quantities are computed using *pwelch* and *cpsd* functions in MATLAB. In practice, since I used inputs with naturalistic statistics, I fit the transfer function to the population-averaged bode plot obtained for gain and phase during naturalistic stimuli.

For controlled simulations, I kept the transfer functions similar across the population and used the following parameters: T_1=0.0175 s; T_2=0.027 s; T_c=5.7 s; k=2.1 (spk/s)/(deg/s).

4.1.3. Leaky Integrate-and-Fire model

To generate spiking activity, the output of the linear transfer function was fed to an LIF model (Lapicque, 1907). The membrane potential, V(t), of the simulated neurons is calculated by solving the following equation:

$$\begin{gathered} \mathrm{C_m} \frac{\mathrm{d}\mathbf{V}(\mathrm{t})}{\mathrm{dt}} = -\mathrm{g}\mathbf{V}(\mathrm{t}) + \mathrm{I_{bias}} + \mathrm{k}\,\mathbf{s_c}(\mathrm{t}) + \sigma\,\mathbf{n_c}(\mathrm{t}) \\ \text{if } \mathrm{V}(\mathrm{t_0}) \geq \theta \rightarrow \mathrm{V}(\mathrm{t}) = 0 \;\; (\mathrm{t_0} \leq \mathrm{t} \leq \mathrm{t} + \mathrm{t_{ref}}). \end{gathered} \tag{4.5}$$

C_m, g, I_{bias}, k, σ, θ, and t_{ref} are membrane capacitance, membrane conductance, the bias current, input gain in the model, standard deviation of the noise, spike threshold, and refractory period, respectively. $s_c(t)$ denotes the input to the LIF model, and $n_c(t)$ denotes the noise term.

I obtained the distribution of signal and noise correlation coefficients and populated positive definite covariance matrices accordingly. The distribution of signal and noise correlation coefficients was approximated with normal distributions. Thereafter, the covariance matrices, C_{sig} and C_{noi} were populated so that the distribution of the correlation coefficients followed the normal distributions. The input signal to the LIF model was correlated as follows:

$$\mathbf{s_c}(\mathrm{t}) = \mathrm{L_{sig}}\mathbf{s_f}(\mathrm{t}) \tag{4.6}$$

$$\boldsymbol{s_f}(\mathrm{t}) = [\mathrm{s_1}(\mathrm{t}), \ldots, \mathrm{s_N}(\mathrm{t})] \tag{4.7}$$

where $s_f(t)$ is the output of the transfer function, $H_{VO}(f)$, and L_{sig} is the Cholesky factor of the signal covariance matrix, C_{sig} (Benoit, 1924). Moreover, the correlated noise at the input was simulated as follows:

$$\mathbf{n}(\mathrm{t}) = \mathrm{L}_{\mathrm{noi}}\boldsymbol{\xi}(\mathrm{t}) \tag{4.8}$$

$$\boldsymbol{\xi}(\mathrm{t}) = [\xi_1(t) \dots \xi_n(t)] \tag{4.9}$$

where L_{noi} is the Cholesky decomposition of the noise covariance matrix, C_{noi}, and ξ_i (t) for i=1, …, N are white Gaussian noise with mean zero and unit variance. For my simulations, I used C_m=1 nF, g=0.4 μS, I_{bias}=7.3 nA, k=0.025 nA (deg/s)/(spk/s), σ=2 nA, θ=0, and t_{ref}=2 ms with which the resting discharge, coefficient of variation, variability, neural gain and phase of the simulated neurons matched that of population average values. These values were found by *fminsearch* function in MATLAB where the parameters were input to the parameter estimation algorithm. The algorithm generated 20 seconds of activity during rest and during artificial stimulation from which the resting discharge, coefficient of variation, variability, neural gain, and phase of the simulated neurons were used to evaluate a mean squared error objective function of the estimated parameters. The correlated signal input was used as the signal component of the LIF model, whereas the correlated noise input was used as the noise component of the LIF model. The mean of the off-diagonal correlation coefficients of covariance matrices as well as their standard deviations, could vary systematically. Higher mean values corresponded to higher levels of noise and signal correlations. For homogenous population activity, I assumed σ_{hmg}=0.03 whereas for heterogenous population activity σ_{htg}=0.15 was assumed, where σ_{hmg} and σ_{htg} are the standard deviation of the correlation coeffcients in homogenous and heterogenous populations, respectively. These choices of parameters were consistent with our hypothesis (for homogenous population) and data (for heterogenous population). For populating large correlation matrices with values drawn from a normal distribution with a given standard deviation (i.e., heterogeneity vs. homogeneity) and mean value (mean value of signal and noise correlations), I used an algorithm based on vines and extended onion method (Lewandowski et al., 2009). This method was used because populating the off-diagonal elements of the covariance matrices with values randomly driven from a given normal distribution resulted in non-positive definite covariance matrices for large populations (e.g., N>10 neurons).

4.1.4. Decoding and calculating mutual information

Here, we used the stimulus reconstruction method to decode stimulus from the population activity of simulated VO neurons (Dan et al., 1998; Warland et al., 1997). Our choice of decoder is consistent with recent findings in the posterior ventrolateral thalamus, in which the vestibular target neurons —which receive input from VO neurons in VN and decode the vestibular self-motion information in the thalamus— faithfully encode self-motion information (Carriot et al., 2022). The estimated stimulus is obtained by convolving each neural activity with a kernel:

$$s_{est}(t) = \sum_{i=1}^{N} (k_i * r_i)(t). \tag{4.10}$$

Here $r_i(t)$ is the firing rate, and $k_i(t)$ is the optimal kernel of the neuron i. The kernels are obtained from the following equation:

$$\begin{pmatrix} K_1(f) \\ \vdots \\ K_N(f) \end{pmatrix} = \begin{pmatrix} P_{r_1r_1}(f) & \cdots & P_{r_1r_N}(f) \\ \vdots & \ddots & \vdots \\ P_{r_Nr_1}(f) & \cdots & P_{r_Nr_N}(f) \end{pmatrix}^{-1} \begin{pmatrix} P_{sr_1}(-f) \\ \vdots \\ P_{sr_N}(-f) \end{pmatrix} \tag{4.11}$$

where $K_i(f)$ is the Fourier transform of $k_i(t)$, $P_{r_ir_j}(f)$ is the cross-spectrum between $r_i(t)$ and $r_j(t)$, and $P_{sr_i}(f)$ is the cross-spectrum stimulus, $s(t)$, and $r_i(t)$. The noise in the reconstruction and mean squared error (MSE) is characterized as

$$n(t) = s_{est}(t) - s(t) \tag{4.12}$$

and

$$\varepsilon = < n^2(t) >_t, \tag{4.13}$$

respectively, where $\langle \ldots \rangle_t$ denotes an average over time. The signal-to-noise ratio (SNR) is computed as

$$\mathrm{SNR}(f) = \frac{P_{ss}(f)}{P_{nn}(f)} \tag{4.14}$$

in which $P_{ss}(f)$ and $P_{nn}(f)$ are the power spectrum of stimulus and reconstruction noise, respectively. The mutual information rate is then given by:

$$\mathrm{MI}(f) = \int_0^{20} \log_2(1 + \mathrm{SNR}(f)\,)\,df \tag{4.15}$$

where the limits of integration correspond to the frequency range of natural self-motion(Rieke et al., 1996). Information rate values were normalized by the lowest value obtained, which was for a homogeneous population with zero mean signal and highest mean noise correlations.

4.1.5. Covariance analysis

To gain intuition as to how noise correlations benefit population coding for neuronal populations with heterogenous signal and noise correlation structures, I looked at the contributions of individual terms towards determining the mean square error. Specifically, one can write an expression for the MSE as:

$$\varepsilon^2 = \langle\left(\sum_{i=1}^{N} \sigma_i\right)^2\rangle = \sum_{i=1}^{N}\langle\sigma_i^2\rangle + 2\sum_{i=2}^{N}\sum_{j=1}^{i-1}\langle\sigma_i\sigma_j\rangle \tag{4.16}$$

where N is the population size, $\sigma_i$is the contribution of neuron i to the error, which is given by

$$\sigma_i = \frac{s(t)}{N} - (k_i * r_i)(t). \tag{4.17}$$

It can be easily seen that the equation above is then a sum of variance and covariance terms.

4.1.6. Double-power law fitting function

MSE was fit with double power law function defined as

$$\varepsilon(n) = c_1 n^a \left[1 + \left(\frac{c_2}{c_1} n^{b-a} - 1\right) u(n - n_c)\right] \tag{4.18}$$

where n is the population size, u(n) is the Heaviside function, c_1 and c_2 are scaling factors, n_c is the critical (knee) population size, and a and b are power exponents for small and large populations, respectively. To find the parameters of the model, I fit a piecewise linear model to logarithmic values of n and ε.

4.2. Simulation results

The model was implemented in MATLAB ((R2020a), Natick, Massachusetts: The MathWorks Inc.; 2020). The results were robust for the simulation time steps chosen to solve the differential equations. Additionally, sufficient time was provided to allow the transient dynamics to dissipate.

4.2.1. Heterogeneity dramatically influences the effect of correlation structure on population coding

In order to gain an understanding of how heterogeneity and correlations influence population coding, we built a computational model of the vestibular nuclei neural population that incorporated their known tuning properties (Figure 4.1; see section 4.1 for the model description). We then considered both homogeneous and heterogeneous populations and systematically varied both signal and noise correlations. For the homogenous population, the correlation coefficient distribution had a standard deviation of 0.03, whereas the heterogenous population led to a correlation coefficient distribution of 0.15 (similar to the observed distribution of correlation coefficients in data from VN). We varied the mean of the correlation coefficient distribution from 0 to 0.6 by increments of 0.1 for both signal and noise correlations. Each condition was characterized by three factors: heterogeneity or homogeneity of the neural response and the mean value of signal and noise correlations. Each condition was simulated 40 times, and the results were averaged across the simulations.

The result of the simulations is shown in Figure 4.2. We quantified the information rates for homogenous (Figure 4.2A) and heterogenous (Figure 4.2B) conditions and normalized them to the lowest value in both graphs —which corresponded to the homogenous condition with mean signal and noise correlation values of 0 and 0.6, respectively— to provide a better comparison between the homogenous and heterogenous populations. Our simulation results demonstrated a dramatic difference between the homogenous and heterogenous conditions: for homogeneous populations, the highest information was obtained when signal correlations were maximal, and noise correlations were near zero (Figure 4.2A). Increasing noise correlations led to a decrease in mutual information irrespective of signal correlations by increasing redundancy. This result is consistent with those of previous studies (Zohary et al., 1994). In contrast, for heterogeneous populations, the highest information was obtained when signal correlations were near zero, and noise correlations were highest (Figure 4.2B). Additionally, the information decreased with either increase in signal correlation or a decrease in noise correlations.

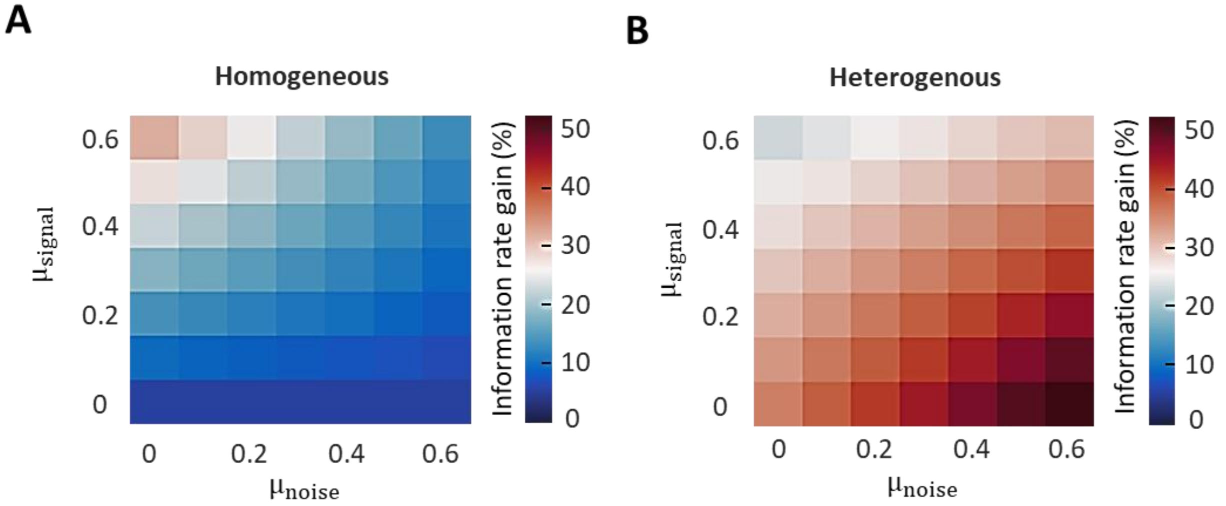

Figure 4.2. The effect of heterogeneity and correlation structure on population coding naturalistic self-motion. (A) Mutual information rate gain as a function of mean signal and noise correlation for homogenous population coding. The information rate gain is calculated by comparing the information in a given condition to the minimum information decoded across all simulated conditions (i.e., $\mu_{noise} = 0.6$, $\mu_{signal} = 0$ under homogenous conditions) (N=40 simulations). **(B)** Same as in A, except the simulations are done for a heterogenous population activity (N=40 simulations).

We wanted to compare the relationship between the populations (homogeneous versus heterogeneous population) as a function of the correlation structure. We fixed the amount of the signal correlation so that maximum information was obtained from each condition and varied the amount of mean noise correlation for both conditions. This corresponded to the conditions with μ_{signal}=0.6 for homogenous and μ_{signal}=0 for heterogeneous populations. Overall, our simulation results demonstrate that for given signal correlations, increasing noise correlations led to increased information for heterogeneous populations but instead led to decreased information for homogeneous populations. (Figure 4.3). Furthermore, the information gain was consistently higher in heterogenous populations than in homogenous populations.

4.2.2. Increased noise correlations during naturalistic stimulation benefits population coding by heterogeneous vestibular neural populations

Next, we plotted the reconstructed stimulus for homogenous and heterogenous populations (N=128 neurons). The reconstructed stimulus is more similar to the original

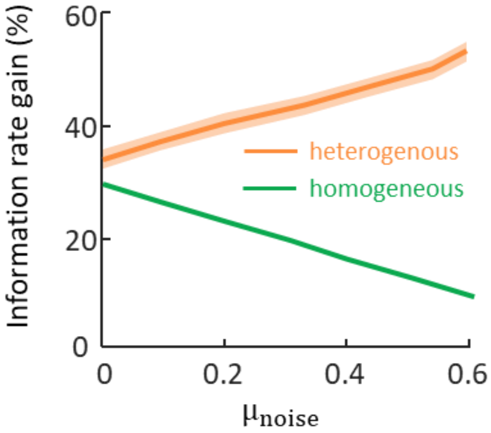

Figure 4.3. Correlation structures differentially affect population coding in heterogeneous and homogeneous neural population. Information rate gains were calculated for homogenous (green line; μ_{signal}=0.6) and heterogenous (orange line; μ_{signal}=0) conditions. The solid lines illustrate the average information gain rate and the shaded error bands denote 1SEM computed from 40 simulations for each condition. For homogenous populations, information gain decreases with noise correlations whereas for heterogenous information, the information increases. The information gain is higher for heterogenous population across all noise correlation levels.

stimulus for the heterogeneous population and therefore provides a better estimation of the stimulus (Figure 4.4A). Thus, an important question is why increased noise correlations benefit information transmission for heterogeneous but not homogeneous neural populations. To answer this important question, we calculated the reconstruction error by subtracting the estimated stimulus from the original stimulus and plotted the error as the function of the population size (Figure 4.4B). Overall, in both cases, reconstruction error decreased initially more slowly and then faster with increasing population (Figure 4.4B). The reconstruction error was higher for small homogenous populations but was lower for large homogenous populations when compared to heterogenous populations as the information decreased faster for large heterogenous populations. To quantify the effect of population size on information in the populations, the error curves were fitted using two different power laws for low and high population sizes. Overall, the power law exponent for high and low population sizes was significantly more negative for a heterogeneous than for a homogeneous population (Figures 4.4C and 4.4D). Moreover, the “critical population size” at which this transition occurred was lower for heterogeneous populations (Figure 4.4E).

4.2.3. Covariance structure decreases the estimation error in heterogeneous populations

To understand why the reconstruction error is smaller for heterogeneous populations, we considered the respective contributions of individual model neurons. Specifically, the reconstruction error can be written as a sum of variance and covariance terms between the

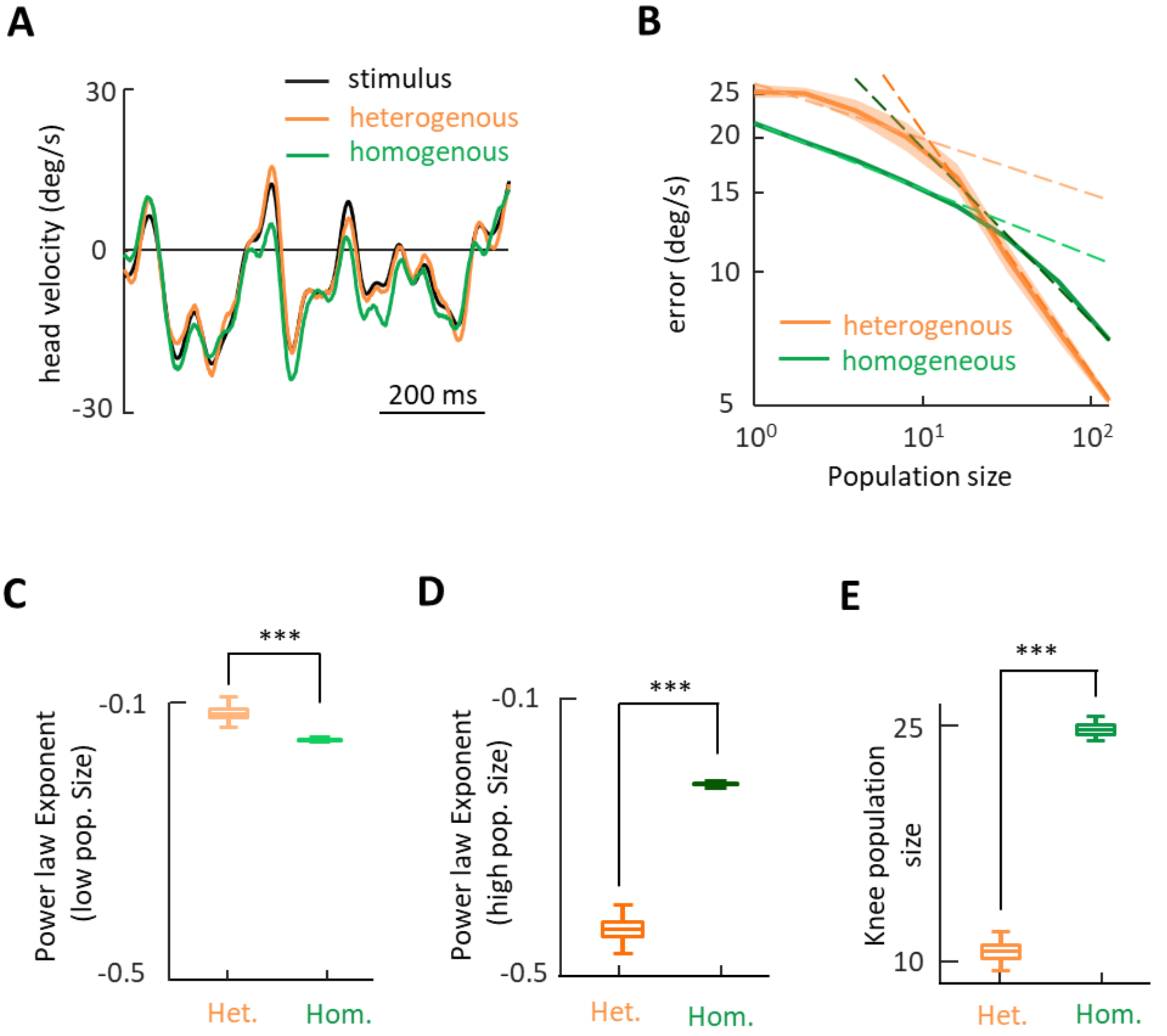

Figure 4.4. Heterogenous populations predict stimulus timecourse more accurately than homogenous populations. (A) Stimulus and reconstructed stimulus from populations with optimum correlation structure for heterogenous (μ_{noise}=0.6, μ_{signal}=0) and homogenous (μ_{noise}=0, μ_{signal}=0.6) conditions (N=128). The black, green and orange solid lines display the timecourse of the stimulus, reconstructed stimulus from homogeneous and heterogenous population activities, respectively. **(B)** Estimation error as a function population size for the same populations as in panel A. Error bands indicate 1 SEM. Each curve is fitted with a double power law functions over the low and high population sizes, indicated with dashed lines. **(C)** The magnitude of power law exponents above the knee population sizes is significantly higher in heterogenous condition (Wilcoxon rank sum test, N=1000 simulations, $p=2.5\times10^{-33}$). **(D)** The magnitude of power law exponents below the knee population sizes is significantly lower in heterogenous condition (Wilcoxon rank sum test, N=1000 simulations, $p=2.5\times10^{-33}$). **(E)** Upper right inset: the knee populations size for heterogenous conditions is significantly lower than that of homogenous condition (Wilcoxon rank sum test, N=1000 simulations, $p=4.9\times10^{-33}$).

errors of individual model neurons (Eq. (4.16)). While variance terms are positive by definition, the cross-covariance terms can be negative and thus contribute to reducing the overall error. Our results show that the distribution of cross-covariance terms was more skewed towards negative values for heterogeneous populations and was thus negative on average (Figure 4.5A and insets). In contrast, the distribution of covariance terms for the homogeneous population was more symmetric and displayed an average that was closer to zero (same figure). Quantification of the mean variance terms revealed overall higher variances for heterogeneous as compared to homogeneous populations ($p=2.1\times10^{-8}$, Kruskal-Wallis test; Figure 4.5B). However, the more negative cross-covariance terms help more to reduce the overall error for heterogeneous populations than for homogeneous populations ($p=2.1\times10^{-8}$, Kruskal-Wallis test; Figure 4.5B).

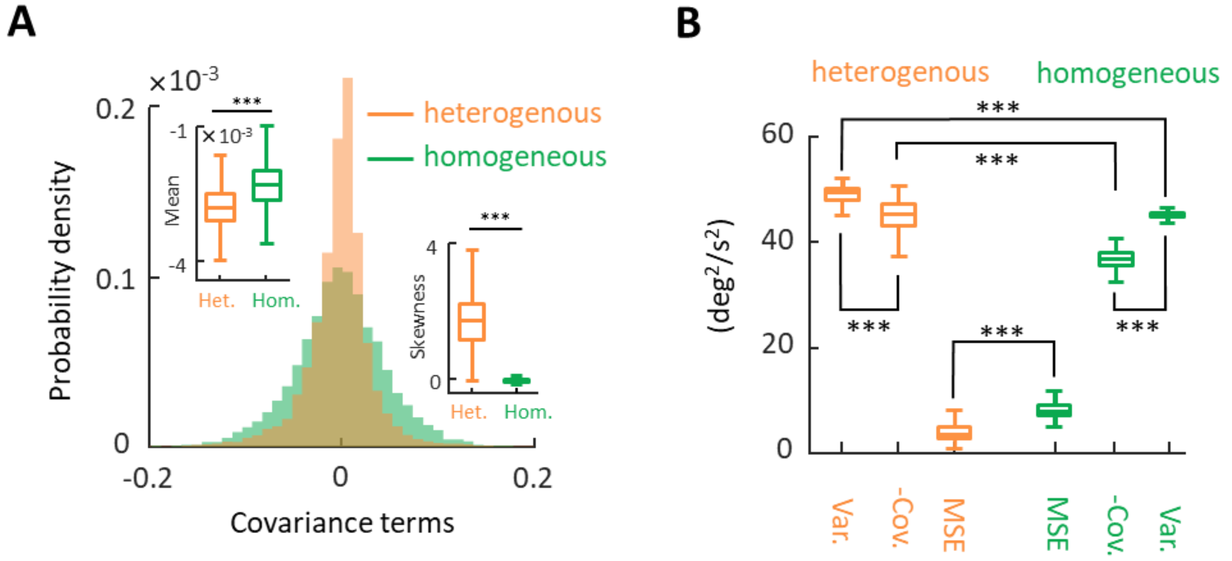

Figure 4.5. Covariance structure favors population coding in heterogenous populations. (A) The distribution of covariance terms of the covariance matrices computed from reconstruction error signals during the same heterogenous and homogenous conditions as in Figure 4.4A. **Insets.** Left: Mean of the covariance terms for heterogenous condition is significantly lower than that of homogenous condition (Wilcoxon rank sum test, N=1000 simulations, $p=2.1\times10^{-8}$). Right: The skewness of the distribution for the heterogenous and homogenous conditions (Wilcoxon rank sum test, N=1000 simulations, $p=2.1\times10^{-8}$). The heterogenous population is skewed towards negative values and therefore has negative mean value. **(B)** Summed variance terms (Var.), summed covariance terms (Cov.), and mean squared error (MSE) for covariance matrices computed from reconstruction error signals for heterogenous and homogenous conditions. All quantities compared are significantly different than each other (Wilcoxon rank sum test, N=1000 simulations, $p=2.1\times10^{-8}$).

4.3 Summary of results

In this chapter, we used computational modeling to expand on the role of correlation plasticity and heterogeneity on efficient population coding. We simulated large neural populations which included known properties of VO neurons in VN. The parameters of the model were varied to simulate neural population with different correlation magnitudes which either exhibited homogenous or heterogenous activity. Remarkably, our model demonstrated that efficient coding strategies employed by neural populations depended on the correlations and their heterogeneity/homogeneity. Strikingly, contrary to homogenous populations where efficient population codes had lowest noise correlation and highest signal correlation, efficient coding in heterogenous populations was obtained when the noise correlations were maximized, and signal correlations were minimized. Additionally, sufficiently large (N>50 neurons) heterogenous neural populations consistently transmitted more information. By characterizing the covariance structure in heterogenous and homogenous populations, we observed estimation error of the decoder depended on the variance and covariance of neurons' prediction errors, increasing with the magnitude of the former and decreasing with magnitude of the latter due to its negative sign. Importantly, while the heterogenous neural population demonstrated larger variance terms compared to homogenous populations, its covariance terms were higher in magnitude and closer to that of variance terms compared to the homogenous population, which ultimately resulted in smaller stimulus estimation errors. Our results revealed important property of heterogenous neural populations in which high noise correlation benefit information in the population. Our results were used to interpret our findings in VN and PIVC (see 7.1.3).

5. A SET-POINT ADAPTATION MECHANISM ACCOUNTS FOR THE EMERGENCE OF NEGATIVE OPTOKINETIC AFTERNYSTAGMUS IN LARVAL ZEBRAFISH

In this chapter, I present a mathematical model which introduces a set-point adaptation mechanism that explains adaptation during prolonged stimulation and negative optokinetic afternystagmus after prolonged unidirectional optokinetic stimulation. I use the data gathered by our collaborators, Dr. Ting Feng Lin and Dr. Melody Ying-Yu Huang, at the University of Zurich, in order to estimate the parameters of the model. At the beginning of the chapter, I present the behavioral data. Next, I introduce the model, and finally, I present the simulation results.

5.1 Introduction to larval zebrafish model

5.1.1 Larval zebrafish -an ideal model to study neural substrates of behavior

One of the most fundamental functions of the brain is to make behavioral choices. To do so, the brain integrates sensory information and produces motor signals accordingly. Much is known about how the retina extracts visual features and relays this information to downstream areas. Similarly, how specific motor patterns are encoded in the response of neural populations in motor areas as well as the brainstem and spinal cord is abundantly studied. By far, the most challenging question in understanding how the brain generates behavior is forming a comprehensive view of how visual and motor information are integrated at visual and motor areas to give rise to the behavior. The problem, in part, arises from the high level of complexity in large animals such as primates. A promising way to approach this problem is to study the principles of neural computation and sensorimotor integration in simpler animal models and apply them to the study of larger animal models.

The larval zebrafish offers unique advantages among the vertebrate models for studying the neural basis of behavior at the molecular, cellular, circuit, and whole brain network level (Bilotta and Saszik, 2001; Bollmann, 2019; Friedrich et al., 2010). These advantages have made the larval zebrafish an ideal model for studying of development, structure, and function of neural circuits. The neural circuits range from simple reflex pathways to complex distributed circuits, which might represent an ancestral form of the subcortical pathways involved in selective attention (Krauzlis et al., 2018). The larval zebrafish's small brain volume and translucent skin present opportunities for combining genetic tools with whole-brain functional imaging techniques and targeted electrophysiological recordings in the intact nervous system (Neuhauss, 2003). Additionally, the transparent nature of the larva's skin allows researchers to simultaneously track its behavior in response to intricate visual stimuli. Recent efforts have been directed towards integrating genetic, anatomical, and functional data from various experiments into standardized atlases, further enhancing the power of the zebrafish model for neuroscientific research.

5.1.2 Using larval zebrafish as a model to investigate optokinetic response and aftereffects

Sensory-motor learning is essential for precise performance and motor coordination in animals during both reflex and voluntary behaviors (Bastian, 2008; Della-Maggiore et al., 2015). Various factors, such as environmental changes, injuries to peripheral or central motor systems, and inherent motor command variations, can affect movement accuracy. To enhance movement control, the brain employs mechanisms such as neural adaptation (Thoroughman et al., 2007; Wolpert et al., 2001) and habituation (Hall and Cox, 2009; Shepard et al., 1990). The optokinetic system, responsible for reflexive eye tracking in response to visual motion, serves as a valuable model for studying sensorimotor learning. It stabilizes the visual image on the retina, enabling high-resolution vision.

The optokinetic system is a highly conserved behavior among vertebrates (Masseck and Hoffmann, 2009). The 5-day post-fertilization (5-dpf) zebrafish larvae demonstrate a wide range of behaviors, including optokinetic response (OKR) to whole-field visual motion. As mentioned in the introduction, the vestibular and visual systems share the same velocity storage neural substrate, and therefore, the study of the neural circuit in one system is affected by stimuli from the other modality. 5-dpf larvae lack fully developed and functional semicircular canals, which allows us to study the neural substrate underlying the optokinetic reflex in response to horizontal optokinetic stimuli without the influence of the vestibular signals (Bever and Fekete, 2002; Lambert et al., 2008). Note that at this stage, although the otolith organs are developed (same reference), their effect on the larvae behavior is minimal due to animal immobilization.

Following the offset of the optokinetic stimulus, the subjects continue to produce persistent eye movements in the dark. The eye movements generated after the optokinetic stimulation are referred to as optokinetic afternystagmus (OKAN) and are attributed to the velocity storage mechanism, integrating visual and head velocity information (Cohen et al., 1981). OKAN is classified as positive or negative OKAN if the eyes persist in moving in the same or in the opposite direction of the stimulus, respectively, after the stimulus is removed (Brandt et al., 1974; Waespe and Henn, 1978). Researchers have observed both positive and negative OKAN responses in various species, with the longer-lasting negative OKAN initially masked by the shorter-lasting positive OKAN (Büttner et al., 1976). These responses exhibit a reciprocal relationship, with stronger negative OKAN following weaker positive OKAN as optokinetic stimulation persists.

In this study, larval zebrafish served as a model to investigate negative optokinetic afternystagmus (OKAN). Leveraging their inconspicuous positive OKAN, we induced robust negative OKAN by subjecting 5-dpf larvae to sustained optokinetic stimulation. During the stimulation, we observed a gradual decrease in the slow-phase velocity (SPV) of the optokinetic nystagmus (OKN), followed by the emergence of negative OKAN with various timescales after the stimulation ceased. We propose that this SPV decay results from both sensory habituation and set-point adaptation of the retinal slip velocity (as explained below), which leads to the occurrence of negative OKAN. To support our hypothesis, we proposed a mathematical model and simulated SPV using the same stimuli used in the study. Our simulation results aligned well with the experimental data, incorporating both sensory habituation and set-point adaptation mechanisms. In summary, the larval zebrafish offers a unique and valuable model for studying sensorimotor learning and gaining deeper insights into the neurophysiological mechanisms underlying negative OKAN.

5.2 Description of the behavioral data

5.2.1. Negative OKN in larval zebrafish

The aim of this study was to investigate set-point adaptation in the ocular motor system by observing optokinetic nystagmus (OKN) and the resulting optokinetic afternystagmus (OKAN) under various stimulus conditions in larval zebrafish. We recorded the eye movements during three phases (Figure 5.1A, top black strip; see sections 2.2.3, 2.2.4, and 2.2.5): a 5-minute baseline period in darkness, followed by 20 minutes of continuous unidirectional 10 deg/s optokinetic stimulation, and finally, another 20 minutes in darkness. Representative eye-position traces are illustrated in Figure 5.1. We identified quick-phase eye movements in both positive and negative directions for the recorded eye movement (denoted by red and green circles in Figure 5.1A). We further magnified the transitions between each phase in Figure 5.1A, showcasing the transition period from pre-stimulation

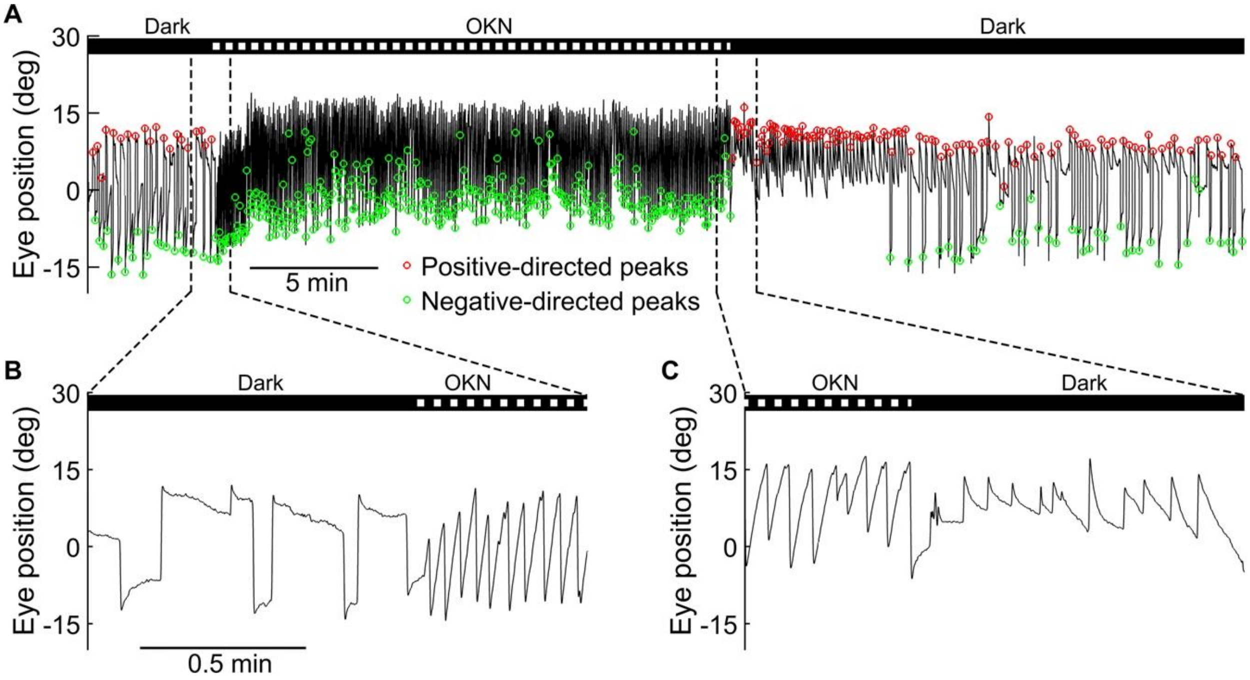

Figure 5.1. Negative OKAN manifests after prolonged unidirectional optokinetic stimulation. The visual stimulus was presented over three time periods: 5 minutes of darkness, followed by 20 minutes of visual stimulation with vertical gratings rotating horizontally at a constant 10 deg/s in one direction, which in turn was followed with 20 minutes of darkness. An exemplar eye-position trace of a larva during the dark period, the 20-minute optokinetic stimulation, and the negative OKAN in the dark is shown, with positive and negative quick-phase velocity peaks marked in red and green, respectively. Magnifications of the transition phases from pre-stimulation to optokinetic nystagmus (OKN) and from OKN to negative OKAN are presented for clarity. Figure adapted from (Lin et al., 2019).

to stimulation (Figure 5.1B) and the transition period from stimulation to post-stimulation (Figure 5.1C). Prior to optokinetic stimulation, the animal spontaneously saccades in both directions, which is followed by slow drifts toward the center of the visual field (Figure 5.1B). Following sustained optokinetic stimulation, we observed that the animal's eye started beating in the opposite direction to the prior stimulus, characterized by a transition from negatively directed to positively directed quick phases during the transition from stimulation to darkness (note the transition from green to red circles in Figure 5.1A). The eye movements in the opposite direction to the stimulus in the post-stimulation phase constitute the negative OKAN, which here lasted approximately 7 minutes after extinguishing the stimulus (Figures 5.1A and 5.1C). Intriguingly, during the negative OKAN, the beating field deviated toward the side of the previous stimulus direction (0 to 15 degrees, Figure 5.1A). In contrast, during spontaneous eye movements in both the pre- and post-stimulatory phases, the eyes moved across a broader range (±15 degrees, Figure 5.1A).

5.2.2. Quantification of OKN and negative OKN

To quantify the negative OKAN, we analyzed the slow-phase velocities (SPVs) between each consecutive pair of quick-phases. The average SPVs were calculated in 10-second intervals over the entire 45-minute recording period (Figures 5.2A and 5.2C; see section 2.2.5 for more details). Moreover, we computed the quick-phase frequency (QPF) by counting the number of quick-phases during 10-second temporal intervals. QFP was obtained separately for positive and negative quick phases (Figure 5.1A). The difference (ΔQPF) was obtained by subtracting the positive QPF from the negative QPF (Figures 5.2B and 5.2D). Overall, quantification of SPV and ΔQPF revealed adaptation during OKN and negative OKN build-up and decay during the post-stimulatory darkness period. Before the onset of the stimulus, the eye movements spontaneously moved to either direction resulting in average SPV and ΔQPF values close to zero (Figure 5.2, panels A-D, pre-stimulatory darkness period denoted by the black bar on top of the panels). Upon the stimulus onset, the SPV and ΔQPF increase quickly to a maximum value and then decay gradually to a steady-state value as the stimulation is continued (Figure 5.2, panels A-D, OKN period). Upon the offset of the stimulus, SPV and ΔQPF decrease and change signs as the magnitude of these quantities build up and reach a plateau, after which they slowly decay to zero (Figure 5.2, panels A-D, post-stimulatory darkness period denoted on the black bar on top of the panels). Additionally, due to the temporal-to-nasal asymmetry in lateral-eyed animals (Qian et al., 2005; Wallman and Velez, 1985), the right eyes exhibited faster SPV than the left eyes in response to counterclockwise-rotating optokinetic stimulation.

We estimated the dynamics of OKN adaptation during the stimulation phase by fitting with a second-order exponential decay function as in Eq. (2.8). The time constants of SPV adaptation during OKN for the right and left eyes were $\tau_1=0.54 \pm 0.23$ min, $\tau_2=6.15 \pm 4.66$ min, and $\tau_1=0.35 \pm 0.36$ min, $\tau_2=1.93 \pm 0.82$ min, respectively. Additionally, we estimated the time constants of negative OKAN dissipation using a first-order exponential function as in

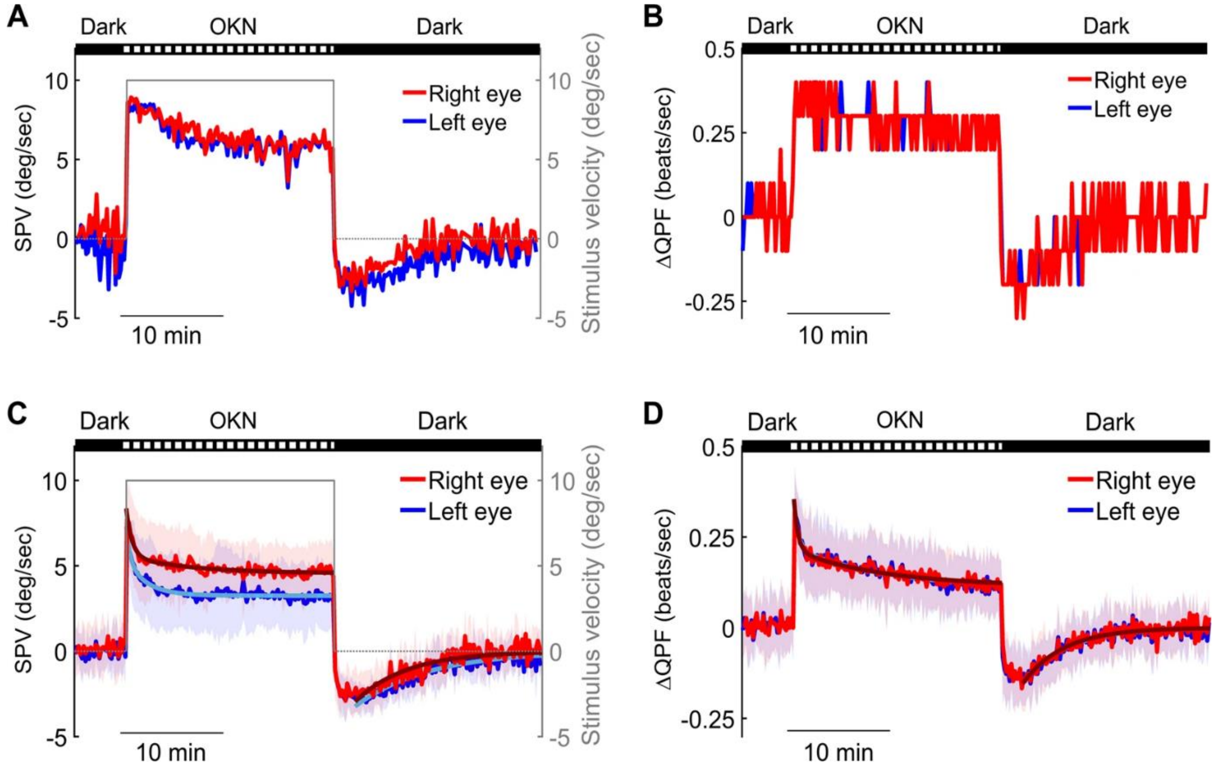

Figure 5.2. Quantification of OKN and negative OKAN in Larval Zebrafish. The slow-phase velocity (SPV) and ΔQPF (difference in quick-phase frequency) were analyzed during the entire 45-minute recording period, which included 5 minutes in the dark, followed by 20 minutes of optokinetic stimulation at a constant velocity of 10 deg/s in one direction, and another 20 minutes in the dark. The average SPV data from a single subject (Figure 5.1A) and the average values of 15 subjects are shown in **(A)** and **(C)**, respectively, with the stimulus velocity depicted by the gray line. The ΔQPF data for each 10-second interval throughout the recording are presented in **(B)** and **(D)**, with separate lines for the right eye (red) and left eye (blue) data. Cyan and dark red lines represent the fitting curves for the OKN adaptation and negative OKAN decay in the dark, respectively. To minimize the masking effect of the velocity-storage components during the build-up phase of the absolute OKAN velocity, the first 2 minutes of OKAN velocity data were excluded from the fitting process. The shaded areas indicate the standard deviation. Figure adapted from (Lin et al., 2019).

Eq. (2.9). For right and left eyes, we obtained τ_3=5.02 ± 0.81 min and τ_3=7.03 ± 0.79 min, respectively. Furthermore, we calculated the time constants for ΔQPF during OKN adaption and negative OKAN dissipation. For the right eye, during OKN adaptation, we obtained τ_1=0.39 ± 0.17min, τ_2=8.86 ± 1.28 min, and τ_3=3.94 ± 0.55 min during negative OKAN decay. For the left eye, during OKN adaptation, we obtained τ_1=0.41 ± 0.21 min, τ_2=8.86 ± 1.28 min, and τ_3=4.22 ± 0.60 min during negative OKAN decay.

These findings align with previous results observed in human and mouse subjects, indicating that both SPV and QPF analyses provide comparable estimates of the negative OKAN (Cahill and Nathans, 2008; Waddington and Harris, 2013). In summary, our study demonstrates that quantifying negative OKAN through both SPV and QPF analyses yields consistent and comparable results in larval zebrafish.

5.2.3. Dependence of negative OKAN dynamics on stimulus duration

We studied the dynamics of negative OKAN by subjecting the animals to differential stimulus durations for 4, 5, 7, 10, 20, and 40 minutes with the same unidirectional 10 deg/s stimulation. Zebrafish larvae exhibited robust negative OKAN in response to the stimuli reflected both in SPV (Figures 5.3A, B) and ΔQPF (Figures 5.3G, H) obtained from both eyes. To estimate the time constant of negative OKAN for different stimulus durations, we used the same method used above (Eq. (2.9)) and fitted a first-order exponential decay function to the SPV and ΔQPF data. Note that the relatively low negative OKAN amplitude resulted in decreased signal-to-noise ratio, and as such, the data for 3 and 4 minutes were not fitted. The normalized fit traces of SPV (Figures 5.3C, D) and ΔQPF (Figures 5.3I, J) decay were plotted for both left and right eyes, respectively, which revealed that overall, the negative OKAN decay time constant increases with stimulus duration. To quantify this result, we plotted the decay time constate as the function of stimulus duration (SPV: Figures 5.3E, F; ΔQPF: 5.3K, L) and calculated Pearson's correlation coefficient between the two quantities. The analysis of SPV and ΔQPF revealed increased decay time constant during negative OKAN with the stimulus duration for both eyes (SPV: $r = 0.87$, $p = 0.023$, $n = 6$ in left eye and $r = 0.93$,

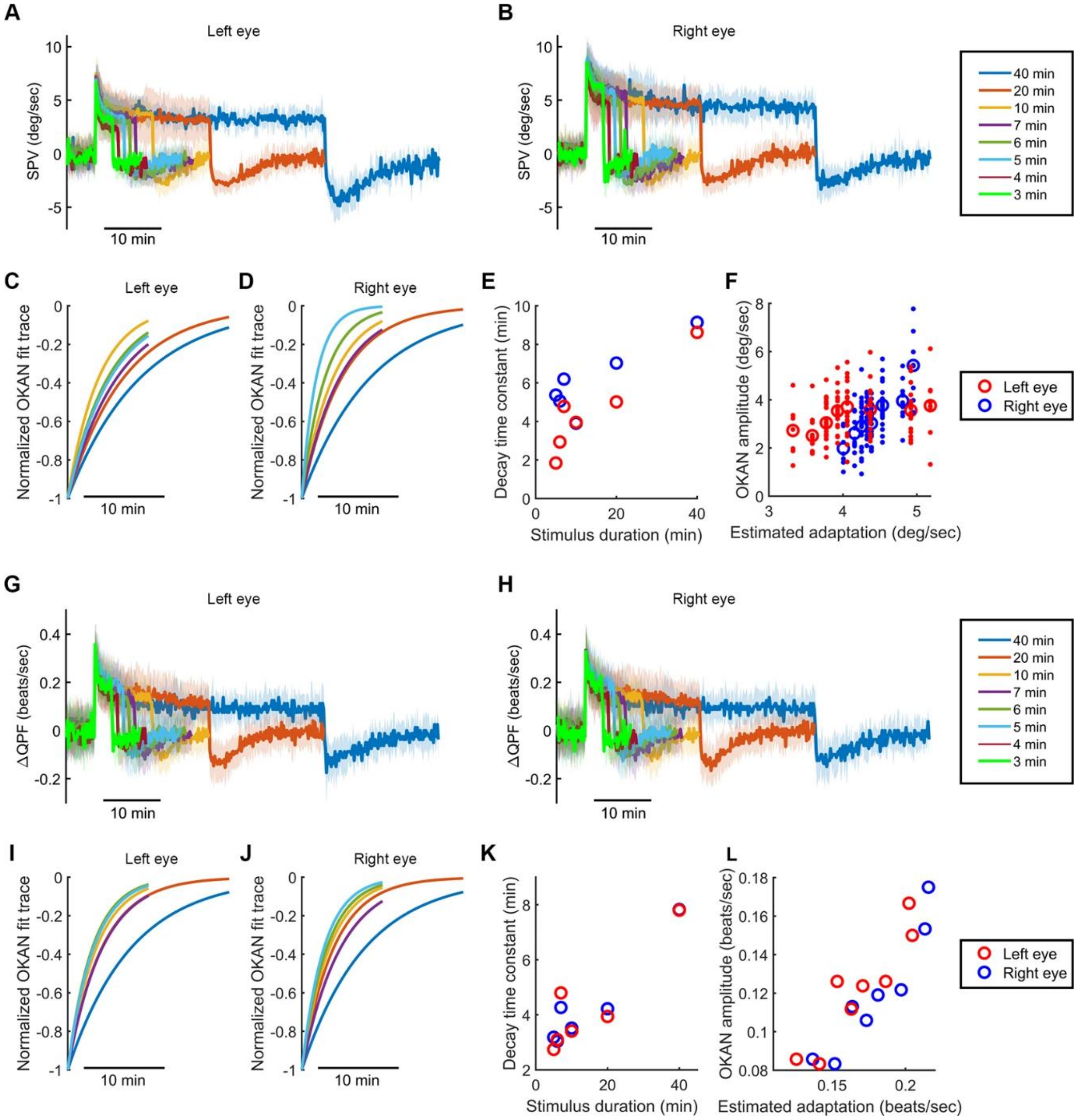

Figure 5.3. Negative OKAN dynamics depend on the stimulus duration. (A, B, G, H) The mean ± standard deviation of slow-phase velocity (SPV) (A, B) and quick-phase frequency difference (ΔQPF) (G, H) obtained from 10-second windows during the whole stimulation protocol. The durations of optokinetic stimulation varied, including 5 minutes in the dark, followed by 3, 4, 5, 6, 7, 10, 20, and 40 minutes of continuous stimulation at a constant velocity of 10 deg/s in one direction. After each stimulation period, there were subsequent dark periods lasting for 5, 6, 10, 10, 10, 10, 20, and 20 minutes, respectively. The sample size for the stimuli were N = 7, 12, 23, 17, 21, 23, 15, and 8, respectively. **(C, D, I, J)** The normalized fitting curves depicted the decay of negative OKAN after 5, 6, 7, 10, 20, and 40 minutes of optokinetic stimulation, which were estimated from SPV (C, D) and ΔQPF (I, J). **(E, K)** The decay time constants, estimated from SPV (E) and ΔQPF (K), were then plotted against the stimulus duration. **(F, L)** The negative OKAN amplitudes were evaluated after 3, 4, 5, 6, 7, 10, 20, and 40 minutes of optokinetic stimulation, estimated from SPV (F) and ΔQPF (L), and were plotted against the estimated OKN adaptation. The data for the left-eye were represented by blue circles, while red circles represented the right-eye data. Figure adapted from (Lin et al., 2019).

p = 0.007, n = 6 in right eye; ΔQPF: r = 0.95, p = 0.004, n = 6 in left eye and r = 0.89, p = 0.017, n = 6 in right eye; Pearson correlation analysis).

5.3 Conceptual and mathematical model of negative OKAN

So far, our behavioral data (SPV and QPF) have established that prolonged unidirectional stimulation leads to a decrease in OKN gain during stimulation and robust negative OKAN during post-stimulation darkness, which eventually decays to zeros if remained unperturbed. Based on the observation and previous literature, we proposed a mathematical model and a set-point adaptation mechanism that accounted for adaptation during OKN and subsequent negative OKAN.

5.3.1 Intuition behind the mathematical model

We hypothesized the reversal in eye velocity sign and the subsequent decay to zero is indicative of a leaky integrator component which directly contributes and has an opposing effect to the oculomotor command during stimulation. On the offset of the stimulus, the visual input to the oculomotor plant disappears, and the only input to the plant would come from the leaky integrator component. As such, we assumed the output of the leaky integrator is subtracted from the visual input to the oculomotor command, which could explain the reversal in the eye velocity sign upon the offset of the stimulus. This idea is consistent with previous models proposed for optokinetic response and VOR adaptation (Furman et al., 1989; Jareonsettasin et al., 2016; Leigh et al., 1981). Additionally, our observation from our data suggests differential time constants of OKN adaptation and negative OKAN dynamics. The lack of systematic relation between the time constants of OKN adaptation and negative OKAN dynamics across stimulus conditions suggests additional dynamics (at least one first-order transfer function) would be required to explain both OKN adaptation and negative OKAN during the onset and after the offset of the stimulus, respectively.

5.3.2 Conceptual model of set-point adaptation

To investigate our proposed model, we used a conceptual model illustrated in Figure 5.4A. In this model, the control system delivers a motor command to the eyes based on the error signal, which reflects the difference between the retinal slip velocity and its "internal" set point. Ordinarily, the set-point for the retinal slip velocity is maintained at 0 to stabilize the visual image on the retinae, as intended by the optokinetic system. The motor command also activates the adaptation operator, denoted by a leaky velocity integrator (the red component in Figure 5.4A), which redefines the set-point. Consequently, during sustained optokinetic stimulation, the change in the set-point enables the optokinetic system to slow down its eye tracking without increasing the error signal despite an increase in actual retinal slip. The habituation transfer function serves as a sensory filter, reducing the sensory input (i.e., the retinal slip velocity) over time. When the light is turned off, the current set-point is subtracted from the sensory input of 0 (no visual input in the dark), generating an error signal with the set-point value but opposite in sign. This error signal drives the eyes to move in the opposite direction, resulting in a negative OKAN. The decay of negative OKAN represents the discharge of the set-point adaptation operator.

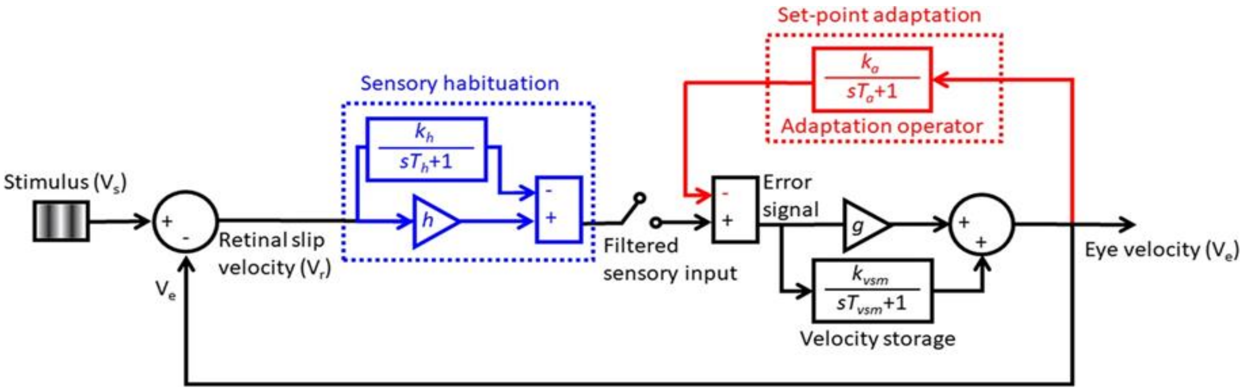

Figure 5.4. The proposed Conceptual model of negative OKAN. The diagram illustrates the optokinetic negative feedback control of the retinal slip velocity, incorporating the velocity storage mechanism and oculomotor plant (represented in black). The set-point adaptation is depicted in red, with an adaptation operator composed of a leaky velocity integrator. The time constant, T_a, and the reciprocal of k_a, indicate the adaptation intensity. The sensory habituation is shown in blue, consisting of a gain and a leaky integrator. This mechanism adjusts the efficiency of converting initial sensory input into electrochemical signals. The time constant, T_h, and the reciprocal of k_h, determine the dynamic and intensity of habituation.

5.3.3 Mathematical description of the model

In order to gain insight into the experimentally observed set-point adaptation, we employed a nonlinear model consisting of adaptation and habituation leaky integrators (depicted in Figure 5.4A). This model is characterized by different sets of equations during the presentation of the stimulus and after the stimulus is turned off (i.e., in darkness). Specifically, during the stimulation phase, the model is governed by the following set of differential equations:

$$\dot{X} = \frac{1}{1+gh}\begin{bmatrix} -\frac{1+g(k_a+h)}{T_a} & \frac{k_a}{T_a} & -\frac{gk_a}{T_a} \\ -\frac{k_{VSM}}{T_{VSM}} & -\frac{1+h(k_{VSM}+g)}{T_{VSM}} & \frac{k_{VSM}}{T_{VSM}} \\ \frac{gk_h}{T_h} & -\frac{k_h}{T_h} & -\frac{1+g(k_h-h)}{T_h} \end{bmatrix} X + \frac{1}{1+gh}\begin{bmatrix} \frac{ghk_a}{T_a} \\ \frac{k_{VSM}h}{T_{VSM}} \\ \frac{k_h}{T_h} \end{bmatrix} V_S \qquad (5.1)$$

$$V_e = \frac{1}{1+gh}[-g, \quad 1, \quad -g]\, X + \left(\frac{gh}{1+gh}\right) V_s \qquad (5.2)$$

where $X = [A, Q, H]^T$, V_e denotes the eye velocity, and V_s is the stimulus velocity. The parameters A, Q, and H correspond to the outputs of the respective leaky integrators. Furthermore, we have g as the oculomotor gain; k_{VSM} and T_{VSM} representing velocity storage gain and time constant; k_a as the adaptation gain, and T_a as the adaptation time constant; h as the habituation gain; k_h as the habituation gain, and T_h as the habituation time constant. Finally, V_r signifies the retinal slip velocity.

After stimulus offset (extinguishing the stimulus), the model is described by the following set of differential equations:

$$\dot{Y} = \begin{bmatrix} -\frac{1 + gk_a}{T_a} & \frac{k_a}{T_a} \\ -\frac{k_{VSM}}{T_{VSM}} & -\frac{1}{T_{VSM}} \end{bmatrix} Y \tag{5.3}$$

$$V_e = [-g, \quad 1]\, Y \tag{5.4}$$

where $Y = [A, Q]^T$ and A and Q are defined as mentioned before. The model was implemented using Simulink in MATLAB (Mathworks, Natick, MA). For estimation purposes, we employed global optimization (*globalSearch* function in MATLAB) to maximize the variance-accounted-for (VAF) as per the definition:

$$VAF = 1 - \frac{\mathrm{var}\left(V_e - V_{e,measured}\right)}{\mathrm{var}\left(V_{e,measured}\right)} \tag{5.5}$$

where $V_{e,est}$ and $V_{e,measured}$ are the simulated and experimentally measured values of eye velocity, respectively, and var(.) denotes the variance. We used the nonlinear least squares method and trust-region-reflective algorithm to optimize the parameters of the model.

5.3.3 Simulation results

Figure 5.5 illustrates the model simulations alongside the empirical slow-phase velocities (SPVs). A comprehensive list of all estimated parameters is provided in Table 5.1. Additionally, we demonstrate the simulation results of the partial models, which included only the set-point adaptation or the habituation component. Notably, a partial model with only a set-point adaptation mechanism (Figure 5.6A) and or one with only a habituation mechanism (Figure 5.6B) is not sufficient to explain both OKN adaptation and negative OKAN. While the partial model with the adaptation component explained the negative OKAN, it underestimated OKN (Figure 5.6C). Additionally, the partial model with only the habituation component failed to exhibit negative OKAN (Figure 5.6D). Together, our simulation results indicate that the set-point adaptation mechanism is crucial for the emergence of negative OKAN and therefore is a necessary condition to explain the behavior

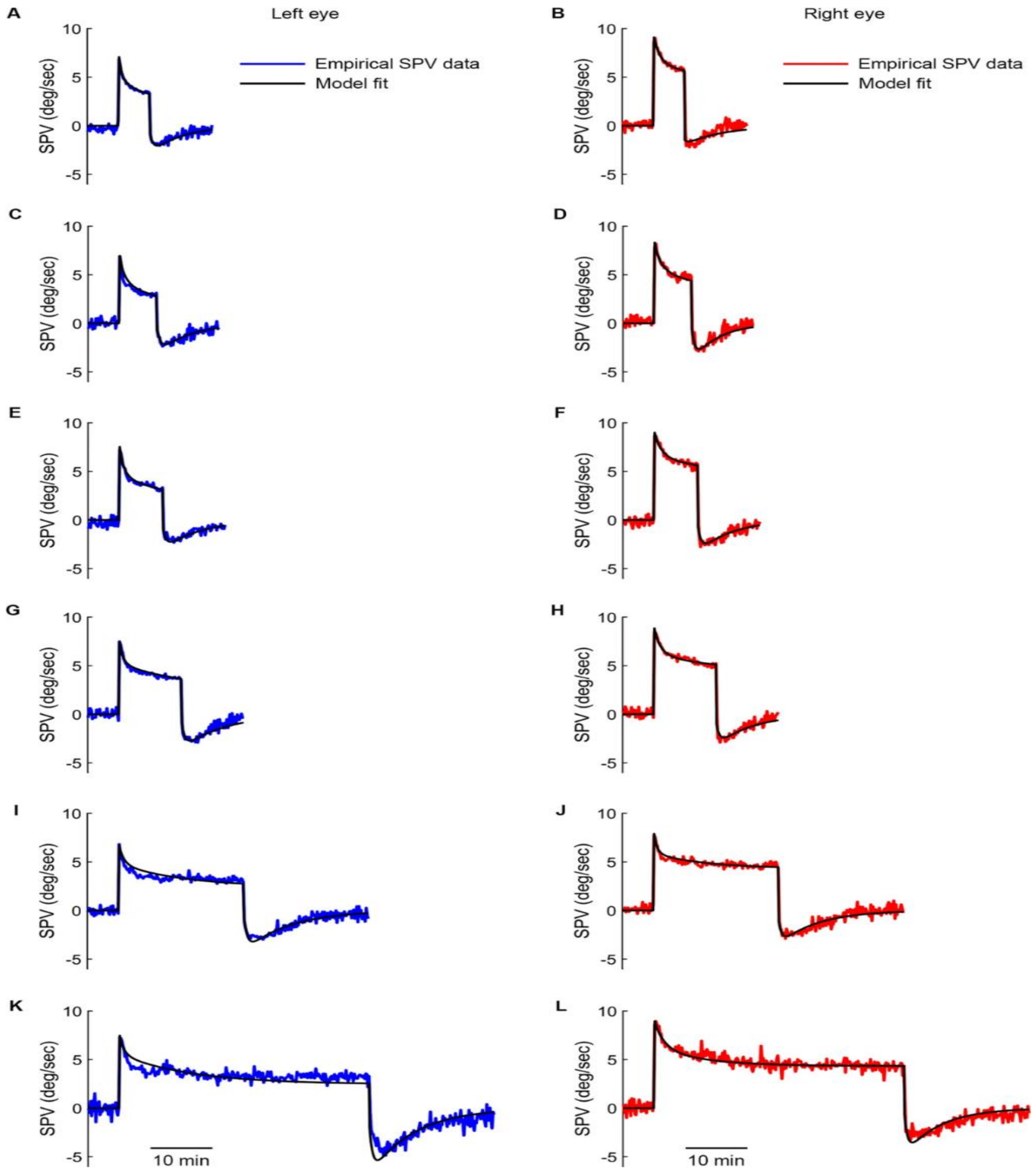

Figure 5.5. Comparing the simulation results with the empirical data. (SPV; Figures 5.3A, B). Simulated SPVs and empirical SPV data are shown under 5- (A, B), 6- (C, D), 7- (E, F), 10- (G, H), 20- (I, J), and 40- (K, L) minute optokinetic stimulation at 10 deg/s. The SPVs from the left eye and right eye are depicted in blue and red traces, respectively (refer to Fig. 5A, B), and the simulation results are shown in black. The optimized parameters used in the simulations are provided in Table 5.1.

Table 5.1. The parameter list for simulation of the model in Figure 5.4. SD: Stimulus duration in minutes; VAF: variance-accounted-for (%). See the definition of the parameters of the model in the caption of Figure 5.4.

	Left Eye						Right eye					
SD	5	6	7	10	20	40	5	6	7	10	20	40
T_a	1300	1300	1300	1300	1300	1300	700	700	700	700	700	700
T_{vsm}	30	30	30	30	30	30	30	30	30	30	30	30
T_h	10	10	10	10	10	10	10	10	10	10	10	10
g	0.9	0.7	0.9	0.9	0.5	0.9	1.6	0.9	1.7	1.5	0.7	0.3
k_{vsm}	0.5	0.8	0.5	0.7	0.7	0.5	1	0.6	0.7	0.55	0.3	1.2
k_a	2.2	2	1.8	1.4	0.6	1.4	0.5	1.1	0.45	0.45	0.85	0.4
h	3.5	4	4.5	5	5	5.1	9	7.2	7.2	7	7	8
k_h	2.9	3.5	3.9	4.35	4.25	4.2	8	6.3	6.4	6.2	5.6	7.2
VAF	0.98	0.97	0.98	0.98	0.97	0.96	0.98	0.98	0.99	0.99	0.98	0.97

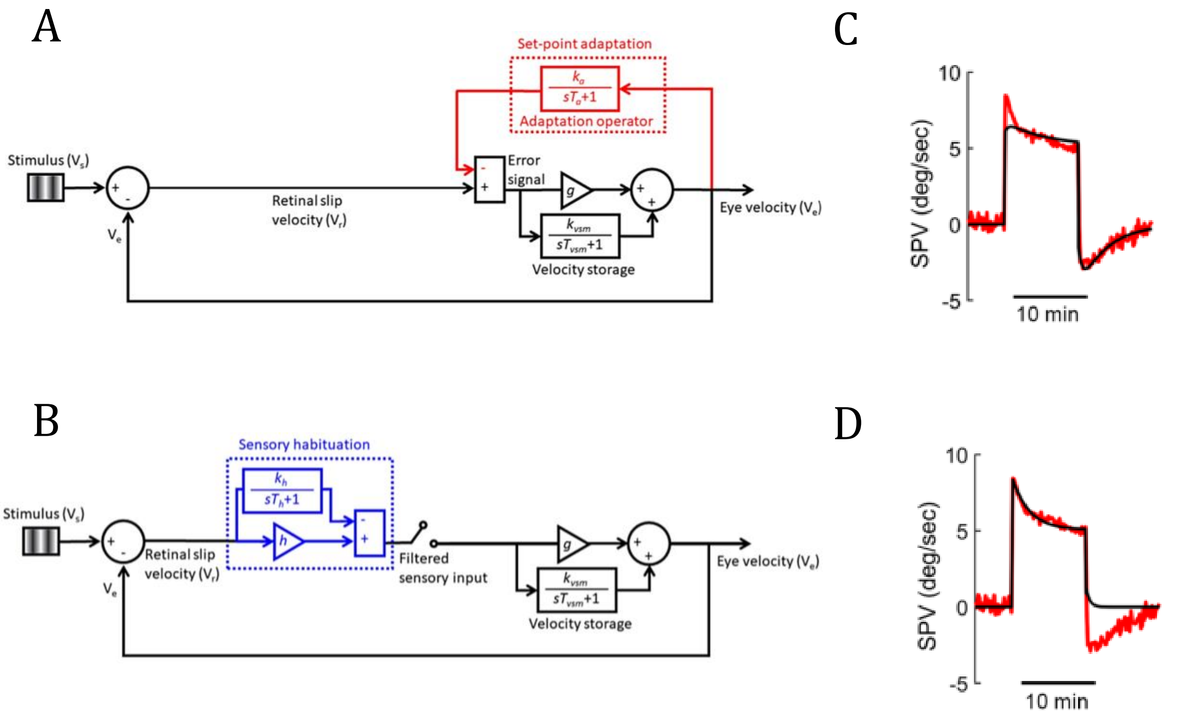

Figure 5.6. Partial models fail to explain observed behavioral data. (A) A partial model derived from our proposed model only comprising the adaptation component. **(B)** A partial model derived from our proposed model with only habituation component. The definition of parameters in panels A and B are same as in Figure 5.4. **(C, D)** Data and simulations of partial model with adaptation component and partial model with habituation component, respectively. The data is the population averaged SPV recorded from the right eye of the animals for 10-minutes stimulation condition and is depicted in red in all panels. The simulation results are illustrated by black solid traces. The parameters were optimized for each model. See table 5.2 for the description of parameters.

of the animal during prolonged optokinetic stimulation. However, it is not sufficient; A habituation mechanism is required to account for the decrease in OKN gain during stimulations.

5.4 Summary of results

Here, we investigated OKN response of larval zebrafish in response to prolonged unidirectional stimulation. The unidirectional stimuli elicit robust OKN, which diminished to a steady state value. Upon offset of the stimulus, a robust negative OKAN was evoked, which then decayed to zero. We proposed that a set-point adaptation together with habituation mechanism could explain the OKN adaptation and the negative OKAN ensuing the offset of the stimulus. Using a mathematical model incorporating set-point adaptation and habituation mechanisms, we tested this hypothesis and demonstrated that a set-point adaptation mechanism is in play in larval zebrafish by which a negative OKAN is elicited upon the offset of the stimulus.

Table 5.2. The parameter list for simulation of the partial models in Figure 5.6. All parameters are defined similarly as in Table 5.1.

	Right eye	
SD	Habituation	Set-point adaptation
T_a		438
T_{vsm}	30	30
T_h	32	
g	1.5	1.5
k_{vsm}	0.55	0.55
k_a		0.45
h	3.6	
k_h	3.1	

6. OPTOKINETIC SET-POINT ADAPTATION: AN INTERNAL DYNAMIC CALIBRATION MECHANISM FOR OCULOMOTOR DISEQUILIBRIUM

Advancement in technology has made larval zebrafish an excellent model for the study of visuomotor learning and control. In the previous chapter, we proposed a novel set-point adaptation mechanism in larval zebrafish, by which the animal adjust the eye movement based on visual experience. Using a mathematical model, we demonstrated that the set-point adaptation mechanism allows the animal to decrease the eye tracking velocity during prolonged unidirectional stimulation by decreasing the error signal input to the oculomotor system. However, the specific physiological and functional relevance of this mechanism remains elusive. Additionally, the unidirectional stimulation used in the previous study does not represent the natural visual stimulation in larval zebrafish. Here, I present our findings on the physiological relevance of set-point adaptation during more natural bidirectional stimulation. The behavioral data for this study was gathered by our collaborators, Dr. Ting Feng Lin and Dr. Melody Ying-Yu Huang, at the University of Zurich.

6.1. Advantages of using sustained bidirectional over unidirectional optokinetic stimulation

During early development and before the onset of vestibular functions (<7-dpf), larval zebrafish mainly rely on the visual system for swimming (Beck et al., 2004; Bever and Fekete, 2002; Lambert et al., 2008). Previous studies of negative OKAN have mostly used prolonged unidirectional stimulation to elicit the behavior (Brandt et al., 1974; Maioli, 1988; Pérez-Schuster et al., 2016; Wu et al., 2020b). The study designs are far from the animals' natural exploratory behavior; Freely-swimming larval zebrafish exhibit spontaneous turns, alternating between one direction (Figure 6.1A) and the other, which is more consistent with a direction-alternating stimulation paradigm (Figure 6.1B). Thus, to understand the significance of the set-point adaptation mechanism, we used a direction-alternating

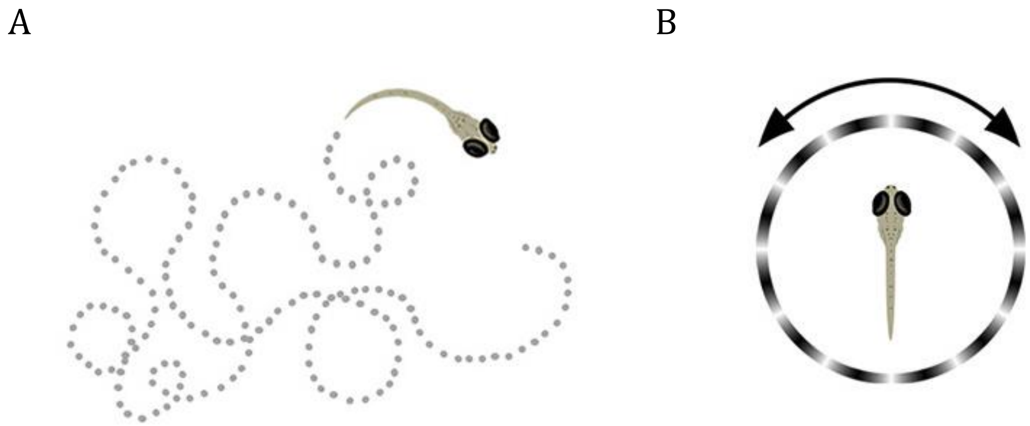

Figure 6.1. Schematic comparing visual experience of the animal during natural exploration and bidirectional stimulation in experimental settings. (A) The animal swimming freely and exploring in natural environment. The direction of the animal movement, and so the retinal image of whole visual field, changes spontaneously. **(B)** The animal viewing a bidirectional rotating drum consistently changing direction after a fixed amount of time. Adapted from (Lin et al., 2022).

optokinetic stimulation paradigm that more resembles the natural swimming patterns of the animal.

For this study, we used a simplified form of the direction-alternating stimulus: the bidirectional stimulation protocol, which during the simulation phase consists of a rotating drum changing rotation direction every 15 seconds. The stimulus velocity may or may not be the same for the directions (referred to as symmetric and asymmetric stimulation, respectively; see section 2.2.4). Our modeling results from the previous study predicted an asymmetric direction-alternating stimulus could elicit adaptation and negative OKAN. Accordingly, we investigated OKN and negative OKAN using the bidirectional optokinetic stimulation paradigm to understand the functional significance of the set-point adaptation mechanism in animals.

6.2. Zebrafish behavior during bidirectional optokinetic stimulation

To investigate how the differences in the visual experience may affect the optokinetic set-point and the oculomotor behavior, we measured the eye position of the animal before, during, and after symmetric direction-alternating (SA) and asymmetric direction-alternating (AA) stimulation. The eye position and corresponding slow phase eye velocity (SPV) of an

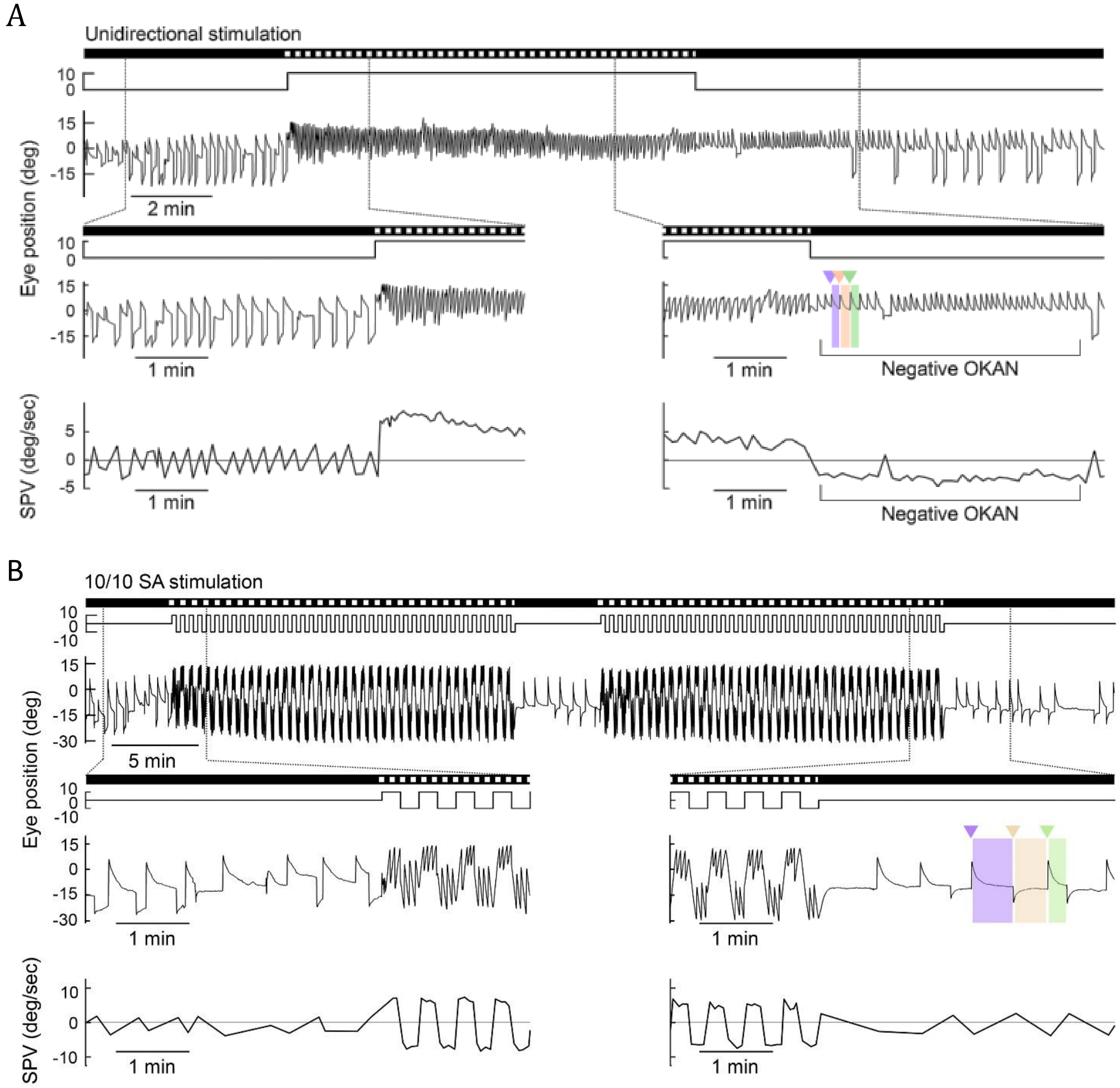

Figure 6.2. Comparison of larval OKN and negative OKAN during unidirectional and SA stimuli. (A) Unidirectional stimulus induces OKN adaptation and negative OKAN in larval zebrafish. Top panel: The stimulus image pattern (darkness or gratings) and the stimulus velocity are shown on the top as horizontal bars and lines, respectively. The eye position of the animal is show at bottom. Middle panel: magnification of eye position during the transition from pre-stimulation darkness to optokinetic nystagmus (OKN) on left and the transition from OKN to post-stimulation darkness on right. The SPV was estimated as the median velocity in the first second of each slow phase (shaded area) after discarding the quick-phase eye movement (triangle). At the bottom, the magnified SPV traces are shown to better demonstrate the transition phases from pre-stimulatory darkness to OKN on left and from OKN to post-stimulatory darkness on right. Positive values represent movements to the left (counterclockwise), and negative values represent movements to the right (clockwise). **(B)** Same as in A, except the stimulus was 10/10 symmetric direction-alternating (SA) stimulation. Adapted from (Lin et al., 2022).

exemplar animal during SA, AA, and unidirectional stimulation (for comparison) are shown in Figures 6.2 and 6.3. During the darkness before the onset of the stimulation, the animal's eye spontaneously makes saccade movements in either direction (Figures 6.2A-B, 6.3A-B, left middle, and bottom panels with corresponding windows on the left top panel). After each saccade, the eye drifts back to the center of the visual field due to the velocity storage integrator (Figures 6.2A, 6.3A, left middle panels) (Chen et al., 2014b). During this period, the direction of the eye movement was not biased towards either direction across all conditions (i.e., stimulus paradigms). During unidirectional stimulation, the SPV decreased over time, suggesting an ongoing adjustment of the oculomotor input signal through set-point adaptation (Figure 6.2A, bottom left panel) consistent with our observation in the previous study (see Chapter 5 for more details). Upon the offset of the stimulus, the direction of the eye movement reversed, and the eye started to beat in the direction of the stimulus, manifesting as negative OKAN (Figure 6.2A, middle and bottom left panels). Unlike the unidirectional stimulation, the symmetric direction-alternating stimulation —where 10 deg/s stimuli were presented with direction alternating every 15 seconds— did not elicit noticeable negative OKAN, and SPV velocity was close to zero during post-stimulation darkness (Figure 6.2B, middle, bottom, and top right panels).

Next, we investigated whether an asymmetric direction-alternating (AA) stimulus can induce OKN adaptation and negative OKAN based on the prediction from our modeling study. We used two AA stimuli: 10/5 AA stimulus (Figure 6.3A) and 20/5 AA stimulus (Figure 6.3B). 10/5 AA stimulus is generated by rotating the drum with a velocity of 10 deg/s in one direction and 5 deg/s in the other direction and by alternating between the two every 15 seconds. 20/5 AA stimulus is similar to 10/5 AA stimulus, except the drum rotates with the velocity of 20 deg/s in the faster direction. Our results revealed that most larvae did not exhibit negative OKAN during 10/5 AA stimulation (Figure 6.3A, bottom left). However, during 20/5 AA stimulation, SPV magnitude decreased in the faster direction, and negative OKAN manifested with SPV directing opposite to the faster stimulation (Figure 6.3B, bottom left). Together, our result showed that given sufficient contrast in asymmetric stimulation, negative OKAN can be elicited in 5-pfd larval zebrafish.

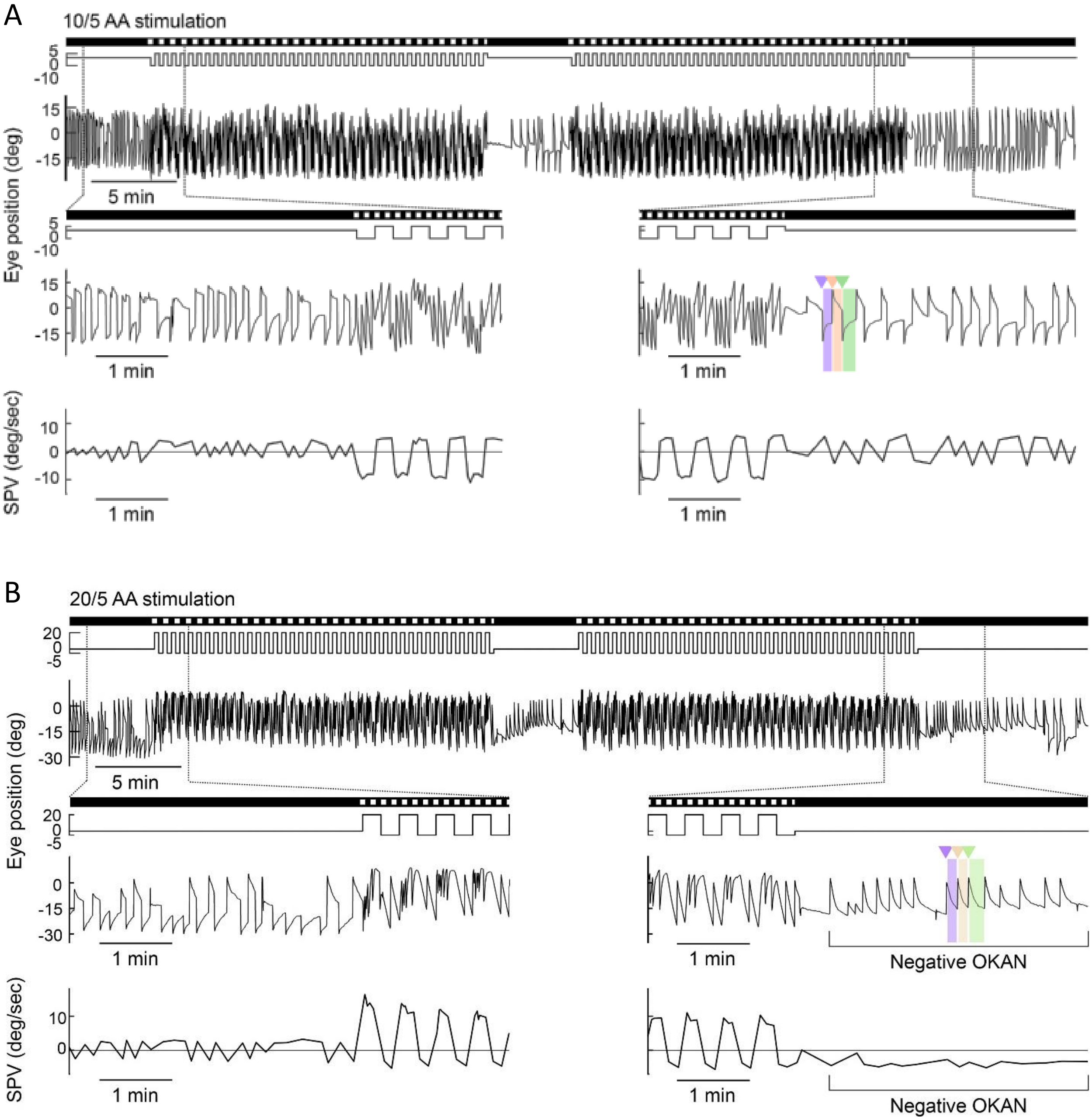

Figure 6.3. Asymmetric optokinetic stimulation can elicit negative OKAN. (A) 20/5 asymmetric alternating-direction (AA) stimulus induces OKN adaptation and negative OKAN in larval zebrafish. Top panel: The stimulus image pattern (darkness or gratings) and the stimulus velocity are shown on the top as horizontal bars and lines, respectively. The eye position of the animal is show at bottom. Middle panel: magnification of eye position during the transition from pre-stimulation darkness to optokinetic nystagmus (OKN) on left and the transition from OKN to post-stimulation darkness on right. The SPV was estimated as the median velocity in the first second of each slow phase (shaded area) after discarding the quick-phase eye movement (triangle). At the bottom, the magnified SPV traces are shown to better demonstrate the transition phases from pre-stimulatory darkness to OKN on left and from OKN to post-stimulatory darkness on right. Positive values represent movements to the left (counterclockwise), and negative values represent movements to the right (clockwise). **(B)** Same as in A, except the stimulus was 10/5 (AA) stimulation. Adapted from (Lin et al., 2022).

6.3. Mathematical model of set-point adaptation during asymmetric direction-alternating stimulation

We adapted our proposed model in the previous study (See Chapter 5) to bidirectional stimulation and simulated the behavior of larval zebrafish. The previous model (Figure 5.4) was adapted for unidirectional stimulation; however, for bidirectional stimulation, the habituation model needed to be modified. Here, I initially describe the modified model and how the parameters of the model were estimated, and next, I present the population-median data and the simulation results.

6.3.1. Model description

The schematic of the adapted model is shown in Figure 6.4. When the stimulus is presented, the retinal slip signal, V_r, is calculated by subtracting the eye velocity, V_e, from the stimulus velocity, V_s (Eq. (6.1)). The retinal slip velocity is rectified and integrated by leaky integrator with a time constant of T_h and gain of k_h (Eq. 6.2). Additionally, the retinal velocity is scaled with a gain of h from which the output of the integrator, H(t), is subtracted with an appropriate sign. Together, the integrator and the habituation gain, h, constitute the habituation mechanism in retinal ganglion cells and downstream areas (Pérez-Schuster et al., 2016) (See Eq. 6.3). Since the previous model was designed for unidirectional stimulation, we made adjustments to preserve the functionality of each operator under direction-alternating stimuli. Specifically, we included an absolute value function and corrected the sign of the habituated retinal slip velocity signal, as the habituation of the signal remains consistent regardless of the direction of the stimulus (See Figure 4Ai in (Pérez-Schuster et al., 2016)).

$$V_r(t) = V_s(t) - V_e(t) \tag{6.1}$$

$$\frac{dH(t)}{dt} = -\frac{1}{T_h}H(t) + \frac{k_h}{T_h}|V_r(t)| \tag{6.2}$$

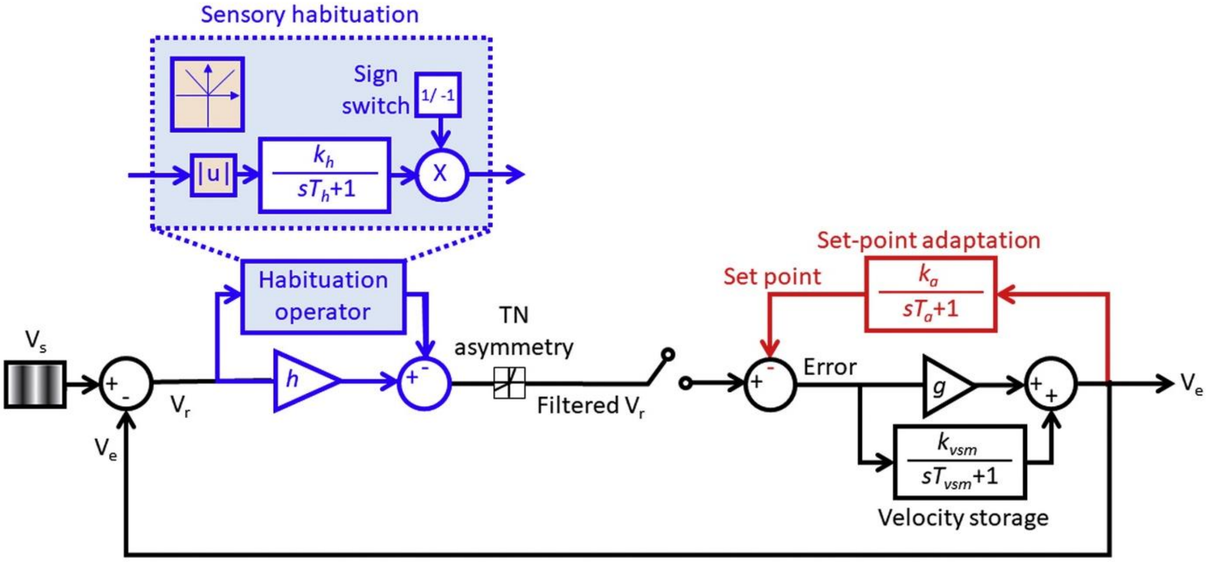

Figure 6.4. Schematic of the mathematical model of set-point adaptation. The retinal slip velocity (V_r), which is the difference between the stimulus velocity (V_s) and the eye velocity (V_e), undergoes several processing steps. During habituation, V_r is rectified and integrated by a time constant of T_h and a gain of k_h (depicted in the blue shaded area). Here, |u| is used to calculate the absolute value of the input (shown in the orange shaded area), and together with a sign switch at the output, it leads to a continuous habituation effect when subtracted from V_r, irrespective of the stimulus direction. Note that the habituation gain, h, with the habituation integrator gain, k_h, determine the efficacy of the habituation. The habituated (or filtered) V_r is then processed through a nonlinear gain (T-N gain) to capture the T-N asymmetry. The error between the filtered V_r and the set point is scaled by the oculomotor gain (g) and combined with the velocity storage mechanism (VSM) to control the eye velocity (V_e). The VSM contains a leaky integrator with a time constant of T_{vsm} and a gain of k_{vsm}, contributing to the eye velocity. Finally, V_e is integrated with a time constant of T_a and a gain of k_a to adjust the set-point. Adapted from (Lin et al., 2022).

Our behavioral data showed that nasal and temporal gains are different, which is consistent with findings from previous studies (Huang and Neuhauss, 2008a; Mueller and Neuhauss, 2010; Qian et al., 2005). These gains are modeled using a piecewise linear function that varies based on the direction of eye movement, whether it is nasalward or temporalward. The nasal and temporal gains are obtained by averaging and scaling the eye velocity during corresponding movements (see Table 6.1). Subsequently, the filtered retinal slip signal, denoted as $V_f(t)$, is derived as

$$V_f(t) = g_{T/N}\left[h\, V_r(t) - \mathrm{sign}\big(V_r(t)\big)\, H(t)\right] \tag{6.3}$$

where sign(.) is the sign function, h is the habituation gain, and $g_{T/N}$ is the temporal/nasal asymmetry. As the eyes move, the adaptation integrator —denoted by the red box in Figure 6.4— is charged, which in turn defines the internal set-point of the oculomotor system as

$$E(t) = V_f(t) - A(t) \tag{6.4}$$

where A(t) is the output of the adaptation integrator and E(t) is the error signal input to the oculomotor system. This signal drives the oculomotor system and generates eye movement, described in the following equation:

$$V_e(t) = gE(t) + Q(t) \tag{6.5}$$

g is the oculomotor gain, and Q(t) is the output of the velocity storage integrator. The description of A(t) and Q(t) are given using the following system of equations:

$$\frac{dQ(t)}{dt} = -\frac{1}{T_{vsm}} Q(t) + \frac{k_{vsm}}{T_{vsm}} E(t) \tag{6.6}$$

$$\frac{dA(t)}{dt} = -\frac{1}{T_a} A(t) + \frac{k_a}{T_a} V_e(t) \tag{6.7}$$

Table 6.1. Temporal-Nasal asymmetry gain was calculated for all stimulus conditions.

Stimulus condition	20/5 AA	10/10 SA	10/5 AA
g_N	0.9	1.6	1.8
g_T	0.77	1.27	1.46

where T_{vsm} and T_a are the velocity storage and adaptation time constants, and k_{vsm} and k_a are the velocity storage and adaptation gains, respectively. Upon offset of the stimulus, $V_f(t)=0$, and therefore, $E(t) = -A(t)$, signifying a change in the direction of the eye movement. During the post-stimulation phase, the integrator is discharged, which manifests as negative OKAN. The differential equations above were solved using *ode45* function in MATLAB for a given set of parameters.

6.3.2. Estimation of the model parameters

We estimated the model parameters (k_a, T_a, k_h, T_h, k_{vsm}, T_{vsm}, h, and g) using the system identification toolbox in MATLAB. Specifically, we used the nonlinear least square method and trust-region algorithm with fixed time steps of 0.1 second to find a plausible set of parameters that maximized the variance-accounted-for (VAF) defined as:

$$\mathrm{VAF} = \left[1 - \frac{\mathrm{var}(\mathrm{V_{data}} - \mathrm{V_{est}})}{\mathrm{V_{data}}}\right] \times 100\% \tag{6.8}$$

where V_{data} and V_{est} are the measured and estimated eye velocity, and var(.) denotes the variance. A model that perfectly estimates the eye velocity would give a VAF of 100%, and any deviation from the data would result in a VAF value less than 100%.

For the median population behavior, we used data from the 10/10 SA stimulus condition to estimate the parameters of the model. Each stimulation protocol consisted of a 5-minute period of darkness, followed by the first stimulatory phase with 20 minutes of stimulus presentation, then 5 minutes of darkness, and finally, the second stimulatory phase consisting of 20 minutes of stimulus followed by 10 minutes of darkness. We estimated the model's parameters using data from one stimulatory phase and evaluated its performance using data from the other stimulatory phase. We built the first model using data from the first stimulatory phase and validated it with data from the second stimulatory phase, and vice versa for the second model. Both models exhibited similar qualitative and quantitative performance and resulted in similar parameter sets (refer to Table 6.2). For all the representative simulations, we only used the predictions from the first model.

For model validation, we used the same parameter set for all conditions except for the temporal/nasal gain ($g_{T/N}$); $g_{T/N}$ was estimated during each condition separately (see Table 6.1). After obtaining the parameter estimates using data from a specific stimulus condition, we assessed the goodness of fit for each condition. In this study, we present the parameters estimated and tested using 10/10 SA stimulus and validated with 20/5 SA and 10/5 SA stimulus conditions (refer to Table 6.2). Remarkably, qualitatively similar results were observed when employing other stimulus conditions for parameter estimation (results not shown).

Table 6.2. Estimated parameters for population-median data for all conditions as well as goodness-of-fit (GoF) characterized by VAF for each stimulus condition. In model 1, parameters are estimated using the first stimulatory phase from 10/10 SA condition whereas for model 2, the parameters are estimated from the second stimulatory phase and valid. Both models are validated using the data from the other conditions (i.e., 20/5 and 10/5 AA stimulation).

Parameter/GoF	Model 1	Model 2
k_a	1.8	1.8
k_h	0.43	0.64
k_{vsm}	0.45	0.45
T_a (s)	583	735
T_h (s)	120	95
T_{vsm} (s)	3	2.5
g	0.042	0.07
h	3.2	4.3
$VAF_{20/5}$ (%)	90	89
$VAF_{10/10}$ (%)	95	95
$VAF_{10/5}$ (%)	93	92

6.4. Model predictions closely match population-median SPV data across stimulus conditions.

To investigate and compare the oculomotor responses to both symmetric and asymmetric stimulation, we calculated the population-median slow-phase velocity (SPV) for both 10/10 SA (Figures 6.5A-C) and 20/5 AA (Figures 6.5D-F) stimuli. Under 10/10 SA stimulation, the SPV decreased equally in both directions over time (Figures 3A, B), and no negative OKAN was observed after the stimulation (Figures 6.5C). In contrast, during 20/5 AA stimulation, the SPV gradually decreased in the faster stimulus direction while remaining largely unaffected in the other direction, which mitigated the temporal-nasal (T-N) asymmetry in OKN over time (Figure 6.5D, E), despite the sustained velocity difference in both directions. Additionally, negative OKAN emerged after the 20/5 AA stimulation (Figure 6.5F). However, such asymmetric SPV adaptation and subsequent negative OKAN were less prominent in the milder 10/5 AA stimulation group (Figure 6.6A-C).

In order to understand the mechanisms underlying negative OKAN under different stimulation conditions, we used the mathematical model incorporating sensory habituation and set-point adaptation introduced above. Overall, our model effectively reproduced the observed eye movements during direction-alternating stimulation. For instance, the predicted slow-phase velocity (SPV) from the model was compared with empirical data for both 10/10 SA (Figure 6.5A-C) and 20/5 AA (Figure 6.6D-F) stimulations. Under SA stimulation, the model's set-point adaptation operator exhibited opposite charging cycles, leading to a relatively constant set-point. In contrast, under AA stimulation, the adaptation integrator was charged more in the faster-stimulus direction, resulting in the gradual build-up of a set-point over time. Conceptually, adjusting the set-point alone should decrease the SPV in the direction of the faster stimulus and increase it by the same amount in the opposite direction. However, when we consider sensory habituation in our model, it predicts a relatively consistent SPV in the slower-stimulus direction while showing a significant decrease in SPV in the faster-stimulus direction. Furthermore, during the post-stimulation period following the 20/5 AA stimulus, the non-zero set-point contributed to negative OKAN (Figure 6.5F). The model also demonstrated SPV similar to experimental data during 10/5 AA stimulation (Figures 6.6A-C), although the negative OKAN was less pronounced compared to the 20/5 AA condition and was not evident in the experimental data (compare Figures 6.5F and 6.6C).

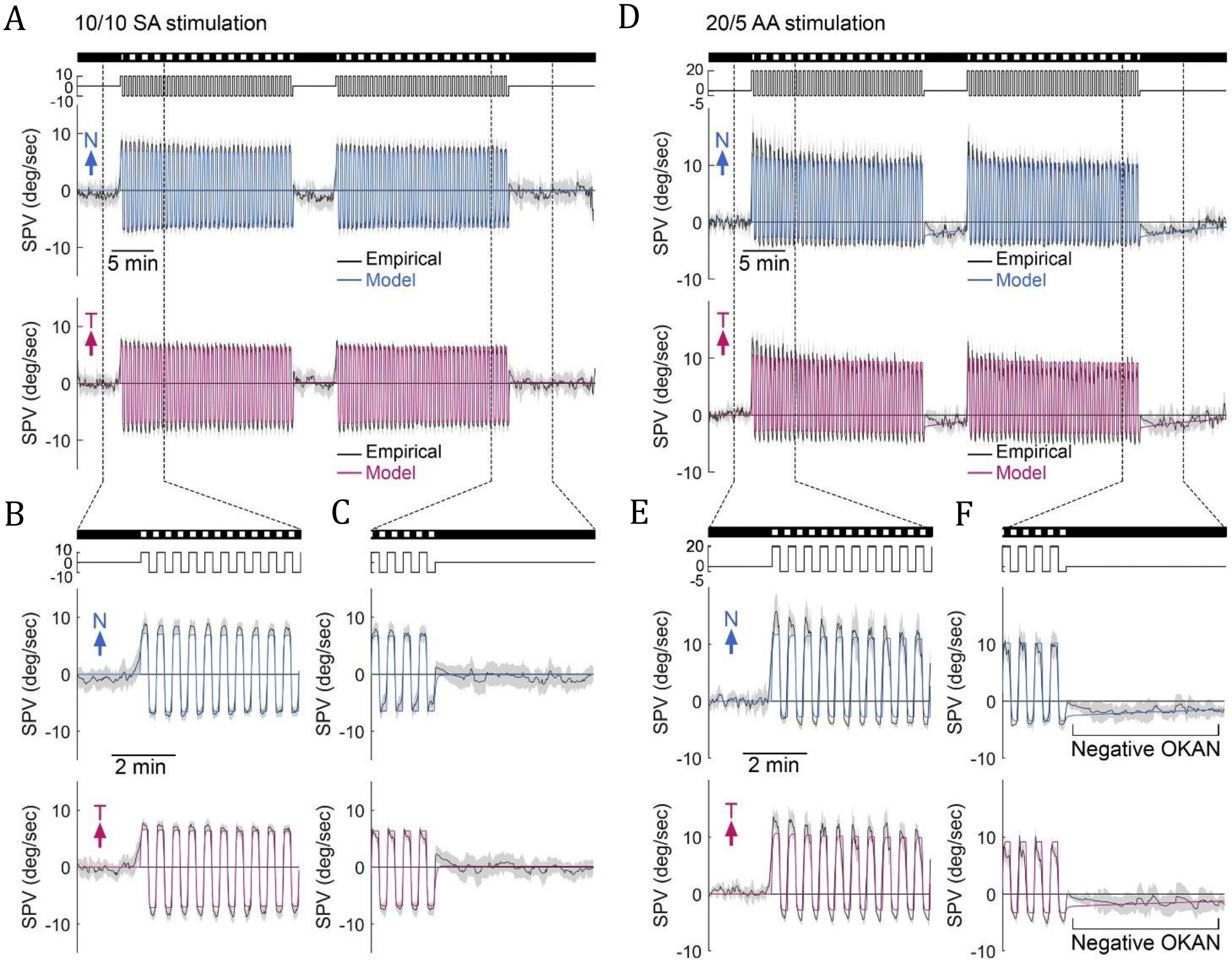

Figure 6.5. Optokinetic set-point adaptation model predicts the observed SPV in larval zebrafish. Panels **(A–F)** display the model-predicted population-median slow-phase velocity (SPV) represented by colored lines, overlaid on the median ± median absolute deviation (black line with gray shadow) of empirical SPVs during 10/10 symmetric alternating stimulations (SA, n = 29) **(A–C)** and 20/5 asymmetric alternating stimulations (AA, n = 18) **(D–F)**. To ensure consistency, we aligned the first stimulus direction as positive rather than specifying it as left or right. Hence, the plots exhibit one eye starting with a nasalward movement (blue trace) and the other eye starting with a temporalward movement (red trace). The stimulus image pattern (darkness or gratings) and stimulus velocity are indicated at the top as horizontal bars and lines, respectively. Adapted from (Lin et al., 2022).

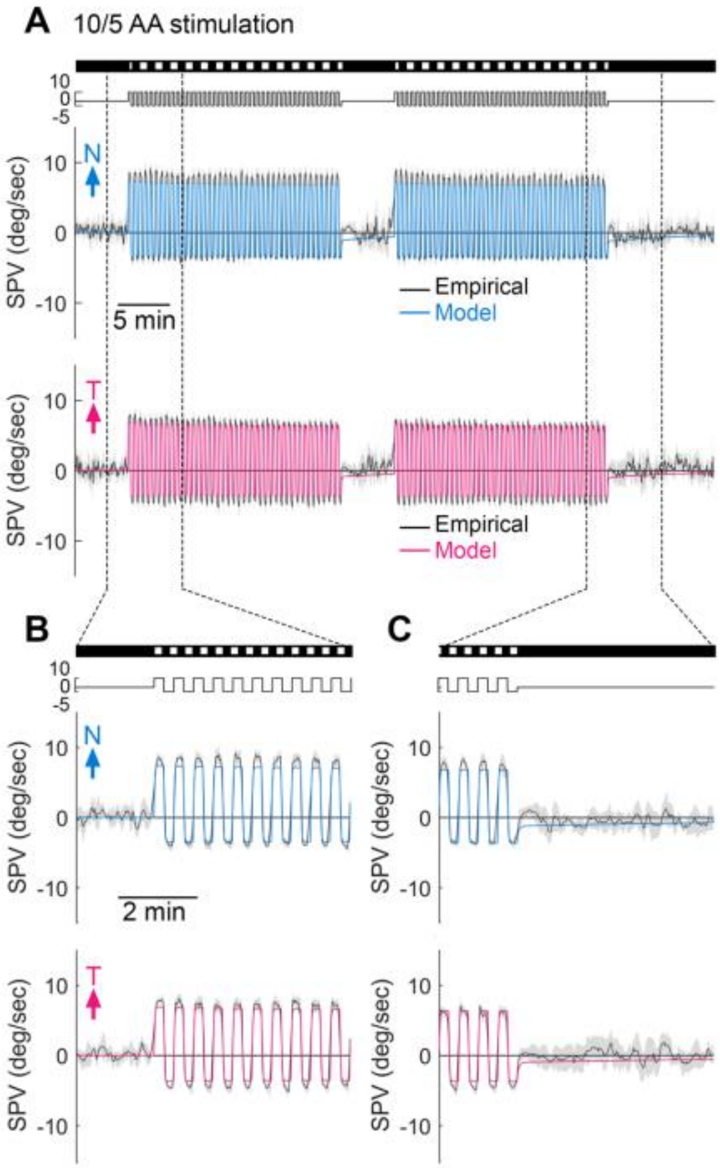

Figure 6.6. Low-contrast SA stimulation is not sufficient to elicit significant negative OKAN consistent with the prediction of the mathematical model. The predicted SPV (colored lines) is superimposed on the median ± median absolute deviation of empirical SPVs during 10/5 asymmetric alternating (AA, n = 21) stimulation. To maintain consistency, we aligned the first stimulus direction as positive, irrespective of whether it was left or right. Consequently, the plots display one eye initiating with a nasalward movement (blue trace) and the other eye starting with a temporalward movement (red trace). The stimulus image pattern (darkness or gratings) and stimulus velocity are illustrated at the top as horizontal bars and lines, respectively. Adapted from (Lin et al., 2022).

6.5. Behavioral asymmetry was observed during symmetric stimulation in individual larvae.

Based on the population SPV median, only the asymmetric stimulation induced set-point adaptation and resulted in negative OKAN (Figure 6.5). Surprisingly, some individual larvae displayed negative OKAN under symmetric stimulation. A representative larva showed robust negative OKAN following 10/10 SA stimulation, suggesting a potential bias in the preceding SPV. To address this, we calculated the population SPV median (n = 29) as the standard response curve and compared it to single larva behavior (Figure 6.7B). Results confirmed that the representative larva had a faster SPV in the positive direction during early OKN (Figure 6.7B; left magnified panel), followed by negative OKAN in the negative direction (Figure 6.7B; right magnified panel). To visualize the SPV difference, we calculated ΔSPV, indicating the variation in the SPV of individual larvae, by subtracting the population median from the individual's SPV (Figures 6.7C). The ΔSPV of the representative individual exhibited an asymmetric positive bias during early OKN (Figure 6.7C; left magnified panel), which was mitigated towards the late phase of the OKN (Figure 6.7C; right magnified panel).

To quantify the asymmetric responses and adaptation under symmetric stimulation across individuals, we calculated average ΔSPVs for each individual larva during specific time windows: 4 minutes before the stimulus onset (denoted by "pre"), 4 minutes after the onset of the stimulus in the first stimulatory phase (depicted by "early"), the last 4 minutes of the second stimulatory phase (shown as "late"), and the duration from 1 to 5 minutes after offset of the stimulus at the end of the second stimulatory phase (denoted by "post") (bottom panels of Figures 6.7B, C). The probability distribution plots showed normal distributions centered around 0 deg/s for both early and late OKN, with the late OKN distribution being narrower and taller, indicating mitigated behavioral asymmetry over prolonged stimulation (Figure 6.8A). We plotted late ΔSPV against early ΔSPV, revealing a significant positive correlation with a slope smaller than one, consistent with the reduced variance in late ΔSPV distribution (Figure 6.8B). This means that fewer larvae exhibited asymmetric responses after prolonged stimulation. Note that the observed correlations did not arise from regression towards the mean (Furrow, 2019), as the slope of the null expectation derived from temporally shuffled data was significantly different than the slope obtained from the

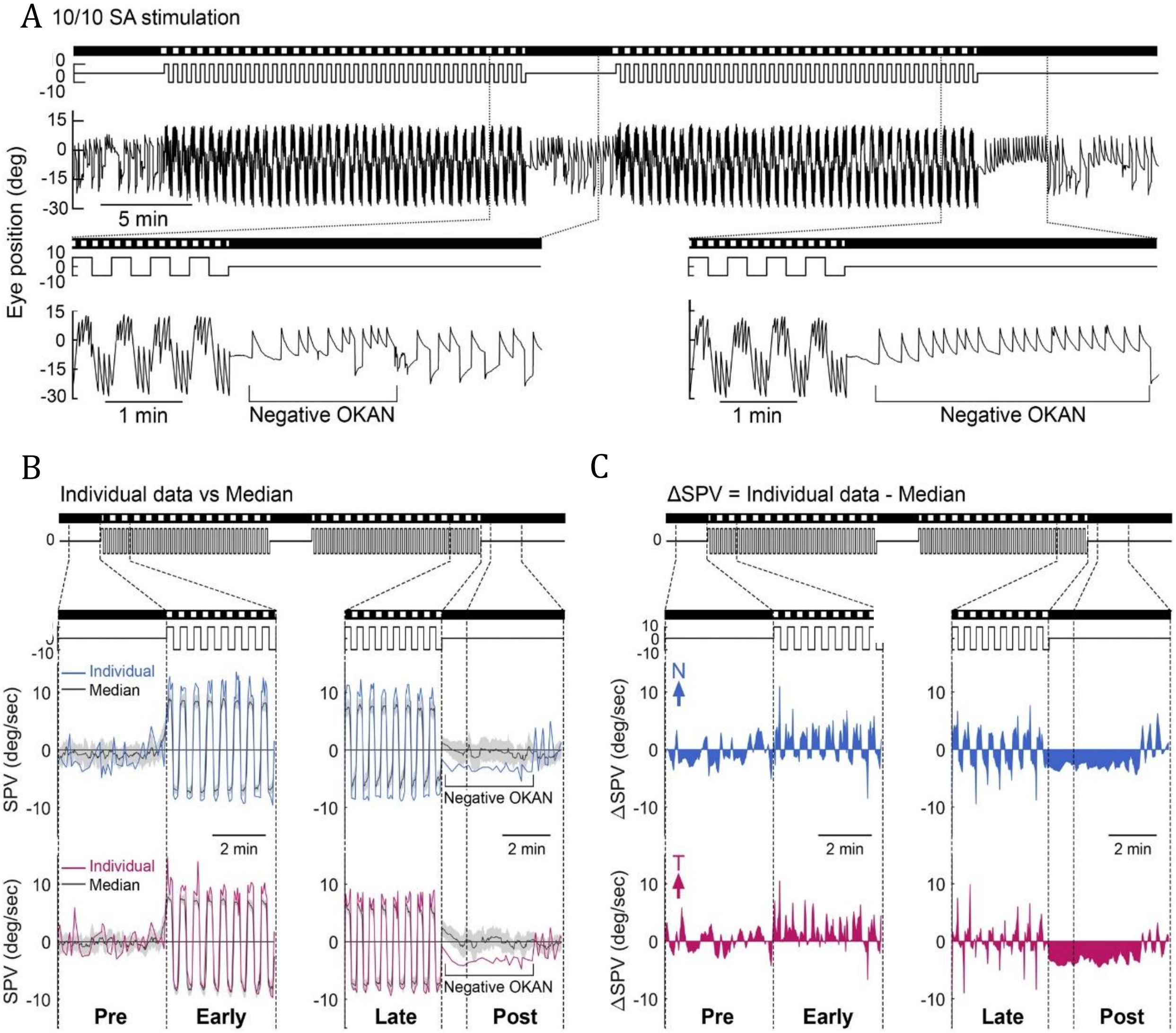

Figure 6.7. Individual larval zebrafish display negative OKAN during symmetric stimulation. (A) A representative eye-position trace of a single larva exhibiting OKN during 10/10 SA stimulation, followed by negative OKAN. The bottom plots provide magnifications to illustrate the transition phases from OKN to inter-stimulatory and post-stimulatory periods, respectively. **(B)** Magnifications comparing SPV of the exemplar larva to the median SPV for nasalward (blue; middle panel) and temporalward (red; bottom panel) at abovementioned transition phases. Top panel exhibits the stimulus image pattern and velocity are shown using a horizontal bar and a line. The magnified windows indicate the pre-stimulatory (pre), early/later stimulatory (early/late), and post-stimulatory (post) phases. **(C)** Same as in (B) except the difference between the larva's SPV and the median SPV is shown. Adapted from (Lin et al., 2022).

data. Moreover, the changes in ΔSPV across stimulus phases (ΔΔSPV) plotted over early ΔSPV showed a negative correlation, suggesting that greater inherent behavioral asymmetry (i.e., early ΔSPV) led to more optokinetic set-point adaptation (Figure 6.8C). Furthermore, a significant negative correlation was observed between changes in eye movements in the dark

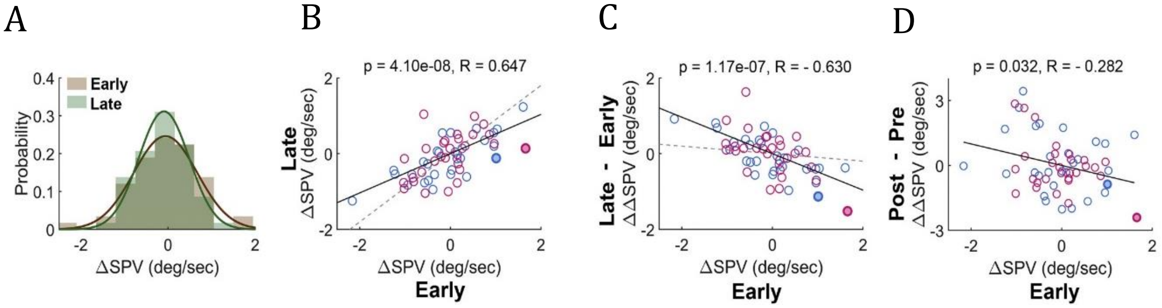

Figure 6.8. Response asymmetry during early phase of stimulation predicts OKN adaptation and negative OKAN. (A) The probability distribution of ΔSPV for 29 fish during the early and late periods is shown. Two lines indicate the fitting of the distributions with a Gaussian function. **(B)** The late ΔSPV plotted against the early ΔSPV. The slope of the solid line representing the linear regression is significantly smaller than 1 and the dashed line (representing temporally shuffled data; $p=1.8\times10^{-8}$ and $p=4.2\times10^{-6}$, respectively; interactive analysis of covariance). **(C)** Changes in ΔSPV across stimulus phases (late ΔSPV – early ΔSPV, ΔΔSPV) plotted against the early ΔSPV. The slope pf the solid line representing the linear regression is significantly smaller than the slope of the dashed line (representing temporally shuffled data; $p=4.2\times10^{-6}$, respectively; interactive analysis of covariance). **(D)** Changes in the eye movements before and after OKN (post-ΔSPV – pre-ΔSPV, ΔΔSPV) plotted against the early ΔSPV. Data from the animal is depicted in (A) as filled circles, and linear regression fit of the empirical data is represented by black solid lines. The plots align the first stimulus direction as positive, showing one eye with nasalward movement (blue trace) and the other with temporalward movement (red trace). "p" represents p-values, and "R" represents correlation coefficients obtained through Pearson correlation. Adapted from (Lin et al., 2022).

before and after OKN (ΔΔSPV) and early ΔSPV, indicating a dependence of negative OKAN on inherent OKN asymmetry and inherent bias (Figure 6.8D). Overall, the behavior suggests that some individual larvae demonstrate inherent asymmetry in their response which manifests as OKN adaptation and negative OKAN. Additionally, the asymmetry in the response is mitigated gradually during prolonged stimulation.

6.6. Inter-individual variations and behavioral asymmetries can be explained by innate bias in the optokinetic system.

Based on the observed data, we propose that individual larvae showing set-point adaptation and negative OKAN under symmetric stimulation might possess an inherent directional bias in their optokinetic system. To test this idea, we introduced a constant "bias" value in our conceptual model (Figure 6.9). The model predictions demonstrate that varying this bias can either predict no asymmetry in SPV (Figures 6.10A-C) or significant asymmetry with resulting negative OKAN (Figures 6.10D-F) under symmetric stimulation. Specifically, we estimated the innate bias value of each individual larva by using the parameters of the

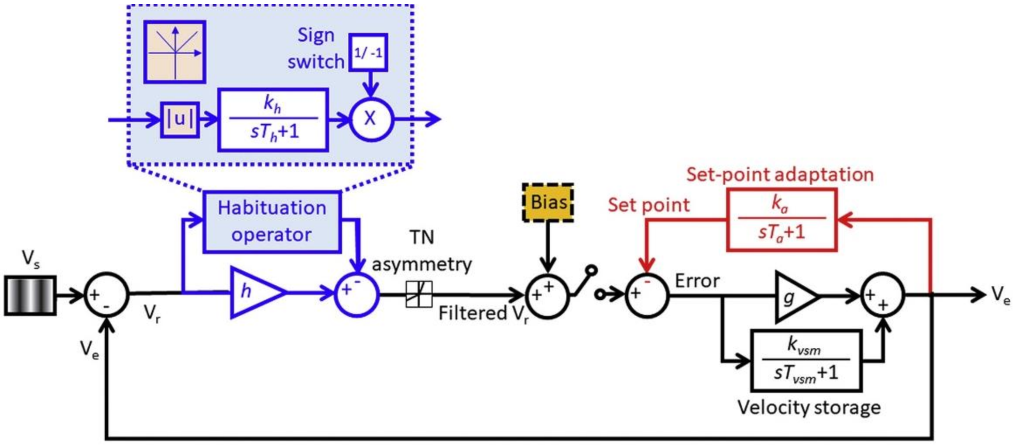

Figure 6.9. Conceptual model with innate bias. The bias is a constant value that simulates the OKN adaptation and negative OKAN observed in some individual larvae across dataset. All other parameters are defined and termed same as in Figure 6.4. Adapted from (Lin et al., 2022).

model obtained from the population (i.e., median data). Here, the SPV traces of two exemplar larval zebrafish and the model predictions are shown (Figures 6.10A-F). Individual fish 1 exhibited no significant asymmetric response (Figure 6.10B), OKN adaptation (Figure 6.10A), or negative OKAN (Figure 6.10C). Regardless, the model was able to explain most of the variance in data (B=3.5, VAF=90%). On the other hand, individual neuron 2 demonstrated a clear asymmetric response (Figure 6.10E) and OKN adaptation (Figure 6.10D) which later manifested as negative OKAN (6.10F). Additionally, our model successfully explains the asymmetry in SPV, OKN adaptation, and negative OKAN (B=13.5, VAF=87%).

The distribution of the estimated innate bias is shown in Figure 6.10G. The distribution is roughly symmetric and centered around 0 deg/s, with a few outliers biased in either direction and as such, population median SPV does not exhibit asymmetric OKN or negative OKAN. Moreover, the innate bias predicts the ΔSPV during the early and later phases of the stimulation (Figures 6.10H, I, respectively). Interestingly, the correlation between the estimated bias values and empirical data during the early phase of the estimation is higher than that between the estimated bias values and empirical data during the late phase of the stimulation, indicating that set-point adaptation can compensate for the ocular motor asymmetry caused by the innate bias (R=0.673, $p=6.98\times10^{-9}$, Figure 6.10H; R=0.355, p=0.006, Figure 6.10I). Furthermore, the bias also predicts the change in eye movements in the dark (post-ΔSPV – pre-ΔSPV, ΔΔSPV; Figure 6.10J), suggesting that the manifestation of

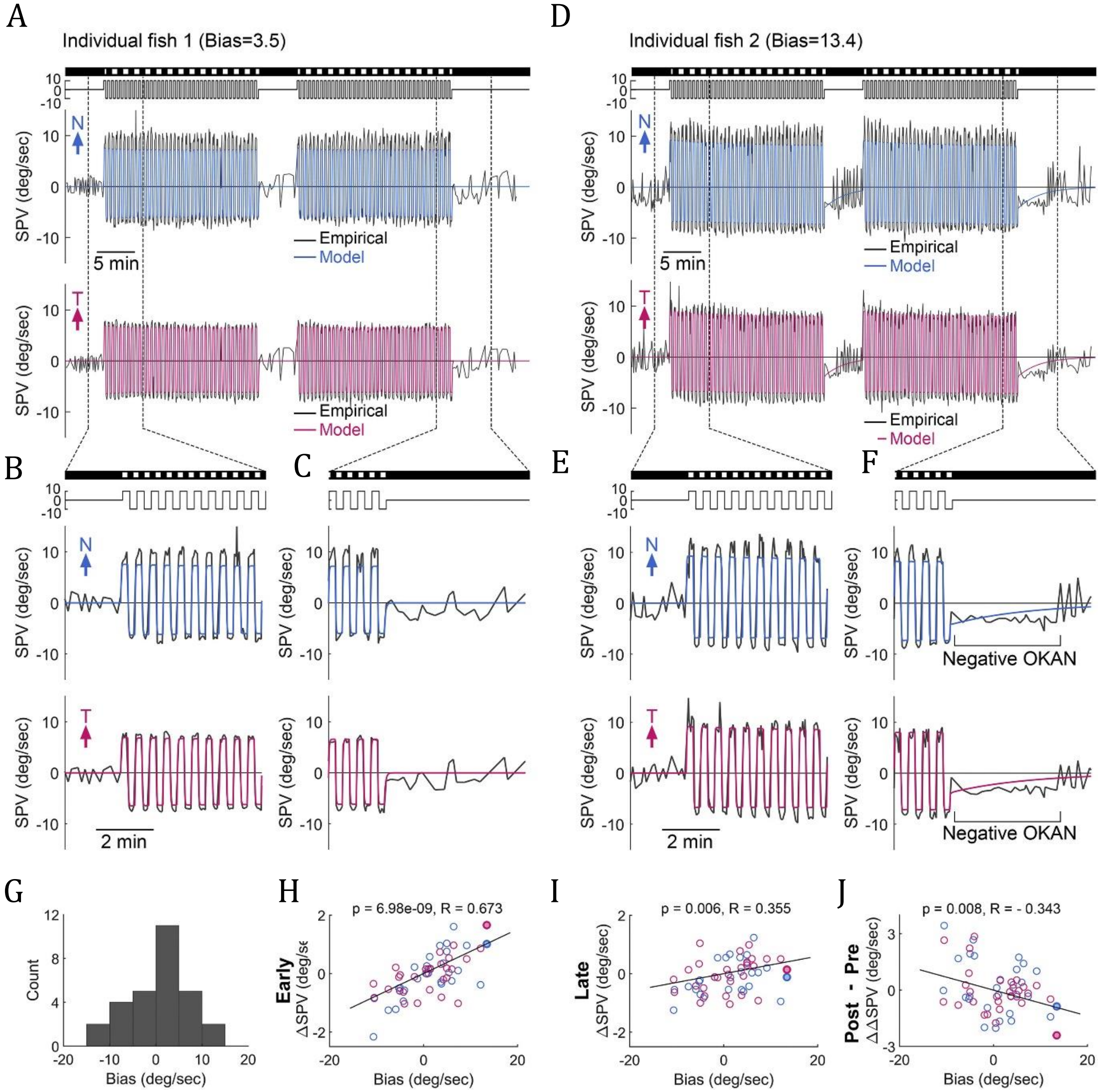

Figure 6.10. Asymmetric OKN and the corresponding set-point adaptation under the symmetric stimulus are accounted for with an inherent bias in the optokinetic system. (A) SPV traces of an exemplar larval zebrafish (in black) and the prediction of the modified model with inherent bias (blue and red traces for nasalward and temporalward SPV simulation). **(B)** and **(C)** depict the magnifications of the transition from pre-stimulatory to stimulatory phase and from stimulatory to post-stimulatory phase, respectively. The larva does not exhibit significant OKN set-point adaptation and negative OKN, with an estimated bias value of 3.5. **(D, E, F)** are same as in (A-C) for an exemplar larval zebrafish that demonstrate significant asymmetric response, OKN adaptation and negative OKAN. The model with an estimated bias of 13.4 predicts the asymmetric response, OKN adaptation, and negative OKAN. Through (A-F), the stimulus and its pattern are shown at top. **(G)** Distribution of estimated bias values across population (N=29). **(H-J)** Early, late, and the changes of the eye movements in darkness before and after OKN (post-ΔSPV – pre-ΔSPV, ΔΔSPV) as a function of bias across the population (N=29). The data points illustrated by filled circles correspond to simulation for the animal shown in (A-F). Adapted from (Lin et al., 2022).

the negative OKAN depends on the inherent bias. In conclusion, adjusting the innate bias in the model allows us to predict the extent of behavioral asymmetry, the resulting set-point adaptation, and the manifestation of negative OKAN.

Additionally, we asked whether the model could predict the experimentally observed relation between different phases of the stimulation protocol (Figures 6.7 and 6.8). Thus, we employed the estimated biases to simulate ΔSPV (Figure 6.11) for all the animals used in the

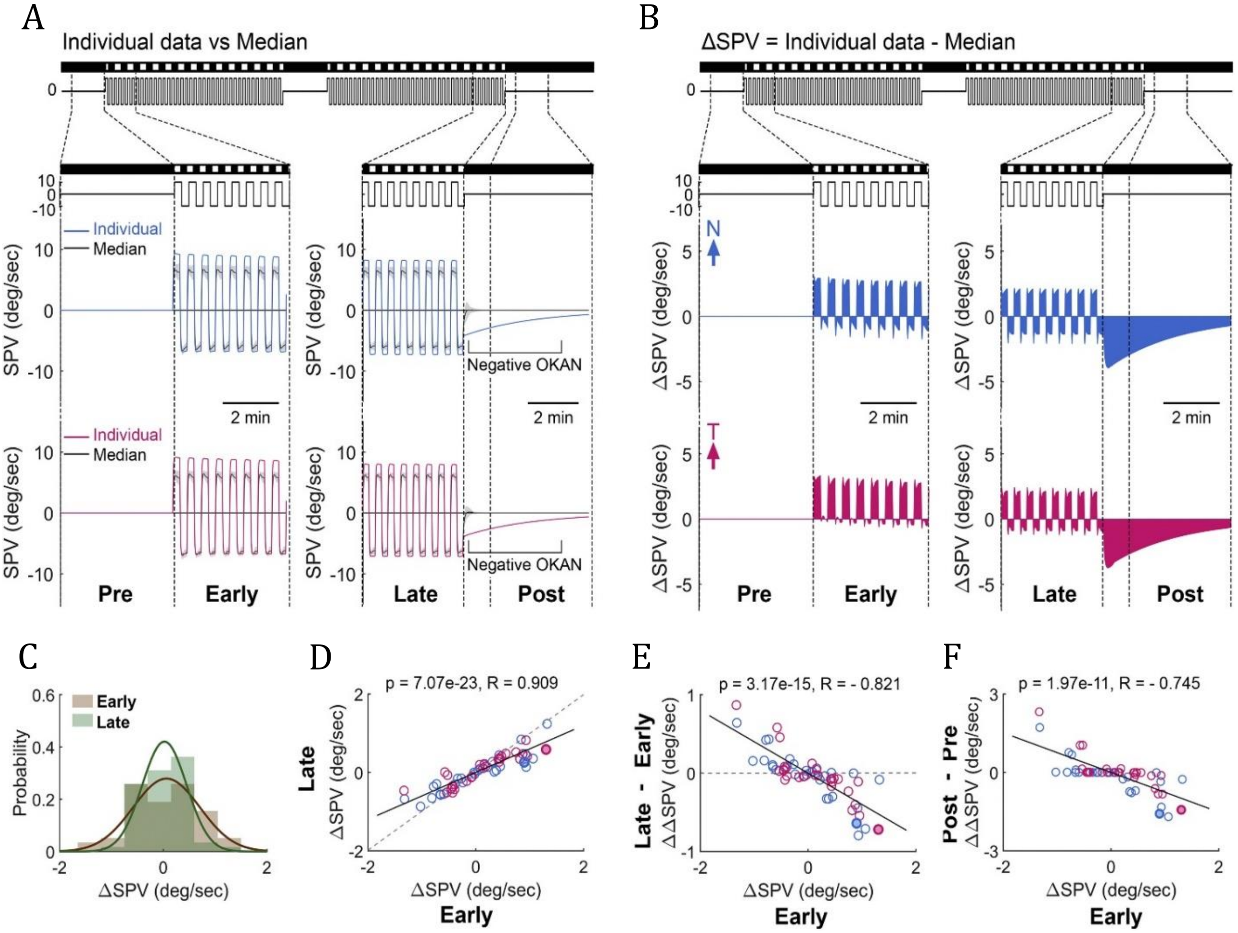

Figure 6.11. The mathematical model predicts the relationship between asymmetric response, OKN adaptation, and negative OKAN observed experimentally across all population. (A) Comparing the model estimations of median SPV (across the population) and individual fish 2 in Figure 6.9D-F. “Pre”, “Early”, “Late”, and “Post” are defined same as in Figure 6.6. The gray shadow represents the median absolute deviation obtained over the estimates for all individual larvae across the population. The stimulus and its image pattern are shown at the top. **(B)** ΔSPV calculated from the panel A with the estimates for the same Larva. **(C)** Distribution of early and late ΔSPV calculated over the SPV estimation of all larvae obtained as in panels A and B (N=29). **(D, E, F)** The late ΔSPV (D), the changes in ΔSPV across stimulus phases (late ΔSPV – early ΔSPV, ΔΔSPV) (E), and the changes of the eye movements in the dark before and after optokinetic nystagmus (post-ΔSPV – pre-ΔSPV, ΔΔSPV) (F) plotted as a function of the early ΔSPV. The data points illustrated by filled circles correspond to simulation for the animal shown in (A, B); N=29. Adapted from (Lin et al., 2022).

study and compared it to the simulation obtained for the median population data. The model simulations successfully capture all key features observed in the empirical data (compare Figures 6.7 and 6.8 to Figure 6.11). Specifically, the variance of the ΔSPV distribution decreases consistently throughout the stimulation (Figures 6.11C-E). Additionally, we observed a significant negative correlation between the change in eye movements in the dark (post-ΔSPV – pre-ΔSPV, ΔΔSPV) and the early ΔSPV (Figure 6.11F). This confirms that the model is generalizable across individual larvae, and the innate biases are responsible for the inter-individual variation.

Lastly, as part of our investigation, we also explored an alternative model where we introduced an innate bias at the motor level (Figure 6.12A). We estimated the bias values using the parameters estimated for the median population data in an attempt to simulate the SPV across the population and predict the variation in response asymmetry across individual larvae. Our simulations demonstrated that the alternative model resulted in behavioral asymmetry even before the optokinetic stimulus (Figure 6.12F), which contradicts our empirical observations. Moreover, while the alternative model could predict the relation between the innate bias and response asymmetry (Figures 6.12I; also see Figures 6.12B, C, E, F) as well as negative OKAN (Figures 6.12K; also see Figures 6.12D, G), it failed to replicate the compensation of behavioral asymmetry observed during symmetric stimulation (Figures 6.12H, J). Thus, the proposed model remains more consistent with our experimental findings.

6.7 Summary of results

OKN during bidirectional stimulation. Our mathematical model predicted OKN during bidirectional stimulation. Furthermore, the model predicted asymmetric bidirectional stimuli lead to OKN adaptation and elicit negative OKAN. Indeed, our experimental data confirmed this prediction. While, on average, the animals did not exhibit negative OKAN during darkness after symmetric stimulation, a stimulus with sufficient asymmetry elicited OKN adaptation and ensuing negative OKAN after the offset of the stimulus. Furthermore, we looked at the response of individual larvae across the population and observed some individual larvae demonstrate asymmetric response and negative OKAN even during

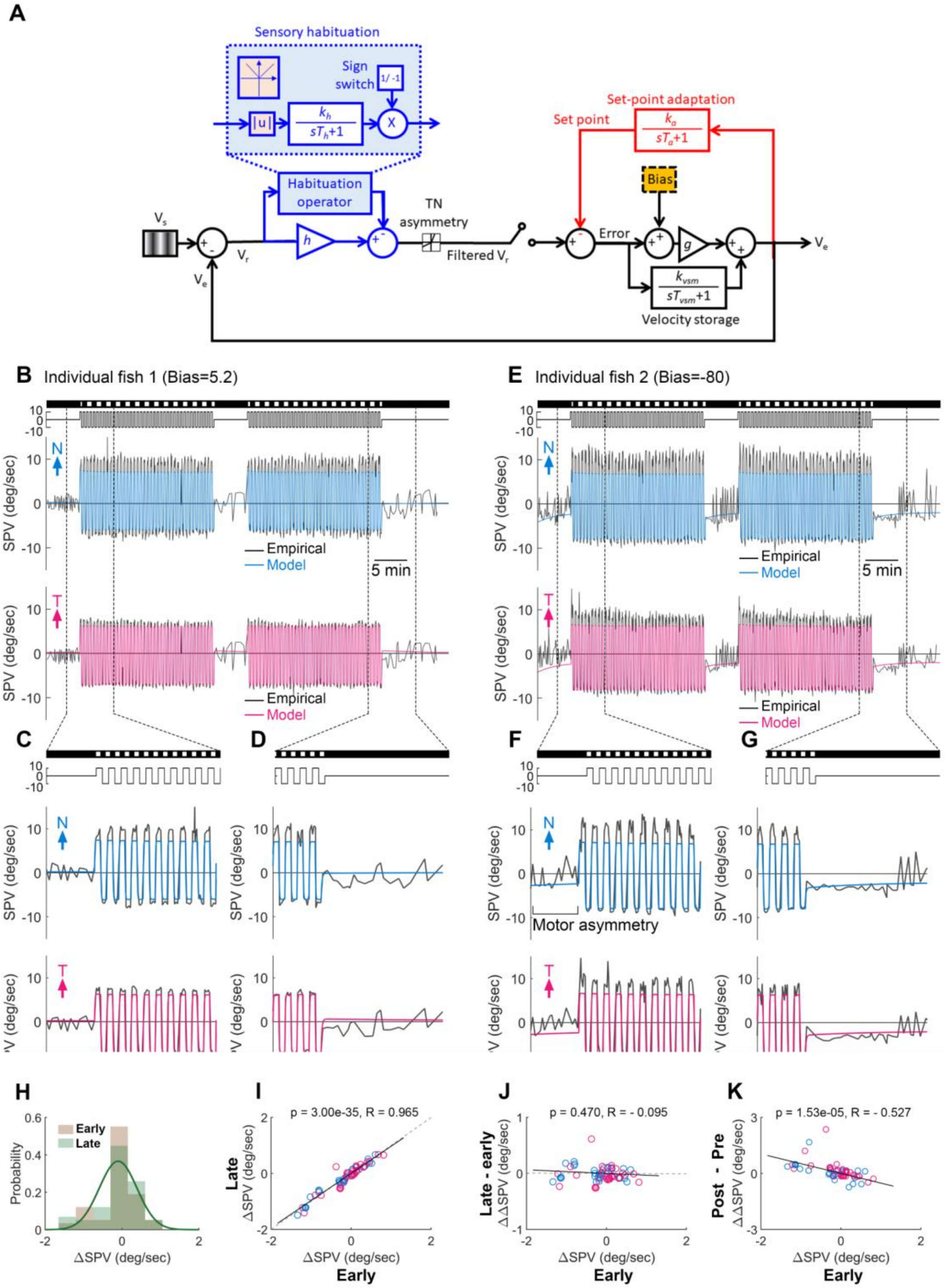

Figure 6.12. The mathematical model comprising an innate bias at motor level fails to predict observed SPV across the population and the inter-individual variations. Caption continued on the next page ¬

Figure 6.12. Caption continued: **(A)** A modified mathematical model similar to that in Figure 6.8, with a bias constant input at the motor level (yellow box). **(B-D)** Model prediction of the data from individual fish 1 (same as in Figures 6.6, 6.7, and 6.9). **(E-G)** Same as in (B-D) except the simulation were done for individual fish 2. For (B-G), "Pre", "Early", "Late", and "Post" are defined same as in Figure 6.6. The gray shadow represents the median absolute deviation obtained over the estimates for all individual larvae across the population. The stimulus and its image pattern are shown at the top. **(H)** The probability distribution of ΔSPV for 29 fish during the early and late periods is shown. Two lines indicate the fitting of the distributions with a Gaussian function. **(I)** The late ΔSPV plotted against the early ΔSPV. The slope of the solid line representing the linear regression close to 1; ($R=0.965$, $p=3.0\times10^{-35}$). **(J)** Changes in ΔSPV across stimulus phases (late ΔSPV – early ΔSPV, ΔΔSPV) plotted against the early ΔSPV. The correlation is not significant ($R=-0.095$, $p=0.470$). **(K)** Changes in the eye movements before and after OKN (post-ΔSPV – pre-ΔSPV, ΔΔSPV) plotted against the early ΔSPV ($R=-0.527$, $p=1.53\times10^{-5}$). Data from the individual larvae is depicted in as filled circles, and linear regression fit of the empirical data is represented by black solid lines. The plots align the first stimulus direction as positive, showing one eye with nasalward movement (blue trace) and the other with temporalward movement (red trace). "p" represents p-values, and "R" represents correlation coefficients obtained through Pearson correlation. Adapted from (Lin et al., 2022).

symmetric stimulation. We hypothesized this could be due to an innate bias in the oculomotor system. By including a bias constant in the model, our model predicted a bias in the oculomotor system would lead to an asymmetric response and negative OKAN, thereby confirming our hypothesis. Our results indicated that set-point adaptation serves to mitigate response asymmetry in larvae exhibiting innate bias.

7. GENERAL SUMMARY AND DISCUSSION

Growing evidence suggests that behavior and perception depend on the distributed and coordinated activity of neural populations within local (i.e., within a given brain area) and long-range (i.e., across different brain areas) networks. Multiunit recordings have provided insight into how neural populations' heterogeneity, spike time, correlations, intrinsic mechanisms, and internal states shape activity and sensory representation. On the other hand, functional imaging and anatomical studies have demonstrated the neural substrates and the integration of sensory information in distributed networks. These two approaches constitute different scales at which sensory systems are studied. The former studies neural ensemble in a brain region and its impact on local information processing, and the latter investigates how different brain regions coordinate activities to generate a behavioral outcome. Accordingly, the models used to understand our question of interest and make valid predictions should be adapted to the scales at which the sensory system is studied. In my thesis, we used a combination of data analysis and computational modeling at neural population and neural circuit levels to study how neural populations and circuits underlie behavior and perception.

The first question in this thesis was how self-motion information is encoded in neural populations in the central pathway. In chapter 3, we first investigated how vestibular-only (VO) neural populations responded to artificial and naturalistic head motion stimuli within the vestibular nuclei (VN). We considered neuronal dynamics and tuning properties and found that, despite displaying similar tuning during artificial and naturalistic stimuli, responses were highly heterogenous. Upon a closer look at the spike trains during naturalistic stimulation, we showed that neural responses varied significantly from one neuron to another but also from one trial to another trial for a given neuron. However, most of the heterogeneity in response to naturalistic stimuli was attributed to variability across neural responses in the population. During artificial stimuli, the neural activity was heterogenous, albeit to a lesser degree than the response during naturalistic stimuli, and was attributed to both variability across the population and trial-to-trial variability. Next, we characterized the correlation between the activity of VO neurons in VN by computing signal and noise correlations during artificial and naturalistic stimuli. We found that the correlation structure in VN was plastic. Specifically, while signal correlations during natural and artificial correlation were not significantly different than each other, noise correlations during naturalistic stimulation were significantly higher.

Additionally, we investigated the neural response of vestibular neurons in PIVC to naturalistic and vestibular stimuli. Our analysis revealed that neural activity was heterogenous during artificial and naturalistic stimuli, with response to the latter stimuli demonstrating more heterogeneity. Although both neural variability across the population and trial-to-trial variability contributed to the heterogeneity, most of the heterogeneity was associated with the former. Next, we characterized the correlation structure in the vestibular neural population in PIVC. While signal correlation during artificial stimuli on average was close to zero, during naturalistic stimulation, the signal correlation was positive and significantly higher than that of during artificial stimulation. Moreover, although noise correlations were significantly different during naturalistic and artificial stimulation, they were close to zero on average indicative of decorrelation in neural populations.

To understand the implications of correlations and heterogeneity observed in our dataset, in chapter 4, we used computational modeling that incorporated the known neurophysiological properties of vestibular neurons. Interestingly, the information decoded from the population activity depended on both heterogeneity and noise correlation. Our simulation revealed that in a homogenous population, the most information is obtained when the correlation structure maximizes signal correlation and minimizes the noise correlation. However, in a heterogeneous population, similar to the neural activity in the VN population, the decoded information was maximized when noise correlations were the highest and signal correlations were the lowest. Thus, our model demonstrated that both noise correlations and heterogeneity benefited population coding in VN during naturalistic stimulation. As such, our study, for the first time, showed that the population coding of natural self-motion in the early vestibular pathway is efficient and adapted to the statistics of the naturalistic stimuli.

In chapters 5 and 6, we investigate the optokinetic response (OKN) to prolonged stimulation. In chapter 5, we demonstrated that OKN adaptation and negative OKAN could robustly be elicited using prolonged unidirectional stimulation followed by a darkness period. Furthermore, we proposed a mathematical model that explained the observed negative OKAN at the circuit level. Specifically, we proposed a set-point adaptation mechanism that accounted for the manifestation of negative OKAN upon the offset of the stimulus. Additionally, the set-point adaptation was not sufficient to explain both OKN adaptation and negative OKAN. We included a habituation integrator in the model, which, together with the set-point adaptation mechanism, successfully explained both OKN adaptation and negative OKAN.

In chapter 6, we further investigated OKN and negative OKAN using bidirectional stimuli that resembled naturalistic stimuli more than that of unidirectional stimuli. Our empirical data showed that while the symmetric bidirectional stimulation did not elicit negative OKAN, a bidirectional stimulus by sufficiently large asymmetry was sufficient to induce OKN adaptation and negative OKAN. We adapted our proposed model to bidirectional stimuli and showed that our model successfully predicted the OKN adaptation and negative OKAN during and after the stimulation, respectively. Additionally, we observed that some individual fish exhibited asymmetric responses even during symmetric stimulation. Interestingly, the response became less asymmetric during the stimulation and then, upon the offset of the stimulus, manifested as negative OKAN. We hypothesized the asymmetric response was due to innate bias in the optokinetic system. When our model included an innate bias, it successfully explained the asymmetric OKN response, OKN adaptation, as well as the following negative OKAN. Together, this result highlighted the significance and physiological relevance of the set-point adaptation mechanism, which mitigates asymmetric response in individuals with innate OKN bias.

In addition to addressing the specific questions posited in the thesis, the results from this thesis provide important insights into several areas of research, medicine, and technology. Neuroscience models aid our understanding of the underlying mechanism of neurological and psychiatric disorders, which have important implications for treatments. Additionally, insights from these models contribute to the development of artificial neural networks and deep learning algorithms, which have implications in various artificial intelligence fields. Finally, understanding the brain at population and circuit levels helps us to gain insight into how the brain processes information, generates behavior, and perceives the world around us. Such insights are crucial for the development of brain-computer interfaces, which help individuals with paralysis and sensory and motor disabilities to interact with the world.

7.1. Population coding of self-motion in the central vestibular pathway

7.1.1. Stimulus-dependent noise correlations in VN neural populations: implications for coding

Our findings reveal distinct correlation structures within neural populations of VN when subjected to naturalistic versus artificial stimuli. Particularly, during naturalistic stimulation, positive noise correlations benefit information transmission by taking the diversity of responses among VN neurons into account. In contrast, artificial stimulation yields noise correlations that are, on average, close to zero and minimally affect information transmission. This aligns with the only previous investigation of population coding in ascending central vestibular pathway, which exclusively examined population coding using low-frequency artificial stimuli (Liu et al., 2013). Taken together, our findings firmly establish the stimulus-dependent nature of noise correlations among VN neural activities.

The effect of noise correlations on population coding in response to natural versus artificial stimuli has been explored across sensory systems, such as visual (Brackbill et al., 2020; Montijn et al., 2016; Simmons et al., 2013; Yoshida and Ohki, 2020), auditory (Heller et al., 2020; Mizrahi et al., 2014; Robin et al., 2013), somatosensory system (Bale et al., 2015), olfactory system (Iurilli and Datta, 2017), electrosensory systems (Metzen and Chacron, 2021; Wang and Chacron, 2021), and gustatory system (Levitan et al., 2019) (see (Averbeck et al., 2006; Hofmann and Chacron, 2018; Kohn et al., 2016; Moreno-Bote et al., 2014; Panzeri et al., 2022) for review). Unlike the distinct coding properties exhibited by individual neurons across different conditions, previous studies in these systems have demonstrated a general similarity in the distribution of noise correlations and their impact on population coding.

Particularly, noise correlations, on average, tend to be close to zero and have, at most, minimal effects on information transmission during naturalistic stimulation. Initially, these findings might seem contradictory to our current results, where we have established significant positive noise correlations during naturalistic self-motion stimulation led to improved information transmission. However, it is essential to note that the conditions under which these previous studies were conducted did not elicit fully natural forms of stimulation. For instance, in the case of the visual system, earlier investigations used stimuli that were natural with respect to spatial attributes but lacked natural temporal characteristics. This was due to the fact that sequences of natural images were introduced in a pseudorandom manner, with each image being displayed for a brief duration (100-200 ms) (Brackbill et al., 2020; Montijn et al., 2016; Yoshida and Ohki, 2020). Consequently, the temporal dynamics of the stimuli used were different from those encountered in everyday natural behaviors, which could account for the disparities between the findings of previous studies and our current results. Additionally, in the context of the auditory and electrosensory systems, the natural stimuli employed exhibited significantly higher frequency components compared to the natural self-motion stimuli used in our present study (ranging from 0 to 20 Hz) (refer to (Cullen, 2019) for an overview), which could potentially contribute to the observed differences. Further investigations are required to validate these hypotheses.

Furthermore, it is important to note that a distinctive feature of natural auditory and electrosensory stimuli, the time-varying amplitude or envelope that carries important information (Metzen and Chacron, 2019; Shannon et al., 1998), tends to contain significantly lower temporal frequencies (<100 Hz) (Fotowat et al., 2013; Heil, 2003), consistent with the temporal frequency range of natural self-motion stimuli. This leads us to speculate that similar results will be obtained when investigating population coding of natural sound envelopes within the ascending auditory and electrosensory pathways. Further studies are needed to test these predictions as our current understanding of natural envelope coding in the auditory and electrosensory systems is based on single-unit recordings (see, e.g., (Metzen and Chacron, 2019; Zhou and Wang, 2010)).

7.1.2. What is the origin of noise correlations amongst VN neurons during naturalistic vs. artificial stimulation?

Our findings indicate that noise correlations are significantly positive under naturalistic self-motion stimulation conditions but not during artificial stimulation. This raises an intriguing question: what accounts for the stimulus-dependent nature of noise correlations in the early vestibular pathways? Previous research has demonstrated that correlation magnitude is markedly affected by the nonlinearity in neural responses (de la Rocha et al., 2007). Therefore, a possible explanation is that the stimulus-dependent noise correlations emerge from response nonlinearities in VN neurons elicited differentially by naturalistic versus artificial stimuli. However, it is worth noting that naturalistic self-motion stimuli contain higher amplitudes when compared to their artificial counterparts (for a comprehensive overview, refer to (Cullen, 2019)) and, as a result, are expected to decrease the noise correlation rather than increase in during naturalistic. Consequently, the proposition that the observed stimulus-dependent noise correlation magnitude arises from response nonlinearities fails to explain our experimental findings.

An alternative explanation for the observed stimulus-dependence of noise correlations in the early vestibular pathways could be related to the neurons receiving differential synaptic input during naturalistic and artificial stimulation. It is conceivable that the balance between excitation and inhibition, a key factor in determining correlation magnitude (as detailed in (Doiron et al., 2016)), differs across these two stimulation conditions. Within this context, the elevated noise correlation magnitude during naturalistic stimulation might potentially arise from an increased level of excitation, attributed to a more effective activation of gap junctions among neighboring VN neurons (Beraneck et al., 2009; Condorelli et al., 2000), consequently promoting synchrony. However, the similarity in response dynamics exhibited by VN neurons in response to both artificial and naturalistic self-motion stimuli (Carriot et al., 2022; Mitchell et al., 2018) (Figure 3.4) suggests otherwise.

Alternatively, the differential synaptic input might arise from the activation of feedback from cortical areas onto VN neurons (Lopez and Blanke, 2011) during naturalistic stimulation. This alternate supposition is supported by recent findings that highlight the varying response dynamics of vestibular-sensitive neurons in the posterior ventral lateral

(VPL) area of the thalamus, which project to the cortex. These results indicate that these neurons display differential response dynamics to naturalistic and artificial self-motion stimuli (Carriot et al., 2022). Specifically, the activities of these neurons faithfully follow the time course of the naturalistic stimuli but not during artificial stimuli. Further investigations are required to gain a comprehensive understanding of the mechanisms underlying the changes in noise correlations within the neural populations of VN during naturalistic and artificial self-motion stimulation.

7.1.3. Coding of self-motion by VN and PIVC neural populations: implications for self-motion perception.

Besides the observed differences in noise correlation, our results revealed that neurons in VN exhibit heterogeneity in their spiking activity. Heterogeneity has been widely observed across systems and species (Hubel and Wiesel, 1962; Kilgard and Merzenich, 1999; Ringach et al., 2002; Staiger et al., 2004) and is thought to be beneficial tin information transmission (Berry Ii et al., 2019; Chelaru and Dragoi, 2008; Ecker et al., 2011; Marsat and Maler, 2010; Marsat and Pollack, 2010; Mejias and Longtin, 2012; Panzeri et al., 2015; Perez-Nieves et al., 2021a; Tripathy et al., 2013). Computational modeling studies have consistently demonstrated that heterogenous populations of neurons exhibit enhanced information transmission rates regardless of the correlation structure. This enhancement occurs in addition to the beneficial impact of positive noise correlations mentioned earlier. Hence, the increased noise correlations manifesting during naturalistic self-motion stimulation constitute an adaptation to the statistical characteristics of natural stimuli. This adaptation effectively increases information transmission by leveraging the combined effects of neuronal heterogeneity and increased noise correlations within the neural populations of the VN. Consequently, our results, for the first time, provide evidence that coding in the early vestibular pathway is adapted to the natural stimulus statistics through the synergistic interplay of heterogeneity and noise correlations contributing to increased information transmission.

We note that similar results were obtained in the rat whisker-barrel system (Adibi et al., 2013). Specifically, Adibi et al. (2013) recorded from pairs of neurons in the rat barrel cortex during sinusoidal stimulation of the whiskers. They employed three adaptor stimuli with increasing amplitude which correspondingly induced stronger adaptation in neural response. Notably, they observed that adaptation transferred the response state of the neurons to lower rates and higher noise correlations and Fano factor. Thus, following adaptation, noise correlations were significantly positive, and response heterogeneity was increased. Next, using a linear decoder to estimate the information in the population, they demonstrated that the overall information increased with adaptation. The authors attributed the increase in the information to the increase in single-neuron level information, outweighing the decrease in information due to redundant correlation structure. Nevertheless, we predict that the synergy between noise correlations and heterogeneity, at least in part, is responsible for the observed beneficial effect of positive noise correlation in population coding.

Previous studies have shown that noise correlations can increase information via several mechanisms (Adibi et al., 2013; Franke et al., 2016; Kohn et al., 2016; Metzen et al., 2015; Stefanini et al., 2020). For example, Stefanini et al. recorded simultaneously from tens of neurons in CA1 of the hippocampus in freely moving mice and estimated the animal's position from the neural population's activity (Stefanini et al., 2020). They showed that eliminating noise correlations in their data decreased information decoded from the population. Further analysis revealed that the CA1 population encodes multiple sensory variables other than the animal's position, which explains the noise variance, and as such, removing noise correlations removed information about other sensory variables from the data. We note that this is not the case in the VO neural populations of the VN. In rhesus macaques, these neurons only respond to vestibular stimuli as they lack both eye movement and neck proprioceptive sensitivity (Sadeghi et al., 2009), and as such, their response does not encode other sensory variables such as eye position or eye velocity. Additionally, consistent with previous studies (Cullen, 2012), our data (Figure 3.4) shows that vestibular neural populations exhibit similar dynamical properties in VN. This suggests that contrary to the hippocampus —in which the population coding is distributed, and multiple sensory variables are encoded in the population activity— the population coding in VN is not distributed as different neurons would not be encoding various degrees of head acceleration, velocity, and position. Our model employed neurons with similar dynamical tuning properties across the population and predicted increased information rate with noise correlation in heterogenous neural populations. As such, we further predict that the increase in the information is attributed to the plastic nature of the correlation structure and the observed heterogeneity in the population, as discussed above, rather than encoding multiple sensory variables.

Furthermore, Metzen et al. recorded simultaneously from the electrosensory lateral line lobe of electric fish and canal afferents of rhesus macaque during naturalistic stimuli (Metzen et al., 2015). This study revealed that the slow-frequency envelope of the stimulus was encoded by the magnitude of noise correlations, and single-neuron activity did not provide information about the envelope of the stimulus. A question arises regarding whether the increased information predicted by the model could be linked to the noise correlation carrying information about the envelope of the naturalistic stimulus. We note that decoding information by calculating the noise correlation coefficient involves nonlinear transformations. The decoder in our model, however, consisted only of linear transformations, and therefore, such information could not be decoded from the neural activity in the population in our simulations. Nevertheless, it does not rule out the possibility that noise correlation in VN carries information about the envelope of the naturalistic stimuli. Further investigation is needed to test this hypothesis. The data collection for the envelope encoding in the central vestibular pathway from VN, thalamus, and PIVC has begun in our lab, and conclusive results are pending further data collection and analysis.

VO neurons within the VN project directly to the VPL area of the thalamus (VPL) and are a key input to the posterior corticothalamic vestibular pathway (Marlinski and McCrea, 2009). As mentioned above, VPL neural activity faithfully follows the detailed timecourse of naturalistic but not artificial self-motion stimuli (Carriot et al., 2022). This finding implies that information transmitted about the stimulus' detailed timecourse by VN neural populations is likely decoded by target neurons in the VPL. Additionally, VPL neurons demonstrate gain control adaptation and decrease their gain in response to higher amplitude stimuli, such as during naturalistic stimulation (Carriot et al., 2022; Marlinski and McCrea, 2008a). Studies of population coding have shown that adaptation can increase (Adibi et al., 2013) or decrease (Gutnisky and Dragoi, 2008; Nigam et al., 2023) noise correlations which depend on the mechanism by which the adaptation occurs. For example, using a modeling study, Cortes et al. showed that spike-frequency adaptation would increase noise correlations, whereas adaptation in the form of short-term synaptic depression can increase the noise correlation (Cortes et al., 2012). However, recent studies suggest that gain control adaptation would lead to decorrelation (Duong et al., 2023a; Duong et al., 2023b), and as such, we predict that noise correlations decrease in the VPL thalamus. Further investigations are needed to investigate this hypothesis. The data collection to address this question has started in our lab, and so far, our preliminary data and analysis are consistent with the hypothesis (unpublished data).

Furthermore, neurons in VPL project to multiple cortical areas such as the parietoinsular vestibular cortex (PIVC), the ventral intraparietal cortex (VIP), area 2v of the intraparietal sulcus, and area 3a in the sulcus centralis (Akbarian et al., 1994; Dieterich et al., 2005; Lopez and Blanke, 2011; Matsuzaki et al., 2004). We recorded from PIVC pairs and demonstrated that neural activities are decorrelated in PIVC during both artificial and naturalistic stimuli, which is a signature of efficient coding. This is further supported by markedly decreased signal and noise correlation coefficient distribution in PIVC compared to VN during naturalistic stimulation (compare Figures 3.10 and 3.21 for signal correlations and Figures 3.13 and 3.24 for noise correlations). The correlation structure in PIVC becomes more homogenous compared to VN during naturalistic stimulation, and therefore, our model predicts neural population in PIVC benefits from the decorrelation. Furthermore, Benucci et al. recorded from the primary visual cortex of cats while many stimuli were presented over time across different orientations. When a biased stimulus was presented, they showed that the tuning of neurons in the V1 neural population adapts over time so that the activity of the population is equalized for all the neurons in the population (Benucci et al., 2013). Notably, for an unbiased stimulus, the tuning of the neurons in the population is homogenous; however, when the biased is introduced, the neural population becomes heterogeneous. Interestingly, noise correlations were not affected by the adaptation. Based on our experimental data from PIVC, we predict that PIVC neurons may employ a similar coding strategy to optimize coding. PIVC neurons share several features with V1, which supports this hypothesis: Firstly, PIVC neurons seem to adapt to stimulus amplitude. The dynamic tuning of the PIVC neurons was different during artificial and naturalistic stimulation; the response gain demonstrated high pass tuning during both artificial and naturalistic stimulation and was dramatically reduced during naturalistic stimulation compared to artificial stimulation. Secondly, the spiking activity of the neurons in PIVC is highly heterogenous during both artificial and naturalistic stimuli. Thirdly, noise correlations during artificial and naturalistic stimuli are close to zero and did not change significantly with the stimulus. As such, it is possible that PIVC neurons equalize their response over time by adapting to high amplitude stimulus. Nevertheless, the fact that neural activity in PIVC is decorrelated is a signature of efficient coding. Further studies are required to investigate adaptation and efficient coding in PIVC during naturalistic versus artificial self-motion.

Integration of vestibular with extra-vestibular information in both PIVC and VIP plays a key role in our perception of self-motion and spatial orientation (Brandt et al., 1994; Chen et al., 2013a; Penfield, 1957). It is possible that the extra-vestibular information synergistically shapes and alters intrinsic neural- and population-level properties such as the correlation structure and adaptation. Except for this study, there has been a lack of investigation into population coding related to natural self-motion within the PIVC, and no such investigations have been conducted within the VIP as these areas were studies mainly using artificial stimuli (Bremmer et al., 2002; Klam and Graf, 2003; Schlack et al., 2002; Shinder and Newlands, 2014). Further neurophysiological and behavioral studies are required to investigate efficient coding in PIVC and VIP. Specifically, suppose the increased vestibular information transmitted by VN is decoded in vestibular cortical areas. In that case, we expect to observe a decrease in perceptual detection (i.e., the minimum stimulus amplitude that can be detected) and discrimination (i.e., the minimum change in stimulus amplitude that can be detected) thresholds during naturalistic than during artificial self-motion stimulation. Further work is needed to test these predictions as all previous studies of vestibular perception have used artificial stimuli (see, e.g., (Grabherr et al., 2008; Mallery et al., 2010; Nesti et al., 2015; Nouri and Karmali, 2018; Valko et al., 2012))

7.1.4. Noise correlation and heterogeneity in VN: implications for population coding of vestibulo-ocular reflex

Besides VO neurons, position-vestibular-pause (PVP) neurons and eye-head (EH) neurons receive vestibular input and mediate vestibulo-occular reflex (VOR). In VN, PVP neurons are the primary premotor neurons driving VOR, while EH neurons contribute to the adaptation and calibration of VOR when the vestibular input does not match the visual input or following vestibular lesion (Boyden et al., 2004; Curthoys and Halmagyi, 1995). Previous studies have investigated the coding strategies employed by vestibular neurons in VN during artificial and naturalistic (Mackrous et al., 2020; Mitchell et al., 2018). One of the key findings in these studies was the role of variability in establishing coding strategies by single neurons. Specifically, neurons displaying high resting discharge heterogeneities demonstrated efficient coding via temporal whitening of their response. Neurons with low heterogeneity in their resting discharge did not whiten their response, rather, they faithfully represented the detailed time course of the stimuli. Faithfull and efficient coding was observed across a spectrum in each group of neurons; Interestingly, however, PVP neurons, on average, demonstrated less heterogeneity in the resting discharge and faithfully encoded stimuli which was essential for generating reliable compensatory VOR eye movements.

To the best of our knowledge, noise correlations have not been studied among eye-sensitive vestibular neurons in VN (i.e., PVP and EH neural populations). Our modeling study, however, predicts that if PVP neural populations efficiently encode natural stimuli, noise correlations would be required to be small as PVP neurons display lower response heterogeneities. This is consistent with previous modeling studies which characterized the VOR function using neural population (Hospedales et al., 2008) and cascade (Minor et al., 1999) models. On the other hand, it is possible that PVP neural populations exhibit significant noise correlations. Indeed, studies in areas involved in VOR display high levels of noise correlations manifested as excess synchrony (Dale and Cullen, 2015). Specifically, Dale and Cullen showed that neurons in nucleus propositus hypoglossi (NPH) exhibited excess synchrony when the animal fixated on a visual target positioned contralaterally. Similarly, they showed that abducens motoneuron displayed excess synchrony. Although gap junctions are unlikely to play a role in the manifestation of noise correlation in VO populations, they could potentially synchronize the activity of PVP neurons (Beraneck et al., 2009) as PVP neurons already employ differential coding strategy in single-neuron level as mentioned earlier. In this case, we speculate that PVP neural populations employ other encoding schemes, such as redundancy reduction, to efficiently encode eye movements during VOR.

We note that while VO neurons do not encode multiple sensory variables, PVP and EH neurons indeed encode oculomotor variables such as eye position and velocity during VOR and OKN. Specifically, PVP neurons encode head velocity and eye position, whereas EH neurons encode head and eye velocity. If noise correlations are significant in PVP and EH neural populations, it is possible that such neural populations benefit from noise correlations. For example, noise correlations, when the signal input is considered to be the activation of vestibular afferents, could arise from eye movements. Indeed, Dale and Cullen showed that noise correlation magnitude in NPH changed with the eye position, whereas it was relatively constant in abducens nuclei (Dale and Cullen, 2015). Likewise, it is possible that noise correlations would be affected by eye position or velocity in eye-sensitive vestibular populations in VN, providing an additional channel to transmit information about sensory variables (e.g., in this case, eye velocity and position). Further investigation is required to characterize the structure of noise correlation in PVP and EH neural populations in VN.

As mentioned above, VN receive feedback projections from PIVC and other cortical areas (Akbarian et al., 1994; Akbarian et al., 1993; Fukushima, 1997). It is generally assumed that these feedback projections terminate on VO neurons in VN as these neurons mediate and transmit information about self-motion (Akbarian et al., 1988; Akbarian et al., 1993; Chen et al., 2010; Chen et al., 2016). However, as illustrated in (Akbarian et al., 1993), all subnuclear structures in VN receive a diverse range of feedback projections from PIVC and other vestibular cortical areas. As such, although speculative, it is possible that PVP and EH neurons also receive vestibular feedback input from cortical areas. Feedback projections are key modulatory and driving projections (Bastos et al., 2012; Hupé et al., 1998) and have been shown to mediate efficient coding via attentional mechanism (Cohen and Maunsell, 2009; Cohen and Newsome, 2008; Ruff and Cohen, 2019; Srinath et al., 2021). As such, it is possible that feedback projections provide the VOR and OKN pathways with self-motion information. Alternatively, feedback projections could enhance information in PVP populations by reducing noise correlations (Cohen and Maunsell, 2009). Further studies are needed to address these questions. Specifically, this can be tested by recording from vestibular neurons in VN while deactivating the neural populations in cortical areas such as PIVC using chemical injections (e.g., muscimol injection (Chen et al., 2016)), cryoloops (Lomber, 1999), or optogenetic stimulation (Mattis et al., 2012) of the vestibular cortical areas. Modulation of neural activity in these conditions or lack thereof would demonstrate the relevance and functional role of feedback on vestibular neurons in VN.

7.2. Set-point adaptation underlies optokinetic response adaptation and negative optokinetic after nystagmus.

7.2.1. Velocity storage mechanism and negative optokinetic afternystagmus in larval zebrafish

Vestibular and optokinetic systems share common structures related to velocity storage mechanism (Demer and Robinson, 1983). In humans and nonhuman primates, positive optokinetic and post-rotatory after-nystagmus are ubiquitously observed following optokinetic and vestibular nystagmus, respectively, which arise from the velocity storage networks (Raphan et al., 1979; Ter Braak, 1936). Furthermore, following labyrinthectomy, positive OKAN is diminished (Ireland and Jell, 1982; Tomlinson et al., 1984). As such, the vestibular system plays a key role in the manifestation of positive OKAN. Accordingly, the lack of positive OKAN in larval zebrafish has been attributed to underdeveloped vestibular endorgans (Beck et al., 2004; Lambert et al., 2008). Another explanation for the lack of positive OKAN in larval zebrafish is provided by Chen et al., which demonstrated that the neural substrates underlying velocity-to-position integrator are not fully developed (Chen et al., 2014a). Consequently, the position signals decay quickly to zero, thereby not exhibiting positive OKAN.

Our experimental data and predictions from the proposed mathematical model provide a new perspective consistent with the explanations above. Notably, following the offset of the stimulus, a build-up phase is evident as the negative OKAN manifests (Figures 5.2B, C). We hypothesized this arose due to the presence of, at least partially developed, velocity storage mechanism. Our mathematical model incorporating a velocity storage mechanism predicted an eye velocity decay to zero with a time constant that is less than one minute following the offset of the stimulus (Figure 5.6D). If the velocity storage was not present in them model, the eye velocity would fall to zero immediately following the offset of the stimulus in the partial model. When the set-point adaptation integrator is added to the partial model, the decay in the velocity storage model, together with the output of the integrator, constitutes the build-up phase observed in the data. As such, based on experimental data, our mathematical model suggests that the velocity storage mechanism is present in 5pdf larval zebrafish.

7.2.2 Larval zebrafish as a novel model to study negative OKAN

We argue that larval zebrafish is an ideal model for studying negative OKAN as it takes advantage of the absence of masking mechanisms observed across species. Notably, one such mechanism is the smooth pursuit afternystagmus mechanism (Lisberger et al., 1981; Marti et al., 2005; Muratore and Zee, 1979) which manifests following tracking of a moving target in human and nonhuman primates and obscures the negative OKAN (Lin et al., 2018). Interestingly, following labyrinthectomy, human subjects rarely exhibit positive OKAN, and the offset of the stimulus is often followed by negative OKAN (Zee et al., 1976). Moreover, contrary to human and nonhuman primates, afoveate animals do not exhibit pursuit after nystagmus; however, even after brief optokinetic stimulation can induce positive OKAN (Evinger and Fuchs, 1978; Stahl, 2004), which dominates the negative OKAN. Larval zebrafish, on the other hand, do not exhibit pursuit afternystagmus and rarely manifest positive OKAN which becomes obsecured as the animal ages (Huang and Neuhauss, 2008a). As such, larval zebrafish are suitable for eliciting robust negative OKAN and studying its dynamics. Based on our data, the time constant of negative OKAN increases with stimulus presentation, which suggests that motor learning and adaptation occur in multiple timescales. Our results are consistent with a recent investigation on set-point adaption in the vestibular system, where more than one timescale was used in the mathematical model to account for optokinetic adaptation and its post-rotatory aftereffect (Jareonsettasin et al., 2016).

7.2.3 Negative OKAN demonstrates a set-point adaptation in the optokinetic system

Based on our experimental data, we proposed that a set-point adaptation mechanism underlies OKN adaptation during optokinetic stimulation and negative OKAN after stimulus removal. Specifically, the retinal image slip during unidirectional stimulation produces sustained nystagmus, which shifts the null position to a value above zero (in the direction of the stimulus). An adaptive process is manifested to mitigate the shift in the null positions. Upon the removal of the adaptive stimulus, an aftereffect emerges, characterized by slow phases moving in the opposite direction, thereby revealing the preceding adaptation.

Our model is the first to apply set-point adaptation of retinal slip velocity to explain OKN adaptation and negative OKAN. Leigh et al. previously suggested that negative OKAN arises from an adaptive mechanism similar to set-point adaptation (Leigh et al., 1981). Nevertheless, a significant aspect of optokinetic set-point adaptation —specifically, the reduction in slow-phase velocities during sustained OKN— has not been previously addressed, except for a recent study in zebrafish larvae (Pérez-Schuster et al., 2016). We speculate that the decrease in OKN gain has not been observed in rodent or primate models due to cerebellar learning behavior, which instead would increase the OKN gain during sustained optokinetic stimulation (Inoshita and Hirano, 2018; Wada et al., 2014). Conversely, zebrafish larvae do not exhibit a gain-increase adaptation during OKN, rendering them a suitable model to investigate the set-point adaptation hypothesis for negative OKAN.

We note that our model with only set-point adaptation mechanism predicted the negative OKAN and the decrease in OKN gain; however, it did not accurately predict the amplitude of OKN and timescales at which OKN gain decreased (Figure 5.6C). Therefore, we introduced a sensory habituation mechanism in addition to the set-point adaptation during optokinetic stimulation. This additional mechanism modulates sensitivity to sustained optokinetic stimuli over time (Figure 5.6D) and is well supported by neurophysiological data from retinal ganglion cells in larval zebrafish, which illustrate a reduced response to visual stimuli over time (Pérez-Schuster et al., 2016). In our conceptual framework, sustained optokinetic stimulation reduces the sensitivity at the initial stage (for instance, within the retina) before the signal is propagated downstream areas. Altogether, our empirical data and the results of model simulations suggest that set-point adaptation and sensory habituation collectively contribute to the reduction in SPV during OKN. However, it is important to emphasize that mainly set-point adaptation contributes to the generation of negative OKAN. The precise implementation of these dual mechanisms at the circuit level remains a topic of future investigation.

7.2.4 Set-point adaptation emerges from temporal integration of visual experience

It is not common for zebrafish larvae to consistently turn themselves in a manner that perceives rotation consistently in the same direction, except in pathological conditions. Naturally, as the animal navigates in the environment, it turns in either direction so that over large timescales, the animal's movement is not biased toward one direction (Dunn et al., 2016; Le Goc et al., 2021). As such, the brain is expected to be capable of adjusting set-point amid dynamic visual conditions. This would enable the brain to extract and approximate the net sensory asymmetry over an extended temporal span. Our findings indeed demonstrated that direction-alternating stimulation can elicit OKAN by temporally integrating a set-point adaptation signal. This revelation highlights the distinct attributes of set-point adaptation and the subsequent emergence of negative OKAN, setting them apart from velocity storage mechanisms (VSM) and the resulting positive OKAN (Waespe and Henn, 1978; Waespe et al., 1978; Waespe and Wolfensberger, 1985).

7.2.5 An innate bias in the oculomotor system may lead to asymmetric OKN and negative OKAN

As mentioned above, the exploratory behavior of the animal displays a symmetric distribution of right and left turning angles. Since the visual experience of the animal is generally symmetric, we asked what the physiological and functional implications of the underlying set-point adaptation mechanism are. We found that while most animals in the population displayed symmetric or near symmetric behavior before, during, and after stimulation, some induvial larvae demonstrated asymmetric behavior during similar stimulation protocol and exhibited negative OKAN following the offset of the stimulus (Figures 6.9A-G). We note that individuals with manifest latent nystagmus (MLN) and those affected by infantile nystagmus syndrome (INS) (Fatima et al., 2001) and even the zebrafish INS models known as belladonna strain (Huang and Neuhauss, 2008b; Huber-Reggi et al., 2012) exhibit similar response asymmetry and negative OKAN observed in individual larvae with the asymmetric response.

We modified the model by including a constant "innate" directional bias factor in the mathematical model incorporating sensory habituation and set-point adaptation. Indeed, the modified model predicted the response asymmetry and the subsequent negative OKAN across larvae in the dataset (Figure 6.9), which correlated with the magnitude of the innate bias constant. Importantly, the model also predicted mitigated OKN asymmetry over the stimulation period and reproduced the results obtained from empirical data (Figures 6.9G-J and Figures 6.10C-F). As such, set-point adaption serves to mitigate response asymmetry observed in individuals with an innate bias.

The animals used in the study were wild-type and did not carry artificial factors that would cause behavioral asymmetry. Thus, a question arises as to how innate bias might emerge in the oculomotor systems of the induvial animals. During developmental stages, coarse neural wiring and fine-tuning remain in effect via molecular guidance and experience, respectively (Cline, 2003). It is possible that before undergoing experience-dependent fine-tuning, inherent structural and functional asymmetry could spontaneously emerge as a result of natural stochastic processes. In fact, the occurrence of unintended developmental asymmetry during the initial stages of development is quite common. For instance, during the embryonic stage of zebrafish development, the initial formation of somites frequently exhibits differences in length and positioning between the left and right sides. After, as the process advances to the fine-tuning stage, this initial asymmetry can be rectified through molecular signaling mechanisms that respond to surface tension (Naganathan et al., 2022). It is likely that the set-point adaptation mechanism plays a similar role in fine-tuning the optokinetic system aiming to attain equilibrium through symmetric visual experience. Innate bias can further emerge from unilateral or asymmetric physical conditions associated with injuries and medical conditions.

Similar mechanisms have been suggested to exist in the vestibular system. Vestibular signals from both endorgans are constantly compared for estimation of head rotation on the horizontal plane, and an imbalance in the vestibular signals from both sides due to unilateral stimulation or vestibular loss can lead to a behavioral asymmetry, namely the vestibular nystagmus (Fetter and Zee, 1988; Fetter et al., 1988). It has been suggested that the recovery process involves set-point adaptation (Jareonsettasin et al., 2016). In this study, we used a similar mathematical model to simulation the adaptation process under optokinetic asymmetry (Jareonsettasin et al., 2016; Leigh et al., 1981; Zee et al., 2017), and our results extend the prediction of the model to explain experimental findings.

7.2.6 Multiple underlying mechanisms of set-point adaptation in the oculomotor system

In addition to behavioral aspects of optokinetic set-point adaptation, numerous studies have employed molecular markers and neurophysiological recordings to address its underlying mechanisms. These findings have identified the brain areas involved in set-point adaptation suggesting the process involves multiple stages. Wu et al. identified direction-selective neurons in larval zebrafish brains using imaging studies and, in combination with optogenetic techniques, demonstrated that direction-selective neurons in pretectal areas are crucial for the manifestation of negative OKAN following OKN (Wu et al., 2020a). Additionally, multiple studies have demonstrated that unidirectional stimulation alters the molecular expression profile of the floccular Purkinje cells involved in neural plasticity (Barmack and Qian, 2002; Barmack et al., 2010; Qian et al., 2012). It is possible that similar molecular signaling cascades could be responsible for adjusting the dynamic calibration process within oculomotor control.

Negative OKAN has been previously identified and studied in the vestibular system (Waespe and Henn, 1977, 1978). Such studies may be insightful in understanding the underlying mechanisms involved in optokinetic set-point adaptation. To investigate the long-term vestibular imbalance and the ensuing recovery of the vestibular functions, many studies have used unilateral labyrinthectomy (Darlington and Smith, 2000) to study the plasticity in VN (Johnston et al., 2001; Lim et al., 2010; Nelson et al., 2017; Vibert et al., 2000). Interestingly, while the ipsilateral VN neurons exhibited increased excitability following the labyrinthectomy within the first 24 hours, their activity returned to baseline levels as behavioral restoration remained intact (Nelson et al., 2017). This suggests that besides plasticity in VN, additional mechanisms are involved in the restoration of vestibular functions. Further studies are required for a comprehensive understanding of mechanisms underlying set-point adaptation. As larval zebrafish allow whole-brain imaging and screening neural activity in large functional networks, it provides a unique opportunity to study dynamic set-point adaptation mechanistically.

7.3. Efficient population coding in optokinetic system

7.3.1. Implications of population coding of self-motion perception in optokinetic system

The stabilization of gaze in orbit during natural behavior involves the coordination of two complementary reflexes, VOR and OKN, which stabilize gaze in space. VOR reflex is driven by the mechanics of semicircular canals and otolith endorgans as well as the afferents innervating them and, thus, has high-pass tuning properties with a corner frequency of 0.02 to 0.05 Hz in primates (Fernandez and Goldberg, 1971). As such, VOR gain is very close to unity in high frequencies (f>0.1 Hz)(Huterer and Cullen, 2002) and drops below unity (down to 0.5 in darkness) for lower frequencies. OKN complements VOR by compensating for the decrease in gain for low frequencies (f<0.1 Hz) to increase its dynamical range and stabilize the retinal image in response to the motion of the large visual fields. OKN gain is near unity for stimulus velocities less than 40 to 60 deg/s in primates and decreases with higher velocity stimuli (Cohen et al., 1977).

Although the population coding OKN in subcortical neural substrates is not studied, it is possible to make predictions based on the data from VO neural populations in VN. As OKN mainly tracks low-frequency stimuli during whole field motion (f<0.1Hz), the timescale in which such computations are performed should be large (i.e., t>10s), and therefore, we predict that during OKN, eye-sensitive neurons in VN encode the optokinetic information on large timescales. Additionally, our data from VN suggests that noise correlation on a large timescale might be substantial (See Figures 3.11 and 3.12). Even for the pairs whose noise correlation is negligible in low timescales (e.g., t<500 ms), correlations can be large at timescales greater than 1 second. That is because by increasing the timescale, the integral bellow the residual cross-correlation function extends over larger ranges. Therefore, even if the noise correlations in PVP or EH neural populations are negligible, due to the large timescale at which OKN functions, the noise correlations might be substantial. Additionally, the abducens premotor neurons send command signals to extraocular muscles to accurately track the stimulus during slow phases and thus should be able to reconstruct the detailed time course of the stimulus (Mackrous et al., 2020). However, since PVP neural populations, on average, exhibit less heterogeneity compared to EH neurons, the population coding of optokinetic stimuli may be less efficient when compared to population coding in EH neural populations. Further investigation is required to test these hypotheses by recording from PVP and EH neural populations during optokinetic stimulation.

7.3.2 Optokinetic response adaptation: implications for efficient coding in optokinetic system

Our experimental data from larval zebrafish showed that the optokinetic response gain gradually decreases overtime and reaches a steady state gain. A question then arises as to whether such adaptation affects population coding in the optokinetic system. Indeed, previous studies have shown adaptation benefits population coding regardless of its effect on noise correlations (Adibi et al., 2013; Benucci et al., 2013; Gutnisky and Dragoi, 2008). As such, it is important to investigate the neural substrates at which adaptation appears as well as its effect on heterogeneity and correlation structure. For example, Gutnisky and Dragoi showed that efficient coding of the V1 following the adaptation was achieved by a decrease in mean and variability of noise correlation. Adibi et al. reported increased noise correlation and increased information with adaptation. Benucci et al. observed that mean noise correlation did not change in the population; instead, adaptation mediated efficient coding by introducing heterogeneity in response to biased stimuli. These results suggest that population coding of optokinetic sensory variables is likely to benefit from such adaptation.

However, one needs to investigate population coding across optokinetic neural pathways and characterize single neurons and population-level attributes (e.g., heterogeneity, adaptation, correlation structure, decoding) to arrive at definitive conclusions.

7.3.3 Population coding in VN provides insight into understanding the velocity storage mechanism and its implications in the optokinetic system

As mentioned above, vestibular and optokinetic systems share a common premotor and velocity storage structure which includes VN, NPH, and abducens nuclei (Cullen et al., 2009; Demer and Robinson, 1983; Mustari et al., 1994). As such, the study of the vestibular system is beneficial in understanding how optokinetic stimuli are encoded. For example, the VO neurons studied in this thesis are crucial elements of the velocity storage mechanism (Yakushin et al., 2017), and as such, understanding how populations of VO neurons contribute to velocity storage would be beneficial in the study of velocity storage mechanism in the optokinetic system (Demer and Robinson, 1983). Indeed, population coding in the optokinetic system, at least to some degree, has been studied by characterizing correlation structure in NPH and abducens nuclei, as the optokinetic system shares such structures (Dale and Cullen, 2015), as mentioned previously.

We add that understanding the velocity storage mechanism in neural populations further requires investigating population coding in PVP and EH neural populations. A previous study provides evidence that plasticity in the velocity storage mechanism is mediated by floccular target neurons (FTN), a subset of EH neurons that receive projections for flocculus (Blazquez et al., 2007). Additionally, previous studies have shown that adaptation during VOR can be implemented using the cerebellar pathway (floccular projections from the cerebellum), or it can be due to the plasticity in projections to PVP neurons in VN (Beraneck and Cullen, 2007; Mitchell et al., 2016). It is likely that similar mechanisms, at least in part, are involved in the adaptation of OKN during prolonged stimulation. Future studies are required to test this hypothesis.

7.4 Future directions

7.4.1. Population-wide coverability: exploring beyond pairwise correlation

In the study of population coding, we characterized the correlations in the population by measuring the correlation between two neurons, referred to as pairwise correlations. However, in practice, neural populations and correlation structures extend beyond two neurons and their pairwise correlations. A critical question is how well pairwise correlations represent the correlation structure with higher-order correlations. Schneidmann et al., Investigated this question by measuring the weak pairwise correlations in the retina of salamanders and demonstrated that strongly correlated networks could be predicted by models that only captured pairwise correlations and ignored higher-order correlations (Schneidman et al., 2006). As such, it is possible the infer the consequences of correlations in neural populations without the need to record simultaneously from large populations and calculate higher-order correlations, which grow exponentially with the number of neurons in the population. Indeed, in this study, recording from more than two neurons in VN proved to be difficult as VN was located in deep subcortical structures and possessed a nuclear structure rather than a layered one. Moreover, recording from PIVC yielded more neurons and more simultaneously recorded cells compared to VN despite being a deep cortical structure; however, likewise, we were not able to record from a large number of neurons simultaneously.

In a recent study, Umakantha et al. established a mathematical and empirical relation between pairwise correlations and population metrics and applied it to data from large populations of V4 neurons in macaques and mice (Umakantha et al., 2021). They reported that attentional states could be predicted from pairwise correlations and reduced population metrics using dimensionality reduction. Importantly, however, when they considered population-wide covariability—which extended beyond pairwise correlations—they observed a change in pairwise correlation that could be explained by multiple ways the covariance matrix changed. For example, in their dataset, they observed that attention decreased mean pairwise correlations. However, in some cases, this corresponded with a somewhat uniform decrease in pairwise correlations, and hence, being decorrelated. In another case, this corresponded with the strength of pairwise correlations becoming stronger. Finally, in the third case, different subsets of neurons exhibited independent or a mix of changes mentioned above. They concluded although reducing the dimensionality of neural activity and correlations may preserve the main state of the population activity, it may fail to reflect the mechanism by which such states are manifested. In our dataset, we could not investigate the covariance matrix in large populations as our dataset mainly consisted of pairwise correlations. However, with the advent of high-density probes for deep brain structures, it will be possible to look beyond pairwise correlations to gain further insight into population activities.

7.4.2. Naturalistic stimulus: a reduced form of complex natural stimuli

In the study of population coding, we used naturalistic stimuli which were obtained from the horizontal yaw rotation of naturally behaving macaques. We note, however, that natural stimuli also consist of animal's movement in other dimensions (rotations in the pitch and roll axes as well as translations along all three axes) (Carriot et al., 2017a; Carriot et al., 2017b; Carriot et al., 2013b). Carriot et al. investigated neural coding in convergent VO neurons in VN that received both canal and otolith input (Carriot et al., 2015). By applying passive rotation and translation stimuli in isolation and in combination, they demonstrated the response of convergent VO neurons to the combined stimuli was nonlinear and sub-additive and did not follow the principle of superposition. Such nonlinearities and multivariate responses can have important implications in neural coding (Angelaki et al., 2009; Cullen, 2012; de la Rocha et al., 2007; Gu et al., 2008; Oude Lohuis et al., 2022). Our dataset mainly consisted of neurons that did not exhibit convergence. However, it did not address the relevance of convergence in natural self-motion perception. It is important to investigate population coding in VN using multidimensional natural stimuli as the perception of self-motion and reflexes generally involve the integration of information from multiple vestibular endorgans.

7.4.3. Natural optokinetic stimuli are more complex than unidirectional and bidirectional optokinetic stimuli used in the study

In our study of the optokinetic system in larval zebrafish, we demonstrated the presence of a refined sensory adaptation mechanism within the optokinetic system aimed at mitigating the inherent neurobehavioral asymmetry. Nevertheless, it is important to note that the alternating duration of stimuli in the natural environment is dynamic and averages around 6 seconds (Dunn et al., 2016), a pattern not perfectly replicated by our optokinetic stimulus paradigm. Additionally, we delivered a relatively robust visual stimulus—characterized by high contrast and stimulus velocity—over a relatively short recording period of one hour. To stimulate the natural conditions more accurately, it might be beneficial to conduct experiments with milder stimuli, albeit over extended recording times, or through repeated exposures. This approach could potentially elicit a more prolonged adaptation response. While our current experimental procedure effectively demonstrates the role of set-point adaptation as an internal calibration mechanism for oculomotor imbalance in zebrafish, a comprehensive understanding of its significance in neural development necessitates further investigation is required on cross-age comparisons of innate biases in zebrafish raised within relatively natural environments.

7.5 Conclusion

This thesis provides insights into the efficient coding of natural self-motion information in the central vestibular pathway. It signifies the role of correlations, heterogeneity, and their synergy in shaping efficient population codes. Additionally, this thesis provides insights into mechanisms underlying the observed adaption in the optokinetic system and the ensuing aftereffect. It also highlights the functional role of the observed adaptation in mitigating inherent and developmental deficits in the optokinetic system. As both vestibular and optokinetic systems are highly preserved across species and share similarities with other sensory systems, the results obtained here will be applicable in the study of other sensory systems and species.

8. References

Abbott, L.F., and Dayan, P. (1999). The Effect of Correlated Variability on the Accuracy of a Population Code. Neural Computation 11, 91-101.

Adibi, M., McDonald, J.S., Clifford, C.W., and Arabzadeh, E. (2013). Adaptation improves neural coding efficiency despite increasing correlations in variability. J Neurosci 33, 2108-2120.

Adibi, M., McDonald, J.S., Clifford, C.W., and Arabzadeh, E. (2014). Population decoding in rat barrel cortex: optimizing the linear readout of correlated population responses. PLoS Comput Biol 10, e1003415.

Akbarian, S., Berndl, K., Grusser, O.J., Guldin, W., Pause, M., and Schreiter, U. (1988). Responses of single neurons in the parietoinsular vestibular cortex of primates. Ann N Y Acad Sci 545, 187-202.

Akbarian, S., Grusser, O.J., and Guldin, W.O. (1994). Corticofugal connections between the cerebral cortex and brainstem vestibular nuclei in the macaque monkey. J Comp Neurol 339, 421-437.

Akbarian, S., Grüsser, O.J., and Guldin, W.O. (1993). Corticofugal projections to the vestibular nuclei in squirrel monkeys: further evidence of multiple cortical vestibular fields. J Comp Neurol 332, 89-104.

Amin, N., Gastpar, M., and Theunissen, F.E. (2013). Selective and efficient neural coding of communication signals depends on early acoustic and social environment. PLoS One 8, e61417.

Angelaki, D.E. (1998). Three-dimensional organization of otolith-ocular reflexes in rhesus monkeys. III. Responses To translation. J Neurophysiol 80, 680-695.

Angelaki, D.E., and Dickman, J.D. (2000). Spatiotemporal processing of linear acceleration: Primary afferent and central vestibular neuron responses. J Neurophysiol 84, 2113-2132.

Angelaki, D.E., Gu, Y., and DeAngelis, G.C. (2009). Multisensory integration: psychophysics, neurophysiology, and computation. Curr Opin Neurobiol 19, 452-458.

Arrenberg, A.B. (2016). Fiber optic-based photostimulation of larval zebrafish. Zebrafish: Methods and Protocols, 343-354.

Attias, H., and Schreiner, C.E. (1997). Low-order temporal statistics of natural sounds. Advances in Neural Information Processing Systems 9, 27-33.

Attneave, F. (1954). Some Informational Aspects of Visual Perception. Psychol Rev 61, 183-193.

Averbeck, B.B., Latham, P.E., and Pouget, A. (2006). Neural correlations, population coding and computation. Nat Rev Neurosci 7, 358-366.

Averbeck, B.B., and Lee, D. (2006). Effects of noise correlations on information encoding and decoding. J Neurophysiol 95, 3633-3644.

Bale, M.R., Ince, R.A., Santagata, G., and Petersen, R.S. (2015). Efficient population coding of naturalistic whisker motion in the ventro-posterior medial thalamus based on precise spike timing. Front Neural Circuits 9, 50.

Bannister, N.J., and Larkman, A.U. (1995a). Dendritic morphology of CA1 pyramidal neurones from the rat hippocampus: I. Branching patterns. Journal of Comparative Neurology 360, 150-160.

Bannister, N.J., and Larkman, A.U. (1995b). Dendritic morphology of CA1 pyramidal neurones from the rat hippocampus: II. Spine distributions. Journal of Comparative Neurology 360, 161-171.

Barlow, H.B. (1961). Possible principles underlying the transformation of sensory messages. In Sensory Communication, W. Rosenblith, ed. (MIT Press), pp. 217-234.

Barmack, N.H., and Qian, Z. (2002). Activity-dependent expression of calbindin in rabbit floccular Purkinje cells modulated by optokinetic stimulation. Neuroscience 113, 235-250.

Barmack, N.H., Qian, Z., and Yakhnitsa, V. (2010). Climbing fibers induce microRNA transcription in cerebellar Purkinje cells. Neuroscience 171, 655-665.

Bastian, A.J. (2008). Understanding sensorimotor adaptation and learning for rehabilitation. Curr Opin Neurol 21, 628-633.

Bastos, A.M., Usrey, W.M., Adams, R.A., Mangun, G.R., Fries, P., and Friston, K.J. (2012). Canonical microcircuits for predictive coding. Neuron 76, 695-711.

Beck, J.C., Gilland, E., Baker, R., and Tank, D.W. (2004). Instrumentation for measuring oculomotor performance and plasticity in larval organisms. Methods in Cell Biology 2004, 385-413.

Beitz, A.J., and Anderson, J.H. (1999). Neurochemistry of the vestibular system (CRC Press).

Benoit, C. (1924). Note sur une méthode de résolution des équations normales provenant de l'application de la méthode des moindres carrés à un système d'équations linéaires en nombre inférieur à celui des inconnues (Procédé du Commandant Cholesky). Bulletin géodésique 2, 67-77.

Benucci, A., Saleem, A.B., and Carandini, M. (2013). Adaptation maintains population homeostasis in primary visual cortex. Nature Neuroscience 16, 724-729.

Beraneck, M., and Cullen, K.E. (2007). Activity of vestibular nuclei neurons during vestibular and optokinetic stimulation in the alert mouse. J Neurophysiol 98, 1549-1565.

Beraneck, M., Uno, A., Vassias, I., Idoux, E., De Waele, C., Vidal, P.P., and Vibert, N. (2009). Evidence against a role of gap junctions in vestibular compensation. Neurosci Lett 450, 97-101.

Berry Ii, M.J., Lebois, F., Ziskind, A., and da Silveira, R.A. (2019). Functional Diversity in the Retina Improves the Population Code. Neural Computation 31, 270-311.

Bever, M.M., and Fekete, D.M. (2002). Atlas of the developing inner ear in zebrafish. Developmental dynamics: an official publication of the American Association of Anatomists 223, 536-543.

Bilotta, J., and Saszik, S. (2001). The zebrafish as a model visual system. International Journal of Developmental Neuroscience 19, 621-629.

Blazquez, P.M., Davis-Lopez de Carrizosa, M.A., Heiney, S.A., and Highstein, S.M. (2007). Neuronal substrates of motor learning in the velocity storage generated during optokinetic stimulation in the squirrel monkey. J Neurophysiol 97, 1114-1126.

Bollmann, J.H. (2019). The Zebrafish Visual System: From Circuits to Behavior. Annual Review of Vision Science 5, 269-293.

Boyden, E.S., Katoh, A., and Raymond, J.L. (2004). CEREBELLUM-DEPENDENT LEARNING: The Role of Multiple Plasticity Mechanisms. Annual Review of Neuroscience 27, 581-609.

Brackbill, N., Rhoades, C., Kling, A., Shah, N.P., Sher, A., Litke, A.M., and Chichilnisky, E.J. (2020). Reconstruction of natural images from responses of primate retinal ganglion cells. eLife 9, e58516.

Brandt, T., Dichgans, J., and Büchele, W. (1974). Motion habituation: inverted self-motion perception and optokinetic after-nystagmus. Exp Brain Res 21, 337-352.

Brandt, T., Dieterich, M., and Danek, A. (1994). Vestibular cortex lesions affect the perception of verticality. Ann Neurol 35, 403-412.

Bremmer, F., Klam, F., Duhamel, J.R., Ben Hamed, S., and Graf, W. (2002). Visual-vestibular interactive responses in the macaque ventral intraparietal area (VIP). Eur J Neurosci 16, 1569-1586.

Brodal, A. (1984). The vestibular nuclei in the macaque monkey. Journal of Comparative Neurology 227, 252-266.

Busettini, C., Miles, F.A., and Schwarz, U. (1991). Ocular responses to translation and their dependence on viewing distance. II. Motion of the scene. J Neurophysiol 66, 865-878.

Büttner, U., Waespe, W., and Henn, V. (1976). Duration and direction of optokinetic after-nystagmus as a function of stimulus exposure time in the monkey. Archiv für Psychiatrie und Nervenkrankheiten 222, 281-291.

Cadieu, C.F., and Olshausen, B.A. (2012). Learning Intermediate-Level Representations of Form and Motion from Natural Movies. Neural Computation 24, 827-866.

Cahill, H., and Nathans, J. (2008). The optokinetic reflex as a tool for quantitative analyses of nervous system function in mice: application to genetic and drug-induced variation. PloS one 3, e2055.

Cannon, S.C., and Robinson, D.A. (1987). Loss of the neural integrator of the oculomotor system from brain stem lesions in monkey. J Neurophysiol 57, 1383-1409.

Carriot, J., Brooks, J.X., and Cullen, K.E. (2013a). Multimodal integration of self-motion cues in the vestibular system: active versus passive translations. J Neurosci 33, 19555-19566.

Carriot, J., Jamali, M., Brooks, J.X., and Cullen, K.E. (2015). Integration of canal and otolith inputs by central vestibular neurons is subadditive for both active and passive self-motion: implication for perception. J Neurosci 35, 3555-3565.

Carriot, J., Jamali, M., Chacron, M.J., and Cullen, K.E. (2014). Statistics of the vestibular input experienced during natural self-motion: implications for neural processing. J Neurosci 34, 8347-8357.

Carriot, J., Jamali, M., Chacron, M.J., and Cullen, K.E. (2017a). The statistics of the vestibular input experienced during natural self-motion differ between rodents and primates. J Physiol 595, 2751-2766.

Carriot, J., Jamali, M., Cullen, K.E., and Chacron, M.J. (2017b). Envelope statistics of self-motion signals experienced by human subjects during everyday activities: Implications for vestibular processing. PLoS One 12, e0178664.

Carriot, J., Jamali, M., Schneider, A.D., Chacron, M.J., and Cullen, K.E. (2013b). Natural statistics of the vestibular stimuli. In 2013 Neuroscience Meeting Planner S.f. Neuroscience, ed. (San Diego, CA).

Carriot, J., McAllister, G., Hooshangnejad, H., Mackrous, I., Cullen, K.E., and Chacron, M.J. (2022). Sensory adaptation mediates efficient and unambiguous encoding of natural stimuli by vestibular thalamocortical pathways. Nature communications 13, 2612.

Carruthers, I.M., Natan, R.G., and Geffen, M.N. (2013). Encoding of ultrasonic vocalizations in the auditory cortex. J Neurophysiol 109, 1912-1927.

Chacron, M.J., and Bastian, J. (2008). Population coding by electrosensory neurons. J Neurophysiol 99, 1825-1835.

Chelaru, M.I., and Dragoi, V. (2008). Efficient coding in heterogeneous neuronal populations. PNAS 105, 16344-16349.

Chelaru, M.I., and Dragoi, V. (2016). Negative Correlations in Visual Cortical Networks. Cereb Cortex 26, 246-256.

Chen, A., DeAngelis, G.C., and Angelaki, D.E. (2010). Macaque parieto-insular vestibular cortex: responses to self-motion and optic flow. J Neurosci 30, 3022-3042.

Chen, A., DeAngelis, G.C., and Angelaki, D.E. (2011). A comparison of vestibular spatiotemporal tuning in macaque parietoinsular vestibular cortex, ventral intraparietal area, and medial superior temporal area. J Neurosci 31, 3082-3094.

Chen, A., Deangelis, G.C., and Angelaki, D.E. (2013a). Functional specializations of the ventral intraparietal area for multisensory heading discrimination. J Neurosci 33, 3567-3581.

Chen, A., Gu, Y., Liu, S., DeAngelis, G.C., and Angelaki, D.E. (2016). Evidence for a Causal Contribution of Macaque Vestibular, But Not Intraparietal, Cortex to Heading Perception. J Neurosci 36, 3789-3798.

Chen, C.C., Bockisch, C.J., Bertolini, G., Olasagasti, I., Neuhauss, S.C., Weber, K.P., Straumann, D., and Ying-Yu Huang, M. (2014a). Velocity storage mechanism in zebrafish larvae. J Physiol 592, 203-214.

Chen, C.C., Bockisch, C.J., Bertolini, G., Olasagasti, I., Neuhauss, S.C.F., Weber, K.P., Straumann, D., and Ying-Yu Huang, M. (2014b). Velocity storage mechanism in zebrafish larvae. The Journal of physiology 592, 203-214.

Chen, X., Deangelis, G.C., and Angelaki, D.E. (2013b). Diverse spatial reference frames of vestibular signals in parietal cortex. Neuron 80, 1310-1321.

Cheron, G., Godaux, E., Laune, J.M., and Vanderkelen, B. (1986). Lesions in the cat prepositus complex: effects on the vestibulo-ocular reflex and saccades. The Journal of physiology 372, 75-94.

Chichilnisky, E.J. (2001). A simple white noise analysis of neuronal light responses. Network 12, 199-213.

Clifford, C.W., Webster, M.A., Stanley, G.B., Stocker, A.A., Kohn, A., Sharpee, T.O., and Schwartz, O. (2007). Visual adaptation: neural, psychological and computational aspects. Vision Res 47, 3125-3131.

Cline, H. (2003). Sperry and Hebb: oil and vinegar? Trends Neurosci 26, 655-661.

Cohen, B., Henn, V., Raphan, T., and Dennett, D. (1981). Velocity storage, nystagmus, and visual-vestibular interactions in humans. Annals of the New York Academy of Sciences 374, 421-433.

Cohen, B., Matsuo, V., and Raphan, T. (1977). Quantitative analysis of the velocity characteristics of optokinetic nystagmus and optokinetic after-nystagmus. The Journal of physiology 270, 321-344.

Cohen, M.R., and Kohn, A. (2011). Measuring and interpreting neuronal correlations. Nature Neuroscience 14, 811-819.

Cohen, M.R., and Maunsell, J.H. (2009). Attention improves performance primarily by reducing interneuronal correlations. Nature Neuroscience 12, 1594-1600.

Cohen, M.R., and Newsome, W.T. (2008). Context-dependent changes in functional circuitry in visual area MT. Neuron 60, 162-173.

Condorelli, D.F., Belluardo, N., Trovato-Salinaro, A., and Mudò, G. (2000). Expression of Cx36 in mammalian neurons. Brain Research Reviews 32, 72-85.

Conrad, J., Baier, B., Eberle, L., Ruehl, R.M., Boegle, R., Zwergal, A., and Dieterich, M. (2023). Network Architecture of Verticality Processing in the Human Thalamus. Annals of Neurology.

Contini, D., Zampini, V., Tavazzani, E., Magistretti, J., Russo, G., Prigioni, I., and Masetto, S. (2012). Intercellular K+ accumulation depolarizes Type I vestibular hair cells and their associated afferent nerve calyx. Neuroscience 227, 232-246.

Cortes, J.M., Marinazzo, D., Series, P., Oram, M.W., Sejnowski, T.J., and van Rossum, M.C.W. (2012). The effect of neural adaptation on population coding accuracy. Journal of Computational Neuroscience 32, 387-402.

Crawford, J.D., Cadera, W., and Vilis, T. (1991). Generation of Torsional and Vertical Eye Position Signals by the Interstitial Nucleus of Cajal. Science 252, 1551-1553.

Cullen, K.E. (2011). The neural encoding of self-motion. Curr Opin Neurobiol 21, 587-595.

Cullen, K.E. (2012). The vestibular system: multimodal integration and encoding of self-motion for motor control. Trends Neurosci 35, 185-196.

Cullen, K.E. (2016). Chapter 2 - Physiology of central pathways. In Handbook of Clinical Neurology, J.M. Furman, and T. Lempert, eds. (Elsevier), pp. 17-40.

Cullen, K.E. (2019). Vestibular processing during natural self-motion: implications for perception and action. Nat Rev Neurosci 20, 346-363.

Cullen, K.E., Minor, L.B., Beraneck, M., and Sadeghi, S.G. (2009). Neural substrates underlying vestibular compensation: contribution of peripheral versus central processing. J Vestib Res 19, 171-182.

Cullen, K.E., and Taube, J.S. (2017). Our sense of direction: progress, controversies and challenges. Nature Neuroscience 20, 1465-1473.

Curthoys, I.S., Grant, J.W., Pastras, C.J., Fröhlich, L., and Brown, D.J. (2021). Similarities and Differences Between Vestibular and Cochlear Systems – A Review of Clinical and Physiological Evidence. Frontiers in neuroscience 15.

Curthoys, I.S., and Halmagyi, G.M. (1995). Vestibular compensation: a review of the oculomotor, neural, and clinical consequences of unilateral vestibular loss. J Vestib Res 5, 67-107.

Dale, A., Carriot, J., and Cullen, K.E. (2013). Neuronal ensemble coding in early vestibular pathways during self-motion Paper presented at: SFN conference abstracts

Dale, A., and Cullen, K.E. (2015). Local population synchrony and the encoding of eye position in the primate neural integrator. J Neurosci 35, 4287-4295.

Dale, A., and Cullen, K.E. (2019). The Ventral Posterior Lateral Thalamus Preferentially Encodes Externally Applied Versus Active Movement: Implications for Self-Motion Perception. Cereb Cortex 29, 305-318.

Dan, Y., Alonso, J.-M., Usrey, W.M., and Reid, R.C. (1998). Coding of visual information by precisely correlated spikes in the lateral geniculate nucleus. Nature Neurosci 1, 501-507.

Darlington, C.L., and Smith, P.F. (2000). Molecular mechanisms of recovery from vestibular damage in mammals: recent advances. Progress in neurobiology 62, 313-325.

de la Rocha, J., Doiron, B., Shea-Brown, E., Josic, K., and Reyes, A. (2007). Correlation between neural spike trains increases with firing rate. Nature 448, 802-806.

DeAngelis, G.C., and Angelaki, D.E. (2012). Frontiers in Neuroscience

Visual–Vestibular Integration for Self-Motion Perception. In The Neural Bases of Multisensory Processes, M.M. Murray, and M.T. Wallace, eds. (Boca Raton (FL): CRC Press/Taylor & Francis

Copyright © 2012 by Taylor & Francis Group, LLC.).

deCharms, R.C., and Merzenich, M.M. (1996). Primary cortical representation of sounds by the coordination of action-potential timing. Nature 381, 610-613.

Deecke, L., Schwarz, D.W., and Fredrickson, J.M. (1977). Vestibular responses in the rhesus monkey ventroposterior thalamus. II. Vestibulo-proprioceptive convergence at thalamic neurons. Exp Brain Res 30, 219-232.

Della-Maggiore, V., Landi, S.M., and Villalta, J.I. (2015). Sensorimotor adaptation: multiple forms of plasticity in motor circuits. The Neuroscientist 21, 109-125.

Demer, J.L., and Robinson, D.A. (1983). Different time constants for optokinetic and vestibular nystagmus with a single velocity-storage element. Brain Res 276, 173-177.

Desbordes, G., Jin, J., Weng, C., Lesica, N.A., Stanley, G.B., and Alonso, J.-M. (2008). Timing Precision in Population Coding of Natural Scenes in the Early Visual System. PLoS Biol 6, e324.

Dieterich, M., Bartenstein, P., Spiegel, S., Bense, S., Schwaiger, M., and Brandt, T. (2005). Thalamic infarctions cause side-specific suppression of vestibular cortex activations. Brain 128, 2052-2067.

Doiron, B., Litwin-Kumar, A., Rosenbaum, R., Ocker, G.K., and Josic, K. (2016). The mechanics of state-dependent neural correlations. Nat Neurosci 19, 383-393.

Downer, J.D., Niwa, M., and Sutter, M.L. (2015). Task engagement selectively modulates neural correlations in primary auditory cortex. J Neurosci 35, 7565-7574.

Dunn, T.W., Mu, Y., Narayan, S., Randlett, O., Naumann, E.A., Yang, C.-T., Schier, A.F., Freeman, J., Engert, F., and Ahrens, M.B. (2016). Brain-wide mapping of neural activity controlling zebrafish exploratory locomotion. eLife 5, e12741.

Duong, L., Lipshutz, D., Heeger, D., Chklovskii, D., and Simoncelli, E.P. (2023a). Adaptive Whitening in Neural Populations with Gain-modulating Interneurons.

Duong, L.R., Bredenberg, C., Heeger, D.J., and Simoncelli, E.P. (2023b). Adaptive coding efficiency in recurrent cortical circuits via gain control. arXiv preprint arXiv:230519869.

Eatock, R.A., and Songer, J.E. (2011). Vestibular hair cells and afferents: two channels for head motion signals. Annu Rev Neurosci 34, 501-534.

Ecker, A.S., Berens, P., Tolias, A.S., and Bethge, M. (2011). The effect of noise correlations in populations of diversely tuned neurons. J Neurosci 31, 14272-14283.

Escabí, M.A., Miller, L.M., Read, H.L., and Schreiner, C.E. (2003). Naturalistic auditory contrast improves spectrotemporal coding in the cat inferior colliculus. J Neurosci 23, 11489-11504.

Evinger, C., and Fuchs, A.F. (1978). Saccadic, smooth pursuit, and optokinetic eye movements of the trained cat. J Physiol 285, 209-229.

Fairhall, A.L., Lewen, G.D., Bialek, W., and de Ruyter van Steveninck, R.R. (2001). Efficiency and ambiguity in an adaptive neural code. Nature 412, 787-792.

Fatima, S.S., Christopher, M.H., and David, S.I.T. (2001). Spontaneous reversal of nystagmus in the dark. British Journal of Ophthalmology 85, 428.

Fernandez, C., and Goldberg, J.M. (1971). Physiology of peripheral neurons innervating semicircular canals of the squirrel monkey. II. Response to sinusoidal stimulation and dynamics of peripheral vestibular system. J Neurophysiol 34, 661-675.

Fernandez, C., Goldberg, J.M., and Abend, W.K. (1972). Response to static tilts of peripheral neurons innervating otolith organs of the squirrel monkey. J Neurophysiol 35, 978-987.

Fetter, M., and Zee, D.S. (1988). Recovery from unilateral labyrinthectomy in rhesus monkey. J Neurophysiol 59, 370-393.

Fetter, M., Zee, D.S., and Proctor, L.R. (1988). Effect of lack of vision and of occipital lobectomy upon recovery from unilateral labyrinthectomy in rhesus monkey. J Neurophysiol 59, 394-407.

Fotowat, H., Harrison, R.R., and Krahe, R. (2013). Statistics of the electrosensory input in the freely swimming weakly electric fish Apteronotus leptorhynchus. J Neurosci 33, 13758-13772.

Franke, F., Fiscella, M., Sevelev, M., Roska, B., Hierlemann, A., and da Silveira, R.A. (2016). Structures of Neural Correlation and How They Favor Coding. Neuron 89, 409-422.

Friedrich, R.W., Jacobson, G.A., and Zhu, P. (2010). Circuit neuroscience in zebrafish. Current Biology 20, R371-R381.

Fuchs, A.F., and Robinson, D.A. (1966). A method for measuring horizontal and vertical eye movement chronically in the monkey. J Appl Physiol 21, 1068-1070.

Fukushima, K. (1997). Corticovestibular interactions: anatomy, electrophysiology, and functional considerations. Exp Brain Res 117, 1-16.

Furman, J.M.R., Hain, T.C., and Paige, G.D. (1989). Central adaptation models of the vestibulo-ocular and optokinetic systems. Biological cybernetics 61, 255-264.

Furrow, R.E. (2019). Regression to the Mean in Pre–Post Testing: Using Simulations and Permutations to Develop Null Expectations. CBE—Life Sciences Education 18, le2.

Garcia-Lazaro, J.A., Ahmed, B., and Schnupp, J.W. (2006). Tuning to natural stimulus dynamics in primary auditory cortex. Curr Biol 16, 264-271.

Gdowski, G.T., and McCrea, R.A. (2000). Neck proprioceptive inputs to primate vestibular nucleus neurons. Exp Brain Res 135, 511-526.

Gervain, J., and Geffen, M.N. (2019). Efficient Neural Coding in Auditory and Speech Perception. Trends Neurosci 42, 56-65.

Ghanem, T.A., Breneman, K.D., Rabbitt, R.D., and Brown, H.M. (2008). Ionic composition of endolymph and perilymph in the inner ear of the oyster toadfish, Opsanus tau. Biol Bull 214, 83-90.

Gjorgjieva, J., Drion, G., and Marder, E. (2016). Computational implications of biophysical diversity and multiple timescales in neurons and synapses for circuit performance. Curr Opin Neurobiol 37, 44-52.

Glasauer, M.D.T.B.S. (2001). Modeling the Role of the Interstitial Nucleus of Cajal in Otolithic Control of Static Eye Position. Acta Oto-Laryngologica 121, 105-107.

Goldberg, J.M. (2000). Afferent Diversity and the Organisation of central vestibular pathways. Exp Brain Res 130, 277-297.

Goldberg, J.M., and Cullen, K.E. (2011). Vestibular control of the head: possible functions of the vestibulocollic reflex. Exp Brain Res 210, 331-345.

Goldberg, J.M., Wilson, V.J., Cullen, K.E., Angelaki, D.E., Broussard, D.M., Büttner-Ennever, J.A., Fukushima, K., and Minor, L.B. (2012a). 22Structure of the Vestibular Labyrinth. In The Vestibular System: A Sixth Sense, J.M. Goldberg, V.J. Wilson, K.E. Cullen, D.E. Angelaki, D.M. Broussard, J. Buttner-Ennever, K. Fukushima, and L.B. Minor, eds. (Oxford University Press), pp. 0.

Goldberg, J.M., Wilson, V.J., Cullen, K.E., Angelaki, D.E., Broussard, D.M., Büttner-Ennever, J.A., Fukushima, K., and Minor, L.B. (2012b). 136Neuroanatomy of Central Vestibular Pathways. In The Vestibular System: A Sixth Sense, J.M. Goldberg, V.J. Wilson, K.E. Cullen, D.E. Angelaki, D.M. Broussard, J. Buttner-Ennever, K. Fukushima, and L.B. Minor, eds. (Oxford University Press), pp. 0.

Goldberg, J.M., Wilson, V.J., Cullen, K.E., Angelaki, D.E., Broussard, D.M., Büttner-Ennever, J.A., Fukushima, K., and Minor, L.B. (2012c). Physiology of the Vestibular Organs. In The Vestibular System: A Sixth Sense, J.M. Goldberg, V.J. Wilson, K.E. Cullen, D.E. Angelaki, D.M. Broussard, J. Buttner-Ennever, K. Fukushima, and L.B. Minor, eds. (Oxford University Press), pp. 0.

Goldberg, J.M., Wilson, V.J., Cullen, K.E., Angelaki, D.E., Broussard, D.M., Büttner-Ennever, J.A., Fukushima, K., and Minor, L.B. (2012d). Vestibulo-Ocular Reflexes. In The Vestibular System: A Sixth Sense, J.M. Goldberg, V.J. Wilson, K.E. Cullen, D.E. Angelaki, D.M. Broussard, J. Buttner-Ennever, K. Fukushima, and L.B. Minor, eds. (Oxford University Press), pp. 0.

Grabherr, L., Nicoucar, K., Mast, F.W., and Merfeld, D.M. (2008). Vestibular thresholds for yaw rotation about an earth-vertical axis as a function of frequency. Exp Brain Res 186, 677-681.

Grusser, O.J., Pause, M., and Schreiter, U. (1990). Vestibular neurones in the parieto-insular cortex of monkeys (Macaca fascicularis): visual and neck receptor responses. J Physiol (lond) 430, 559-583.

Gu, Y., Angelaki, D.E., and Deangelis, G.C. (2008). Neural correlates of multisensory cue integration in macaque MSTd. Nature Neuroscience 11, 1201-1210.

Guldin, W.O., and Grüsser, O.J. (1998). Is there a vestibular cortex? Trends in Neurosciences 21, 254-259.

Gupta, D., Młynarski, W., Sumser, A., Symonova, O., Svatoň, J., and Joesch, M. (2023). Panoramic visual statistics shape retina-wide organization of receptive fields. Nature Neuroscience 26, 606-614.

Gutnisky, D.A., and Dragoi, V. (2008). Adaptive coding of visual information in neural populations. Nature 452, 220-224.

Haffter, P., Granato, M., Brand, M., Mullins, M.C., Hammerschmidt, M., Kane, D.A., Odenthal, J., JM van Eeden, F., Jiang, Y.-J., and Heisenberg, C.-P. (1996). The identification of genes with unique and essential functions in the development of the zebrafish, Danio rerio. Development 123, 1-36.

Haggard, M., and Chacron, M.J. (2023). Coding of object location by heterogeneous neural populations with spatially dependent correlations in weakly electric fish. PLoS Comp Biol 19, e1010938.

Hall, C.D., and Cox, L.C. (2009). The role of vestibular rehabilitation in the balance disorder patient. Otolaryngologic Clinics of North America 42, 161-169.

Heil, P. (2003). Coding of temporal onset envelope in the auditory system. Speech Communication 41, 123-134.

Heller, C.R., Schwartz, Z.P., Saderi, D., and David, S.V. (2020). Selective effects of arousal on population coding of natural sounds in auditory cortex. bioRxiv, 2020-2008.

Hernandez, E., and J, M.D. (2023). Neuroanatomy, Nucleus Vestibular. In StatPearls (Treasure Island (FL) ineligible companies. Disclosure: Joe M Das declares no relevant financial relationships with ineligible companies.).

Hitier, M., Besnard, S., and Smith, P.F. (2014). Vestibular pathways involved in cognition. Frontiers in Integrative Neuroscience 8.

Hofmann, V., and Chacron, M.J. (2018). Population Coding and Correlated Variability in Electrosensory Pathways. Front Integr Neurosci 12, 56.

Hong, S., Ratte, S., Prescott, S.A., and De Schutter, E. (2012). Single neuron firing properties impact correlation-based population coding. J Neurosci 32, 1413-1428.

Hospedales, T.M., van Rossum, M.C., Graham, B.P., and Dutia, M.B. (2008). Implications of noise and neural heterogeneity for vestibulo-ocular reflex fidelity. Neural Comput 20, 756-778.

Huang, C.G., Metzen, M.G., and Chacron, M.J. (2018). Feedback optimizes neural coding and perception of natural stimuli. Elife 7, e38935.

Huang, C.G., Zhang, Z.D., and Chacron, M.J. (2016). Temporal decorrelation by SK channels enables efficient neural coding and perception of natural stimuli. Nature communications 7, 11353.

Huang, Y.-Y., and Neuhauss, S.C. (2008a). The optokinetic response in zebrafish and its applications. Front Biosci 13, 1899-1916.

Huang, Y.Y., and Neuhauss, S.C. (2008b). The optokinetic response in zebrafish and its applications. Front Biosci 13, 1899-1916.

Hubel, D.H., and Wiesel, T.N. (1962). Receptive fields, binocular interaction and functional architecture in the cat's visual cortex. J Physiol (lond) 160, 106-154.

Huber-Reggi, P.S., Chien-Cheng, C., Lea, G., Dominik, S., Stephan, C.F.N., and Melody Ying-Yu, H. (2012). Severity of Infantile Nystagmus Syndrome-Like Ocular Motor Phenotype Is Linked to the Extent of the Underlying Optic Nerve Projection Defect in Zebrafish belladonna Mutant. The Journal of Neuroscience 32, 18079.

Hullar, T.E., Della Santina, C.C., Hirvonen, T., Lasker, D.M., Carey, J.P., and Minor, L.B. (2005). Responses of irregularly discharging chinchilla semicircular canal vestibular-nerve afferents during high-frequency head rotations. J Neurophysiol 93, 2777-2786.

Hunsberger, E., Scott, M., and Eliasmith, C. (2014). The competing benefits of noise and heterogeneity in neural coding. Neural Comput 26, 1600-1623.

Hupé, J.M., James, A.C., Payne, B.R., Lomber, S.G., Girard, P., and Bullier, J. (1998). Cortical feedback improves discrimination between figure and background by V1, V2 and V3 neurons. Nature 394, 784-787.

Huterer, M., and Cullen, K.E. (2002). Vestibuloocular reflex dynamics during high-frequency and high-acceleration rotations of the head on body in rhesus monkey. J Neurophysiol 88, 13-28.

Imagawa, M., Graf, W., Sato, H., Suwa, H., Isu, N., Izumi, R., and Uchino, Y. (1998). Morphology of single afferents of the saccular macula in cats. Neurosci Lett 240, 127-130.

Imagawa, M., Isu, N., Sasaki, M., Endo, K., Ikegami, H., and Uchino, Y. (1995). Axonal projections of utricular afferents to the vestibular nuclei and the abducens nucleus in cats. Neurosci Lett 186, 87-90.

Inoshita, T., and Hirano, T. (2018). Occurrence of long-term depression in the cerebellar flocculus during adaptation of optokinetic response. eLife 7, e36209.

Ireland, D.J., and Jell, R.M. (1982). Optokinetic after-nystagmus in man after loss or reduction of labyrinthine function - a preliminary report. J Otolaryngol 11, 86-90.

Iurilli, G., and Datta, S.R. (2017). Population Coding in an Innately Relevant Olfactory Area. Neuron 93, 1180-1197.e1187.

Jamali, M., Carriot, J., Chacron, M.J., and Cullen, K.E. (2013). Strong Correlations between Sensitivity and Variability Give Rise to Constant Discrimination Thresholds across the Otolith Afferent Population. J Neurosci 33, 11302-11313.

Jamali, M., Carriot, J., Chacron, M.J., and Cullen, K.E. (2019). Coding strategies in the otolith system differ for translational head motion vs. static orientation relative to gravity. Elife 8, e44573.

Jamali, M., Chacron, M.J., and Cullen, K.E. (2016). Self-motion evokes precise spike timing in the primate vestibular system. Nature communications 7, 13229.

Jareonsettasin, P., Otero-Millan, J., Ward, B.K., Roberts, D.C., Schubert, M.C., and Zee, D.S. (2016). Multiple time courses of vestibular set-point adaptation revealed by sustained magnetic field stimulation of the labyrinth. Current Biology 26, 1359-1366.

Johannesma, P., and Aertsen, A. (1982). Statistical and dimensional analysis of the neural representation of the acoustic biotope of the frog. Journal of Medical Systems 6, 399-421.

Johnston, A.R., Him, A., and Dutia, M.B. (2001). Differential regulation of GABA(A) and GABA(B) receptors during vestibular compensation. Neuroreport 12, 597-600.

Josić, K., Shea-Brown, E., Doiron, B., and de la Rocha, J. (2009). Stimulus-dependent correlations and population codes. Neural Comput 21, 2774-2804.

Kato, I., Harada, K., Hasegawa, T., Igarashi, T., Koike, Y., and Kawasaki, T. (1986). Role of the nucleus of the optic tract in monkeys in relation to optokinetic nystagmus. Brain research 364, 12-22.

Kheradmand, A., and Zee, D.S. (2012). The bedside examination of the vestibulo-ocular reflex (VOR): An update. Revue Neurologique 168, 710-719.

Kilgard, M.P., and Merzenich, M.M. (1999). Distributed representation of spectral and temporal information in rat primary auditory cortex. Hear Res 134, 16-28.

Kirsch, V., Keeser, D., Hergenroeder, T., Erat, O., Ertl-Wagner, B., Brandt, T., and Dieterich, M. (2016). Structural and functional connectivity mapping of the vestibular circuitry from human brainstem to cortex. Brain Structure and Function 221, 1291-1308.

Klam, F., and Graf, W. (2003). Vestibular signals of posterior parietal cortex neurons during active and passive head movements in macaque monkeys. Ann N Y Acad Sci 1004, 271-282.

Klöcker, A., Wiertlewski, M., Théate, V., Hayward, V., and Thonnard, J.-L. (2013). Physical Factors Influencing Pleasant Touch during Tactile Exploration. PLOS ONE 8, e79085.

Knudsen, J.T., Tollsten, L., and Bergström, L.G. (1993). Floral scents—a checklist of volatile compounds isolated by head-space techniques. Phytochemistry 33, 253-280.

Kohn, A., Coen-Cagli, R., Kanitscheider, I., and Pouget, A. (2016). Correlations and Neuronal Population Information. Annu Rev Neurosci 39, 237-256.

Kohn, A., and Smith, M.A. (2005). Stimulus dependence of neuronal correlation in primary visual cortex of the macaque. J Neurosci 25, 3661-3673.

Komiyama, T., Sato, T.R., O'Connor, D.H., Zhang, Y.-X., Huber, D., Hooks, B.M., Gabitto, M., and Svoboda, K. (2010). Learning-related fine-scale specificity imaged in motor cortex circuits of behaving mice. Nature 464, 1182-1186.

Krauzlis, R.J., Bogadhi, A.R., Herman, J.P., and Bollimunta, A. (2018). Selective attention without a neocortex. Cortex 102, 161-175.

Lambert, F.M., Beck, J.C., Baker, R., and Straka, H. (2008). Semicircular canal size determines the developmental onset of angular vestibuloocular reflexes in larval Xenopus. J Neurosci 28, 8086-8095.

Lapicque, L. (1907). Recherches quantitatives sur l'excitation électrique des nerfs traitée comme une polarisation. Journal of Physiology, Pathology, and Genetics 9, 620-635.

Laudanski, J., Edeline, J.-M., and Huetz, C. (2012). Differences between Spectro-Temporal Receptive Fields Derived from Artificial and Natural Stimuli in the Auditory Cortex. PLOS ONE 7, e50539.

Laughlin, S. (1981). A simple coding procedure enhances a neuron's information capacity. Z Naturforsch C 36, 910-912.

Le Goc, G., Lafaye, J., Karpenko, S., Bormuth, V., Candelier, R., and Debrégeas, G. (2021). Thermal modulation of Zebrafish exploratory statistics reveals constraints on individual behavioral variability. BMC Biology 19, 208.

Lee, C.C.Y., Kheradpezhouh, E., Diamond, M.E., and Arabzadeh, E. (2020). State-Dependent Changes in Perception and Coding in the Mouse Somatosensory Cortex. Cell Rep 32, 108197.

Leigh, R.J., Robinson, D.A., and Zee, D.S. (1981). A hypothetical explanation for periodic alternating nystagmus: instability in the optokinetic-vestibular system. Annals of the New York Academy of Sciences 374, 619-635.

Levitan, D., Lin, J.Y., Wachutka, J., Mukherjee, N., Nelson, S.B., and Katz, D.B. (2019). Single and population coding of taste in the gustatory cortex of awake mice. J Neurophysiol 122, 1342-1356.

Lewandowski, D., Kurowicka, D., and Joe, H. (2009). Generating random correlation matrices based on vines and extended onion method. Journal of multivariate analysis 100, 1989-2001.

Lewicki, M.S. (2002). Efficient coding of natural sounds. Nat Neurosci 5, 356-363.

Lim, R., Callister, R.J., and Brichta, A.M. (2010). An increase in glycinergic quantal amplitude and frequency during early vestibular compensation in mouse. J Neurophysiol 103, 16-24.

Lin, T.F., Gerth-Kahlert, C., Hanson, J.V.M., Straumann, D., and Huang, M.Y. (2018). Spontaneous Nystagmus in the Dark in an Infantile Nystagmus Patient May Represent Negative Optokinetic Afternystagmus. Front Neurol 9, 151.

Lin, T.F., Mohammadi, M., Cullen, K.E., Chacron, M.J., and Huang, M.Y. (2022). Optokinetic set-point adaptation functions as an internal dynamic calibration mechanism for oculomotor disequilibrium. iScience 25, 105335.

Lin, T.F., Mohammadi, M., Fathalla, A.M., Pul, D., Luthi, D., Romano, F., Straumann, D., Cullen, K.E., Chacron, M.J., and Huang, M.Y. (2019). Negative optokinetic afternystagmus in larval zebrafish demonstrates set-point adaptation. Sci Rep 9, 19039.

Lindeman, H.H. (1969). Studies on the morphology of the sensory regions of the vestibular apparatus (Berlin: Springer-Verlag).

Lisberger, S.G., Miles, F.A., Optican, L.M., and Eighmy, B.B. (1981). Optokinetic response in monkey: underlying mechanisms and their sensitivity to long-term adaptive changes in vestibuloocular reflex. J Neurophysiol 45, 869-890.

Liu, S., Gu, Y., DeAngelis, G.C., and Angelaki, D.E. (2013). Choice-related activity and correlated noise in subcortical vestibular neurons. Nat Neurosci 16, 89-97.

Lomber, S.G. (1999). The advantages and limitations of permanent or reversible deactivation techniques in the assessment of neural function. Journal of Neuroscience Methods 86, 109-117.

Lopez, C., and Blanke, O. (2011). The thalamocortical vestibular system in animals and humans. Brain Res Rev 67, 119-146.

Lyamzin, D.R., Barnes, S.J., Donato, R., Garcia-Lazaro, J.A., Keck, T., and Lesica, N.A. (2015). Nonlinear transfer of signal and noise correlations in cortical networks. J Neurosci 35, 8065-8080.

Machens, C.K., Gollisch, T., Kolesnikova, O., and Herz, A.V.M. (2005). Testing the efficiency of sensory coding with optimal stimulus ensembles. Neuron 47, 447-456.

Mackrous, I., Carriot, J., Cullen, K.E., and Chacron, M.J. (2020). Neural variability determines coding strategies for natural self-motion in macaque monkeys. Elife 9, e57484.

Maioli, C. (1988). Optokinetic nystagmus: modeling the velocity storage mechanism. J Neurosci 8, 821-832.

Mallery, R.M., Olomu, O.U., Uchanski, R.M., Militchin, V.A., and Hullar, T.E. (2010). Human discrimination of rotational velocities. Exp Brain Res 204, 11-20.

Manfredi, L.R., Saal, H.P., Brown, K.J., Zielinski, M.C., Dammann, J.F., 3rd, Polashock, V.S., and Bensmaia, S.J. (2014). Natural scenes in tactile texture. J Neurophysiol 111, 1792-1802.

Manzoni, D. (2009). Vestibulo-spinal Reflexes. In Encyclopedia of Neuroscience, M.D. Binder, N. Hirokawa, and U. Windhorst, eds. (Berlin, Heidelberg: Springer Berlin Heidelberg), pp. 4245-4250.

Marlinski, V., and McCrea, R.A. (2008a). Activity of ventroposterior thalamus neurons during rotation and translation in the horizontal plane in the alert squirrel monkey. J Neurophysiol 99, 2533-2545.

Marlinski, V., and McCrea, R.A. (2008b). Coding of self-motion signals in ventro-posterior thalamus neurons in the alert squirrel monkey. Exp Brain Res 189, 463-472.

Marquez, M.M., and Chacron, M.J. (2020). Serotonin modulates optimized coding of natural stimuli through increased neural and behavioural responses via enhanced burst firing. J Physiol 598, 1573-1589.

Marsat, G., and Maler, L. (2010). Neural heterogeneity and efficient population codes for communication signals. J Neurophysiol 104, 2543-2555.

Marsat, G., and Pollack, G.S. (2010). The structure and size of sensory bursts encode stimulus information but only size affects behavior. Journal of Comparative Physiology A 196, 315-320.

Marti, S., Bockisch, C.J., and Straumann, D. (2005). Prolonged asymmetric smooth-pursuit stimulation leads to downbeat nystagmus in healthy human subjects. Invest Ophthalmol Vis Sci 46, 143-149.

Masseck, O.A., and Hoffmann, K.-P. (2009). Comparative Neurobiology of the Optokinetic Reflex. Annals of the New York Academy of Sciences 1164, 430-439.

Massot, C., Chacron, M.J., and Cullen, K.E. (2011). Information transmission and detection thresholds in the vestibular nuclei: single neurons versus population encoding. J Neurophysiol 105, 1798-1814.

Massot, C., Schneider, A.D., Chacron, M.J., and Cullen, K.E. (2012). The vestibular system implements a linear-nonlinear transformation in order to encode self-motion. PLoS Biol 10, e1001365.

Matsuzaki, R., Kyuhou, S., Matsuura-Nakao, K., and Gemba, H. (2004). Thalamo-cortical projections to the posterior parietal cortex in the monkey. Neurosci Lett 355, 113-116.

Mattis, J., Tye, K.M., Ferenczi, E.A., Ramakrishnan, C., O'Shea, D.J., Prakash, R., Gunaydin, L.A., Hyun, M., Fenno, L.E., and Gradinaru, V. (2012). Principles for applying optogenetic tools derived from direct comparative analysis of microbial opsins. Nature methods 9, 159-172.

Mejias, J.F., and Longtin, A. (2012). Optimal heterogeneity for coding in spiking neural networks. Phys Rev Lett 108, 228102.

Meng, H., and Angelaki, D.E. (2010). Responses of ventral posterior thalamus neurons to three-dimensional vestibular and optic flow stimulation. J Neurophysiol 103, 817-826.

Meng, H., May, P.J., Dickman, J.D., and Angelaki, D.E. (2007). Vestibular signals in primate thalamus: properties and origins. J Neurosci 27, 13590-13602.

Metzen, M.G., and Chacron, M.J. (2014). Weakly electric fish display behavioral responses to envelopes naturally occurring during movement: implications for neural processing. J Exp Biol 217, 1381-1391.

Metzen, M.G., and Chacron, M.J. (2019). Envelope Coding and Processing: Implications for Perception and Behavior. In Electroreception: Fundamental Insights from Comparative Approaches, B. Carlson, J. Sisneros, A. Popper, and R. Fay, eds. (Cham: Springer), pp. 251-277.

Metzen, M.G., and Chacron, M.J. (2021). Population coding of natural electrosensory stimuli by midbrain neurons. J Neurosci 41, 3822-3841.

Metzen, M.G., Jamali, M., Carriot, J., Avila-Akerberg, O., Cullen, K.E., and Chacron, M.J. (2015). Coding of envelopes by correlated but not single-neuron activity requires neural variability. PNAS 112, 4791-4796.

Minor, L.B., Lasker, D.M., Backous, D.D., and Hullar, T.E. (1999). Horizontal Vestibuloocular Reflex Evoked by High-Acceleration Rotations in the Squirrel Monkey. I. Normal Responses. J Neurophysiol 82, 1254-1270.

Mitchell, D.E., Della Santina, C.C., and Cullen, K.E. (2016). Plasticity within non-cerebellar pathways rapidly shapes motor performance in vivo. Nature communications 7, 11238.

Mitchell, D.E., Kwan, A., Carriot, J., Chacron, M.J., and Cullen, K.E. (2018). Neuronal variability and tuning are balanced to optimize naturalistic self-motion coding in primate vestibular pathways. Elife 7, e43019.

Mizrahi, A., Shalev, A., and Nelken, I. (2014). Single neuron and population coding of natural sounds in auditory cortex. Curr Opin Neurobiol 24, 103-110.

Montijn, J.S., Goltstein, P.M., and Pennartz, C.M.A. (2015). Mouse V1 population correlates of visual detection rely on heterogeneity within neuronal response patterns. eLife 4, e10163.

Montijn, Jorrit S., Meijer, Guido T., Lansink, Carien S., and Pennartz, Cyriel M.A. (2016). Population-Level Neural Codes Are Robust to Single-Neuron Variability from a Multidimensional Coding Perspective. Cell Reports 16, 2486-2498.

Moreno-Bote, R., Beck, J., Kanitscheider, I., Pitkow, X., Latham, P., and Pouget, A. (2014). Information-limiting correlations. Nat Neurosci 17, 1410-1417.

Mueller, K.P., and Neuhauss, S.C.F. (2010). Quantitative measurements of the optokinetic response in adult fish. Journal of neuroscience methods 186, 29-34.

Mullins, M.C., Hammerschmidt, M., Haffter, P., and Nüsslein-Volhard, C. (1994). Large-scale mutagenesis in the zebrafish: in search of genes controlling development in a vertebrate. Current Biology 4, 189-202.

Muratore, R., and Zee, D.S. (1979). Pursuit after-nystagmus. Vision Res 19, 1057-1059.

Musallam, S., and Tomlinson, R.D. (2001). Nonlinear behavior of vestibulo-only cells. Annals of the New York Academy of Sciences 942, 473-474.

Mustari, M.J., Fuchs, A.F., Kaneko, C.R., and Robinson, F.R. (1994). Anatomical connections of the primate pretectal nucleus of the optic tract. J Comp Neurol 349, 111-128.

Mustari, M.J., and Ono, S. (2009). Optokinetic Eye Movements. In Encyclopedia of Neuroscience, L.R. Squire, ed. (Oxford: Academic Press), pp. 285-293.

Naganathan, S.R., Popović, M., and Oates, A.C. (2022). Left–right symmetry of zebrafish embryos requires somite surface tension. Nature 605, 516-521.

Nelken, I., Rotman, Y., and Yosef, O.B. (1999). Responses of auditory-cortex neurons to structural features of natural sounds. Nature 397, 154-157.

Nelson, A.B., Faulstich, M., Moghadam, S., Onori, K., Meredith, A., and du Lac, S. (2017). BK Channels Are Required for Multisensory Plasticity in the Oculomotor System. Neuron 93, 211-220.

Nesti, A., Beykirch, K.A., Pretto, P., and Bulthoff, H.H. (2015). Human discrimination of head-centred visual-inertial yaw rotations. Exp Brain Res 233, 3553-3564.

Neuhauss, S.C.F. (2003). Behavioral genetic approaches to visual system development and function in zebrafish. Journal of neurobiology 54, 148-160.

Nigam, S., Milton, R., Pojoga, S., and Dragoi, V. (2023). Adaptive coding across visual features during free-viewing and fixation conditions. Nature communications 14, 87.

Nouri, S., and Karmali, F. (2018). Variability in the Vestibulo-Ocular Reflex and Vestibular Perception. Neuroscience 393, 350-365.

Osborne, L.C., Palmer, S.E., Lisberger, S.G., and Bialek, W. (2008). The neural basis for combinatorial coding in a cortical population response. J Neurosci 28, 13522-13531.

Oude Lohuis, M.N., Pie, J.L., Marchesi, P., Montijn, J.S., de Kock, C.P.J., Pennartz, C.M.A., and Olcese, U. (2022). Multisensory task demands temporally extend the causal requirement for visual cortex in perception. Nature communications 13, 2864.

Paige, G.D., and Seidman, S.H. (1999). Characteristics of the VOR in Response to Linear Acceleration. Annals of the New York Academy of Sciences 871, 123-135.

Paige, G.D., and Tomko, D.L. (1991). Eye movement responses to linear head motion in the squirrel monkey. I. Basic characteristics. J Neurophysiol 65, 1170-1182.

Panzeri, S., Macke, J.H., Gross, J., and Kayser, C. (2015). Neural population coding: combining insights from microscopic and mass signals. Trends Cogn Sci 19, 162-172.

Panzeri, S., Moroni, M., Safaai, H., and Harvey, C.D. (2022). The structures and functions of correlations in neural population codes. Nat Rev Neurosci 23, 551-567.

Panzeri, S., Petersen, R.S., Schultz, S.R., Lebedev, M., and Diamond, M.E. (2001). The Role of Spike Timing in the Coding of Stimulus Location in Rat Somatosensory Cortex. Neuron 29, 769-777.

Penfield, W. (1957). Vestibular sensation and the cerebral cortex. Ann Otol Rhinol Laryngol 66, 691-698.

Perez-Nieves, N., Leung, V.C.H., Dragotti, P.L., and Goodman, D.F.M. (2021a). Neural heterogeneity promotes robust learning. Nature communications 12, 5791.

Perez-Nieves, N., Leung, V.C.H., Dragotti, P.L., and Goodman, D.F.M. (2021b). Neural heterogeneity promotes robust learning. Nature communications 12, 5791.

Pérez-Schuster, V., Kulkarni, A., Nouvian, M., Romano, S.A., Lygdas, K., Jouary, A., Dipoppa, M., Pietri, T., Haudrechy, M., and Candat, V. (2016). Sustained rhythmic brain activity underlies visual motion perception in zebrafish. Cell reports 17, 1098-1112.

Perkel, D.H., Gerstein, G.L., and Moore, G.P. (1967). Neuronal spike trains and stochastic point processes. II. Simultaneous spike trains. Biophysical journal 7, 419-440.

Petersen, R.S., Panzeri, S., and Diamond, M.E. (2001). Population coding of stimulus location in rat somatosensory cortex. Neuron 32, 503-514.

Peterson, B.W., and Boyle, R.D. (2004). Vestibulocollic Reflexes. In The Vestibular System, S.M. Highstein, R.R. Fay, and A.N. Popper, eds. (New York, NY: Springer New York), pp. 343-374.

Pitkow, X., and Meister, M. (2012). Decorrelation and efficient coding by retinal ganglion cells. Nat Neurosci 15, 628-635.

Pola, G., Thiele, A., Hoffmann, K.P., and Panzeri, S. (2003). An exact method to quantify the information transmitted by different mechanisms of correlational coding. Network: Computation in Neural Systems 14, 35.

Precht, W., and Strata, P. (1980). On the pathway mediating optokinetic responses in vestibular nuclear neurons. Neuroscience 5, 777-787.

Qian, H., Zhu, Y., Ramsey, D.J., Chappell, R.L., Dowling, J.E., and Ripps, H. (2005). Directional asymmetries in the optokinetic response of larval zebrafish (Danio rerio). Zebrafish 2, 189-196.

Qian, Z., Micorescu, M., Yakhnitsa, V., and Barmack, N.H. (2012). Climbing fiber activity reduces 14-3-3-θ regulated GABA(A) receptor phosphorylation in cerebellar Purkinje cells. Neuroscience 201, 34-45.

Rabbitt, R.D. (1999). Directional coding of three-dimensional movements by the vestibular semicircular canals. Biological cybernetics 80, 417-431.

Raphan, T., Matsuo, V., and Cohen, B. (1979). Velocity storage in the vestibulo-ocular reflex arc (VOR). Exp Brain Res 35, 229-248.

Reisine, H., and Raphan, T. (1992). Neural basis for eye velocity generation in the vestibular nuclei of alert monkeys during off-vertical axis rotation. Exp Brain Res 92, 209-226.

Rieke, F., Bodnar, D.A., and Bialek, W. (1995). Naturalistic stimuli increase the rate and efficiency of information transmission by primary auditory afferents. Proceedings of the Royal Society of London - Series B: Biological Sciences 262, 259-265.

Rieke, F., Warland, D., de Ruyter van Steveninck, R.R., and Bialek, W. (1996). Spikes: Exploring the Neural Code (Cambridge, MA: MIT).

Ringach, D.L., Shapley, R.M., and Hawken, M.J. (2002). Orientation selectivity in macaque V1: diversity and laminar dependence. J Neurosci 22, 5639-5651.

Roberts, M.M., Schira, M.M., Spehar, B., and Isherwood, Z.J. (2022). Nature in motion: The tuning of the visual system to the spatiotemporal properties of natural scenes. J Vis 22, 7.

Robin, A.A.I., Stefano, P., and Christoph, K. (2013). Neural Codes Formed by Small and Temporally Precise Populations in Auditory Cortex. The Journal of Neuroscience 33, 18277.

Robinson, D.A. (1968). The oculomotor control system: A review. Proceedings of the IEEE 56, 1032-1049.

Robinson, D.A. (1981). The use of control systems analysis in the neurophysiology of eye movements. Annu Rev Neurosci 4, 463-503.

Roddey, J.C., Girish, B., and Miller, J.P. (2000). Assessing the Performance of Neural Encoding Models in the Presence of Noise. Journal of Computational Neuroscience 8, 95-112.

Roy, J.E., and Cullen, K.E. (2004). Dissociating self-generated from passively applied head motion: neural mechanisms in the vestibular nuclei. J Neurosci 24, 2102-2111.

Ruderman, D.L. (1994). The statistics of natural images. Network: Computation in Neural Systems 5, 517-548.

Ruderman, D.L., and Bialek, W. (1994). Statistics of natural images: Scaling in the woods. Phys Rev Lett 73, 814-817.

Ruff, D.A., and Cohen, M.R. (2019). Simultaneous multi-area recordings suggest that attention improves performance by reshaping stimulus representations. Nat Neurosci 22, 1669-1676.

Sadeghi, S.G., Chacron, M.J., Taylor, M.C., and Cullen, K.E. (2007a). Neural Variability, Detection Thresholds, and Information Transmission in the Vestibular System. J Neurosci 27, 771-781.

Sadeghi, S.G., and Cullen, K.E. (2015). Vestibular System. In International Encyclopedia of the Social & Behavioral Sciences (Second Edition), J.D. Wright, ed. (Oxford: Elsevier), pp. 63-69.

Sadeghi, S.G., Minor, L.B., and Cullen, K.E. (2007b). Response of vestibular-nerve afferents to active and passive rotations under normal conditions and after unilateral labyrinthectomy. J Neurophysiol 97, 1503-1514.

Sadeghi, S.G., Minor, L.B., and Cullen, K.E. (2011). Multimodal integration after unilateral labyrinthine lesion: single vestibular nuclei neuron responses and implications for postural compensation. J Neurophysiol 105, 661-673.

Sadeghi, S.G., Mitchell, D.E., and Cullen, K.E. (2009). Different neural strategies for multimodal integration: comparison of two macaque monkey species. Exp Brain Res 195, 45-57.

Schiff, D., Cohen, B., Büttner-Ennever, J., and Matsuo, V. (1990). Effects of lesions of the nucleus of the optic tract on optokinetic nystagmus and after-nystagmus in the monkey. Exp Brain Res 79, 225-239.

Schlack, A., Hoffmann, K.P., and Bremmer, F. (2002). Interaction of linear vestibular and visual stimulation in the macaque ventral intraparietal area (VIP). Eur J Neurosci 16, 1877-1886.

Schneider, A.D., Jamali, M., Carriot, J., Chacron, M.J., and Cullen, K.E. (2015). The increased sensitivity of irregular peripheral canal and otolith vestibular afferents optimizes their encoding of natural stimuli. J Neurosci 35, 5522-5536.

Schneidman, E., Berry, M.J., 2nd, Segev, R., and Bialek, W. (2006). Weak pairwise correlations imply strongly correlated network states in a neural population. Nature 440, 1007-1012.

Schwarz, U., Busettini, C., and Miles, F.A. (1989). Ocular Responses to Linear Motion Are Inversely Proportional to Viewing Distance. Science 245, 1394-1396.

Shamir, M., and Sompolinsky, H. (2006). Implications of neuronal diversity on population coding. Neural Comput 18, 1951-1986.

Shannon, R.V., Zeng, F.G., and Wygonski, J. (1998). Speech recognition with altered spectral distribution of envelope cues. J Acoust Soc Am 104, 2467-2476.

Sharpee, T.O., Calhoun, A.J., and Chalasani, S.H. (2014). Information theory of adaptation in neurons, behavior, and mood. Curr Opin Neurobiol 25, 47-53.

Shepard, N.T., Telian, S.A., and Smith-Wheelock, M. (1990). Habituation and balance retraining therapy. A retrospective review. Neurol Clin 8, 459-475.

Shinder, M.E., and Newlands, S.D. (2014). Sensory convergence in the parieto-insular vestibular cortex. J Neurophysiol 111, 2445-2464.

Simmons, K.D., Prentice, J.S., Tkačik, G., Homann, J., Yee, H.K., Palmer, S.E., Nelson, P.C., and Balasubramanian, V. (2013). Transformation of Stimulus Correlations by the Retina. PLoS Comp Biol 9, e1003344.

Simoncelli, E.P., and Olshausen, B.A. (2001). Natural image statistics and neural representation. Annu Rev Neurosci 24, 1193-1216.

Smith, C.A., Lowry, O.H., and Wu, M.L. (1954). The electrolytes of the labyrinthine fluids. Laryngoscope 64, 141-153.

Srinath, R., Ruff, D.A., and Cohen, M.R. (2021). Attention improves information flow between neuronal populations without changing the communication subspace. Curr Biol 31, 5299-5313 e5294.

Stackman, R.W., and Taube, J.S. (1997). Firing properties of head direction cells in the rat anterior thalamic nucleus: Dependence on vestibular input. J Neurosci 17, 4349-4358.

Stahl, J.S. (2004). Using eye movements to assess brain function in mice. Vision Res 44, 3401-3410.

Staiger, J.F., Flagmeyer, I., Schubert, D., Zilles, K., Kotter, R., and Luhmann, H.J. (2004). Functional diversity of layer IV spiny neurons in rat somatosensory cortex: quantitative morphology of electrophysiologically characterized and biocytin labeled cells. Cereb Cortex 14, 690-701.

Stanley, G.B. (2008). Au Naturel. Neuron 58, 467-469.

Stefanini, F., Kushnir, L., Jimenez, J.C., Jennings, J.H., Woods, N.I., Stuber, G.D., Kheirbek, M.A., Hen, R., and Fusi, S. (2020). A Distributed Neural Code in the Dentate Gyrus and in CA1. Neuron 107, 703-716.e704.

Ter Braak, J.W.G. (1936). Untersuchungen uber Optokinetischen Nystagmus. Arch Neurol Physiol 21, 309-376.

Teşileanu, T., Cocco, S., Monasson, R., and Balasubramanian, V. (2019). Adaptation of olfactory receptor abundances for efficient coding. eLife 8, e39279.

Tesileanu, T., Piasini, E., and Balasubramanian, V. (2022). Efficient processing of natural scenes in visual cortex. Front Cell Neurosci 16, 1006703.

Thoroughman, K.A., Fine, M.S., and Taylor, J.A. (2007). Trial-by-trial motor adaptation: a window into elemental neural computation. Progress in brain research 165, 373-382.

Tomlinson, R.D., Rubin, A.M., Wallace, I.R., and Barber, H.O. (1984). Optokinetic afternystagmus and post rotatory nystagmus in patients with unilateral labyrinthine lesions. J Otolaryngol 13, 217-220.

Tripathy, S.J., Padmanabhan, K., Gerkin, R.C., and Urban, N.N. (2013). Intermediate intrinsic diversity enhances neural population coding. PNAS 110, 8248-8253.

Umakantha, A., Morina, R., Cowley, B.R., Snyder, A.C., Smith, M.A., and Yu, B.M. (2021). Bridging neuronal correlations and dimensionality reduction. Neuron 109, 2740-2754.e2712.

Urai, A.E., Doiron, B., Leifer, A.M., and Churchland, A.K. (2022). Large-scale neural recordings call for new insights to link brain and behavior. Nat Neurosci 25, 11-19.

Usrey, W.M., and Reid, R.C. (1999). Synchronous activity in the visual system. Annual review of physiology 61, 435-456.

Valko, Y., Lewis, R.F., Priesol, A.J., and Merfeld, D.M. (2012). Vestibular labyrinth contributions to human whole-body motion discrimination. J Neurosci 32, 13537-13542.

Vibert, N., Beraneck, M., Bantikyan, A., and Vidal, P.P. (2000). Vestibular compensation modifies the sensitivity of vestibular neurones to inhibitory amino acids. Neuroreport 11, 1921-1927.

Vig, E., Dorr, M., and Cox, D. (2014). Large-scale optimization of hierarchical features for saliency prediction in natural images. Paper presented at: Proceedings of the IEEE conference on computer vision and pattern recognition.

Voss, R.F., and Clarke, J. (1975). 1/F noise in music and speech. Nature 258, 317-318.

Wada, N., Funabiki, K., and Nakanishi, S. (2014). Role of granule-cell transmission in memory trace of cerebellum-dependent optokinetic motor learning. Proceedings of the National Academy of Sciences 111, 5373-5378.

Waddington, J., and Harris, C.M. (2013). The distribution of quick phase interval durations in human optokinetic nystagmus. Exp Brain Res 224, 179-187.

Waespe, W., Cohen, B., and Raphan, T. (1983). Effects of flocculectomy on vestibular and optokinetic nystagmus and unit activity in the vestibular nuclei. Adv Otorhinolaryngol 30, 226-229.

Waespe, W., and Henn, V. (1978). Reciprocal changes in primary and secondary optokinetic after-nystagmus (OKAN) produced by repetitive optokinetic stimulation in the monkey. Archiv für Psychiatrie und Nervenkrankheiten 225, 23-30.

Waespe, W., Huber, T., and Henn, V. (1978). Dynamic changes of optokinetic after-nystagmus (OKAN) caused by brief visual fixation periods in monkey and in man. Arch Psychiatr Nervenkr (1970) 226, 1-10.

Waespe, W., and Wolfensberger, M. (1985). Optokinetic nystagmus (OKN) and optokinetic after-responses after bilateral vestibular neurectomy in the monkey. Exp Brain Res 60, 263-269.

Wallman, J., and Velez, J. (1985). Directional asymmetries of optokinetic nystagmus: developmental changes and relation to the accessory optic system and to the vestibular system. J Neurosci 5, 317-329.

Wang, Z., and Chacron, M.J. (2021). Synergistic population coding of natural communication stimuli by hindbrain electrosensory neurons. Sci Rep 11, 10840.

Wark, B., Fairhall, A., and Rieke, F. (2009). Timescales of inference in visual adaptation. Neuron 61, 750-761.

Wark, B., Lundstrom, B.N., and Fairhall, A. (2007). Sensory adaptation. Current Opinion in Neurobiology 17, 423-429.

Warland, D.K., Reinagel, P., and Meister, M. (1997). Decoding visual information from a population of retinal ganglion cells. J Neurophysiol 78, 2336-2350.

Weber, A.I., and Fairhall, A.L. (2019). The role of adaptation in neural coding. Current opinion in neurobiology 58, 135-140.

Whitmire, C.J., and Stanley, G.B. (2016). Rapid sensory adaptation redux: a circuit perspective. Neuron 92, 298-315.

Wiertlewski, M., Hudin, C., and Hayward, V. (2011). On the 1/f noise and non-integer harmonic decay of the interaction of a finger sliding on flat and sinusoidal surfaces. Paper presented at: 2011 IEEE World Haptics Conference.

Wijesinghe, R., Protti, D.A., and Camp, A.J. (2015). Vestibular Interactions in the Thalamus. Front Neural Circuits 9, 79.

Wilke, S.D., and Eurich, C.W. (2002). Representational Accuracy of Stochastic Neural Populations. Neural Computation 14, 155-189.

Wilson, V., Boyle, R., Fukushima, K., Rose, P., Shinoda, Y., Sugiuchi, Y., and Uchino, Y. (1995a). The vestibulocollic reflex. J Vestib Res 5, 147-170.

Wilson, V.J., Boyle, R., Fukushima, K., Rose, P.K., Shinoda, Y., Sugiuchi, Y., and Uchino, Y. (1995b). The vestibulocollic reflex. J Vestib Res 5, 147-170.

Wirth, A.M., and et al. (2018). White Matter Connectivity of the VisualVestibular Cortex Examined by Diffusion-Weighted Imaging. Brain Connectivity 8, 235.

Wolpert, D.M., Ghahramani, Z., and Flanagan, J.R. (2001). Perspectives and problems in motor learning. Trends in cognitive sciences 5, 487-494.

Woolley, S.M., Fremouw, T.E., Hsu, A., and Theunissen, F.E. (2005). Tuning for spectro-temporal modulations as a mechanism for auditory discrimination of natural sounds. Nat Neurosci 8, 1371-1379.

Wright, G.A., and Thomson, M.G.A. (2005). Chapter Eight - Odor Perception and the Variability in Natural Odor Scenes. In Recent Advances in Phytochemistry, J.T. Romeo, ed. (Elsevier), pp. 191-226.

Wu, Y., Dal Maschio, M., Kubo, F., and Baier, H. (2020a). An Optical Illusion Pinpoints an Essential Circuit Node for Global Motion Processing. Neuron 108, 722-734.e725.

Wu, Y., Dal Maschio, M., Kubo, F., and Baier, H. (2020b). An optical illusion pinpoints an essential circuit node for global motion processing. Neuron 108, 722-734.

Xia, J., Marks, T.D., Goard, M.J., and Wessel, R. (2021). Stable representation of a naturalistic movie emerges from episodic activity with gain variability. Nature communications 12.

Yakushin, S.B., Raphan, T., and Cohen, B. (2017). Coding of Velocity Storage in the Vestibular Nuclei. Frontiers in Neurology 8.

Yoshida, T., and Ohki, K. (2020). Natural images are reliably represented by sparse and variable populations of neurons in visual cortex. Nature communications 11, 872.

Yu, X.J., Thomassen, J.S., Dickman, J.D., Newlands, S.D., and Angelaki, D.E. (2014). Long-term deficits in motion detection thresholds and spike count variability after unilateral vestibular lesion. J Neurophysiol 112, 870-889.

Zee, D.S., Jareonsettasin, P., and Leigh, R.J. (2017). Ocular stability and set-point adaptation. Philosophical Transactions of the Royal Society B: Biological Sciences 372, 20160199.

Zee, D.S., Yee, R.D., and Robinson, D.A. (1976). Optokinetic responses in labyrinthine-defective human beings. Brain Res 113, 423-428.

Zeldenrust, F., Gutkin, B., and Denéve, S. (2021). Efficient and robust coding in heterogeneous recurrent networks. PLoS Comp Biol 17, e1008673.

Zheng, Y., Jia, S., Yu, Z., Liu, J.K., and Huang, T. (2021). Unraveling neural coding of dynamic natural visual scenes via convolutional recurrent neural networks. Patterns 2, 100350.

Zhou, Y., and Wang, X. (2010). Cortical processing of dynamic sound envelope transitions. J Neurosci 30, 16741-16754.

Zohary, E., Shadlen, M.N., and Newsome, W.T. (1994). Correlated neuronal discharge rate and its implications for psychophysical performance. Nature 370, 140-143.

Zwicker, D., Murugan, A., and Brenner, M.P. (2016). Receptor arrays optimized for natural odor statistics. PNAS 113, 5570-5575.